TRABECULAR BONE REMODELING AROUND IMPLANTS

by

Edward John Cheal

B.S., Michigan State University
(1980)

S.M. Mechanical Engineering,
Massachusetts Institute of Technology
(1983)

SUBMITTED TO
THE HARVARD-M.I.T. DIVISION OF HEALTH SCIENCES AND TECHNOLOGY
IN PARTIAL FULFILLMENT OF THE REQUIREMENTS
FOR THE DEGREE OF

DOCTORATE OF PHOLOSOPHY

at the
MASSACHUSETTS INSTITUTE OF TECHNOLOGY

June, 1986

Signature of Author _____
Division of Health Sciences and Technology

Certified by _____ 5/2/86
Professor Wilson C. Hayes, Thesis Supervisor

Accepted by _____ 5/2/86
Professor Roger G. Mark, Chairman
Division of Health Sciences and Technology

TRABECULAR BONE REMODELING AROUND IMPLANTS

by

Edward John Cheal

Submitted to the Harvard-M.I.T. Division
of Health Sciences and Technology
on May 2, 1986 in partial fulfillment of the
requirements for the Degree of Doctorate of Philosophy in
Medical Engineering

Abstract

Mechanical stresses are widely assumed to influence the form and structure of bone. The implantation of prosthetic components into trabecular bone are also assumed to alter the stresses in the surrounding trabeculae and these altered stresses are often implicated in the pathogenesis of component loosening. The objective of this investigation was to examine the stress-morphology relationships for trabecular bone around implants for which there was a controlled and predictable alteration in the stress fields. For this purpose two different experimental models were developed using geometrically simplified implants of various materials and surface conditions. Cobalt chromium cylinders with a sintered-bead porous coating were implanted unilaterally into ovine calcanei and stainless steel spheres with either a polished surface or a sintered-bead porous coating were implanted unilaterally into equine patellae. The animals were maintained for periods of 10 to 24 weeks. Stereologic methods were then used to quantify the morphology of the trabecular bone in the experimental specimens and in the untreated contralateral controls. Structural analyses were performed using the displacement-based finite element method to predict the stresses surrounding the implants. The finite element models were validated by comparing the principal stress directions with the material orientation in the control specimens. This assumes that the trabecular architecture was aligned with the principal stress directions in accordance with the trajectorial theory of bone architecture. A linear regression for the control equine patellae yielded an $R^2 = 0.87$. The remodeling response was then evaluated by comparing the stresses and trabecular alignment around the implants in the experimental specimens. A linear regression for the experimental equine patellae yielded an $R^2 = 0.89$. The two models were distinguished by the high degree of trabecular orientation in the ovine calcanei as opposed to the more isotropic architecture of the equine patellae. As a consequence, the changes induced in the trabecular orientation were greater in the equine patellae. In general, the remodeling response around the smooth implants was greater than that around those porous implants which exhibited bone ingrowth. In accordance with these differences, the finite element models predicted greater changes in the stresses adjacent to the smooth implants due to the nonlinear boundary conditions. However, it did not appear that the trajectorial theory, in

its simplest form, was applicable to the remodeling induced by the implants. In both models, the trabeculae were most often aligned with the stress component of the greatest magnitude. However, in the equine models, the alignment was better in regions where tension predominated. In some regions were compression predominated, the principal material direction was 90^{o} to the direction of principal compression. This suggests that cross struts may be formed to resist buckling of the trabeculae under compression. The equine models also demonstrated that, under certain circumstances, small changes in the stress state may result in large changes in the principal material orientation. In contrast, in the ovine models, the highly oriented trabeculae were more often aligned with the direction of principal compression. The stress changes induced by the ingrown porous implants were insufficient to induce significant changes in the trabecular orientation. Both models demonstrated a linear relationship between the change in bone areal density and the change in von Mises effective stress.

Thesis committee: Wilson C. Hayes, Ph.D.
Professor of Biomechanics,
Harvard-MIT Division of Health Sciences and Technology

Augustus A. White, III, M.D., D.M.S.
Professor of Orthopaedic Surgery,
Harvard Medical School and
Harvard-MIT Division of Health Sciences and Technology

David M. Nunamaker, V.M.D.
Jacques Jenny Professor of Orthopaedic Surgery,
University of Pennsylvania,
School of Veterinary Medicine

W. Gilbert Strang, Ph.D.
Professor of Mathematics,
Massachusetts Institute of Technology

Acknowledgments

This thesis exists thanks to the efforts of my supervisor and mentor Toby Hayes as well as the other members of my thesis committee. Toby has created and maintained an exceptional research environment at the Orthopaedic Biomechanics laboratory of the Beth Israel Hospital. I am most grateful for the opportunity to learn and grow under such fine supervision.

Ernie Cravalho deserves much praise for the development of the Medical Engineering and Medical Physics program. This program provided me with a unique educational opportunity from which I will reap the benefits for the rest of my career.

Thanks also to all of my colleagues at the O.B.L. Brian Snyder should probably be a co-author, considering the many ideas he shared and the time we spent in discussion. Special thanks also to Tom Edwards, Tobin Gerhart, Jason Harry, and Jeff Lotz, for their advice and support. I have been surrounded by true professionals.

And thank-you to Anne, for giving me the strength to reach my goals, and much more.

I gratefully acknowledge the financial support of the Medical Engineering program and the National Institutes of Health.

This thesis is dedicated to my mother and my father.

Table of Contents

1.0 Introduction

It is widely assumed that mechanical stresses influence the form and structure of bone. The concept of stress-induced bone remodeling was popularized by the German anatomist Julius Wolff (1892). This ability to adapt to the mechanical environment makes bone a fascinating subject of study. More importantly, the remodeling response of bone to orthopaedic implants may determine their long term success or ultimate failure.

The implantation of prosthetic components into trabecular bone can be expected to alter stresses in the surrounding trabeculae. These altered stresses are often implicated in the pathogenesis of component loosening and in the development of fibrous tissue interfaces between component and bone. One approach toward the elimination of loosening is to design components that create compatible stresses in the surrounding trabeculae, thereby utilizing the remodeling potential of trabecular bone to achieve implant fixation. This investigation concerns the response of trabecular bone to a controlled and predictable alteration in the stress fields around an implant.

Two different experimental models were developed using geometrically simplified implants of various materials and surface conditions. These implants were surgically inserted in the ovine calcaneus and the equine patella. Both of these bones include large regions of highly oriented trabecular bone which are ideal for study of the normal and remodeled internal architecture. The anatomy of these bones, including the tendon

and ligament attachments, are sufficiently simple to allow for structural analysis using standard engineering techniques.

This investigation primarily involved the development and analysis of structural models and the morphologic analysis of experimental trabecular bone specimens for the investigation of implant-induced remodeling. In Chapter 1 the relevant literature is reviewed. Special attention was given to studies of the morphologic response of trabecular bone to implants. In Chapter 2 the experimental models are described and the analytical methods are developed. Much effort was spent on the generation of accurate load and material property data for input to the finite element analyses as well as the development of mesh generation and manipulation techniques. Stereologic methods were used to quantify the morphology of the trabecular bone in the experimental and control specimens. These methods have become standard in the analysis of trabecular bone architecture. Various techniques of statistical analysis were used to examine the relationships between the predictions of the finite element models and the measured morphologic parameters. In Chapter 3 the results of the morphologic and structural analyses are presented and the correlations between the structural predictions and the bone architectural changes are presented. In Chapter 4 the results are discussed as relevant to the performance of orthopaedic implants. The results of this investigation are summarized in Chapter 5.

1.1 Mechanical Properties of Trabecular Bone

The accuracy of mathematical models of bone-implant systems are

dependent on the accuracy of material property representations. Numerous studies have addressed the mechanical properties of trabecular bone as a function of various physical parameters, including bone mineral content, density, and other morphological parameters such as contiguity ratio (a measure of the degree of interconnection between trabeculae) and degree of trabecular orientation. Furthermore, microstructural models of trabecular bone have been formulated and analyzed based on the results of in vitro material tests. Previous investigations on the mechanical properties of trabecular bone which are of particular relevance for the present studies are reviewed.

Normal skeletal tissue is comprised of two types of bone distinguished by different morphological characteristics. The diaphyses of long bones are composed almost entirely of compact or cortical bone with their characteristic Haversian Systems. Compact bone also forms a structural shell over the metaphyses of long bones and the entire surface of the patella, vertebrae, and all other bones. Cancellous or trabecular bone is continuous with the inner surface of the cortical shell and is characterized by a three-dimensional porous architecture. The trabecular structure has been described as a lattice of interconnecting plates and columns of bone with fluid (marrow) filled spaces. It is generally assumed that the material properties of the calcified tissue which forms the trabeculae are similar to those of compact bone. This was demonstrated by mechanical testing of individual trabeculae (Townsend et al. 1975a), but debate continues on this issue (Williams and Lewis 1982). However, it is the structural properties of trabecular bone which are critical for the mechanics of normal and

prosthetically resurfaced joints. These structural properties, or global material properties, are a function of the individual component material properties and the structural organization or architecture. One of the simplest and most critical parameters determining the structural properties of trabecular bone is the bone porosity or, inversely, the volume density of the mineralized component.

1.1.1 Experimental Data

Numerous studies have examined the structural properties of trabecular bone using in vitro mechanical tests (Behrens et al. 1974; Carter and Hayes 1977; Galante et al. 1970; Harrigan et al. 1981; Hayes and Carter 1976; Weaver and Chalmers 1966; Williams and Lewis 1982). Various measures of the proportion of mineralized tissue have been employed for correlation with the structural properties. These measures include volume density (mineralized tissue volume per total tissue volume), apparent density (mineralized tissue mass per total tissue volume), and ash density (ash weight per total tissue volume). Fortunately, the volume density of normal trabecular bone is linearly related to the apparent density and ash density (McElhaney et al. 1970; Muellar et al. 1966). Other parameters have been investigated including the contribution of marrow and effect of strain rate on the structural properties, as well as the viscoelastic component of the structural properties.

Carter and Hayes (1977) investigated the compressive behavior of trabecular bone as a function of strain rate with and without marrow in

<u>situ</u>. Cylindrical specimens of human and bovine trabecular bone were tested in confined compression at strain rates from 0.001 per second to 10.0 per second. Apparent density was measured for correlation with the modulus and strength. They found that the presence of marrow was only significant at the highest strain rate, which is well beyond the physiologic range (Lanyon et al. 1975). An empirical relationship for the compressive strength as a function of the strain rate and apparent density was established:

$$S = 68\dot{\varepsilon}^{0.06}\rho^{2}$$

where S = compressive strength (MPa), $\dot{\varepsilon}$ = strain rate (sec^{-1}), and ρ = apparent density (gm/cc). A similar relationship for the compressive modulus was established:

$$E = 3790\dot{\varepsilon}^{0.06}\rho^{3}$$

where E = compressive modulus (MPa). These relationships suggested that the mechanical behavior of bone is similar to that of fluid-filled porous engineering materials. Carter et al. (1979) later found that the relationship for strength and apparent density was similar in tension and that the modulus in tension was equal to the modulus in compression.

Pugh et al. (1973b) investigated the viscoelastic properties of trabecular bone over a wide frequency range. Fresh and defatted trabecular bone was tested in a viscoelastometer from 100 to 3000 Hz. They also measured the volume fraction and contiguity ratio for

correlation with the viscoelastic properties. They found that the loss tangent (the viscous component) was unmeasurable over the frequency range. They also found a positive correlation between the volume fraction and the stiffness of the specimens and a positive correlation between the contiguity ratio and the stiffness. They concluded that this correlation was a demonstration of the importance of bending deformation with stiffening by lateral support.

1.1.2 Quantitative Morphology

The structure of trabecular bone has been studied using various imaging techniques, including radiographs, scanning electron micrographs, and serial micrographs. The techniques used to quantify the structural parameters are collectively referred to as stereology, with general texts on the subject provided by Weibel and Elias (1967), Dehoff and Rhines (1968), and Underwood (1970). These methods provide a means for the determination of trabecular bone density, degree of anisotropy and direction of principle orientation, and other more specific measures such as average trabecular width and contiguity ratio. These data may then be used to quantify normal trabecular structure and to study pathologic or adaptive remodeling processes. Correlations between trabecular bone structural parameters and the mechanical properties are also under study for the prediction of global material properties (Snyder 1987).

The general technique used to examine trabecular bone architecture is the method of directed secants (Saltykov 1958; Hilliard 1962). This

method uses intersection counts from a test array on plane sections. Merz (1967) developed the application to trabecular bone for the measurement of volume and surface density and average trabecular width. Whitehouse (1974) applied the technique for the measurement of the degree and direction of trabecular bone anisotropy. Harrigan and Mann (1984) showed that, assuming orthotropy, trabecular bone anisotropy can be represented by a second rank symmetric tensor. Applications of stereology to trabecular bone include studies of the human iliac crests (Merz and Schenk 1970a, 1970b; Wakamatsu and Sissons 1969; Whitehouse 1977), vertebrae (Whitehouse et al. 1971), proximal and distal femora (Pugh et al. 1974; Whitehouse and Dyson 1974), sterna (Whitehouse 1975), patellae (Raux et al. 1975), canine ribs (Albright et al. 1978), and a comparative study of a number of bones from man, rhesus monkey, beagle and miniature pig (Beddoe 1978).

A classification of trabecular bone microstructure has been proposed based on microscopic observations (Singh 1978). The general types are based on systems of interconnecting rods, interconnecting rods and plates, and interconnecting plates. An alternate classification system is that of open cells (rods) or closed cells (plates) in an asymmetric or collumnar organization (Gibson 1984; Beaupre and Hayes 1985). These classifications form the basis of microstructural models of trabecular bone, discussed below.

1.1.3 Microstructural Models

One approach for investigating the mechanics of trabecular bone is

the development and analysis of idealized microstructural models. These models can provide insight into the mechanics of trabecular bone deformation and fracture. They can also provide a vehicle for investigating the relationships between trabecular bone architecture and the global mechanical properties. Finally, with careful application, the microstructural models can provide means for calculation of the microscopic stress values based on the global stress values (i.e. those based on an assumption of continuum behavior of an elastic material of properties equivalent to those of trabecular bone).

Several approaches have been taken for the development of microstructural models. Gibson (1985), Harrigan (1985), and Townsend et al. (1975b) used standard beam and plate theories to develop relatively simple models consisting of jointed trusses, beams, and plates. A more complex model was developed by Klever et al. (1985) by extending a plate and beam model with statistical distributions describing the beam orientations. Williams and Lewis (1982) used a two-dimensional finite element analysis with the mesh geometry based on an actual tracing from a trabecular bone specimen. Pugh et al. (1973a) also generated a finite element model where the model geometry was an idealized collection of plate elements based on microscopic observations of a subchondral plate and supporting trabecular bone. Finally, Beaupre and Hayes (1985) developed a three-dimensional finite element model base on an open-celled porous structure.

The elastic modulus of the trabecular bone tissue is an important parameter for microstructural models and is under current debate. The

most common assumption is that the trabecular bone material is similar to compact bone. The only direct experimental data comes from Townsend et al. (1975a) from buckling studies of individual trabeculae. They concluded that the modulus of trabecular tissue is approximately equal to that of compact bone. However, the validity of their data has been questioned (Williams and Lewis 1982). Indirect evidence for the tissue modulus comes from experimental data on the macroscopic modulus of trabecular bone. The tissue modulus can be approximated by extrapolation from a relationship between the modulus and trabecular bone density. The data from Carter and Hayes (1977) suggest that the tissue modulus of trabecular bone is equal to that of compact bone. However, extrapolation of the data from Williams and Lewis (1982) suggests that the tissue modulus is roughly a factor of 10 less than that of compact bone. Indirect experimental data also comes from Murray et al. (1984) in which the modulus of the cortical shell from the proximal tibia was measured. In the proximal metaphysis of the tibia, as in other regions, the cortical shell is quite thin, and appears to be simply a condensation of trabeculae. The data from Murray et al. indicate that the modulus of this shell is as low as a factor of ten less than that of diaphyseal cortical bone. However, extrapolation of experimental data is probably a poor predictor of the tissue modulus, and further direct experimental data is needed.

To evaluate the applicability of a proposed microstructural model, the global stiffness and strength predictions are compared to experimentally measured values as a function of apparent density and anisotropy. Gibson (1985) proposed four microstructural models based on

four assumed classifications of trabecular bone structure: asymmetric open-celled, asymmetric close-celled, columnar open-celled, and columnar close-celled (Figure 1.1). She then established the density dependence for the global stiffness, elastic buckling stress, and plastic collapse stress, for each of the models using standard formulae. Gibson also tabulated published stiffness and strength data grouped by the four assumed classifications. The division between open- and close-celled types was assumed to be at a volume density of 20%. Comparison of the functional dependencies for the longitudinal modulus and strength on volume density between the model predictions and experimental data showed reasonable agreement (Table 1.1). Unfortunately, no statistical data were presented. The straight lines corresponding to the tabulated functional dependencies were simply drawn through the data points on log-log graphs. Also, the experimental data from transverse directions contained too much scatter for comparison with the model predictions. Nonetheless, the demonstrated correspondence between the models and the experimental data is encouraging for the further development of such simple microstructural models.

An alternate approach to the analysis of trabecular bone mechanics has been to develop a structural model which is more closely based on actual observed architecture. Pugh et al. (1973a) analyzed a finite element model constructed of plate elements representing a section of subchondral bone and the supporting trabecular bone. The geometry of the model was based on observations from microscopic sections of proximal tibiae. Thus, the model was a compromise between a highly idealized model of generic trabecular bone and a geometrically accurate

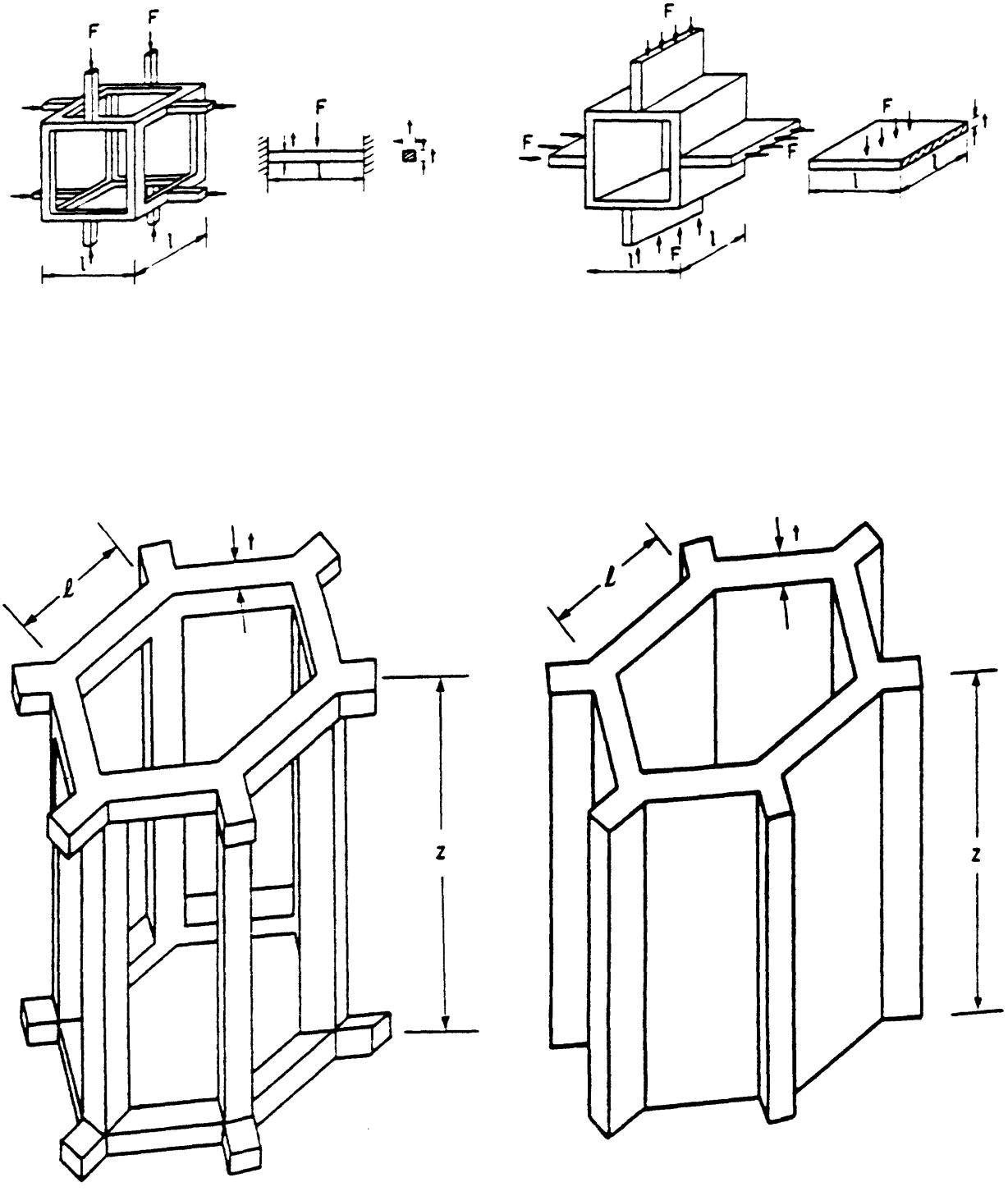

Figure 1.1: Microstructural models of trabecular bone. Clockwise from top-left: asymmetric open-celled, asymmetric close-celled, columnar close-celled, and columnar open-celled. From Gibson (1985).

Table 1.1

Density Dependence of Properties of Cellular Materials
(Adapted from Gibson 1985)

Property	Cubic opened-cell	Cubic closed-cell	Columnar opened-cell	Columnar closed-cell
Elastic modulus	ρ^2	ρ^3	ρ	ρ
Elastic collapse	ρ^2	ρ^3	ρ^2	ρ^3
Plastic collapse	$\rho^{3/2}$	ρ^2	ρ	ρ

model of an actual bone specimen. The results of the analyses suggested the importance of bending in trabecular bone deformation. However, it is not surprising that a model based on plate elements should deform primarily by bending. Williams and Lewis (1982) generated a two-dimensional model from actual tracings of a trabecular bone specimen. Their purpose was to develop a method for predicting the global stiffness coefficients based on analyses of the observed morphology. A horizontal section through columnar trabecular bone was chosen to allow for an assumption of plane strain. The model was then analyzed using applied global strains to establish the elastic constants assuming transverse isotropy for the global material properties. For the axial stiffness, they assumed that the global stiffness was proportional to the volume fraction of trabecular bone. This assumption is valid if the mode of global axial deformation is purely axial deformation of the trabecular columns. Their approach did result in a significant linear correlation between area fraction and elastic modulus thus supporting this assumption. Reasonable agreement was found between the elastic constants predicted by the model and those measured experimentally, although the models tended to overestimate the material stiffness. This is not surprising given the assumption of plane strain. As discussed above, their experimental data suggests that the modulus of trabecular bone tissue is much less than that of cortical bone.

Beaupre and Hayes (1985) developed a three-dimensional finite element model of an open-celled porous foam as a microstructural model of trabecular bone. The unit cell consisted of a body-centered spherical void which intersects with the adjacent voids (Figure 1.2).

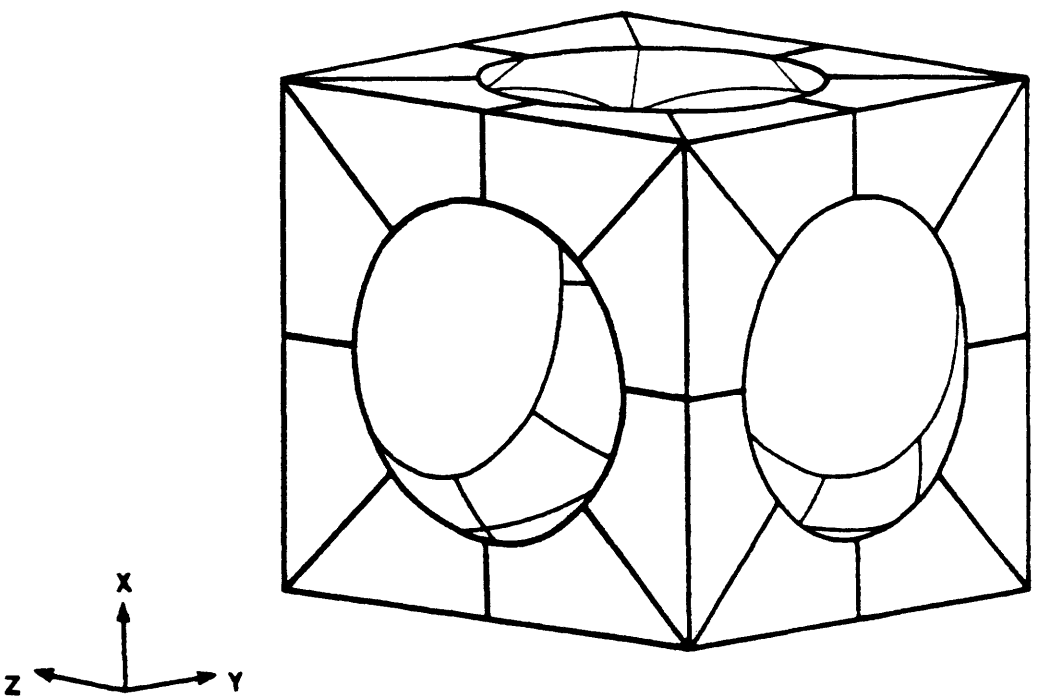

Figure 1.2: Open-celled porous foam model of trabecular bone. From Beaupre and Hayes (1985).

The global material properties for this geometry have cubic symmetry. Note that a more general orthotropic material can be generated using a triaxial ellipsoid rather than a sphere for the void shape. The authors evaluated the material constants by applying defined displacements to the unit cube corresponding to uniaxial strain and shear strain and evaluating the resulting forces on the cube faces. While the model overestimated the global stiffness properties when compared to experimental data for trabecular bone (Figure 1.3), such a model can be expected to provide reasonable predications of the microscopic stress values in contrast to the more highly idealized models utilizing plates and beams. The model performed very well when applied to a natural foam rubber (Figure 1.4). The reason for the overestimation of the trabecular bone properties may thus have been due to an overestimation of the modulus of the bone tissue.

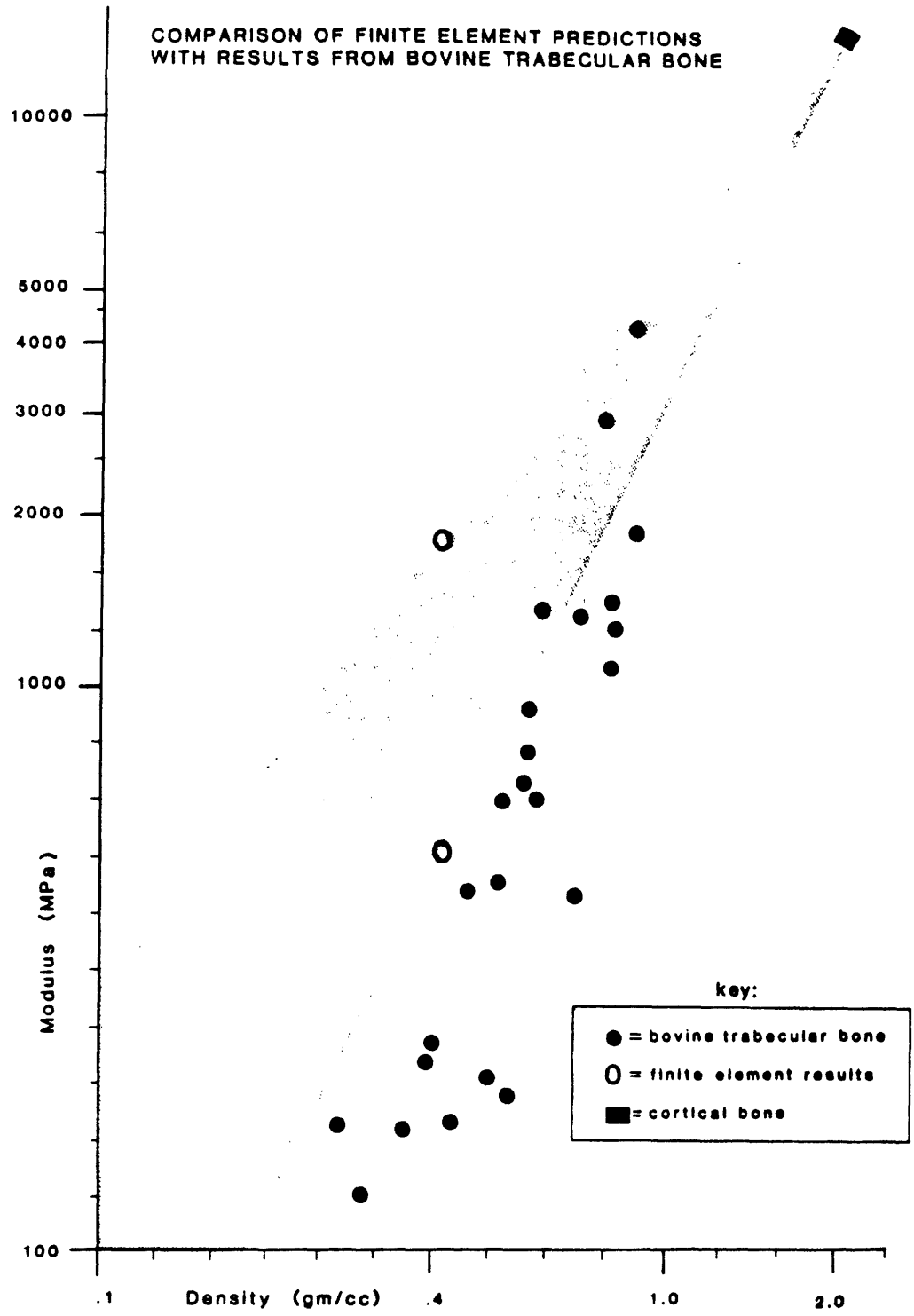

Figure 1.3: Comparison of the predictions of the porous foam finite element model with the results from bovine trabecular bone.

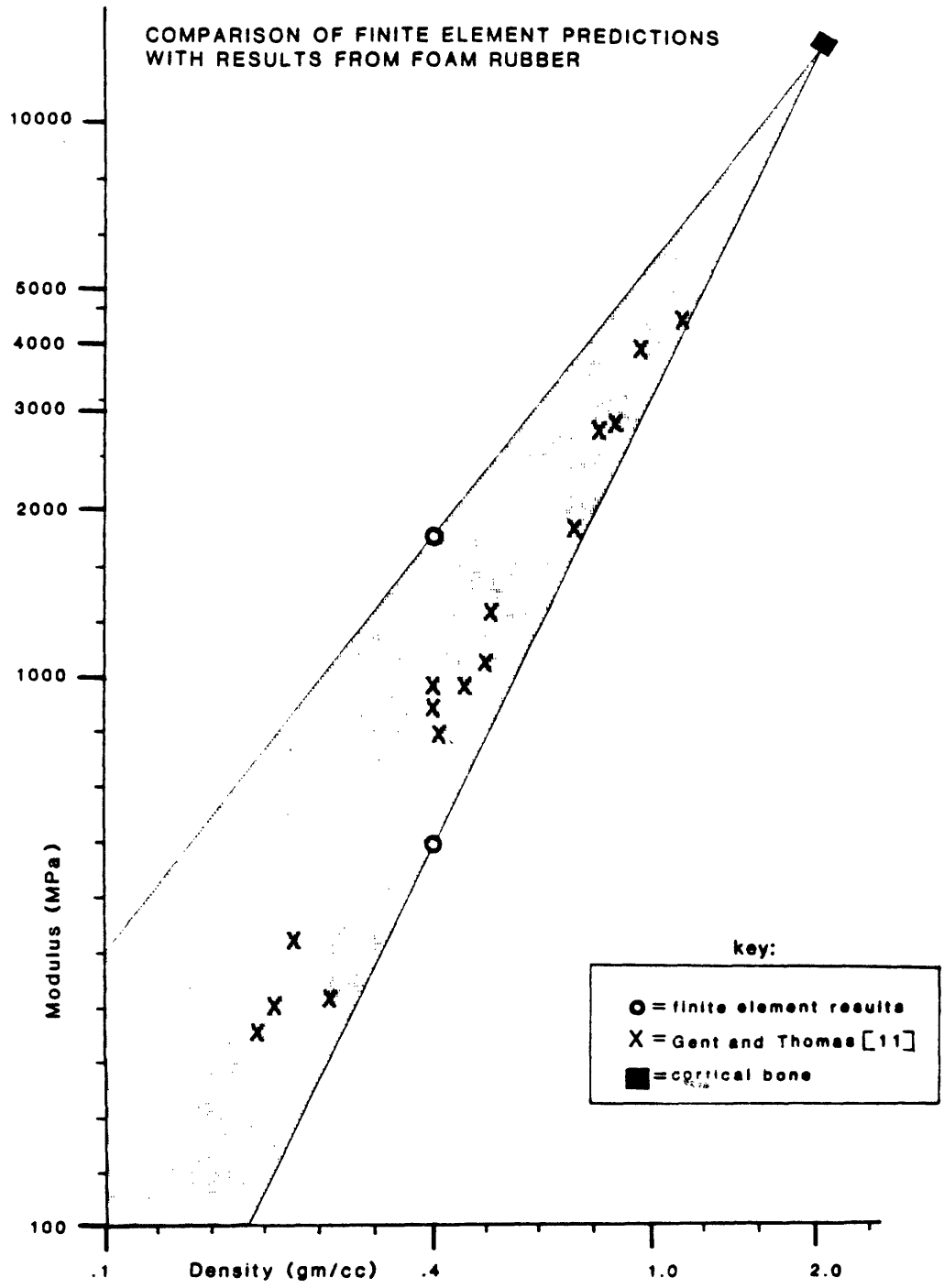

Figure 1.4: Comparison of the predictions of the porous foam finite element model with the results from foam rubber.

1.2 Adaptive Bone Remodeling

Bone, both cortical and trabecular, is a living tissue which responds to its biological and mechanical environment. Furthermore, bone tissue is in a constant state of remodeling; under homeostatic conditions, the resorption and formation of bone are in balance. This balance is maintained by the cellular components which are in turn dependent on and controlled by many physiologic parameters. Frost (1969) characterized remodeling of bone as being either surface or internal remodeling. Surface remodeling of long bones refers to the resorption or deposition of calcified bone on the endosteal or periosteal surfaces. Internal remodeling refers to a process in which osteons are replaced or the lumina are enlarged. The internal remodeling of trabecular bone results in changes in the quantity, thickness, and orientation of the trabeculae. From a mechanics point of view, the observation that the structure of bone can change in response to the imposed mechanical stress by surface and internal remodeling is particularly intriguing. There are many examples of mechanically adaptive bone remodeling including exercise-induced hypertrophy (Jones et al. 1977) and plate-induced osteopenia (Uhthoff and Dubuc 1971). The focus of this review is on the remodeling of trabecular bone, especially in response to artificial implants.

1.2.1 Wolff's Law

It is widely accepted that bone is a mechanically adaptive tissue. The term Wolff's Law comes from the 'law of bone transformation' put

forth by Wolff (1892). However, the first suggestion that trabeculae are organized along principal stress trajectories, referred to as the trajectorial theory of bone structure, comes from Meyer (1867). A review of the early literature on bone architecture was provided by Thompson (1917). While there have been numerous demonstrations of adaptive bone remodeling, there is still much uncertainty over the mechanisms of bone remodeling and the mechanical parameters governing the remodeling response.

Possible Mechanisms of Stress Transduction

Bone remodeling is a cellular process which is dependent on a complex set of bioelectric, biochemical, vascular, biomechanical, and humeral factors. The relevant question for understanding adaptive remodeling is by what mechanism does the imposed stress influence the cellular remodeling process. First of all, it is intuitively obvious that strain, rather than stress, is the mechanical parameter which is 'sensed'. The question remains as to the the mechanism by which strain influences the cellular remodeling process. Several mechanisms have been proposed, including bioelectricity, direct vascular and diffusion effects, and damage accumulation.

A number of the hypotheses on bone remodeling are based on the transduction of material strain by changes in electrical potentials which in turn influence the activity of osteoblasts and osteoclasts. Fukada and Yasuda (1957) first showed that, in vitro, dry bone acts as a piezoelectric material. However, it has now been well established that

the piezoelectric effect *in vivo* is insignificant due to rapid decay, and that the measured potentials in physiologically-moist cortical bone are due to streaming potentials (Gross and Williams 1981). Streaming potentials are the result of ion flow through a porous material with fixed charges. Harrigan (1985) proposed that the changes in potentials are detected by the interconnections between bone cells. Doty (1981) showed that electrically active gap junctions exist between osteocytes and between osteocytes and osteoblasts. The osteocytes with gap junctions may effectively form a network for detecting changes in extracellular potentials. While this is a very attractive theory for cortical bone, the streaming potentials in trabecular bone are insignificant due to the large pore size.

An alternative hypothesis is that the material strains directly effect the osteocyte cell membrane or their extracellular components. The cell membrane properties, such as permeability, may be affected by material strains. This theory is attractive considering the long cellular processes of osteocytes. Rodan et al. (1975) showed changes in cyclic AMP in response to applied deformations for chondrocytes *in vitro*. Justus and Luft (1970) proposed that remodeling is controlled by changes in the solubility of hydroxyapatite. They demonstrated that the solubility of hydroxyapatite is a function of load and they hypothesized that the resulting changes in calcium concentration in the extracellular fluid influence osteoblastic and osteoclastic activity.

Another possible mechanism for the remodeling of trabecular bone is the continuous repair of trabecular microfractures. Radin et al. (1973)

developed an experimental model for the investigation of trabecular bone remodeling using intermittent loading of rabbit tibiae. Axially directed impulse loads roughly equal to the animals body weight were applied unilaterally via splints for a one hour period once per day for variable duration. The loaded specimens exhibited microfractures and generally greater disorganization and greater remodeling activity, with fracture callus present in the majority of the loaded tibiae. Mechanical measurements showed significant stiffening of the loaded trabecular bone following eight days of loading. Also, some evidence of microfractures under various stages of remodeling was found on microscopic examination of normal human proximal tibiae. The authors concluded that trabecular bone acts as a shock absorber with microfractures, and not viscosity, as the mechanism for energy absorption. The microfractures are subsequently remodeled into a stronger and more dense tissue.

It is probable that trabecular bone remodeling is controlled by a combination of mechanisms. While an understanding of these mechanisms is important, especially for the treatment of disease states, the present investigation will not directly address these mechanisms. The mechanical parameters which relate to bone remodeling and which may be predicted analytically are of greater relevance.

Mechanical Parameters Governing Bone Remodeling

One approach to the role of mechanics in bone remodeling was that of bioenergetics. The hypothesis is that bone acts as a reverse

mechanochemical machine (Justus and Luft 1970). Put simply, stress on bone drives chemical flow and thus cellular excitation, which it turn results in bone resorption or deposition. Steinemann (1985) used this approach to suggest that time is a natural parameter and that stress, rather than strain, is the proper mechanical parameter governing bone remodeling.

Cowin and Hegedus (1976) developed a dynamic model of bone remodeling. Hart et al. (1984) used the model with finite element techniques to predict the remodeling of long bones. In this application, a linear relationship was assumed for bone deposition or resorption as a function of longitudinal strain. Cowin et al. (1984) reported good results for model predictions when compared to experimental results. Good agreement was established by proper selection of the remodeling rate coefficient for each experiment. They reported that the optimal value of the coefficient fell within a relatively narrow range. This was essentially an empirical approach which appears to hold promise for the prediction of long bone remodeling. However, the theory does not address changes in material anisotropy and thus in its present development may not be applicable to trabecular bone.

Based on a principle of structural optimization, Fyhrie and Carter (1986) developed a mathematical formulation for trabecular bone orientation and density for a given a state of stress. In the most general case the theory is applicable to an orthotropic material. The basic premise was that trabecular bone remodels so as to form an optimal

structure in which the structural integrity is maximized and the structural mass is minimized. The authors assumed a quadratic form for the objective function which enables the application of material failure criteria. Included in the presentation were the application of strain energy density and an effective stress criterion. The mathematics confirmed the trajectorial theory; namely, the material axis orientation will correspond with the principal stress orientation. To establish the material density, it was necessary to assume a maximum for the objective function. This is analogous to setting a maximum value on the strain energy or effective stress. Functional relationships were developed for the minimum acceptable material density related to the selected objective function. The authors pointed out that the formulation based on strain energy density optimizes the material for stiffness whereas the formulation based on effective stress optimizes the material for strength. The strengths of this presentation are that it provides a mathematical basis for the trajectorial theory and a theoretical framework for the examination of density-stress relationships. This framework is used in the present investigation to examine stress-morphology relationships.

Investigations of Stress-Morphology Relationships

Lanyon (1974) provided some indirect experimental evidence in support of the trajectorial theory of trabecular bone structure. Strain gage rosettes were applied in vivo to the surface of sheep calcanei. The trabecular architecture of the sheep calcaneus is particularly striking, with an orthogonal network of trabeculae which form an arch in

the proximal region. The strain gages were placed on the cortical surface lateral to the first intersections of the trabecular tracts. Lanyon found that the principal strain directions varied throughout each stride but were almost constant during the main wight bearing phase and were little affected by the speed of locomotion. Qualitatively, the tensile principal strain component corresponded with the plantar trabeculae, and the compressive principal strain component corresponded with the dorsal trabeculae. The shear strain component increased from the dorsal to the planter regions. While the comparison of surface strains to internal architecture is inadvisable, this investigation provides valuable data for comparison to model predictions of internal and surface strains.

Hayes et al. (1982) used two-dimensional finite element models of the patella to predict internal stresses due to physiologic loads. They also used stereologic methods to establish the density and anisotropy distribution for a corresponding mid-sagittal section of a normal adult patella. A significant positive correlation was found between predicted principal stress directions and measured trabecular orientations. A significant positive correlation was also found between predicted von Mises stress and measured areal density. In later studies using a three-dimensional finite element model, Stone et al. (1984) found a significant positive correlation between predicted principal tensile stress magnitude and measured areal density but no correlation between von Mises stress and areal density. These studies are both limited by the examination in each case of a single normal patella presumably in homeostasis. Such models cannot be used to predict the short term

remodeling response of trabecular bone subjected to an altered mechanical environment, such as with an orthopaedic implant. It can be assumed that a structural model which very accurately represents the tissue mechanics will predict internal stresses which correlate well with the same tissue architecture on which the model is based. More specifically, if the model material properties are based on the stereologic measures, including modulus based on density and orthotropic axes based on anisotropy, it would not be surprising to find that the calculated stress magnitudes and orientations correspond with the measured densities and anisotropies.

1.2.2 Implant-Induced Remodeling

The biological response to foreign materials is an attempt to eliminate the material from the body. If the material cannot be extruded or ingested by macrophages, the usual response is to wall off the material by formation of a fibrous tissue sheath (Park 1979). Materials used for orthopaedic implants are biologically inert in that they produce a minimal foreign body response. The response of trabecular bone to an orthopaedic implant is at least partially dependent on the mechanical conditions at the bone-implant interface. For a smooth surfaced implant under mechanically neutral conditions, a thin fibrous sheath will form adjacent to the implant (Itami et al. 1982). Relative motion at the bone-implant interface results in a much greater tissue response, with bone resorption and fibrous tissue proliferation (Cameron et al. 1973). Porous-coated implants, on the other hand, result in direct bone ingrowth if certain conditions are met

(Pilliar 1983).

Histologic and Morphologic Response to Orthopaedic Implants

The most extensively studied orthopaedic prosthesis is the femoral component of total hip replacements. The present femoral components are usually constructed of a relatively stiff biocompatable alloy, such as stainless steel, cobalt-chrome, or a titanium alloy. The components have a curved stem of variable length which is inserted into the femoral canal. Polymethylmethacrylate (PMMA) bone cement is still commonly used to secure the prosthesis, though press-fit and porous ingrowth components are becoming more popular. The primary advantage of cemented prostheses is the forgiving nature of the bone cement, whereas press-fit and porous ingrowth components require greater surgical precision.

The changes in bone structure following prosthetic replacement has been studied extensively, especially for total hip replacement (Almby and Hierton 1982; Amstutz et al. 1982; Beckenbaugh and Ilstrup 1978; Bocco et al. 1977; Carlsson and Gentz 1980; Charnley and Cupic 1973; Cotterill et al. 1982; Dunn 1982; Galante 1971; Green et al. 1979; Harris et al. 1982; Marmor 1976; Pellicci et al. 1979; Reckling et al. 1977; Salvati et al. 1981; Stauffer 1982; Sutherland et al. 1982) and total knee replacement (Eftekhar 1983; Hamilton 1982; Insall et al. 1976, 1979, 1982, 1983; Kaufer and Matthews 1981; Lewallen et al. 1984; Tew and Waugh 1982). Radiographic changes are most commonly described, though histologic data from recovered prostheses (Goldring et al. 1983; Heimke et al. 1985; Linder et al. 1983; Shoji et al. 1983; Wright et al.

1979) or animal models (Harris et al. 1983; Hedley et al. 1982; Homsy et al. 1972; Lanyon et al. 1981; Rose et al. 1984; Spector et al. 1983) have been reported. Of primary concern has been the pathologic mechanisms of implant loosening. It is generally believed that the remodeling response of cortical and trabecular bone to prosthetic implants is at least partly controlled by the induced stress fields. Reduced stresses are implicated in calcar resorption (Crowninshield et al. 1980; Lanyon et al. 1981; Oh and Harris 1978; Rose et al. 1984; Sih and Matic 1981; Svensson et al. 1977; Tarr et al. 1979) and elevated stresses are implicated in distal hypertrophy (Cook et al. 1983; Rose et al. 1984; Spector et al. 1983). However, of critical importance to the development of component loosening is the biologic response at the bone-cement or bone-implant interface. The local biologic response to PMMA bone cement may be in large part due to the release of toxic monomer (Freeman et al. 1977; Huiskes 1980; Park et al. 1982; Schoenfeld et al. 1979; Willert et al. 1974) or the exothermic polymerization process (Andersson et al. 1972; Feith 1975; Lindwer and Hooff 1975; Park et al 1982) whereas the biologic response to smooth (press-fit) or porous-coated (porous ingrowth) prostheses appears to be more critically controlled by the local mechanical conditions (Cameron et al. 1973; Cook et al. 1983; Harris et al. 1983; McCarthy and Wells 1977). The vascular damage resulting from prosthetic implantation may also influence the biologic response, especially in the early stages following implantation (Gunst 1980; Huiskes 1980).

Cemented Prostheses

Rose et al. (1984) presented quantitative morphologic data from an animal model of total hip replacement. A cemented total hip replacement was performed unilaterally in sheep and maintained for a period of 0 to 12 months. The volume fraction and contiguity ratio of trabecular bone were measured, along with the thickness, circumference, and area moment of the cortical bone. The histology revealed inconsistent cement penetration into the trabecular bone. In regions of good penetration, the authors noted two distinct regions of trabecular bone separated by a resorptive layer, with decreased density of trabecular bone adjacent to the cement. The resorptive layer resulted in a band of bone resorption separating the cement-bone complex from the endosteal trabecular bone. In regions of poor cement penetration, they noted concentric layers of fibrous tissue adjacent to the cement and dense new bone adjacent to the fibrous tissue. Calcar resorption and cortical thickening were also noted consistent with clinical radiographic data.

Goldring et al. (1983) studied the histological and histochemical characteristics of fibrous tissue excised from the cement-bone interface at the time of surgical revision. They found that the membrane is biologically similar to a synovial lining, with synovial-like cells adjacent to the cement layer. They also found that the membrane has the capacity to produce large amounts of prostaglandin E_2 and collagenase, which may explain progressive bone lysis. They hypothesized that loosening of the component may increase synthetic activity which in turn may increase bone lysis.

Porous-Coated Prostheses

Various materials have been used to form a porous layer on the component surface for bone ingrowth. The first report of powder metal methods was that of Hirschhorn and Reynolds (1969). Hahn and Palich (1970) reported successful bone ingrowth in porous coated titanium cylinders implanted in sheep cortical bone. There was apparent bone ingrowth as early as 14 weeks. Homsy et al. (1972) reported good results using a femoral component coated with a porous polytetrafluoroethylene and pyrolytic graphite polymer implanted in canines. They reported complete infiltration by immature and mature collagen by 3 weeks, dense mature collagen by 10 weeks, and some ingrown mineralized bone by 15 months. Hedley et al. (1982) reported the presence of a fluorochrome label which was given 2 weeks after surgical implantation in the porous surface of a femoral surface component.

Several important parameters have been identified for successful bone ingrowth into a porous material. Welsh et al. (1971) found that a minimum pore size of 50 microns is necessary for mineralization of ingrown tissue. Bobyn et al. (1980) found that the optimum pore size is in the range of 50 to 400 microns. They also demonstrated that bone ingrowth for an implant adjacent to trabecular bone is much more rapid than for an implant adjacent to cortical bone. Cameron et al. (1973) found that the success of bone ingrowth is dependent on minimal motion at the bone-implant interface. McCarthy and Wells (1977) reported poor results for a porous coated hip prosthesis implanted in canines. A fibrous tissue interface, with no bone ingrowth, was found which they

attributed to relative motion at the implant-bone interface. Harris et al. (1983) found that, for porous coated acetabular components, good apposition between the component and bone was required for bone ingrowth. Regions of poor apposition resulted in fibrous tissue formation. They also noted trabecular bone hypertrophy adjacent to contact points for cases of discontinuous bone-implant contact suggestive of stress-related remodeling.

The results of Cook et al. (1983) and Kester et al. (1984) support the supposition that the stress transfer from prosthesis to bone critically effects the bone remodeling response. In the former study, porous coated hip prostheses constructed of carbon composite or titanium alloy were implanted in canines. Both demonstrated good fixation by 3 weeks. The carbon composite implants resulted in trabecular bone hypertrophy at the proximal stem and no calcar resorption while the more stiff titanium alloy implants resulted in calcar resorption and trabecular bone hypertrophy at the distal stem. In the latter study, partially porous coated titanium alloy hip prostheses of similar design were implanted in canines. Trabecular bone hypertrophy in the proximal calcar region and adjacent to the porous surface is suggestive of stress-related remodeling. They also noted a fibrous tissue interface at the smooth portion of the stem.

Several studies have noted the formation of a dense layer of trabecular bone adjacent to the porous-coated surface. Hedley et al. (1982) reported results from a porous-coated cobalt-chrome femoral surface replacement implanted in canines. They noted good bone ingrowth

complete by 11 months, with gaps up to 1.5 mm bridged by trabecular bone. They also noted a bone 'plate' of dense trabecular bone adjacent to the porous layer, with no fibrous membrane formation. Spector et al. (1983) reported results from femoral components with a porous polysulfone coating implanted in canines. They noted a radiodense line at the bone-porous interface and a radiodense zone distal to the prosthesis. Histologically, they also noted a dense layer of trabecular bone around the porous coating adjacent to bone ingrowth and fibrous tissue ingrowth. The figures indicate that in some areas the dense layer was separated from the cortical bone by very porous trabecular bone, raising questions on the role of load transmission for the dense layer. One other interesting finding from this study was the presence of fibers (similar to Sharpey's fibers) from areas of fibrous ingrowth inserting into the adjacent trabecular bone.

Mixed results have been reported for human trials of porous-ingrowth prostheses. Engh (1983) reported a 5 year follow-up of 26 patients who received porous-coated Moore prostheses. The porous coating was formed of sintered cobalt-chrome beads. No clinical loosening was reported at 5 years. However, one-third of the patients had radiopaque lines, which the author interpreted as an indication of micromotion at the bone-implant interface. The author described 'healthy bone modeling' by radiography at four years with no evidence of stress shielding. The appearance of the radiopaque lines were similar to those of the animal experiments of Pilliar et al. (1981), indicating hypertrophied trabecular bone separated from the porous surface by ingrown fibrous tissue.

Analytical and Experimental Models

Most analytical models of orthopaedic implants in bone have examined the mechanics of the whole bone-implant structure while employing simplifying assumptions about the mechanics of the bone-implant interface. In addition, the trabecular bone is generally represented in these models as a continuum. While microstructural models of trabecular bone have been developed (see Section 1.1.3 above), these models are impractical for direct application to actual bone-implant systems. Of relevance to the present investigation are finite element studies which focused on the bone-implant interface mechanics. In addition, as in the current study, several experimental studies have used simple implants, such as cylinders, to investigate the biological response as a function of the implant material and surface characteristics.

Bone-Implant Interface Mechanics

Most analytic representations of bone-implant mechanics assume tight bonding at the material interface. This assumption is inaccurate, however, for smooth-surfaced implants and porous-coated implants prior to bone ingrowth. Nonlinear contact, with or without friction, generally requires sophisticated solution techniques. Several authors have presented finite element methods for solution of contact problems, including the detailed presentation by Bathe and Chaudhary (1985). Hampton and Andriacchi (1980) presented results from a two-dimensional nonlinear contact algorithm, with Coulomb friction, applied to stainless steel and PMMA bone cement test specimens. Hipp et al. (1985) presented

results from axisymmetric two-dimensional models of screw threads and dental implants in compact bone for the cases of rigid bonding and frictionless contact. They demonstrated that the maximum tensile and compressive stresses are greater and that the orientation and distribution of stresses are different for frictionless contact in comparison to rigid bonding.

Ducheyne et al. (1978) parametrically investigated the influence of the elastic modulus of the porous coating and the surrounding trabecular bone using macroscopic two-dimensional axisymmetric finite element models. The geometry of the model was that of a geometrically idealized stem of a femoral component. They found that the elastic modulus of the porous coating had little effect on the interface stresses. Increasing the elastic modulus of the adjacent trabecular bone, however, led to decreased interfacial shear stresses, suggesting that there would be a mechanical advantage for a gradient of trabecular bone elastic modulus, with the maximum modulus adjacent to the implant. No attempt was made to relate the stresses predicted by the continuum elements to actual stresses based on a trabecular bone microstructure.

Cook et al. (1982) developed an analytical model for bone ingrowth into a porous surface. The model consisted of an idealized ingrown bone spicule with the geometry defined by assuming a close-packed face-centered cubic structure for the porous surface (Figure 1.5). The maximum free-end deflection of the spicules was solved for a transverse load using beam theory. An 'interface element' for use in three-dimensional finite element analyses was then generated using a continuum

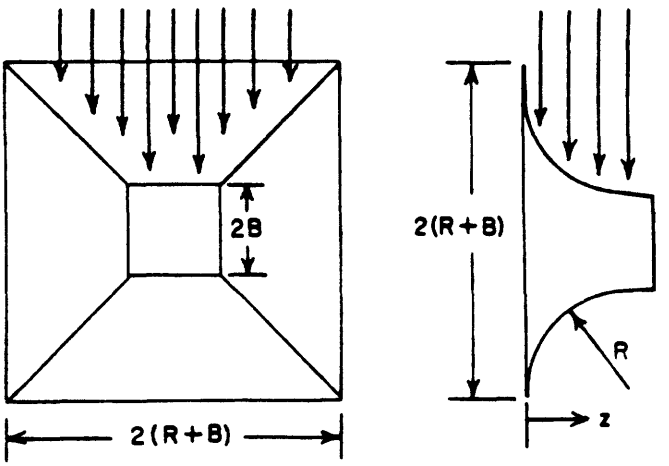

Figure 1.5: Model of ingrown spicule for face-centered cubic close-packed porous material. From Cook et al. (1982).

element which had the same load-displacement characteristics as that calculated for a specific number of ingrown bone spicules. This was done by establishing an effective modulus for the continuum element for different degrees of ingrowth, with the assumption that the degree of ingrowth could be represented by adjusting the number of ingrown spicules. The interface element was then applied in three-dimensional finite element models of a porous dental implant and the load-deflection characteristics were compared to experimental data. While the combination of a microstructural model with a macroscopic continuum formulation is an attractive approach, the validity of the microstructural model is questionable. The model assumes a uniform transverse load over one surface of the bone spicule. However, the mechanics of a relatively compliant bone spicule surrounded by rigid metallic spheres would be more accurately described as a displacement-controlled problem. A preferable approach would have been to establish the applied loads required to achieve the displaced shape which does not violate the displacement boundary conditions imposed by the rigid spheres. Also, no attempt was made to utilize the microstructural model to predict microscopic stress values based on the predictions of the macroscopic finite element models.

Idealized Models

Medige et al. (1982) presented morphologic data from an experimental model of metastatic bone defects in which large silicon rubber plugs were implanted in the distal metaphyses of canines. While no quantitative stress analyses were performed, stress levels in the

surrounding trabecular and cortical bone should be elevated since the low modulus rubber plugs could not be expected to transmit significant load. Radiographically, the rubber implants resulted in a gradual increase in the trabecular bone density and cortical thickening around the implants. Significant changes were noted as early as 2 to 4 weeks. Histologically, a fibrous tissue layer was formed around the implants, with increased trabecular bone density adjacent to the fibrous tissue. Several of the experimental specimens exhibited early microfractures which resulted in increased bone formation and an accelerated recovery of torsional strength.

Brown et al. (1984) developed an analytical and experimental model of a cylindrical metaphyseal implant for the study of chondromalacia. Their purpose was to investigate the hypothesis that chondromalacia is a result of local elevations of the stiffness of the trabecular bone which supports the subchondral plate and cartilage. The experimental model consisted of plastic or porous-coated metal cylinders implanted in an anterior-posterior orientation immediately beneath the subchondral plate in the tibial plateau of sheep. The histological evaluations indicated fibrous encapsulation of the porous-coated implants. The density of the trabecular and subchondral bone in the vicinity of the metal implants was greater than the corresponding bone in the vicinity of the plastic implants. They describe the trabecular bone response as 'corticalization' around the implant adjacent to the fibrous layer. Two-dimensional plane strain finite element models were analyzed with a nonlinear contact formulation for representation of an indenter on the cartilage surface. The results demonstrated that a low modulus fibrous

layer around a metal implant resulted in stresses similar to those for a plastic implant. Corticalization surrounding a low modulus implant resulted in greatly increased stresses in the cortical shell. In summary, the formation of a fibrous tissue layer surrounding the implant mechanically isolated the implant and resulted in elevated stress levels in the adjacent trabecular bone. Increased bone density around the implant further increased the stress levels.

1.3 Objectives

The objective of this investigation was to examine the stress-morphology relationships for trabecular bone around implants for which there was a controlled and predictable alteration in the stress fields. The first objective was to develop an experimental model using geometrically simplified implants of various materials and surface conditions implanted in the trabecular bone of laboratory animals. To meet this objective two different experimental models were used. Cobalt chromium cylinders with a sintered-bead porous coating were implanted unilaterally into ovine calcanei and stainless steel spheres with either a polished surface or a sintered-bead porous coating were implanted unilaterally into equine patellae. The animals were maintained for periods of 10 to 24 weeks.

The second objective was to perform morphologic analyses of the experimental specimens and of the untreated contralateral control specimens. Two-dimensional stereologic analyses were performed using the method of directed secants to measure the trabecular bone areal

density, the principal trabecular orientation, and the degree of anisotropy. The paired data were analyzed to establish the morphology of the trabecular bone response to the implants.

The third objective was to develop displacement-based finite element models of the control and experimental specimens to predict the internal stresses for correlation with the morphologic data. The development of the finite element models required establishment of the structural geometry, the applied loads, and the trabecular bone material properties. Modeling techniques were also developed for automatic mesh generation and bandwidth reduction as well as techniques for representation of the cortical shell and nonlinear bone/implant contact.

The fourth objective was to validate the finite element models. To meet this objective the principal stress directions were compared with the principal material directions for the control specimens. This assumed that the trabecular architecture was aligned with the principal stress directions in accordance with the trajectorial theory of bone architecture. The influence of various structural and morphologic parameters on this alignment was examined.

The final objective was to investigate the stress-morphology relationships for the remodeled trabecular bone around the implants. The alignment of the trabeculae and the principal stresses was examined based on the assumption that the finite element predictions were accurate. Finally, the relationship between the effective stress and the trabecular bone areal density was examined to test the hypothesis that the trabecular architecture corresponded to an optimal structure.

2.0 Methods

Two experimental models were developed for the investigation of implant-induced remodeling of trabecular bone. Porous coated cobalt chromium cylinders were implanted in the calcanei of sheep. Spherical stainless steel implants with either a smooth or porous surface were implanted in the patellae of horses. Structural analyses of these models were performed using a displacement-based finite element formulation and the trabecular bone morphology was quantified using stereologic techniques. Stress-morphology relations were then examined using statistical methods.

2.1 In Vivo Models of Implant-Induced Remodeling

Two different experimental models were used in this investigation. Chronologically, the first model was that of the spherical inclusion in the equine patella. This model had the advantage that the equine patella is composed primarily of a large volume of relatively homogeneous trabecular bone. However, the anatomy of this bone, and especially the geometry of the tendon and ligament attachments and the geometry of the patellofemoral contact load, is quite complex. Also, the representation of a spherical inclusion is particularly difficult using finite element methods. Despite these difficulties, this model gave encouraging results, which lead to the development of the geometrically simpler model of the cylindrical inclusion in the ovine calcaneus. The models and related data are presented in chronological order.

2.1.1 Equine Patella

Anatomy

The equine stifle joint corresponds to the knee joint in the human. The anatomy of the equine stifle joint is described in detail by Getty (1975). It is the largest and most elaborate of all articulations of the horse, consisting of patellofemoral and patellotibial articulations. The equine patella is a large sesamoid bone which articulates with the trochlea of the femur (Figure 2.1). The anterior surface is quadrilateral and convex. The articular surface is also quadrilateral. The patella is oriented such that two of the opposite corners of the quadrilateral surfaces are roughly aligned with the long axis of the tibia. These corners form the base, proximally, and the apex, distally. The articular surface has a vertical rounded ridge which corresponds to the groove on the trochlea of the femur. The medial articular surface is completed by the parapatellar fibrocartilage.

The patellofemoral joint is formed between the trochlea of the femur and the articular surfaces of the patella. The trochlea itself consists of two oblique ridges and a deep groove which provides the articular contact surface. The articular surface of the patella is much smaller than that of the trochlea and is completed medially by a supplementary plate of fibrocartilage which curves over the medial proximal ridge of the trochlea and is attached to the tibia by means of the medial patellar ligament. The horse, in contrast to the human, has three ligaments of insertion of the patella on the tibia (Figure 2.2). These

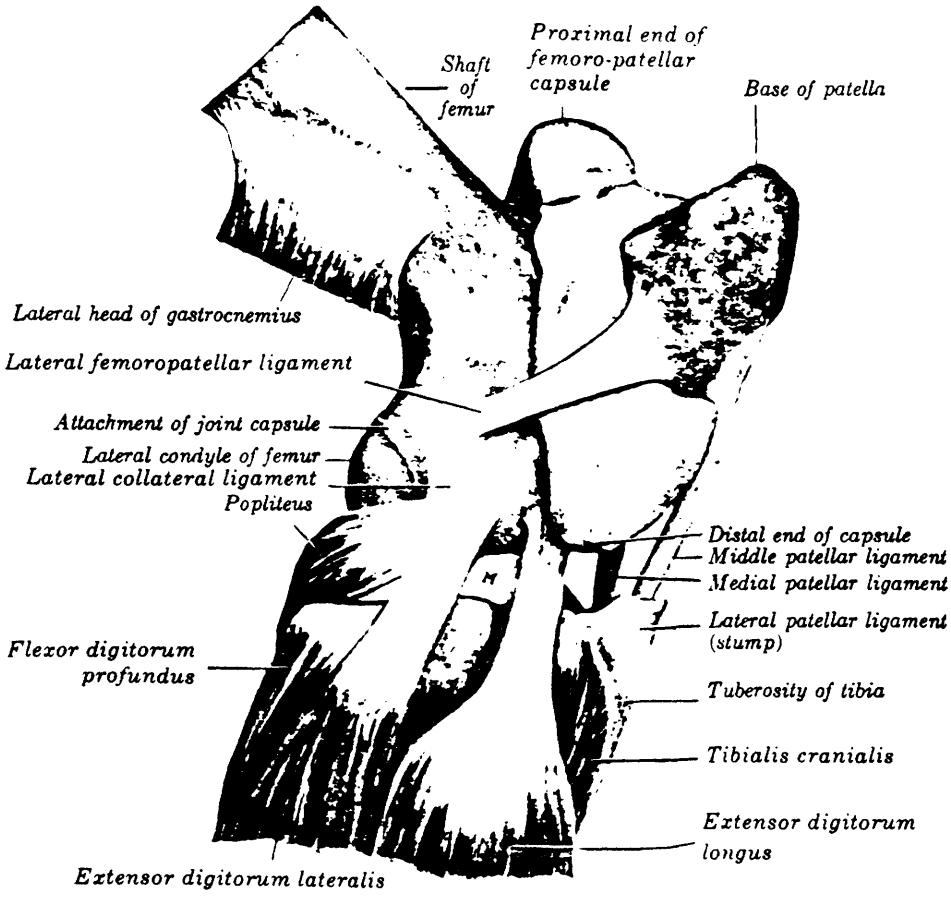

Figure 2.1: Anatomy of the equine stifle joint, lateral aspect. From Getty (1975).

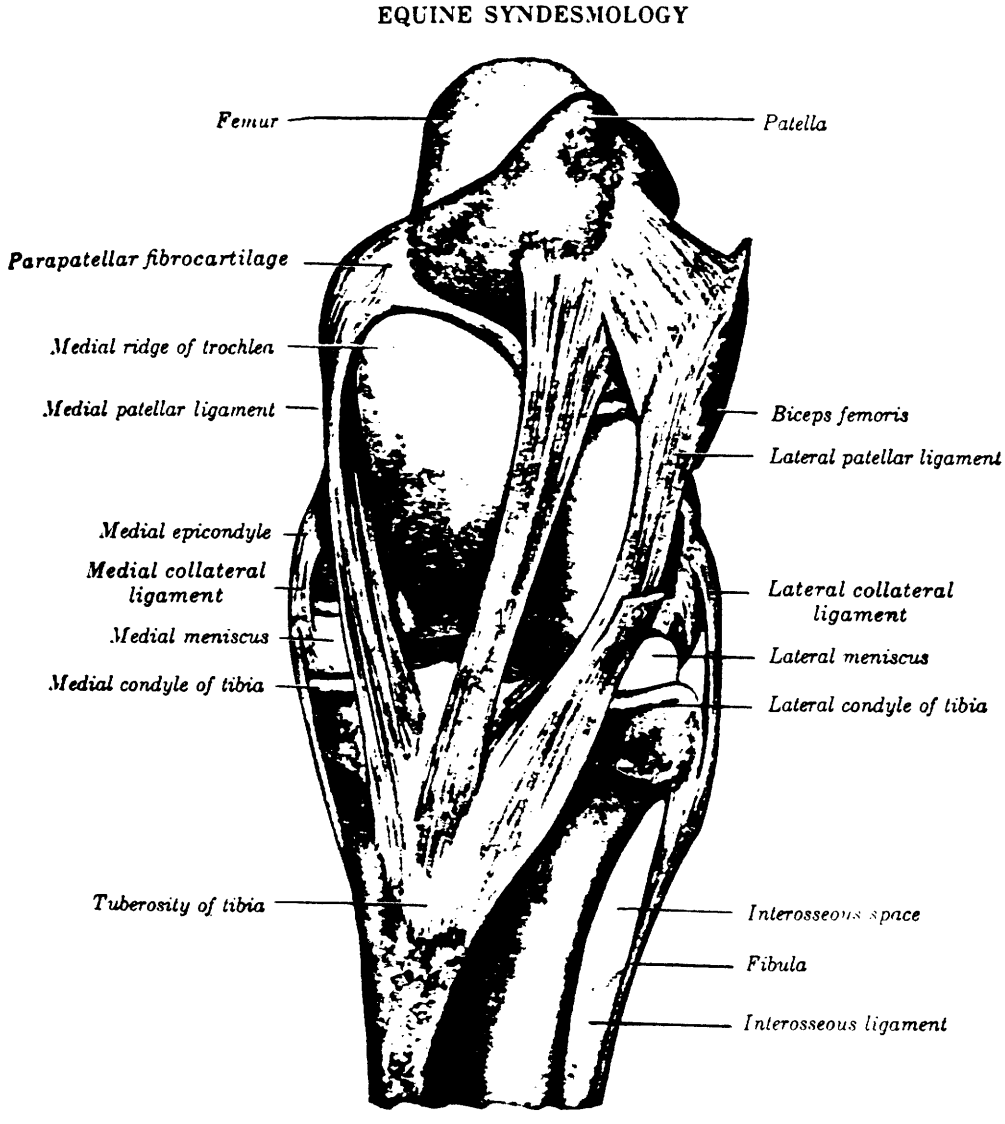

Figure 2.2: Anatomy of the equine stifle joint, anterior aspect. From Getty (1975).

ligaments are the lateral, middle, and medial patellar ligaments. The medial patellar ligament is the smallest of the three and is continuous with the the parapatellar fibrocartilage and ends on the tuberosity of the tibia on the medial side of the groove. The middle patellar ligament extends from the anterior patella to the distal part of the groove on the tuberosity of the tibia. This ligament appears to be aligned along the line of action of the quadriceps muscle group and exerts its force to pull the patella down the trochlear groove during flexion. The lateral patellar ligament extends from the lateral part of the anterior surface of the patella to the lateral part of the tuberosity of the tibia. A fourth ligament, the lateral femoropatellar ligament, extends from the lateral part of the anterior surface of the patella to the lateral epicondyle of the femur. The normal standing angle of the horse allows the knee to be held in approximately 150 degrees of extension. In this position, the fibrocartilage hooks over the upper end of the medial ridge of the trochlea, and the knee is locked in extension. This mechanism allows the horse to sleep while standing. Movement of the patella during flexion is that of gliding to different parts of the opposing articular surfaces. In the ordinary standing position, the actual contact of the patella with the trochlear groove is thought to be a strip about 12-15 mm in width. In the patella, it corresponds closely with the distal border of the articular surface.

Implant Material and Geometry

The implants used in the equine experimental model were smooth and

porous-coated stainless steel spheres. The smooth spheres had a highly polished surface and an outer diameter of 10 mm. The porous coated implants had a solid core of 8 mm diameter and a coating of sintered stainless steel beads of 1 mm depth for a final diameter of 10 mm. The diameter of the beads was 800 um. The porous-coated implants were not perfect spheres. For manufacturing purposes, it was necessary to leave one area uncoated, resulting in a plane of 2 mm depth missing from the sphere.

Experiment Protocol

In two groups of three horses each, a smooth or porous-coated spherical metallic implant was surgically inserted into the anterior trabecular bone of the right patella. The surgery was performed by D. M. Nunamaker V.M.D., a veterinary surgeon, at the New Bolton Center, University of Pennsylvania. Under general anesthesia, a small skin incision was made over the patella proximal to the insertion of the middle patellar ligament. A thin-walled boring tool was used to remove the cortical bone in the anterior patella. Trabecular bone was then removed using a ball ended mill. The implant was then inserted into the cavity. Trabecular bone removed by boring was then packed over the implant to the level of the anterior cortical bone. The incisions were then closed routinely and the animals allowed to recover in a padded recovery stall. Upon arising, the animals were allowed immediate weight bearing and maintained in a box stall for one week. Following one week of stall rest, the animals were turned out to a 35 acre pasture and allowed complete freedom of exercise. They were observed periodically

for the next 6 months after which they were sacrificed. At sacrifice, the control and operated patellae were removed, radiographed, and frozen for storage.

During the six month post-operative period, the animals were given sequential polychrome labels to document the remodeling process (Rahn 1980). These inorganic compounds are incorporated in the extracellular matrix during bone formation. By giving a series of labels, which each fluoresce a different color, the remodeling history was recorded. Each label was given using a standard protocol in which the labels are injected on two sequential days, for two sequential weeks. The labels were given in a sequence of blue (calcein blue), orange (xylenol orange), green (calcein), yellow (oxytetracycline), and red (alizarin).

2.1.2 Ovine Calcaneus

Anatomy

The calcaneus of the sheep articulates with the metatarsals. The tendon of gastrocnemius muscle (the tendo calcaneus) attaches to the free (posterior) end of the calcaneus (Figure 2.3). The tendon of the superficial digital flexor passes over a bursa at the attachment of the tendo calcaneus and continues to the digits. The plantar ligament links the plantar surface of the calcaneus to the distal tarsal bones and the proximal metatarsus. The medial and lateral sides of the calcaneus are free of attachments. The cortical bone of the shaft is fairly thick. The posterior region is composed primarily of highly oriented trabecular

Figure 2.3: Dissection of the ovine calcaneus and related structures, lateral aspect.

bone and a thin external cortical shell. In the sagittal plane, the trabeculae are arranged in two tracts which form an arch (Figure 2.4).

Implant Material and Geometry

The cylinders were composed of porous-coated cobalt chromium. The cylinders were produced by Johnson and Johnson Orthopedics Division (Braintree, Massachusetts) for this investigation. Each cylinder had a solid core with a 3.6 mm diameter and a sintered bead porous coating with a depth of 1.2 mm for the final diameter of 6 mm. The diameter of the spherical beads was approximately 800 um. Cobalt chromium is considered a biologically inert material which has found wide application for orthopaedic implants (Park 1979).

Experiment Protocol

The porous-coated cobalt-chromium cylinders were implanted in the right calcaneus of five sheep. The surgery was performed by D. M. Nunamaker V.M.D., a veterinary surgeon, at the New Bolton Center, University of Pennsylvania. Under general anesthesia, the right calcaneus was exposed using a small incision and lateral approach. A hole was then drilled in a lateral-to-medial orientation using a 6 mm diameter drill bit. The implant was then inserted and the wound closed. The ideal location of the implant is shown graphically in Figure 2.5. The animals were allowed normal weight-bearing after recovery from anesthesia. The animals were kept at pasture for a period of 10 weeks (three animals) or 16 weeks (two animals). After this period, the

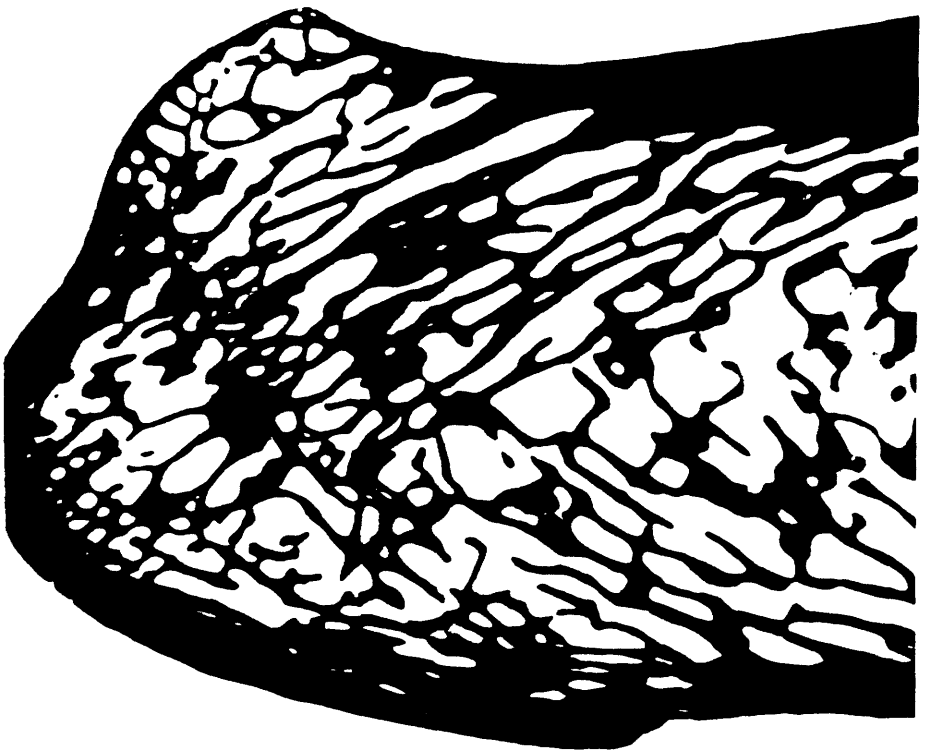

Figure 2.4: Mid-sagittal section of an ovine calcaneus showing trabecular tracts.

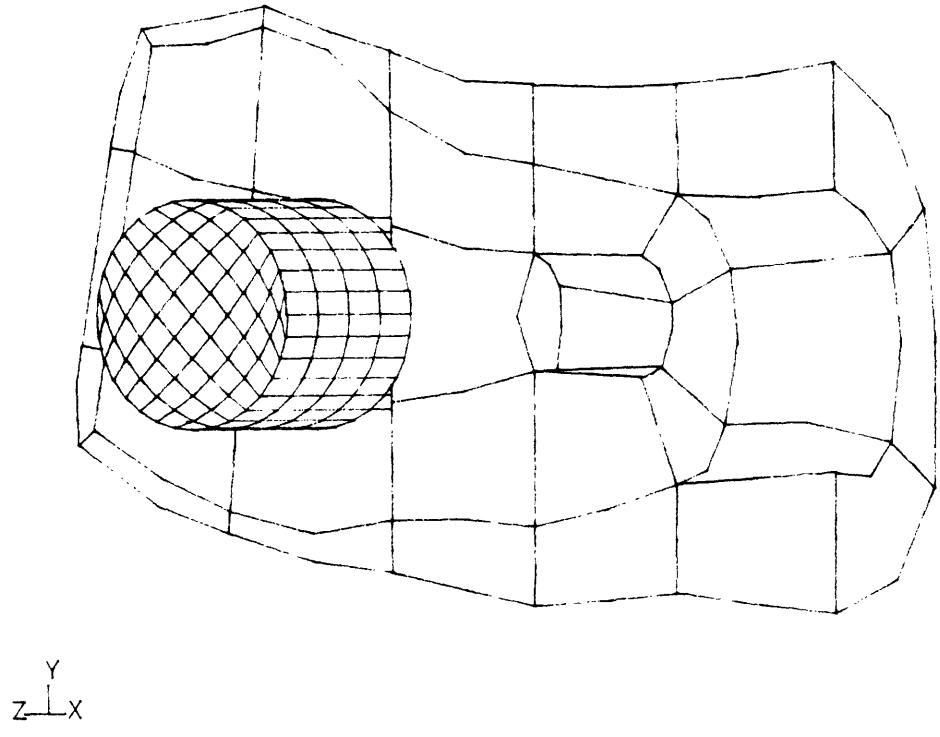

Figure 2.5: Schematic drawing of an ovine calcaneus with a cylindrical implant.

animals were sacrificed and the control (left) and experimental (right) calcanei were removed, radiographed, and frozen for storage.

2.2 Structural Analyses

The accuracy of any numerical model is dependent on the accuracy of the input data. Required input for the finite element models of the ovine calcaneus and equine patella includes the applied loads due to the tendons, ligaments, and joint contact forces (equine patella only), the material properties of the trabecular bone and cortical shell, and the structural geometry. The methods used to establish these input data and the results used in the finite element analyses are presented below. Also presented are mesh generation and manipulation techniques, including an original algorithm for the reduction of the bandwidth of a sparse symmetric matrix. Finally, a series of two-dimensional models of the ovine calcaneus are presented. These were analyzed to develop a simple and accurate technique for the representation of nonlinear contact conditions at the bone/implant interface.

2.2.1 Applied Loads

The most significant load in the posterior region of the ovine calcaneus is that due to the tendo calcaneus. This load is transferred to the tarsals and metatarsals through ligamentous attachments and articular surfaces. The location and direction of the load due to the tendo calcaneus was established from a dissection (Figure 2.3). The finite element models only included the posterior portion of the

calcaneus. Static equilibrium was maintained by enforcement of beam assumptions on the distal cross-section (see Section 2.2.4).

Establishing the applied loads of the equine patella was a particularly difficult task. The remainder of this section is devoted to the solution of this problem. This bone has a complex three-dimensional geometry with multiple muscular and ligamentous attachments. In addition, significant contact forces are generated between the articular surface and the femoral condyles. While the load geometry certainly varies cyclically through gait, multiple loading configurations were not analyzed. Rather, one representative load case was selected with the understanding that the actual in vivo loads cover a range which includes the applied loads used here.

Load Geometry

An excised equine patella with the attached patellar ligaments was suspended in a cubic space frame. Photographs were prepared for the six normal views (Figure 2.6). The global coordinate system of the space frame did not correspond exactly to the coordinate system of the finite element models. To establish a relationship between the two systems, plots of the finite element mesh in various orientations were generated and overlaid on the photographs until the mesh orientation agreed with the space frame orientation. Angular rotations between the two coordinate systems were then used for orthogonal transformation of the load vectors from the space frame coordinate system to the finite element coordinate system. By trial and error, it was found that the

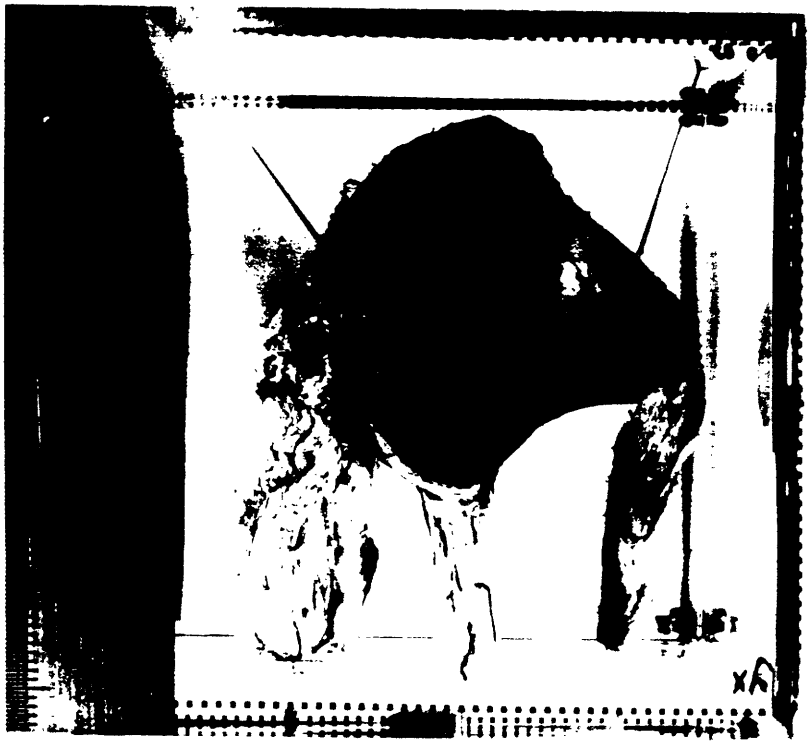

Figure 2.6: Posterior view of an equine patella in the space frame with ligaments intact.

following Euler angle rotations, which do not conform to convention, allowed alignment of the two systems:

ϕ = rotation about y axis to $x^{*}y^{*}z^{*}$ system

Θ = rotation about x^{*} axis to $x^{**}y^{**}z^{**}$ system

ψ = rotation about z^{**} axis to x'y'z' system

The general form for an orthogonal transformation is:

$$\mathbf{x}' = \mathbf{A}\mathbf{x} \tag{2.1}$$

where:

$$\mathbf{x} = \begin{bmatrix} x \\ y \\ z \end{bmatrix} \tag{2.2}$$

$$\mathbf{x}' = \begin{bmatrix} x' \\ y' \\ z' \end{bmatrix} \tag{2.2}$$

$$\mathbf{A} = \begin{bmatrix} a_{11} & a_{12} & a_{13} \\ a_{21} & a_{22} & a_{23} \\ a_{31} & a_{32} & a_{33} \end{bmatrix} \tag{2.3}$$

A is the orthogonal transformation matrix which is composed of the direction cosines between the **x** and the **x'** coordinate systems. Then, for the above defined Euler angles, the final transformation matrix is:

$$\mathbf{A} = \begin{bmatrix} \sin\phi\sin\theta\sin\psi+\cos\phi\cos\psi & \cos\theta\sin\psi & \cos\phi\sin\theta\sin\psi-\sin\phi\cos\psi \\ \sin\phi\sin\theta\cos\psi-\cos\phi\sin\psi & \cos\theta\cos\psi & \cos\phi\sin\theta\cos\psi+\sin\phi\sin\psi \\ \sin\phi\cos\theta & -\sin\theta & \cos\phi\cos\theta \end{bmatrix} \quad (2.4)$$

The Euler angles established by the superposition of the space frame and finite element images were: $\phi = 8.0^{o}$; $\theta = 9.0^{o}$; and $\psi = 11.5^{o}$.

The mesh regions corresponding to the attachments of the patellar ligaments and quadriceps musculature were determined using the space frame reference system. The six normal views of the finite element mesh were each overlaid on the photographs of the patella in the space frame and the regions of attachment on the surface of the finite element mesh were established (Figure 2.7).

A normal intact equine stifle joint was prepared with lead shot markers at the proximal and distal ligament attachments to establish the three-dimensional orientation of the patellar ligaments. All four patellar ligaments were marked, including the lateral, middle, and medial patellar ligaments and the lateral femoropatellar ligament (see Figures 2.1 and 2.2). The distance between the proximal and distal markers was measured for each of the ligaments. The stifle joint was radiographed in the frontal and lateral planes with the joint in 90 degrees of flexion (Figure 2.8). The marker separation distances and angular orientations relative to the patella were measured from the two radiographs. The three-dimensional orientation of each of the patellar ligaments was then solved using the equation for projection of a vector onto a plane. For a vector **v**:

$$\mathbf{v} = a\mathbf{i} + b\mathbf{j} + c\mathbf{k} \tag{2.5}$$

where **i**, **j**, and **k** are unit vectors in the x, y, and z directions. If v_{xy} equals the magnitude of the projection of **v** onto the xy plane (the distance between markers on one radiograph) and θ equals the angle between the projection of **v** and the x axis:

$$v_{xy} = \sqrt{a^2 + b^2} \tag{2.6}$$

$$\theta = \tan\frac{b}{a} \tag{2.7}$$

then combining Equations 2.6 and 2.7 yields:

$$a = \frac{v_{xy}}{\sqrt{1 + (\tan^{-1}\theta)^2}} \tag{2.8}$$

and b may be found from Equation 2.7. Since data were available for two planes one of the vector components could be solved for twice, thus providing a check on the measurements. It was assumed that the quadriceps was parallel to the femur to establish the orientation of the quadriceps musculature. The orientations were first established in the space frame reference system and later transformed to the finite element coordinate system using Equation 2.1.

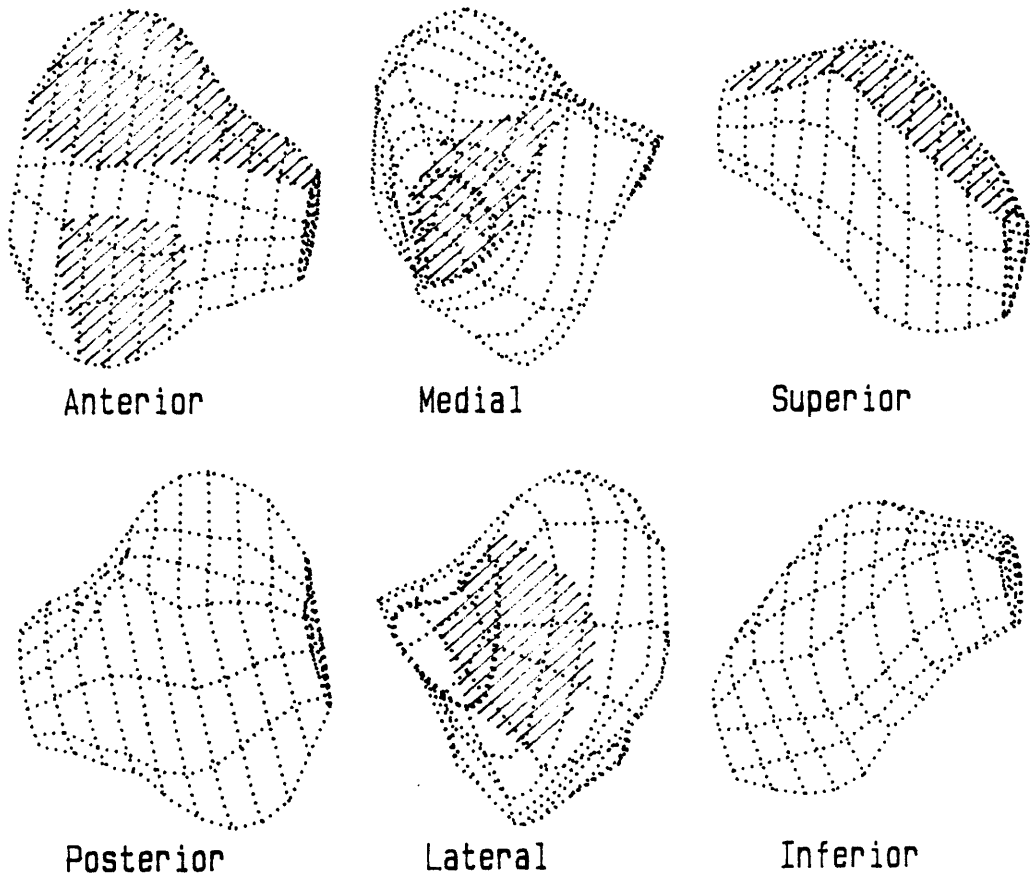

Figure 2.7: Attachment sites of the quadriceps musculature and the patellar ligaments on the three-dimensional finite element model.

Figure 2.8: Anterior-posterior radiograph of an equine stifle joint with markers at the insertions of the patellar ligaments.

In Vitro Load Analysis

An in vitro experimental study was conducted to provide load data for the finite element models of the equine patella. Making use of a loading apparatus developed for testing of human knee joints, co-linear loads were applied to locations representing the equine hip and tarsal joints (Figure 2.9). The quadriceps mechanism was clamped as a single muscle mass and the load was monitored with the uniaxial load transducer. Fuji Prescale Pressure Sensitive Film, enclosed in sheets of polyethylene, was placed in the joint space in the area of patellofemoral contact. Calibration of the load cells and the pressure sensitive film, and data acquisition, were accomplished as described in Huberti and Hayes (1984). The stifle joint was loaded in 90 degrees of flexion, and the quadriceps and axial loads were recorded.

Pressure films of the contact load between the patella and the femoral condyles were obtained from the in vitro load experiments. A typical pressure film is shown in Figure 2.10. The pressure film densities were obtained using a photodensitometer. The films were then placed on an excised patella and the finite element mesh was overlaid using a glass plate to establish the location of the contact loads on the mesh (Figure 2.11). It was assumed that the contact pressure load acts in a direction normal to the contact surface for all locations. This assumption is equivalent to assuming that there is no surface friction between the contacting surfaces.

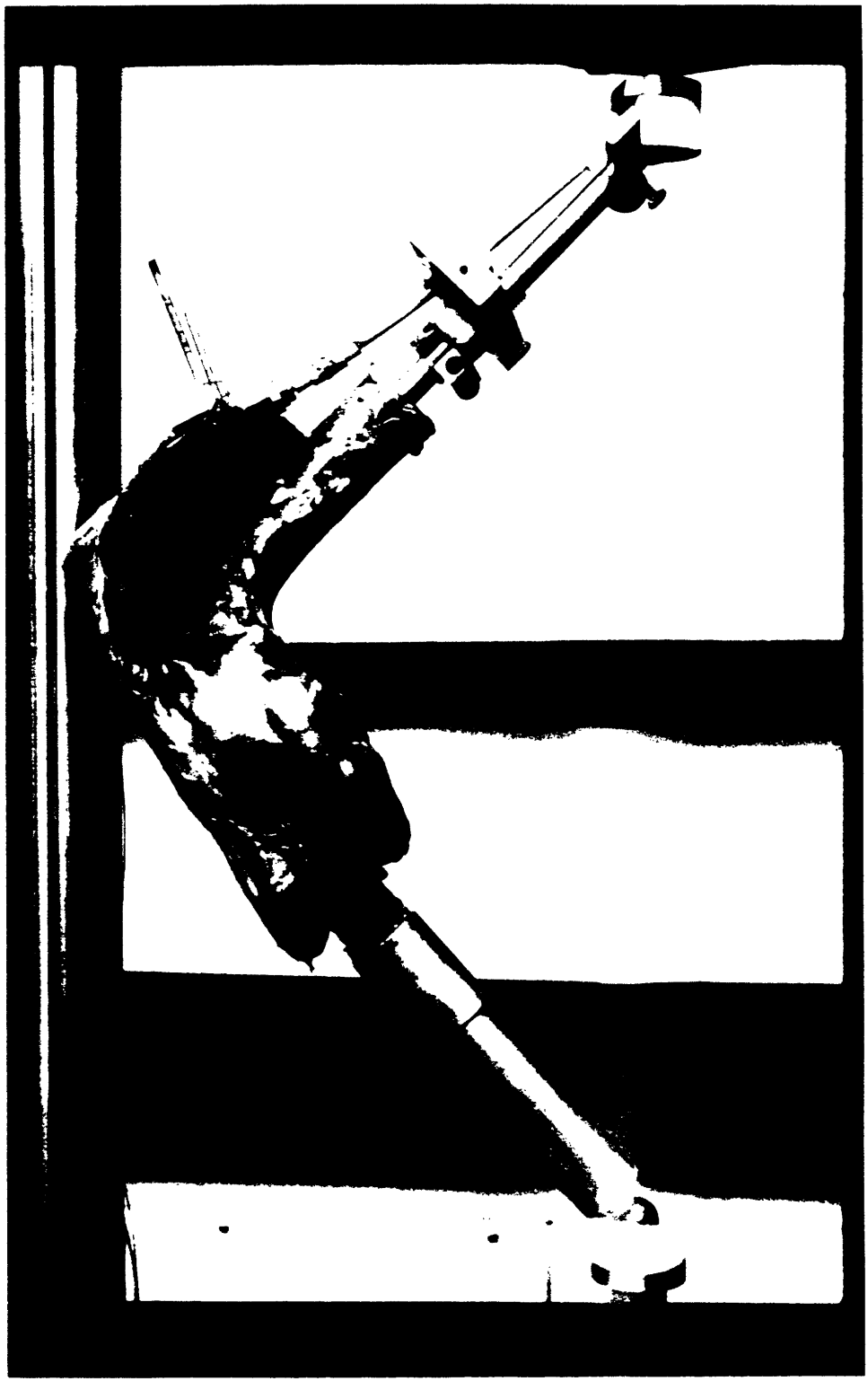

Figure 2.9: Equine stifle joint in the load apparatus. Note the muscle clamp and the load cell.

Figure 2.10: Typical calibration film and contact pressure measurement.

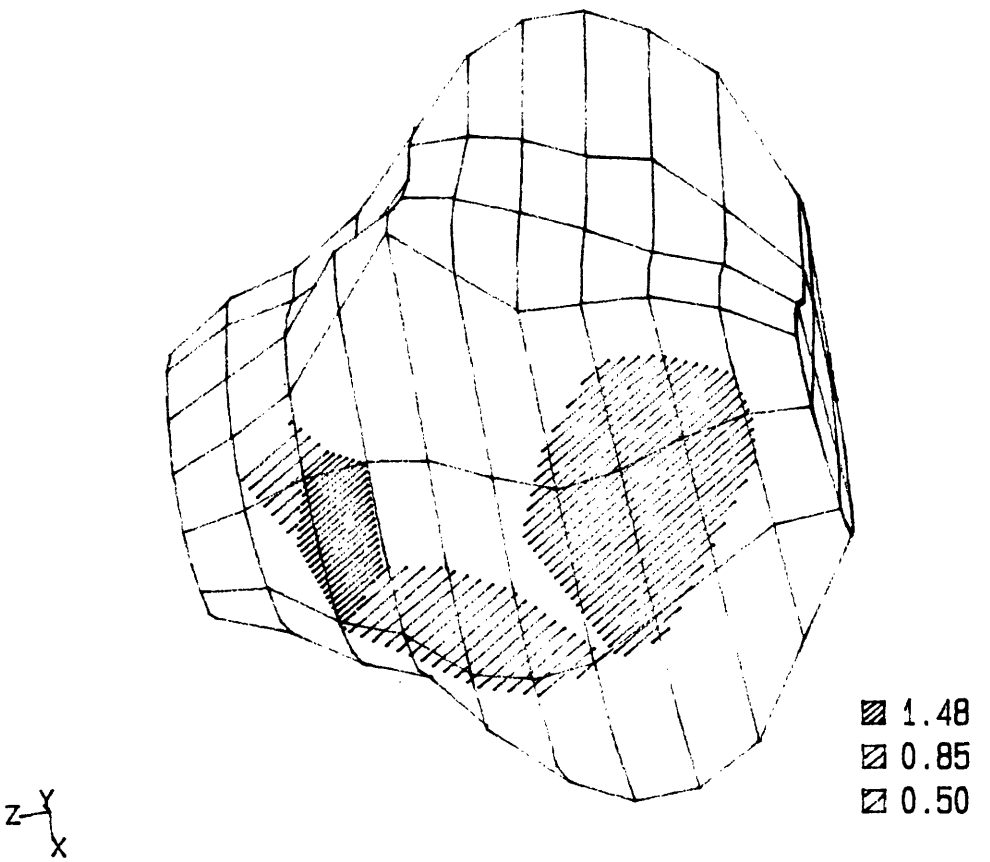

Figure 2.11: Patellofemoral contact pressure distribution on three-dimensional finite element model.

Static Equilibrium

To establish the final load magnitudes and orientations to be applied to the finite element models it was necessary to satisfy static equilibrium exactly. This requires satisfying six linear independent equations, namely the forces in three orthogonal directions and the moments about the three force axes:

$$\mathbf{Ax} = \mathbf{b} \tag{2.9}$$

where:

$$\mathbf{A} = [F_i^{\,1} \quad F_i^{\,2} \quad F_i^{\,3} \quad F_i^{\,4} \quad F_i^{\,5} \quad F_i^{\,6}] \tag{2.10}$$

$$\mathbf{x} = [C^i] \tag{2.11}$$

$$\mathbf{b} = [F_i^{\,0}] \tag{2.12}$$

$$i = 1, 2, \ldots, 6$$

For i equal to 1, 2, or 3, F_i is the force in the x, y, or z direction, respectively for the independent load vectors (indicated by the superscript). Similarly, for i equal to 4, 5, or 6, F_i is the moment about the x, y, or z axis, respectively. The **x** vector is composed of scaler multipliers on the independent load vectors. The **b** vector is composed of the forces and moments of the dependent load. The system of equations can solved by inverting the **A** matrix (provided the **A** matrix is

nonsingular).

The contact pressure load was made the dependent variable since only the quadriceps and contact pressure load were measured in the in vitro study. For the independent load vectors, it was assumed that the magnitudes of the four ligament loads and the quadriceps load were unknown. For a sixth independent variable, the quadriceps was divided into two sections, one which includes the more anterior nodes, and one which includes the more posterior and superior nodes. As initially defined, the load vectors resulted in six linearly independent equations, making solution of the equations possible (a nonsingular **A** matrix). The calculated magnitude of the total quadriceps load provided a check on the solution since this magnitude was measured experimentally.

The solution of a sixth-order linear system is sensitive to the matrix coefficients in a manner which is beyond intuition. It was recognized that the measurement of the vector directions for the various load components was inexact, and thus the solution of the equations of static equilibrium could be manipulated by changing these vector directions. A computer program was written to change each vector direction incrementally. In this procedure, one of the independent load vectors was rotated about a perpendicular axis by an angle theta. The load vector was then rotated about the axis of the original load vector in 14.4 degree increments. After each rotation, Equation 2.9 was resolved. Thus, 25 different vector orientations, forming a cone around the original vector direction, were tried. The best solution was judged

Table 2.1

Applied Loads for Equine Model

Component	Measured	Initial Solution	Final Solution	$\Delta\Theta$
LFL		569.7 N	332.0 N	10.0^{o}
LPL		152.6	302.5	10.0^{o}
MePL		596.5	455.1	9.9^{o}
MiPL		1733.1	1676.5	9.9^{o}
SQ		569.8	839.5	10.7^{o}
AQ		491.9	160.5	10.0^{o}
TQ	1024.0 N	1061.8	1000.0	
PFC	3115.3	3115.3	3115.3	

LFL: Lateral Femoropatellar Ligament
LPL: Lateral Patellar Ligament
MePL: Medial Patellar Ligament
MiPL: Middle Patellar Ligament
SQ: Quadriceps, superior portion
AQ: Quadriceps, anterior portion
TQ: Quadriceps, total
PFC: Patellofemoral contact load
$\Delta\Theta$: Change in angle from initial to final solution

to be the solution which yielded the minimum total load for the six independent loads. In other words, the best solution was that which, in the least redundant manner, balanced the dependent load (the contact pressure load). It was found that the solution could be improved by running the procedure several times for each of the load vectors.

The measured and calculated loads are presented in Table 2.1. For this table, the results were scaled such that the total quadriceps load for the final solution was equal to 1000 N and the patellofemoral contact load was equal for all three solutions. The vector directions for the initial solution were obtained from the radiographs as described above. The absolute angles between the initial and the final solutions are included in the table. The angle between the quadriceps and the middle patellar ligament, which was approximately equal to the flexion angle, was essentially unchanged by the solution process. This angle was equal to 90 degrees for both the in vitro experiment and the final numerical solution. The total of the independent load vectors, the sum of the ligament and quadriceps loads, was equal to 4114 N for the initial solution and 3766 N for the final solution which is a decrease of 8.5 %. The agreement between the measured and calculated total quadriceps load was exceptional, with a difference of less than 3 %. Such close agreement can not be expected for the unmeasured ligament forces.

2.2.2 Material Properties

An in vitro experimental study was performed to determine the

material properties of trabecular bone of the equine patella. Two primary assumptions were made about trabecular bone material properties: a) trabecular bone behaves as an orthotropic material; and b) the local material axis system corresponds to the morphologic axis system of the anisotropy tensor as predicted by the three-dimensional stereologic analysis. Specimens were prepared from an equine patella their density measured. The specimens were then tested in unconfined compression and the data were fit to an orthotropic material model using a least squares fit.

Specimen Preparation and Density Measurement

A normal equine patella was embedded in Alumacast, a fast setting synthetic resin, and sectioned in a manner similar to the experimental patellae (see Section 2.3.1). Six cubic specimens were prepared using a low speed diamond-embedded saw in an orientation relative to the anatomic planes. The locations were selected such that the trabecular bone appeared relatively homogeneous throughout each specimen. Thin sections were taken from three orthogonal faces and analyzed using the automated stereologic system to obtain three-dimensional structural anisotropy data (see Section 2.3.1). The specimens were sanded between two parallel plates to obtain the final dimensions of approximately 7 mm on each edge. The specimen dimensions were accurately measured with Vernier calipers and weighed on an analytical balance for density calculations. The specimens were soaked in physiologic saline overnight prior to testing. The cube faces were coated with Vasoline at the time of testing to minimize surface friction (see below). After testing

along the three cube axes, the specimens were cut into rectangular blocks at a 45^{o} orientation (Figure 2.12) using a modified diamond-embedded wire saw (Figure 2.13). The specimens were then retested along the three rectangular block axes.

Dynamic Compression Testing

Each cube was tested in the wet state in an Instron 1331 closed-loop, servohydraulic materials test system. The cubes were loaded in unconfined compression, with the load monitored by a load cell and the axial deflection monitored by the Instron Linear Variable Differential Transformer (LVDT). The lateral expansion in one of the off-axial directions was monitored by an extensometer (Figure 2.14). The specimens were tested using small amplitude cyclic loading under stroke control. This protocol was chosen to assure linear behavior and to enable the measurement of any viscoelastic stiffness component. Prior to testing, the specimen dimensions were measured:

$$W_i = \text{specimen width along axis } i \qquad (2.13)$$
$$i = x,\ y,\ z,\ y',\ \text{or } z'$$

where the i subscript indicates the specimen axes, with the unprimed axes corresponding to the original cubes and the primed axes corresponding to the rectangular blocks (see Figure 2.12). In the following, the equations will be presented for the first test of each specimen, in which the applied compression is in the direction of the x axis and the measured lateral deformation is in the direction of the y

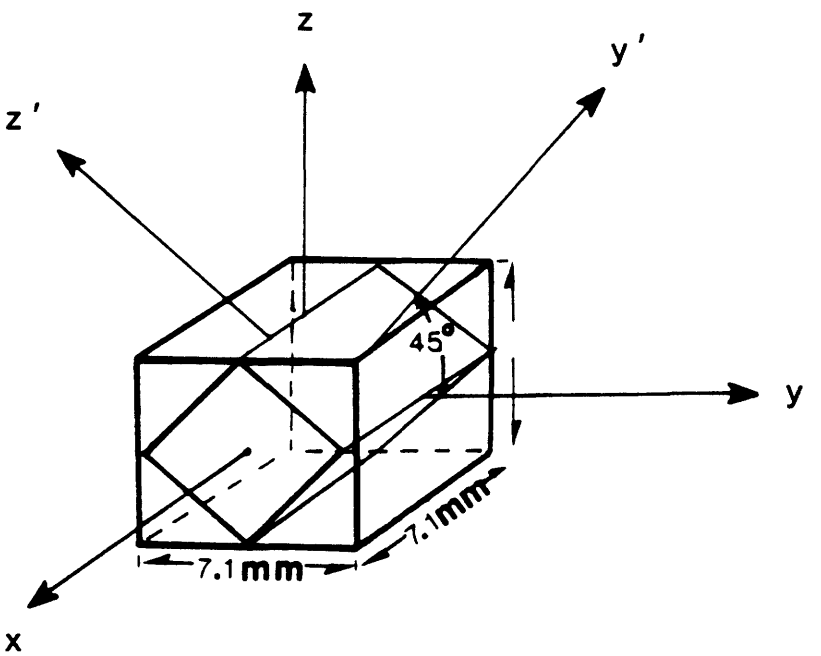

Figure 2.12: Coordinate systems for the original cubes and the inscribed rectangular blocks. Adapted from Snyder (1987).

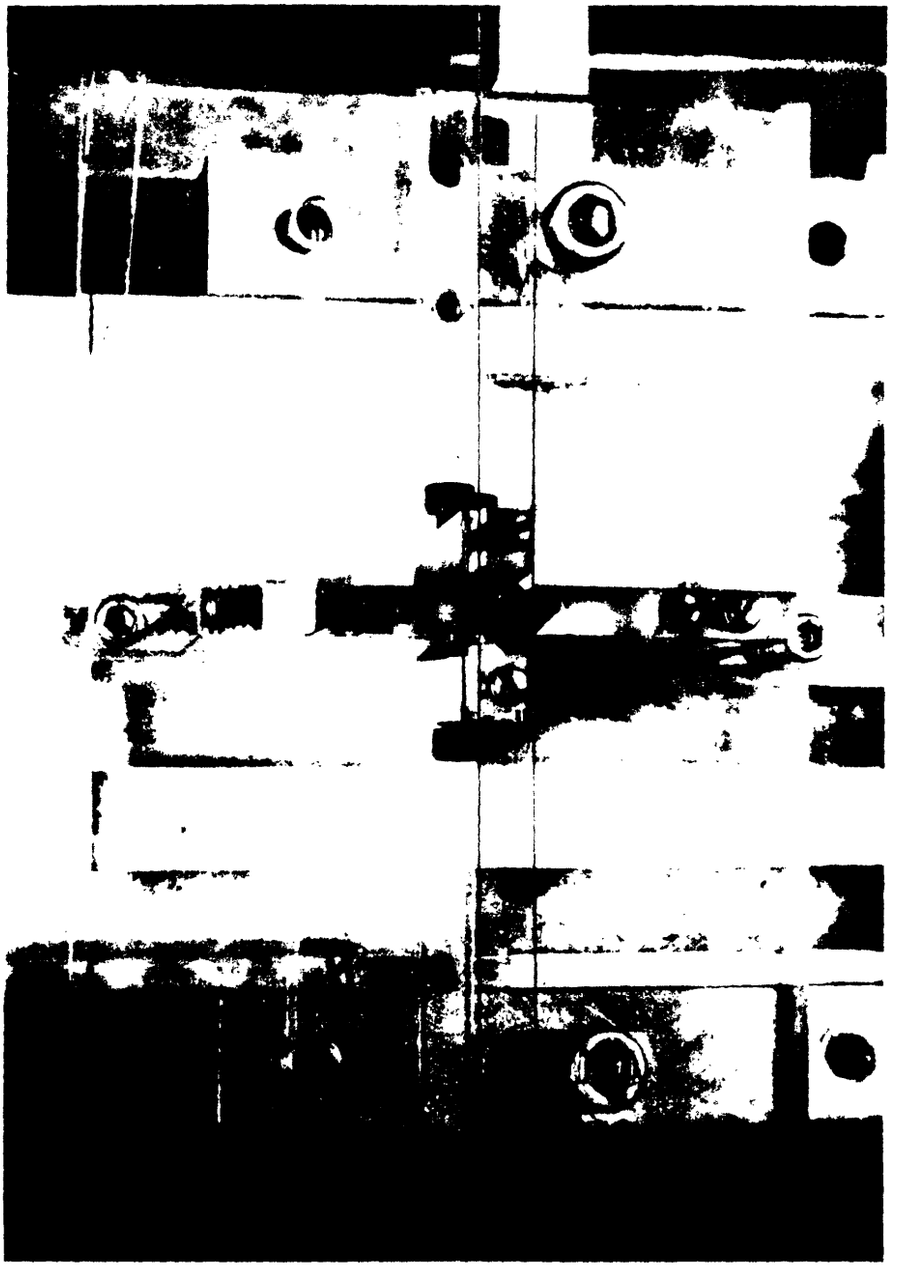

Figure 2.13: Wire saw apparatus for cutting the inscribed rectangular blocks.

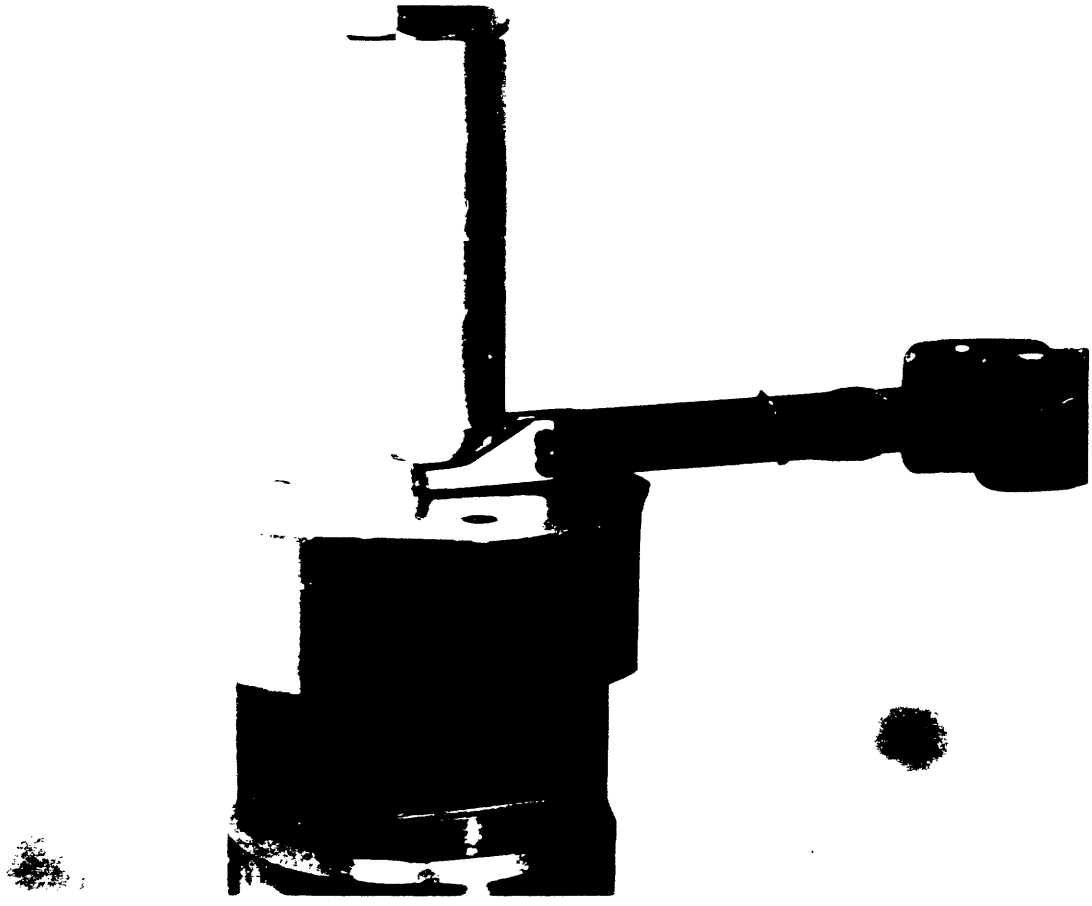

Figure 2.14: Trabecular bone specimen prepared for compression tests. Note the lateral extensometer.

axis. Similar equations may be obtained for the measurements along the other axes. The applied axial compression resulted in sinusoidal axial strain:

$$\varepsilon_{xx} = \frac{D_x^a}{W_x} \sin(\omega t) + \frac{D_x^o}{W_x} \tag{2.14}$$

where $2D_x^a$ is the peak-to-peak amplitude of the applied axial deformation, D_x^o is the mean axial deformation, and ω is the frequency of the applied deformation. Assuming linear viscoelastic behavior, the axial stress can be described as (Ferry 1970):

$$\sigma_{xx} = \frac{D_x^a}{W_x} [E'\sin(\omega t) + E''\cos(\omega t)] + \frac{L_x^o}{W_x W_y} \tag{2.15}$$

where L_x^o is the mean axial load, determining two frequency dependent functions, the storage modulus E' and the loss modulus E''. The term modulus is used to conform to literature descriptions with the understanding that these are better described as stiffnesses since the measurement direction in general does not correspond to a principal material axis. An alternate form is obtained by use of the stress amplitude σ_{xx}^a, the mean stress σ_{xx}^o, and the phase angle δ_x between stress and strain:

$$\begin{aligned} \sigma_{xx} &= \sigma_{xx}^a \sin(\omega t + \delta_x) + \sigma_{xx}^o \\ &= \sigma_{xx}^a \cos(\delta_x)\sin(\omega t) + \sigma_{xx}^o \sin(\delta_x)\cos(\omega t) + \sigma_{xx}^o \end{aligned} \tag{2.16}$$

The storage and loss moduli may then be expressed as:

$$E' = \left(\frac{\sigma_{xx}^{a}}{\varepsilon_{xx}^{a}}\right)\cos(\delta_x) \tag{2.17}$$

$$E'' = \left(\frac{\sigma_{xx}^{a}}{\varepsilon_{xx}^{a}}\right)\sin(\delta_x) \tag{2.18}$$

$$\frac{E''}{E'} = \tan(\delta_x) \tag{2.19}$$

where $\varepsilon_{xx}^{a} = D_x^{a}/W_1$, the strain amplitude.

The voltage from the LVDT, load cell, and extensometer were recorded by computer through analog-to-digital converters. The three channels of data were simultaneously recorded for one displacement cycle. Each channel was then evaluated using a fast Fourier transform (FFT) algorithm (Cooley and Tukey 1965) from the IBM Scientific Subroutine Package. This provided the real and imaginary components of each signal at the fundamental frequency (the frequency of the applied deformation) and at multiples up to the data sampling frequency. The purpose of using the FFT was to effectively filter out noise which was contained in the measured voltage and to calculate the phase angle δ_i between the load and the applied axial deformation. The amplitude and phase at the fundamental frequency was calculated for each of the three signals:

$$A_i = \sqrt{R_i^2 + I_i^2} \tag{2.20}$$

$$\Phi_i = \tan^{-1}\left(\frac{I_i}{R_i}\right) \tag{2.21}$$

$$i = 1, a, \text{ or } t$$

where A_i is the amplitude, R_i is the real component, I_i is the imaginary component, and Φ_i is the phase angle, with the i subscript indicating the data channel (1 for load, a for axial displacement, and t for transverse displacement). The axial modulus, strain ratio, and phase angle δ_i were then calculated:

$$E_x = \frac{A_1}{A_a}\frac{W_x}{W_y W_z}\frac{B_1}{B_a} \tag{2.22}$$

$$\nu_{xy} = \frac{A_t}{A_a}\frac{W_x}{W_y}\frac{B_t}{B_a} \tag{2.23}$$

$$\delta_x = \Phi_1 - \Phi_a \tag{2.24}$$

where B_i are the conversion factors for each channel. The test was repeated after repositioning the extensometer to measure the lateral deformation in the z direction, yielding ν_{xz} and a repeat measurement of E_x and δ_x. Note that the calculated modulus E_x is equal in magnitude to the complex modulus at the frequency ω:

$$E_x = \sqrt{E'^2 + E''^2} \tag{2.25}$$

The compliances were calculated from the measured moduli and strain ratios:

$$S_{xx} = \frac{1}{E_x} \tag{2.26}$$

$$S_{xy} = \frac{-\nu_{xy}}{E_x} \tag{2.27}$$

The test protocol was designed so as to assure linear material behavior, assure the tests were non-destructive, and to produce repeatable data. Mechanical testing of biologic materials invariably displays nonlinear properties. The trabecular bone specimens in this study exhibited an initial stiffening region followed by a linear region (Figure 2.15). The cyclic strains were applied in the linear region at a small amplitude to avoid any nonlinearities. The maximum axial strain never exceeded 2% (approximately one-third of the yield strain) to assure that the testing was non-destructive. A preconditioning regimen was used to improve the repeatability of the data. The test protocol was as follows: 1) the actuator was positioned to the point of contact; 2) the specimen was loaded in compression using a single linear ramp function to 1.5% strain; 3) the specimen was preconditioned by applying cyclic axial compression, with $\varepsilon_{11}^{a} = 1.5 \times 10^{-3}$ mm/mm and $\omega = \pi$ radians/second, such that the peak load occurred at the peak load from step #2. The cyclic loading was continued for two minutes while maintaining the peak load with the stroke mean level; 4) the data was recorded for one cycle (two seconds) at a sampling rate of 512 points/second/channel for a total of 1024 data points for each channel;

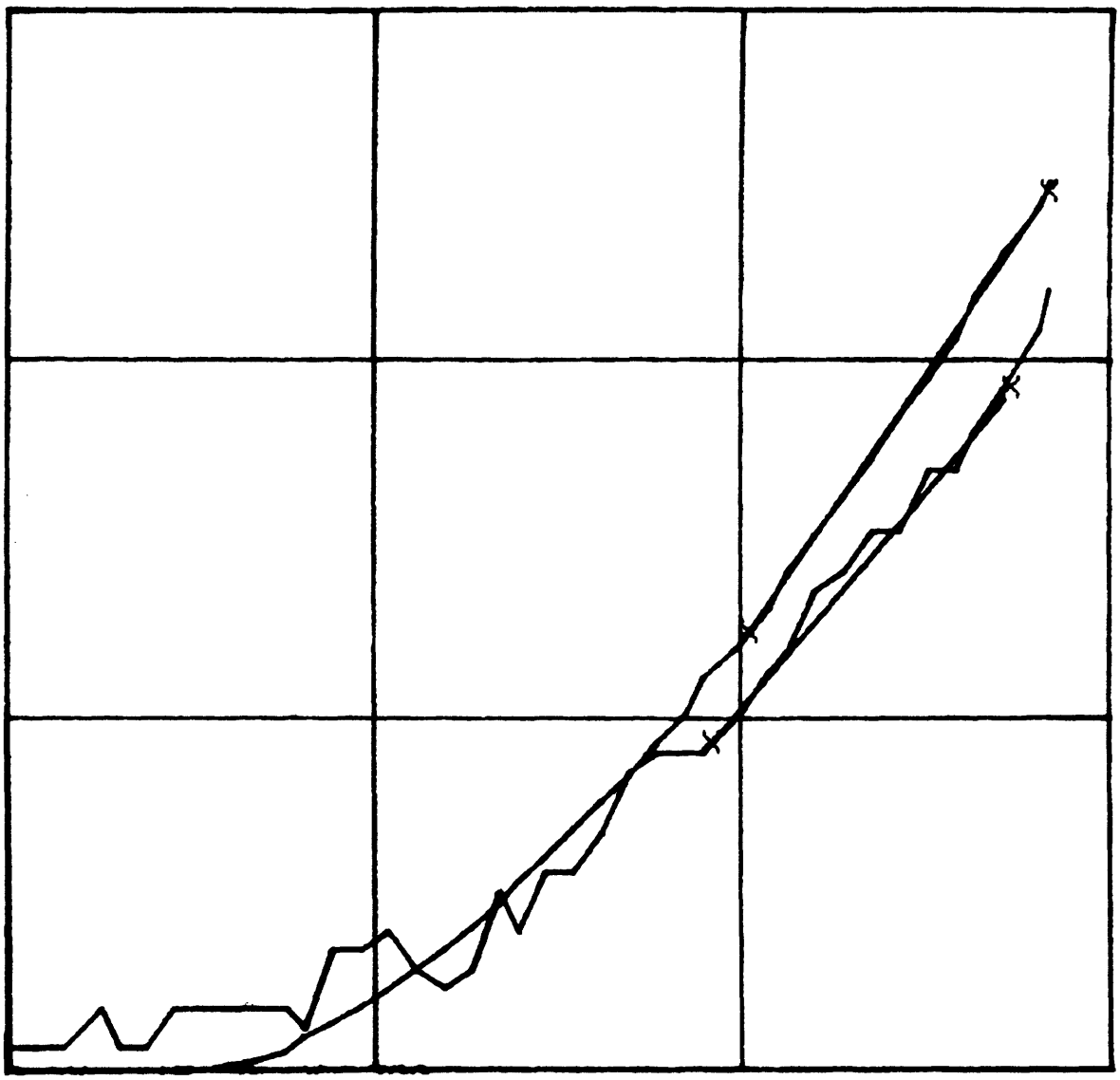

Figure 2.15: Typical load-displacement curves. Horizontal axis: 0.05 mm/division; Vertical axis: 100 N/division or 0.005 mm/division. For this example, E = 426 MPa and ν = 0.12.

5) the FFT was performed and the results recorded for each channel. The extensometer was repositioned to measure the transverse strain in the other lateral direction and the test protocol repeated. This was repeated for each of the three original cube axes and then for the three axes of the rectangular block.

Material Modeling

The analysis of the material property test data was based on the assumption that trabecular bone behaves as a linear elastic orthotropic material. The generalized Hooke's Law relating stress to strain in tensor form may be expressed as (Hearmon 1961):

$$\varepsilon_{ij} = S_{ijkl}\sigma_{kl} \tag{2.28}$$

where i, j, k, l = 1, 2, or 3 and S_{ijkl} are the elastic compliances which comprise a fourth-rank tensor. As Equation 2.28 stands there are 81 constants. However, since $\varepsilon_{ij} = \varepsilon_{ji}$ and $\sigma_{kl} = \sigma_{lk}$, the number of constants are reduced to thirty-six. Furthermore, it can be shown by a thermodynamic argument (Hearmon 1961) that $S_{ijkl} = S_{klij}$ which reduces the number of independent constants to 21 for the most general anisotropic material. For ease of notation, the full tensor suffixes of the strains, stresses, and compliances can be contracted:

$$\begin{bmatrix} \varepsilon_1 \\ \varepsilon_2 \\ \varepsilon_3 \\ \varepsilon_4 \\ \varepsilon_5 \\ \varepsilon_6 \end{bmatrix} = \begin{bmatrix} \varepsilon_{11} \\ \varepsilon_{22} \\ \varepsilon_{33} \\ 2\varepsilon_{23} \\ 2\varepsilon_{13} \\ 2\varepsilon_{12} \end{bmatrix} \tag{2.29}$$

$$\begin{bmatrix} \sigma_1 \\ \sigma_2 \\ \sigma_3 \\ \sigma_4 \\ \sigma_5 \\ \sigma_6 \end{bmatrix} = \begin{bmatrix} \sigma_{11} \\ \sigma_{22} \\ \sigma_{33} \\ \sigma_{23} \\ \sigma_{13} \\ \sigma_{12} \end{bmatrix} \tag{2.30}$$

$$\left\{ \begin{array}{l} S_{ijkl} = S_{qr} \text{ for q, r = 1, 2, or 3} \\ 2S_{ijkl} = S_{qr} \text{ for q = 1, 2, or 3, r = 4, 5, or 6} \\ 4S_{ijkl} = S_{qr} \text{ for q, r = 4, 5, or 6} \end{array} \right\} \tag{2.31}$$

Note that the shear strains ε_i are the engineering strains. Using the contracted notation, if there are three mutually orthogonal planes of symmetry, the stress-strain relations simplify to:

$$\begin{bmatrix}\varepsilon_1\\ \varepsilon_2\\ \varepsilon_3\\ \varepsilon_4\\ \varepsilon_5\\ \varepsilon_6\end{bmatrix} = \begin{bmatrix}S_{11} & S_{12} & S_{13} & 0 & 0 & 0\\ S_{12} & S_{22} & S_{23} & 0 & 0 & 0\\ S_{13} & S_{23} & S_{33} & 0 & 0 & 0\\ 0 & 0 & 0 & S_{44} & 0 & 0\\ 0 & 0 & 0 & 0 & S_{55} & 0\\ 0 & 0 & 0 & 0 & 0 & S_{66}\end{bmatrix}\begin{bmatrix}\sigma_1\\ \sigma_2\\ \sigma^3\\ \sigma_4\\ \sigma_5\\ \sigma_6\end{bmatrix} \qquad (2.32)$$

Note that this relationship holds only when the 1, 2, and 3 axes, of the expanded notation, correspond to the principal material directions and that the number of independent constants for an orthotropic material is nine. The compliance matrix in Equation 2.32 can also be expressed in terms of the engineering constants:

$$[S] = \begin{bmatrix} 1/E_1 & -\nu_{21}/E_2 & -\nu_{31}/E_3 & 0 & 0 & 0\\ -\nu_{12}/E_1 & 1/E_2 & -\nu_{32}/E_3 & 0 & 0 & 0\\ -\nu_{13}/E_1 & -\nu_{23}/E_2 & 1/E_3 & 0 & 0 & 0\\ 0 & 0 & 0 & 1/G_{23} & 0 & 0\\ 0 & 0 & 0 & 0 & 1/G_{31} & 0\\ 0 & 0 & 0 & 0 & 0 & 1/G_{12}\end{bmatrix} \qquad (2.33)$$

where E_i are the elastic moduli, ν_{ij} are the strain ratios, and G_{ij} are the shear moduli.

The axes of the trabecular bone specimens in general did not correspond to the material axes. Therefore, to solve for the nine independent compliance components for an orthotropic material, it was necessary to transform the compliances from the material axis system to

the axis system of the compression tests. The compliances compose a fourth rank tensor, which may be transformed by the following:

$$S^{*}_{ijkl} = a_{im}a_{jn}a_{ko}a_{lp}S_{mnop} \tag{2.34}$$

where a_{ij} are the direction cosines of the axes for which S^{*}_{ijkl} are defined with respect to the axes for which S_{ijkl} are defined. Equation 2.34 can be used to solve for the compliances in the material axis system from the material test data provided the direction cosines between the test axes and the material axes are known. This information can be provided by the three-dimensional stereologic analyses with the assumption that the structural anisotropy axes correspond to the material axes. The material tests described above provide seventeen compliances in the xyz and xy′z′ axis systems, of which nine independent compliances could be selected to solve Equation 2.34 exactly:

$$[a][S]_{123} = [S]_{xyzy'z'} \tag{2.35}$$

where [a] represents the matrix composed of direction cosines between the test axes and the material axes, $[S]_{123}$ represents the compliances in the material axis system, and $[S]_{xyzy'z'}$ represents the measured compliances in the test axis systems. The details of the [a] matrix may be found in Hearmon (1961) on the transformation of compliances. Note that the additional compliances obtained in the xy′z′ axis system are needed because the measurements in the xyz axis system do not provide nine independent compliances.

The measured compliances and the measured structural anisotropies are inexact at best. To take advantage of the additional measures provided by the material tests, the [a] and $[S]_{xyzy'z'}$ matrices in Equation 2.35 were expanded to seventeen rows each to include all experimental data, and solved using a least squares technique. To present this technique, Equation 2.35 is simplified in notation to:

$$\mathbf{Ax} = \mathbf{b} \tag{2.36}$$

where **A** represents the [a] matrix (17 rows by 9 columns), **x** represents the $[S]_{123}$ matrix (9 rows by 1 column), and **b** represents the $[S]_{xyzy'z'}$ matrix (17 rows by 1 column). The objective then is to minimize the error:

$$E^2 = ||\mathbf{Ax} - \mathbf{b}||^2 \tag{2.37}$$

The least squares solution is then (Strang 1976):

$$\mathbf{x} = (\mathbf{A}^T\mathbf{A})^{-1}\mathbf{A}^T\mathbf{b} \tag{2.38}$$

where $\mathbf{A}^T$ is the transpose of **A**.

Results

The density, modulus, and strain ratio data for the six trabecular bone specimens are presented in Table 2.2. Note that these data are for the axis system of the compression tests rather than the material axes

Table 2.2

Material Property Test Data

Property	Cube Number 1	2	3	4	5	6
D [gm/cc]	0.835	0.623	1.131	0.636	0.724	0.585
E_x [MPa]	622.3	536.6	1495.4	187.1	936.9	209.4
E_y [MPa]	755.0	1026.1	2615.0	483.1	1337.9	763.1
E_z [MPa]	939.1	890.3	3546.6	1086.2	842.8	790.8
$E_{y'}$ [MPa]	420.5	1289.2	2284.1	703.6	313.7	380.2
$E_{z'}$ [MPa]	368.3	191.6	1226.7	445.9	735.9	395.9
υ_{xy}	0.30	0.41	0.09	0.20	0.25	0.14
υ_{xz}	0.21	0.33	0.07	0.13	0.38	0.19
υ_{yx}	0.40	0.50	0.35	0.48	0.29	0.51
υ_{yz}	0.32	0.31	0.18	0.25	0.38	0.34
υ_{zx}	0.50	0.34	0.24	0.26	0.33	0.41
υ_{zy}	0.48	0.30	0.29	0.35	0.31	0.29
$\upsilon_{xy'}$	0.22	0.23	0.19	0.07	0.45	0.11
$\upsilon_{xz'}$	0.38	0.42	0.40	0.04	0.39	0.08
$\upsilon_{y'x}$	0.14	0.31	0.26	0.16	0.03	0.17
$\upsilon_{y'z'}$	0.08	0.32	0.23	0.17	0.04	0.19
$\upsilon_{z'x}$	0.21	0.14	0.12	0.35	0.07	0.41
$\upsilon_{z'y'}$	0.14	0.03	0.11	0.07	0.27	0.22

D: Density
E_i: Axial stiffness
ν_{ij}: Strain ratio

as predicted by the stereologic analyses. The data demonstrate that there is considerable variation within each specimen as well as specimen to specimen. Note that the modulus values represent average values from the repeated measurements. E_y, for instance, was measured twice, since each test was repeated once to measure the strain ratio in both transverse directions. E_x was measured four times since the x axis did not change in the rotated system (see Figure 2.12). An analysis of variance was performed on the modulus data for each cube with the test direction as the factor. In each case, at a significance level of 0.05, the assumption that the samples came from populations with equal means could be rejected. Therefore, the material behavior of the trabecular bone of the equine patella is significantly anisotropic; it remains to be demonstrated whether an orthotropic model is appropriate.

The measured phase angle between stress and strain (δ), as a function of the direction of applied compression, is presented in Table 2.3. The average phase angle for all measurements was 5.7^{o} with a standard deviation of 1.9^{o}. From Equation 2.19, this indicates that, on an average, the ratio of the storage modulus to the loss modulus is about 10. Also, the magnitude of the storage modulus is equal to 99.5% of the magnitude of the complex modulus (Equation 2.25). Therefore inclusion of the loss component makes little difference for the compliance calculations based on linear elastic behavior (Equations 2.26 and 2.27).

A statistical analysis was performed to determine whether the measured phase angles were anisotropic (Table 2.3). An analysis of

Table 2.3

Phase Angle Between Stress and Strain (δ)
[Degrees]

	Cube Number					
Direction	1	2	3	4	5	6
x	3.7	4.5	4.6	8.5	4.9	6.8
x	4.3	5.2	3.6	8.6	4.8	6.0
x	6.8	6.8	3.8	9.8	5.1	8.7
x	6.9	5.7	4.4	9.0	5.2	9.8
y	3.3	3.2	4.0	6.9	4.9	5.5
y	3.7	3.6	3.6	8.4	4.6	5.3
z	3.4	4.4	2.9	4.9	4.9	4.8
z	3.6	4.6	4.1	4.5	5.5	5.9
y'	6.9	3.3	2.9	6.4	9.5	7.9
y'	8.1	4.0	3.0	6.8	8.3	7.6
z'	6.6	7.1	3.8	7.5	4.6	6.9
z'	7.8	7.0	4.0	8.5	5.7	7.9
Mean	5.4	4.9	3.7	7.5	5.7	6.9
St Dev	1.9	1.4	0.6	1.6	1.6	1.5
ANOVA	+	+	-	+	+	-

ANOVA: One way analysis of variance with the direction as the factor. A "+" indicates that, at a significance level of 0.05, the assumption that the samples come from populations with equal means can be rejected. A "-" indicates that, at a significance level of 0.05, there is insufficient evidence to reject the null hypothesis that the samples come from populations with equal means.

variance was performed for each cube with the measurement direction as the factor. For two of the six specimens, at a significance level of 0.05, the null hypothesis could not be rejected. In other words, for those two cubes, the variation between directions was no greater than the variation within the repeated measurements for a single direction. However, for the other four specimens, at a significance level of 0.05, the null hypothesis could be rejected. Therefore these four specimens displayed a significant degree of anisotropy in this aspect of their viscoelastic behavior. While this is not surprising considering the anisotropy of the material stiffnesses, the characterization of the anisotropic viscoelastic behavior of trabecular bone is beyond the scope of this thesis.

The three-dimensional stereology data for the six bone specimens are summarized in Table 2.4. Included in this table are the axis lengths, normalized to the length of the major axis, which come from the anisotropy ellipsoid equation (Equation 2.68). The major axis, d_1, represents the axis of maximum orientation, and the minor axis, d_3, represents the axis of minimum orientation. If two axis lengths are similar then the material is approaching transverse isotropy. The anisotropy ellipsoid for cube number 2, for instance, is the closest to a prolate spheroid. That is, the semi and minor axes are roughly equal and both are significantly shorter than the major axis. The anisotropy ellipsoid for cube number 6 is the closest to an oblate spheroid. The major and semi axes are roughly equal and the minor axis is significantly shorter. For a transversely isotropic material, only one axis orientation is significant, that of the axis which differs from the

Table 2.4

Three-Dimensional Stereology Data

	Cube Number					
Property	1	2	3	4	5	6
d_1	1.00	1.00	1.00	1.00	1.00	1.00
d_2	0.96	0.87	0.96	0.96	0.97	0.98
d_3	0.89	0.85	0.91	0.90	0.90	0.93
a_{1x}	-0.41	-0.29	0.61	-0.33	0.46	-0.37
a_{1y}	0.17	0.62	-0.48	0.67	0.75	-0.59
a_{1z}	0.90	0.73	-0.64	0.67	-0.47	0.72
a_{2x}	0.17	-0.52	-0.10	0.13	0.78	0.05
a_{2y}	0.98	0.54	-0.84	0.73	-0.59	0.76
a_{2z}	-0.11	-0.66	0.53	-0.67	-0.18	0.65
a_{3x}	-0.90	-0.81	-0.79	-0.94	-0.41	-0.93
a_{3y}	0.11	-0.57	-0.26	-0.14	-0.28	0.28
a_{3z}	-0.43	0.17	-0.56	-0.33	-0.87	0.25

d_1: Normalized major axis length
d_2: Normalized semi axis length
d_3: Normalized minor axis length
a_{ij}: Direction cosine, ellipsoid axis i relative to global axis j

other two axes. The other four cubes display a greater degree of anisotropy.

The above compliance and anisotropy data were used to solve for the orthotropic elastic constants using Equation 2.38. The results indicated that the system of equations was poorly conditioned. The determinant of $(\mathbf{A}^T\mathbf{A})$ for each of the six specimens was, for all practical purposes, equal to zero.

To investigate this problem, a linear elastic orthotropic finite element model was used to simulate the test conditions. The model consisted of eight 20-node cubic elements arranged with cubic symmetry (four elements stacked on four elements). The material axis system was oriented such that the material axes were aligned with the cube diagonals. The orthotropic constants were those reported by Buskirk et al. (1981) for cortical bone. The material tests were simulated using applied displacements on one face of the cube with displacement constraints on the opposite face. Note that there were no planes of symmetry for the deformation of the cube since the material axes were not aligned with the cube axes. The axial stiffnesses were calculated using the predicted stresses and the strain ratios were calculated using the predicted nodal displacements on the lateral faces. The rotation of the cube to the xy'z' axis system was simulated by rotation of the material axis system. The influence of friction at the faces of applied compression was investigated using displacement constraints simulating infinite friction. Note that for the ideal case, a uniform stress field results, whereas for infinite friction, the stresses are nonuniform,

especially in the region of the applied deformation.

The predictions of the finite element models were evaluated by comparison to the exact compliances. The exact solution was obtained using Equation 2.34 for the transformation of the compliances from the material axis system to the test axis system. The results of the ideal finite element model were all within about 2 % of the exact compliances. For the case of infinite friction, the axial compliances were within about 5 % of the exact compliances.

These simulated test data were then introduced to Equation 2.38 with the same result as that for the bone cube data. This is all despite the fact that using nine of the exact compliances in the test axis systems yields the exact solution for the orthotropic constants. It is apparent that the two-dimensional rotation, from the xyz axis system to the xy'z' axis system yields a poorly conditioned system of equations. Any small amount of error, such as that produced by the ideal finite element model, results in a system of equations which are not solvable. Friction at the faces of applied compression increases the error and is a possible source of error in the experimental data. The models were further analyzed using an additional rotation about the y' axis, thus providing nine more rows for the A matrix. The determinant of $(A^T A)$ for this system was nonzero, and the solution of Equation 2.38 yielded orthotropic material constants which agreed very well with the input constants. For future investigations, it is recommended that a three-dimensional rotation, or an additional two-dimensional rotation about the y' or z' axis, be used to produce a well-conditioned system of

simultaneous equations.

To establish material property data for input to the finite element models, in light of the present results, a simple density-modulus relationship was established. An isotropic modulus, using the average of the measured values for the different directions, was correlated with the measured bone density for each of the six cubes (Figure 2.16). This correlation is clearly unsatisfactory for forming conclusions about the density-modulus relationship for trabecular bone. However, is was decided to use this relationship, rather than the published data of Carter and Hayes (1977) or others, since this data was drawn from the equine patella and included multiaxial tests.

For the three-dimensional finite element models of the control and experimental equine patellae, isotropic material properties were assumed. Heterogeneous properties were used based on the area fractions measured stereologically. The area fraction data were converted to mass densities assuming a tissue density of compact bone of 1.8 gm/cc (Lindahl and Lindgren 1967). The modulus-density relationship of Figure 2.16 was used to assign material properties to the elements of the finite element models. The investigation of the relationships between orthotropic material constants and three-dimensional anisotropy data is being continued by Snyder (1987).

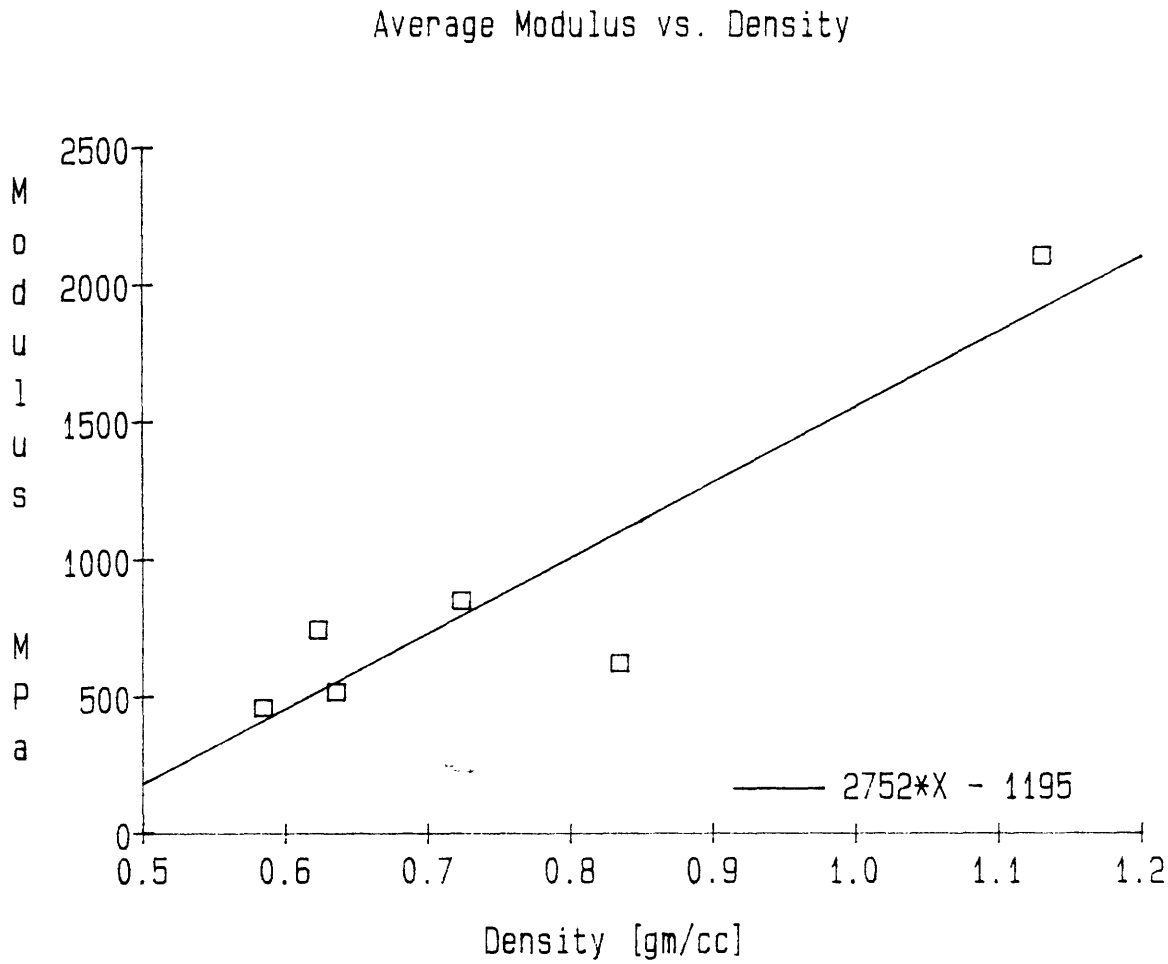

Figure 2.16: Average modulus as a function of density for the six trabecular bone specimens from the normal equine patella.

2.2.3 Model Development

Mesh Generation

The geometric data for the finite element models were obtained from the parallel sections of the embedded ovine calcanei and equine patellae. A rough mesh was first generated from digitized outlines with the aid of FEMGEN and other pre-processing software. The mesh was then refined using projected images of the bone cross-sections on the TALOS digitizer. The two-dimensional models generally were composed of 8-node (quadratic) plane stress elements. The three-dimensional models generally were composed of 20-node (quadratic) brick elements, but also included an assortment of wedge elements and partially-constrained brick elements.

Automatic Mesh Analysis

The accuracy of finite element analyses can be greatly reduced by poor or incorrect mesh definition. Inconsistent element connectivities, for instance, can result in discontinuous material deformation, such as material gap formation or overlap. Poor element geometries, such as acute angles at corner nodes, can result in artificial stress concentrations. For a large three-dimensional mesh, it is very difficult to recognize and correct mesh problems. For this reason, two computer programs were written, one to diagnose and one to repair three-dimensional finite element connectivities.

The first of the computer programs tests a number of characteristics of a finite element mesh. Problems detected fall into two categories: errors, such as missing nodes, and warnings, such as poor element aspect ratios. The program also identified element types including various degenerated elements. The errors for which the program checked included: 1) missing nodes or nodes which are out of sequence; 2) incorrect collapse of degenerated elements (ADINA requires a specific manner of collapse for degenerated elements for the maintenance of spatial isotropy); 3) inconsistent connectivities, such as adjacent elements which share two corner nodes but have different mid-edge nodes, or a mid-edge node with different pairs of corner nodes; and 4) elements defined inside-out, yielding a negative Jacobian determinant. The following characteristics were tested to produce warnings: 1) multiple nodes at one location; 2) unused nodes; 3) poor placement of mid-edge nodes (to avoid stress singularities such as the quarter-point location):

$$d = \frac{|v_{ab}|}{|v_{bc}|} \tag{2.39}$$

where A and C are corner nodes on either side of mid-edge node B, v_{ab} is the vector from node A to node B, and $|v_{ab}| \geq |v_{bc}|$. A warning was produced if d was greater than 1.2; 4) poor angles at mid-edge nodes, where the optimal angle is 180 degrees:

$$\theta = \sin^{-1}\left[\frac{(v_{ab})\times(v_{bc})}{|v_{ab}|\cdot|v_{bc}|}\right] - 180 \tag{2.40}$$

where A and C are corner nodes on either side of mid-edge node B. A warning was produced if $|\theta|$ was greater than 20 degrees; 5) poor angles at corner nodes, where the optimal angle is 90 degrees:

$$\theta = \sin^{-1}\left[\frac{(\mathbf{v}_{ab})\times(\mathbf{v}_{ac})}{|\mathbf{v}_{ab}|\cdot|\mathbf{v}_{ac}|}\right] - 90 \qquad (2.41)$$

where B and C are mid-edge nodes on either side of corner node A. A warning was produced if $|\theta|$ was greater than 30 degrees; and 6) poor element aspect ratio:

$$d = \frac{|\mathbf{v}_{ab}|}{|\mathbf{v}_{cd}|} \qquad (2.42)$$

where A, B, C, and D are corner nodes and $|\mathbf{v}_{ab}|$ is the maximum distance between corner nodes and $|\mathbf{v}_{cd}|$ is the minimum distance between corner nodes. A warning was produced if d was greater than 8.

The second of the computer programs changed the coordinates of selected nodes to improve the mesh geometry. The program was limited to 20-node brick elements which were the predominant element type in the three-dimensional models. Corner nodes which were shared by exactly eight 20-node bricks and mid-edge nodes which were shared by exactly four 20-node bricks were automatically relocated. The corner nodes were positioned such that all angles at the corners approach 90 degrees, and the mid-edge nodes were relocated such that the adjacent corner angles approached 90 degrees and the angle along the edge containing the mid-edge node approached 180 degrees.

The corner nodes were repositioned first since the method for relocation of the corner nodes used only the current locations of the adjacent corner nodes. In contrast, the method for relocation of the mid-edge nodes used the current locations of the adjacent corner nodes and mid-edge nodes. The new location of a corner node was based on the locations of the surrounding six corner nodes, as shown in Figure 2.17, where node T was the node to be relocated and nodes A through F were the adjacent corner nodes. The first step to determine the new location of node T was to find the minimum length line segment which joins line segments **AC** and **BD**. If points G and H are defined as:

$$G_i = \text{point on } \mathbf{AC}$$

$$H_i = \text{point on } \mathbf{BD}$$

Then the coordinates of points G and H can be expressed as linear combinations of the coordinates of A and C, and B and D, respectively:

$$G_i = A_i + l(C_i - A_i) \tag{2.43}$$

$$H_i = B_i + m(D_i - B_i) \tag{2.44}$$

To solve for the unknown constants l and m, the vector $\mathbf{v}_{gh}$ can be expressed as:

$$\mathbf{v}_{gh} = H_i - G_i = (B_i - A_i) + l(D_i - B_i) + m(A_i - C_i) \tag{2.45}$$

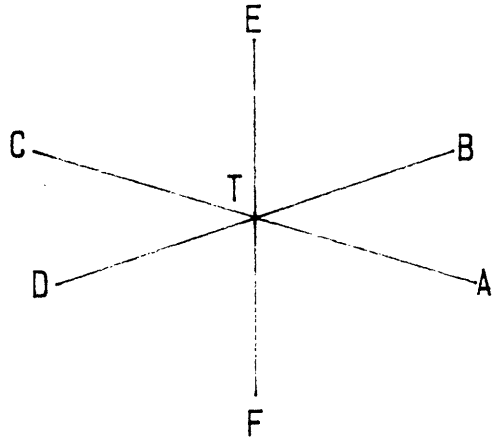

Figure 2.17: Target corner node T and the six adjacent corner nodes.

For G and H to be the end points of the minimum length line segment joining line segments **AC** and **BD**, $\mathbf{v}_{gh}$ must be normal to both $\mathbf{v}_{ac}$ and $\mathbf{v}_{bd}$, providing two equations and two unknowns:

$$\mathbf{v}_{gh} \cdot \mathbf{v}_{ac} = 0 \tag{2.46}$$

$$\mathbf{v}_{gh} \cdot \mathbf{v}_{bd} = 0 \tag{2.47}$$

Solution of Equations 2.46 and 2.47 yielded the coordinates of points G and H. This process was then repeated for line segment pairs **AC** and **EF**, and **BD** and **EF**, to obtain three line segments. Then, the mid-points along the three line segments calculated and these points were averaged to determine the location of the target corner node.

Mid-edge nodes can be repositioned after relocation of any corner nodes. Shown in Figure 2.18 is the target mid-edge node (T), the two adjacent corner nodes (A and B), and the eight mid-edge nodes adjacent to the corner nodes. The first step for determining the location of node T was to find the plane which, for all points on the plane, the distance to node A is equal to the distance to node B:

$$l(x - x_0) + m(y - y_0) + n(z - z_0) = 0 \tag{2.48}$$

where:

$$l = A_x - B_x$$
$$m = A_y - B_y$$

$$n = A_z - B_z$$

$$x_0 = (A_x + B_x)/2$$

$$y_0 = (A_y + B_y)/2$$

$$z_0 = (A_z + B_z)/2$$

The next step was to take the cross-product between vectors from corner node A to two adjacent mid-edge nodes such that the resulting vector is directed towards the plane found above. This was repeated for all pairs, yielding four vectors:

$$\mathbf{v}_1 = \mathbf{v}_{ad} \times \mathbf{v}_{ac} \tag{2.49}$$

$$\mathbf{v}_2 = \mathbf{v}_{ae} \times \mathbf{v}_{ad} \tag{2.50}$$

$$\mathbf{v}_3 = \mathbf{v}_{af} \times \mathbf{v}_{ae} \tag{2.51}$$

$$\mathbf{v}_4 = \mathbf{v}_{ac} \times \mathbf{v}_{af} \tag{2.52}$$

The next step was to normalize and sum the vectors:

$$\mathbf{v}_5 = \frac{\mathbf{v}_1}{|\mathbf{v}_1|} + \frac{\mathbf{v}_2}{|\mathbf{v}_2|} + \frac{\mathbf{v}_3}{|\mathbf{v}_3|} + \frac{\mathbf{v}_4}{|\mathbf{v}_4|} \tag{2.53}$$

The next step was to find the intersection between $\mathbf{v}_5$, with an origin at point A, and the plane (Equation 2.48):

$$\frac{(x - A_x)}{v_{5_x}} = \frac{(y - A_y)}{v_{5_y}} = \frac{(z - A_z)}{v_{5_z}} \qquad (2.54)$$

Substitution of Equations 2.54 into Equation 2.48 yields the coordinates of the intersection point. This process was then repeated for corner node B to yield a second point on the plane. The new location of the target node is taken as the average of the two points on the plane, and thus also lies on the plane.

The methods used to determine the new node locations are empirical. The establishment of the optimum mesh geometry was not attempted since this requires a nonlinear optimization scheme. The objective here was to provide a method to improve the mesh geometry which, while not producing the optimal mesh, is reliable and efficient for the generation of a mesh which produces acceptable results from the finite element analyses.

These techniques were applied in the generation of the mesh geometries for the finite element models of the equine patellae. The mesh generation initially resulted in straight lines connecting the corner nodes, with the exception of the implant border. The algorithm for mid-edge node relocation was applied throughout the mesh for these models whereas the algorithm for corner node relocation was selectively applied. Shown in Figure 2.19 are the mesh geometries before and after application of the these techniques to a model of a control patella. Note that the exact implant geometry was maintained for the models of the experimental patellae. Most notable is the improvement in the

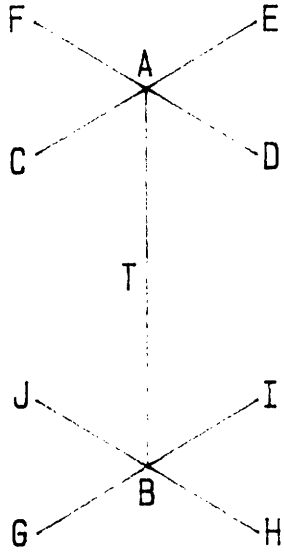

Figure 2.18: Target mid-edge node T, the adjacent corner nodes A and B, and the mid-edge nodes adjacent to A and B.

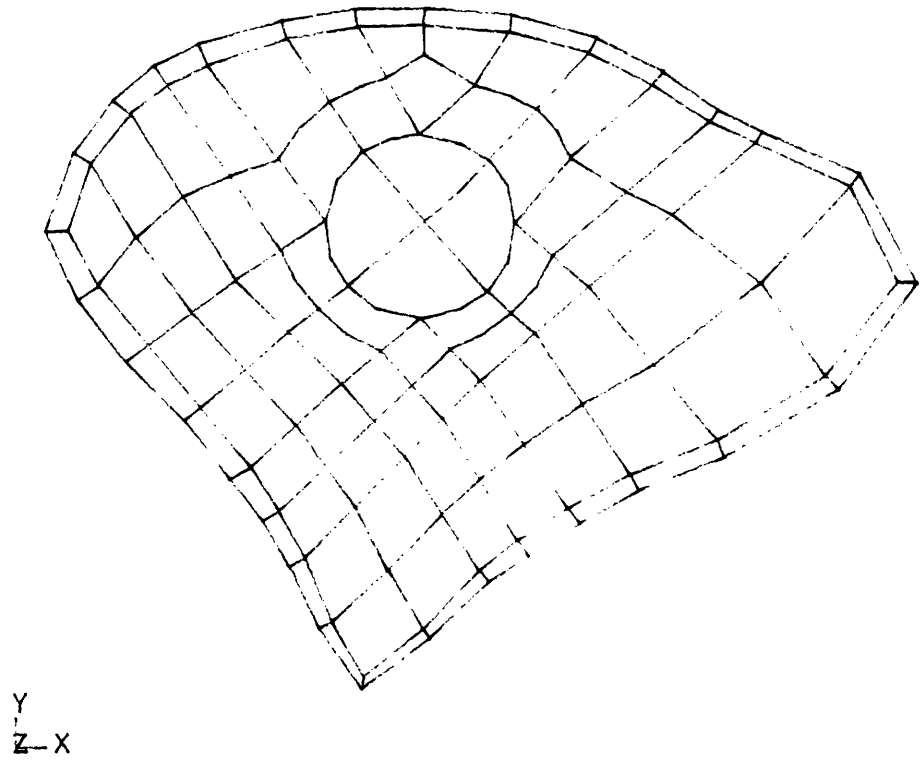

Figure 2.19a: Sagittal section of a three-dimensional finite element mesh, after digitization.

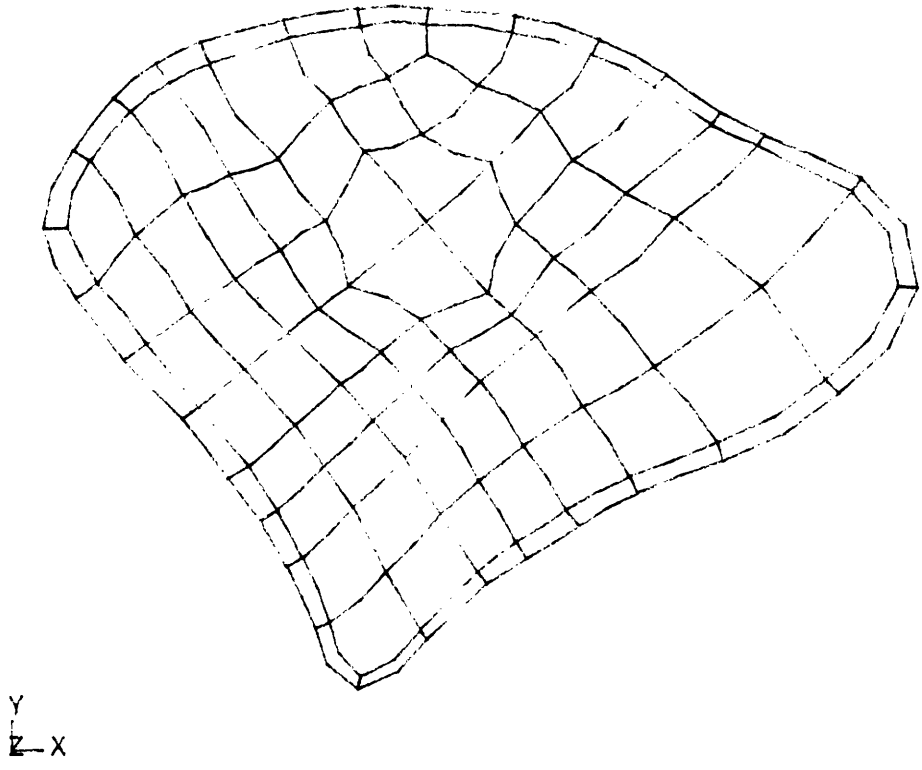

Figure 2.19b: Same mesh section as in Figure 2.19a, after application of the node relocation algorithms.

angles at the corner nodes which resulted from relocation of the mid-edge nodes.

Cortical Shell Representation

The cortical shell in some regions of the finite element models was very thin, resulting in very poor element aspect ratios. Reducing the element aspect ratios would have required either overestimating the thickness of this shell, or using a prohibitive number of elements. Very thin elements can result in numerical ill-conditioning of the stiffness matrix. The stiffness coefficients corresponding to the through-thickness strains are considerably larger than those corresponding to the other strains. This results in excessive shear strain energy stored in these strain components. For this reason, superparametric shell elements have been developed for the analysis of thin shell structures. These elements are based on either Kirchhoff plate theory, in which out-of-plane shear deformations are neglected, or Mindlin plate theory, in which out-of-plane shear deformations are included. Unfortunately, these elements employ displacement interpolation functions which differ from the isoparametric brick elements used in these analyses (Bathe 1982). To avoid this incompatibility, 16-node brick elements were used having no mid-edge nodes through the thickness of the cortical shell. Furthermore, the displacements were constrained in the direction normal to the cortical shell surface such that no strains could occur through the shell thickness. This constraint eliminated the numerical ill-conditioning which results when using elements with poor aspect ratios since the

stiffness terms corresponding to the through-thickness directions are removed. The shell elements based on plate theory assume that the through-thickness stresses are equal to zero. The disadvantage of the present element formulation is that the elements well tend to overestimate the in-plane stiffnesses due to the plane strain, rather than plane stress, condition.

The amount by which the constrained brick elements overestimate the element stiffness can be calculated. Using Hooke's Law, the axial stiffness for a linear isotropic rectangular element in unconfined compression is:

$$k_x = \frac{E w_y w_z}{w_x} \tag{2.55}$$

where E is the elastic modulus and w_i are the dimensions of the element. If the element is constrained in the y direction, the axial stiffness is:

$$k_x' = \frac{E w_y w_z}{w_x} \frac{1}{(1 + \nu)(1 - \nu)} \tag{2.56}$$

Therefore, the stiffness in the direction of applied compression is increased by a factor which is a function of the Poisson's ratio of the material:

$$\frac{k_x'}{k_x} = \frac{1}{(1 + \nu)(1 - \nu)} \tag{2.57}$$

For example, for a Poisson ratio equal to 0.3, the ratio above equals approximately 1.1. To compensate for this factor, the elastic modulus of the cortical shell elements was decreased by the same factor. While this compensation results in an underestimation of the in-plane stresses for these elements, in the present study it was more important to accurately predict the trabecular bone stresses rather than the cortical shell stresses. For the displacement based finite element formulation, this requires an accurate representation of the cortical shell stiffness rather than an accurate prediction of the cortical shell stresses.

Thus, superparametric 16-node elements, which allow strain only in the element planes, were used to represent the thin cortical shell. The overestimation of the in-plane element stiffnesses was compensated for by a reduction of the cortical shell elastic modulus. These elements were used in all regions where the shell geometry resulted in element aspect ratios greater than ten-to-one.

Bandwidth Reduction

The fundamental equation for static finite element analyses is of the form:

$$\mathbf{Ku} = \mathbf{r} \tag{2.58}$$

where **K** is the stiffness matrix, **r** is the load vector, and **u** is the unknown displacement vector. The stiffness matrix is square, symmetric, and in general, sparsely populated. To take advantage of these

properties, solution algorithms termed band-solvers, such as ADINA, store only the matrix elements from the diagonal to the top-most non-zero element of each column. This is termed the half-bandwidth and thus the mean half-bandwidth reflects the storage required for the entire stiffness matrix. For band-solvers the mean half-bandwidth also directly affects the solution time for the effective inversion of the stiffness matrix.

The location of the non-zero elements of **K** depend solely on the numbering of the finite elements. The column height for a particular column i is the difference between i and the smallest numbered node j which is a neighbor of i (two nodes are neighbors if both are part of a common element). Thus, elements should be numbered such that the average maximum difference between neighboring nodes is minimized.

Many algorithms are available for reducing the bandwidth of a sparse matrix. These algorithms seek to reduce both the maximum half-bandwidth and the profile of the stiffness matrix. A simple but effective algorithm essentially passes an inclined plane through the mesh numbering each node as it is intersected. The most commonly used algorithms are based on graph theory, such as the "Cuthill-McKee" (Cuthill and McKee, 1969) or the "Gibbs-Poole-Stockmeyer" (Gibbs et al. 1976). A node connection table is generated and the renumbering proceeds level by level. These procedures are not iterative; the final numbering sequence is independent of the original numbering sequence.

To further reduce the profile of the stiffness matrix an iterative

algorithm was written. This algorithm reduced the matrix profile with each iteration, rather than completely renumbering the finite element mesh. The algorithm essentially searched for columns with height greater than the original mean half-bandwidth and attempted to "swap-up" the top-most non-zero element of that column. The change in the number of matrix elements was calculated for each attempted swap and only the swaps which reduced the total number of matrix elements were made. While this concept is rather simple this would be a very inefficient algorithm if it were not for the complex logic used to minimize the number of calculations. The algorithm is described in detail below in the form of a computer program:

1) Generate the node connection table: Two one-dimensional arrays are used, one which contains the number of nodes to which each node is related (the number of neighbors) and one which contains the identities of those nodes:

```
    nn(i) = number of neighbors, node i
nc(col i) = node neighbors, node i
```

2) Calculate the original mean half-bandwidth and mean number of neighbors:

```
    n = number of columns (nodes)
    i = column number
    j = minimum neighbor of i
ch(i) = column height above diagonal, column i
   pr = matrix profile
   mh = original mean half-bandwidth
   mn = mean number of neighbors
   ch = i - j for j < i
      = 0     otherwise;
   pr = sum of ch(i) for all i
   mh = (pr + n)/n
  imh = integer(mh)
   mn = (sum of nn(i) for all i)/n
  imn = integer(mn)
```

3) Find a column ii where the column height is greater than the original mean half-bandwidth:

```
      ii = n + 1;
   1: ii = ii - 1;
      if ii = imh, ii = n;
      if ch(ii) ≤ imh, go to 1;
```

4) Set i equal to the top-most non-zero element of column ii:

```
      i = min(nc(col ii))
```

5) Find a column j where j is greater than i. If column j is related to ii (ii a neighbor of j), that column is skipped. Start at a column which is some distance dj from column i:

```
      j = i + dj + 1;
   2: j = j - 1;
      if j = i, go to 1;
      if nc(col j) contains ii, go to 2;
```

6) Calculate the decrease in the matrix profile for the swap (dec):

```
dec = 0;
for each k where k is a neighbor of i:
  if k < i, go to next k;
  if k = j, go to next k;
  if k is a neighbor of j, go to next k;
  set l = minimum neighbor of k;
  if l < i, go to next k; (l must = i)
  set l = 2nd minimum neighbor of k;
  if l > k, set l = k;
  if l > j, set dec = dec + j - i
      else, set dec = dec + l - i;
end loop;
if j is not a neighbor of i then:
  set l = minimum neighbor of i;
  if l > i, set dec = dec + l - i;
end if;
```

7) Calculate the increase in the matrix profile for the swap (inc):

```
inc = 0;
for each k where k is a neighbor of j:
  if k ≤ i, go to next k;
  if k is a neighbor of i, go to next k;
  set l = minimum neighbor of k;
  if l ≤ i, go to next k;
  if l < k, set inc = inc + l - i
      else, set inc = inc + k - i;
end loop;
```

```
if i is not a neighbor of j then:
  find l where l is minimum neighbor of j;
  if l > i, set inc = inc + l - i;
end if;
```

8) If the decrease in matrix profile (dec) is greater than the increase in matrix profile (inc) then i is swapped with j, and the algorithm continues at step 3 (label 1). If not, the algorithm continues for the next node j at step 5 (label 2). Rather than updating the node connection table after each swap, two arrays are maintained which relate the original node numbers to the new node numbers, and vice versa.

This algorithm has several limitations. The first limitation is that the algorithm requires storage of the node connection table. In general, this table is too large to be held in core memory. It was possible to implement the program on a PDP 11-23 by using a virtual array for the node connection table. While this significantly slows the procedure, this computer was available for use at no cost. A second limitation is that a suitable range of j values for the swapping procedure must be determined (dj of step 5). While one choice might be to try all columns from the right-most column (column n) to the adjacent column (column i + 1), the poor percentage of successful swaps would make the algorithm quite slow. The most efficient choice of dj was found to be equal to the mean half-bandwidth when the algorithm starts, then updated every 20 iterations to equal twice the value of the average column separation (j - i) of the successful swaps during the previous 20 iterations. The minimum value of dj was set equal to one-quarter the original mean half-bandwidth and the maximum value was set equal to the original mean half-bandwidth. The algorithm efficiency could be increased if the choice of j values for attempted swaps were improved.

2.2.4 Bone/Implant Interface

The mechanics of the bone/implant interface critically influence the stresses in the adjacent trabecular bone. Several interface conditions may be expected between an implant and bone tissue. Implants with a porous layer for bone ingrowth are tightly coupled with the trabecular bone provided bone ingrowth is complete. However, in the early stages following implantation, a nonlinear contact condition is expected wherein this interface cannot support tensile stresses. Smooth implants are never tightly coupled to the adjacent bone since a tight mechanical junction is not possible. The development of a fibrous tissue layer surrounding the implant is possible for both implant types which results in nonlinear interface conditions. The objective here was to investigate various methods of representing the bone/implant interface for application in the remainder of the finite element studies. A series of two-dimensional models of the ovine calcaneus, with and without a cylindrical implant, were analyzed using two different mesh densities and a number of representations of the bone/implant interface.

Modeling Techniques

A two-dimensional mesh was generated from a sagittal section of a normal ovine calcaneus. The outlines of the cortical and trabecular regions were traced and the finite element mesh was sketched. The coordinates of the nodal points were established using a digitizing tablet. The first mesh (Model C1.1) included 57 eight-node elements and 187 nodes. Subsequently, a finer mesh (Model C1.2) was created,

utilizing the same tracing and digitizing methods, but with 40 more elements and 71 more nodes (Figure 2.20). A circular region was included in both meshes to allow for subsequent representation of the cylindrical implant. For Models C1.1 and C1.2 this area was filled with trabecular bone in order to represent the intact calcaneus prior to implantation of the cylinder.

Loads were applied at the proximal end simulating the load applied by the Achilles tendon (tendo calcaneus). The direction and location of the applied tendon load were determined from a dissected calcaneus. For Model C1.1, five nodes were loaded and, for Model C1.2, six nodes were loaded, all at an angle of 60 degrees from the longitudinal axis of the calcaneus (Figure 2.20). The circular region is described using a clock reference system, with 12-o'clock vertical as viewed in Figure 2.20.

Eighteen truss elements were attached to the distal section of the model. Two truss elements were attached to each node, one parallel to the X axis and the other parallel to the Y axis, and the trusses were anchored. The two node trusses were equivalent to simple mechanical springs. The truss rigidities were adjusted, through several iterations, such that the nine nodes remained co-linear and the shear loads were distributed in proportion to the local modulus when the tendon load was applied. Thus it was assumed that the bone acts as a Bernoulli-Euler beam at the distal section.

All of the two-dimensional models assumed homogeneous, isotropic, and elastic material properties. The outer layer of elements for both

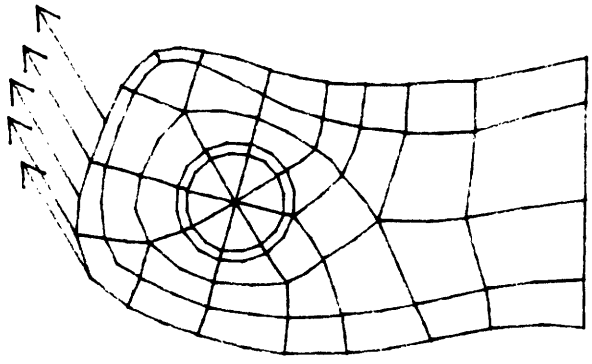

Model C1.1

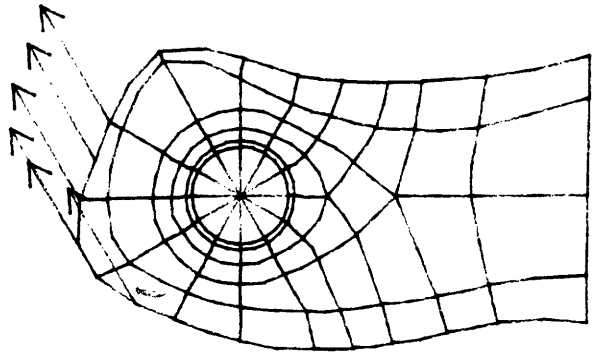

Model C1.2

Figure 2.20: Finite element mesh and applied loads for models C1.1 and C1.2.

models represented cortical bone and had an elastic modulus of 15,000 MPa and a Poisson's ratio of 0.3. Trabecular bone made up the remainder of the models, with an assumed elastic modulus of 500 MPa and a Poisson's ratio of 0.2. Dynamic effects during loading were assumed negligible. Also, the models were assumed to be in plane stress, with a thickness approximately equal to the diameter of the calcaneus (15 mm).

Several methods were employed for representing the implant. Table 2.5 outlines the the significant characteristics of the two-dimensional models. All models subsequent to Models C1.1 and C1.2 incorporated the fine mesh corresponding to Model C1.2. Various assumptions were made for the boundary conditions at the bone-implant interface. These include rigid bonding of the bone to the implant, such as would be expected if bone ingrowth had occurred, and nonlinear contact of the bone and implant surfaces. Assumptions concerning implant rigidity were also examined.

The method of representing the implant in Model C1.3 was to fill the implant region with elements with the same elastic modulus and Poisson's ratio as cobalt-chrome (248,000 MPa and 0.3, respectively). The nodes at the bone-implant interface were shared, thus representing bonding of the surfaces.

For all subsequent models, the elements filling the implant region were removed. The loads carried by the trusses on the distal section were established from Model C1.2 and these trusses were replaced by equivalent loads. The two cases were equivalent since static

Table 2.5

Model Characteristics for Interface Mechanics

Model	Mesh Density	Solution Method	Implant Representation
C1.1	Course	Linear	Intact
C1.2	Fine	Linear	Intact
C1.3	Fine	Linear	High modulus elements
C1.4	Fine	Linear	Interface nodes anchored
C1.5	Fine	Linear	Truss elements at interface
C1.6	Fine	Equilibrium iterations	Nonlinear trusses tangential and normal
C1.7	Fine	Equilibrium iterations	Nonlinear trusses 45 degrees to normal
C1.8	Fine	Stiffness reformation	Nonlinear trusses 45 degrees to normal

equilibrium requirements are similarly met. For Model C1.4 the nodes around the implant were anchored. Anchoring the nodes at the bone/implant interface represents an implant of infinite modulus. For subsequent models, two truss elements were applied to each node at the bone-implant interface. For two perpendicular linear truss elements of equal rigidity, the results are not affected by the alignment of the trusses relative to the bone. Model C1.5 incorporated rigid linear truss elements at the bone-implant interface. The results were contrasted with Models C1.3 and C1.4 to establish that the implant was accurately represented, especially in terms of the apparent modulus of the implant.

Models C1.6 through C1.8 incorporated nonlinear truss elements at the bone-implant interface. The nonlinearity was such that the rigidity in compression was four orders of magnitude greater than in tension. Model C1.6 had one nonlinear truss normal and one linear truss tangential to the bone-implant interface. Models C1.7 and C1.8 had two mutually perpendicular nonlinear trusses placed 45 degrees from the surface normal (Figure 2.21).

The objective for using the nonlinear trusses was to better model the bone-implant interface soon after implantation of the cylinder. In the early stages after implantation there is no bone ingrowth. Consequently, no tensile stresses could be transmitted to the implant across the bone-implant interface. Once ingrowth has occurred, the linear models should more accurately predict the stress fields.

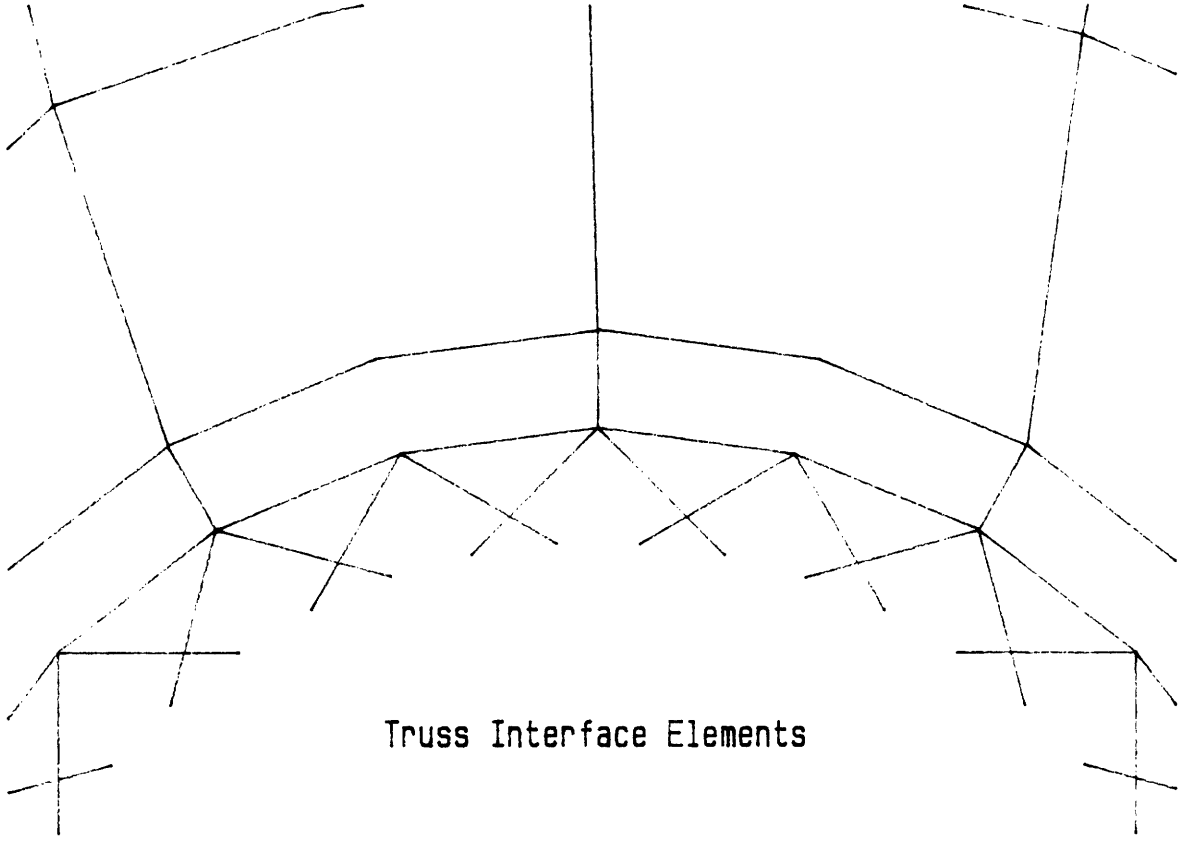

Figure 2.21: Truss elements at the bone/implant interface.

Several analyses were performed to determine the optimal method for the nonlinear analyses. One standard method is Newton-Raphson equilibrium iterations. This method involves initially assuming some force and displacement at each node, then redefining the displacement of each node using the appropriate modulus. The nodal forces are then revised utilizing the updated displacements. This iterative process may be expressed in equation form as:

$$^{t+\Delta t}\mathbf{K}\Delta\mathbf{u}_i = {}^{t+\Delta t}\mathbf{r} - {}^{t+\Delta t}\mathbf{f}_{i-1}, \tag{2.59}$$

$$^{t+\Delta t}\mathbf{u}_i = {}^{t+\Delta t}\mathbf{u}_{i-1} + \Delta\mathbf{u}_i, \tag{2.60}$$

where $\mathbf{r}$ is the load vector, $\mathbf{f}$ is the nodal force vector, $\mathbf{K}$ is the stiffness matrix, and $\mathbf{u}$ is the nodal displacement vector. The left superscript indicates the time and the right subscript indicates the iteration. The left-hand-side of Equation 2.59 are the out-of-balance loads. This process is repeated until the difference between iterations satisfies a prescribed force and displacement tolerance. The convergence criteria used in program ADINA are:

$$\frac{||^{t+\Delta t}\mathbf{r} - {}^{t+\Delta t}\mathbf{f}_{i-1}||^2}{||^{t}\mathbf{r} - {}^{t}\mathbf{f}||^2} \leq r_{tol} \tag{2.61}$$

$$\frac{\Delta\mathbf{u}_i^T(^{t+\Delta t}\mathbf{r} - {}^{t+\Delta t}\mathbf{f})}{\Delta\mathbf{u}_1^T(^{t+\Delta t}\mathbf{r} - {}^{t}\mathbf{f})} \leq e_{tol} \tag{2.62}$$

where r_{tol} and e_{tol} are user-defined tolerances. Modified Newton-Raphson iterations are also used wherein the stiffness matrix is updated

only after convergence, rather than at every iteration. For this investigation the Broyden-Fletcher-Goldbarb-Shanno (BFGS) method of equilibrium iterations was performed. This method involves updating the factorized stiffness matrix using a secant approximation at each iteration. These methods were described in detail by Bathe (1982). An alternate approach was to perform a single stiffness matrix reformation with no equilibrium iterations. The original stiffness matrix, as in the previous methods, was based on the undeformed geometry. The loads were applied in a single increment. After solving for the nodal displacements, the stiffness matrix was reformed based on the current geometry, thus accounting for changes in elemental stiffnesses due to nonlinearities. This method is applicable when, as in the present analyses, the stiffness matrix is approximately linear beyond the initial loading regime. BFGS equilibrium iterations were used for Models C1.6 and C1.7 and a single stiffness reformation with no equilibrium iterations was used for Model C1.8.

After creating the finite element meshes, the two-dimensional models were analyzed with the finite element package ADINA (ADINA Engineering, Inc. Watertown, MA 02172). The results of the ADINA computations were post-processed using FEMVIEW (Jordan, Apostal, Ritter Associates, Inc. Davisville, RI 02854), and graphic results were obtained for the principle stresses.

Model Comparison

Vector plots of the principal stresses around the circular region

were generated. The principle stresses for the coarse and fine meshes which model an intact calcaneus (Models C1.1 and C1.2, respectively) are shown in Figure 2.22. For Model C1.1 the principle stresses tend to be highest at around 2 and 5-o'clock, relative to the circle, with a stress concentration within the circular region. For Model C1.2 the principle stresses remained fairly constant along the longitudinal axis, with no obvious discontinuities.

When the circular region was filled with elements having the modulus of cobalt-chrome (Model C1.3), the principle stresses around the implant were 16% greater in tension and 26% greater in compression than the results for Model C1.2. Moreover, the compressive stress components were highest at the implant around 2 and 8-o'clock, while the tensile stresses were highest around 5 and 11-o'clock (Figure 2.23). This was unlike the uniform distribution encountered in Model C1.2. Although the largest principle stresses were compressive, it is significant that the peak tensile stresses were oriented normal to the bone-implant interface.

The results for the models in which the nodes around the implant were anchored (Model C1.4) and the nodes around the implant were attached to high modulus linear trusses (Model C1.5) were very similar to the results for Model C1.3. Replacing the linear trusses with nonlinear trusses normal to the interface and linear trusses tangential to the interface (Model C1.6), the results yielded tensile stresses which were about 50% greater than those for Models C1.3, 4 and 5 (Figure 2.23). Also, the orientation of the compressive and especially the

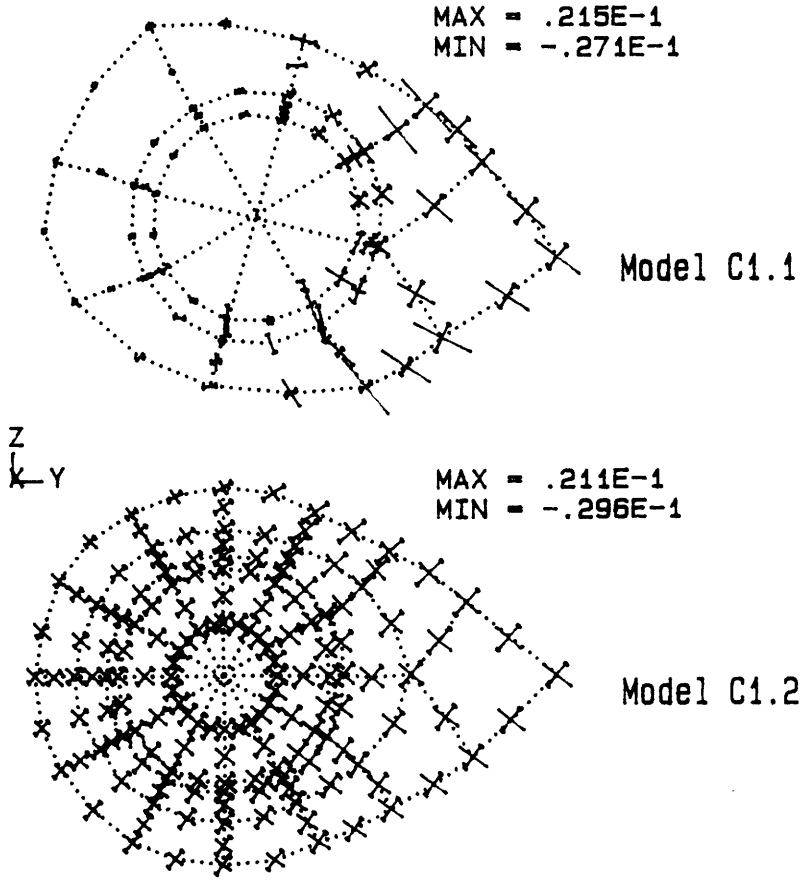

Figure 2.22: Principal stress vectors in the implant region, Models C1.1 and C1.2. The cross-hatches indicate compression.

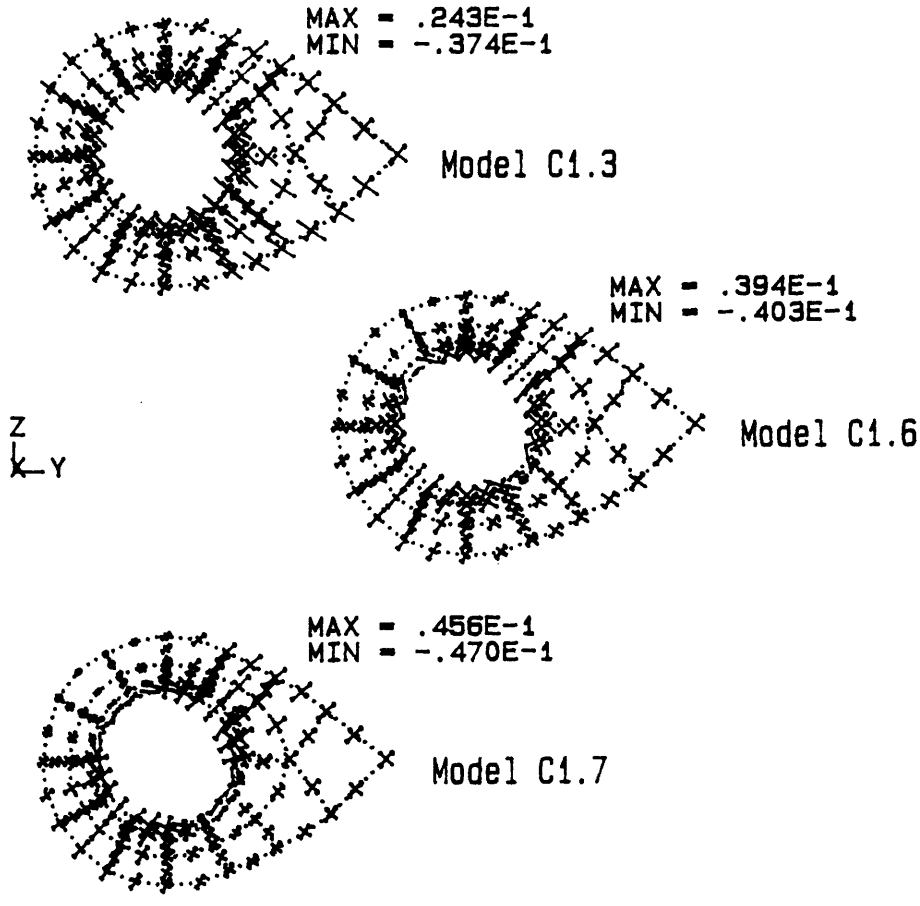

Figure 2.23: Principal stress vectors in the implant region, Models C1.3, C1.6, and C1.7.

tensile stresses were changed.

Results for the nonlinear model with trusses 45 degrees to the normal of the bone-implant interface (Model C1.7) are also shown in Figure 2.23. Specifically, these results are for a model which performed 14 BFGS equilibrium iterations and had a relative displacement tolerance of 0.01% and a relative force tolerance of 1.0%. If the tolerances were less strict the results were essentially the same as Models C1.3, 4, and 5. Results virtually identical to those shown in Figure 2.23 were also obtained if 1 stiffness matrix reformation was performed (Model C1.8), with the stiffness reformation method using about half the CPU time of the equilibrium iteration method. The results for Model C1.7 indicated maximum principle stresses that were 116% greater in tension and 59% greater in compression than those for Model C1.2. Also, the alignment of the principal stresses was different. The tensile principal stresses tended to flow around the implant directed almost tangential to the bone-implant interface.

Discussion

The results from the coarser mesh (Model C1.1) indicate that this mesh is insufficient. The stresses within the trabecular region were non-uniform and high stresses were encountered on isolated nodes near the implant region. In contrast, Model C1.2 predicted much more uniform stresses throughout the calcaneus and no particularly high stresses around the proposed implant region. Thus the finer mesh proved superior to the coarse mesh and, in two-dimensions, was sufficient for predicting

the stresses in the calcaneus.

All the linear models indicated that the tensile stresses occur normal to the implant surface. This is possible only if there is significant ingrowth of bone within the implant, thus these models are useful for determining the stress fields around an implant given time for ingrowth and assuming a fibrous layer does not form. The assumption that the implant acts as an infinitely rigid body, and that trusses may be used to represent this conditions, seem reasonable since the principle stresses and displacements of Models C1.3, 4, and 5 were virtually identical. Since Model C1.4 utilized fewer elements than Models C1.3 and 5 it represented the most efficient, accurate method for determining the stress fields around an implant with ingrowth.

The nonlinear models predicted markedly altered stress fields around the implant. For Model C1.6, where the trusses were normal and tangential to the implant, the principal tensile stresses were about 45 degrees to the bone-implant interface, indicating tensile stress components normal to this interface. In contrast, Model C1.7, with trusses at 45 degrees to the normal of the implant, predicted tensile stresses predominantly tangential to the implant. Thus Model C1.7 represents an improved method of modeling the bone-implant interface in the early stages following implantation.

2.3 Stress-Morphology Analyses

Stereologic methods were used to quantify the structural parameters

of trabecular bone. These structural parameters include the areal density, the average trabecular width, and the degree and direction of anisotropy. These data were then compared to the stress predictions of the finite element models using statistical methods to evaluate the stress-morphology relationships.

For practical reasons the stereologic measurements were made on plane sections and thus are inherently two-dimensional. Three-dimensional structural measures are possible if three orthogonal planes are examined. This technique was applied in the study of the anisotropic material properties of trabecular bone of the horse patella. However, the analyses of the experimental bone sections were limited to the planes through the implants to produce the best yield of critical data. All stereologic analyses were performed using an automated image analysis system. The software for the stereologic analyses, which uses the method of directed secants to predict the morphologic parameters described below, were written by Snyder (1987).

Specimen Preparation

All bone specimens were fresh frozen immediately after animal sacrifice. After a variable storage period, the soft tissues were dissected and the specimens were embedded in either methylmethacrylate (MMA), Alumacast (a synthetic polymer), or Castolite (a styrene polymer). Two techniques were used to prepare sections for stereologic analysis. Contact radiographs of thin sections were used for the first series of ovine calcanei and the bone cube material property specimens

and alumina silicate packing was used for the remainder of the specimens.

The first series of sheep calcanei were embedded in MMA using a standard protocol. This procedure results in infiltration of the marrow space by polymerized MMA which allows for the preparation of very thin sections. Sections of approximately 200 um thickness were obtained with the diamond saw. These sections were then polished to a thickness of 100 um or less on a metallographic polishing wheel. Contact microradiographs were prepared of the thin sections.

The second series of ovine calcanei were embedded in Castolite which is clear and non-infiltrating. A single mid-sagittal cut was made with the diamond saw. A water pick was then used to clean the interstitial spaces and 0.2 um alumina silicate was packed and leveled to provide a reflective filling. This surface was then photographed through a fluorescence microscope to view the polychrome fluorescent labels and the imaging microscope for stereologic analyses.

The equine patellae were embedded in Alumacast which is non-infiltrating. For this purpose, right and left standard molds were prepared of the femoral condyles and proximal tibia. A positive mold of Alumacast was made for each patella and the patellae were placed anatomically prior to embedding. A suture was used to mark the distal pole which is immediately distal to the insertion of the middle patellar ligament as a reference for the mid-sagittal plane. After embedding, the blocks were sectioned sagittally at 10 mm intervals using a

carborundum grinding wheel. The cut surfaces were then prepared and imaged similar to the second series of ovine calcanei.

The cubes prepared for material property tests (see Section 2.2.1) were taken from a normal equine patella prepared as those above. Thin sections were cut from three orthogonal faces of each cube using the diamond saw. The were lightly sanded to a thickness of approximately 100 um. Microradiographs were prepared and imaged similar to the first series of ovine calcanei.

Analytical Methods

The stereological techniques are based on the "method of directed secants" (Saltykov 1958). In this method, a circular region of the two-dimensional image is scanned with an array of equidistant parallel test lines (Figure 2.24). A count is produced of the number of intersections between bone and marrow space for the particular scan line orientation. The test array is then incrementally rotated and the count repeated. This procedure yields the mean path length in bone (Weibel 1967):

$$L_b(\Theta) = \frac{2A_A}{I_L(\Theta)} \tag{2.63}$$

where A_A is the bone areal density, given by the ratio of bone to non-bone pixels, and $I_L(\Theta)$ is the test line density (the number of intersections per unit test line length), given by the scan described above. For random sections, a polar plot of $L_b(\Theta)$ yields a circle for

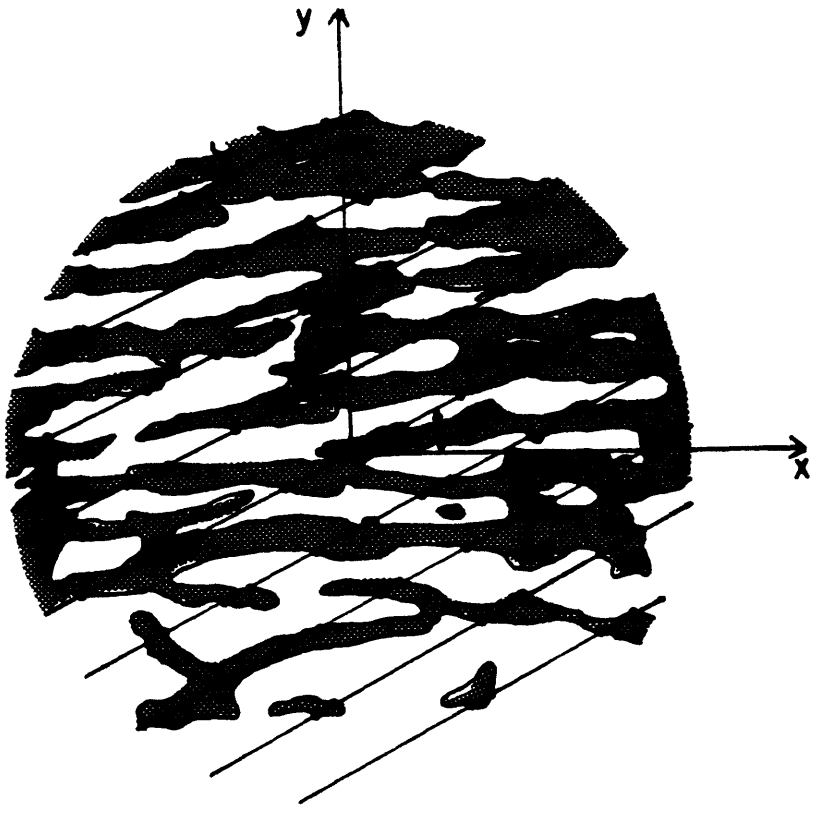

Figure 2.24: Parallel test lines superimposed over trabecular architecture for the method of directed secants. Adapted from Hayes et al. (1982).

isotropic structures and an ellipse for partially oriented structures (Whitehouse 1974). Furthermore, a three-dimensional plot of $L_b(\Theta)$ yields a sphere for isotropic structures and an ellipsoid for partially oriented structures (Harrigan and Mann 1984), with the general formula:

$$Ax_1^2 + Bx_2^2 + Cx_3^2 + Dx_1x_2 + Ex_1x_3 + Fx_2x_3 = 1 \qquad (2.64)$$

Recognizing that Equation 2.64 is the quadratic form of a second rank tensor (Reismann and Pawlik 1980), the ellipsoid may be represented in matrix form as:

$$[X]^T[M][X] = 1 \qquad (2.65)$$

where:

$$[X] = \begin{bmatrix} x_1 \\ x_2 \\ x_3 \end{bmatrix} \qquad (2.66)$$

$$[M] = \begin{bmatrix} A & D & E \\ D & B & F \\ E & F & C \end{bmatrix} \qquad (2.67)$$

Note that [M] is a symmetric second rank tensor which obeys the tensor transformation law. Therefore, the degree and directions of material orientation may be found by solving the eigenvalue-eigenvector problem to yield (Snyder 1987):

$$\frac{x'^2}{d_1^2} + \frac{y'^2}{d_2^2} + \frac{z'^2}{d_3^2} = 1 \tag{2.68}$$

where d_i are the semi-axes of the ellipsoid and x′, y′, and z′ correspond to the principal axis system.

In practice, it is not practical to scan planes at every orientation through a structure. However, this is unnecessary if one recognizes the forms of the equations describing $L_b(\Theta)$ for two and three dimensions. For a two-dimensional analysis, theoretically it is only necessary to scan at three different orientations to obtain the exact solution for an ellipse:

$$Ax_i^2 + Bx_iy_i + Cy_i^2 = b_i \tag{2.69}$$

or in matrix form:

$$\mathbf{Ax} = \mathbf{b} \tag{2.70}$$

where:

$$\mathbf{A} = [x_i^2 \quad x_iy_i \quad y_i^2] \tag{2.71}$$

$$\mathbf{x} = \begin{bmatrix} A \\ B \\ C \end{bmatrix} \tag{2.72}$$

$$\mathbf{b} = [b_i] \tag{2.73}$$

In practice, the test line density is finite, making the intersection count inexact. Therefore it is more practical to scan at a reasonable test line density at greater than three orientations and calculate a best fit to the ellipse. This can be done using a least squares technique where the error is defined as:

$$E^2 = ||\mathbf{b} - \mathbf{Ax}||^2 \tag{2.74}$$

The objective, then, is to minimize E^2, with the solution being (Strang 1976):

$$\mathbf{x}' = (\mathbf{A}^T\mathbf{A})^{-1}\mathbf{A}^T\mathbf{b} \tag{2.75}$$

The procedure is similar when solving for an ellipsoid in three dimensions. In this case, multiple intersection counts from three orthogonal sections are used.

Implementation

The bone sections were analyzed using an automated image processing system. The sections were digitized using an instrumentation grade black and white camera mounted on a low magnification microscope. The analog signal was digitized into 512 by 512 pixels with 256 gray levels by a commercial video digitizer. The magnification used resulted in 57.2 pixels per mm. For a typical trabecular width of 0.2 mm, this corresponds to about 12 pixels. A gray level threshold was applied to the digitized images to distinguish bone and marrow space. The

stereologic software performed mathematical rotation of the digitized image at 15^{o} increments through 180^{o} for the test line scans. Verification of system accuracy has been reported for both two-dimensional and three-dimensional analyses (Snyder et al. 1986). Test patterns consisting of arrays of ellipses and embedded elliptical beads of known geometry and orientation were used for the verification. Linear regression demonstrated highly significant R^2 values ranging from 0.89 - 0.99 with the slopes not significantly different from 1 and the intercepts not significantly different from 0.

3.0 Results

The morphologic data from the ovine and equine control and experimental specimens were studied to characterize the trabecular bone remodeling response to the implants. The stress changes in the trabecular bone surrounding the implants were evaluated using the predictions from the finite element models. The finite element models of the control specimens were then validated based on the assumption that the principal stress directions are aligned with the measured directions of material orientation. Finally, the stress-morphology relations for implant-induced remodeling were investigated based on the assumption that the finite element model predictions were accurate.

3.1 Morphologic Analyses

The morphology of the ovine and equine specimens were analyzed using stereologic techniques. These analyses provided the areal density and the anisotropy ellipse for multiple regions of the trabecular bone surrounding the implants and in the corresponding locations in the control specimens. The present objective was to characterize the remodeling response especially as a function of the implant material and surface characteristics.

3.1.1 Equine Patella

The surgical implantation of the the stainless steel spheres was well tolerated. The only complication during the six month post-

surgical period was a wound infection in one animal which received a porous coated implant (P6). The animal was treated with one dose of antibiotics. On preparation of the patellae for embedding and sectioning, is was noted that the porous coated sphere in specimen P6 was clearly loose with only fibrous tissue holding it in place. At this time, there were no frank signs of infection. Unfortunately, no tissue sample was obtained for pathologic evaluation before the patella was embedded. All twelve patellae were embedded and sectioned as described in Section 2.3.1 and the morphologic analyses were performed using the automated stereologic system.

Contact radiographs of the sectioned patellae were obtained. Radiographs of a sagittal section through the implant for three of the experimental patellae are shown in Figure 3.1. Included are one of the specimens with a smooth sphere (S1), one of the specimens with a porous coated sphere (P7), and the specimen with the porous coated sphere which was frankly loose (P6). Note that increased bone densities are apparent around each of the implants. A fluorescent photomicrograph showing the labeled trabecular bone adjacent to the smooth implant in specimen S2 is shown in Figure 3.1c. The most prominent label was the oxytetracycline, given second to the last. This label appears yellow under fluorescent light. There were also red bands corresponding to the last label (alizarin red). The polychrome labels confirmed that there was a vigorous remodeling response adjacent to the smooth implants and that there was active remodeling during the late stages of the experiment. A photomicrograph showing ingrown trabecular spicules surrounded by the surface beads in specimen P7 is shown in Figure 3.1d. It appeared that

Figure 3.1a: Contact radiographs of a sagittal section of the control and experimental patellae with smooth surfaced implants.

Figure 3.1b: Contact radiographs of a sagittal section of the control and experimental patellae with porous coated implants.

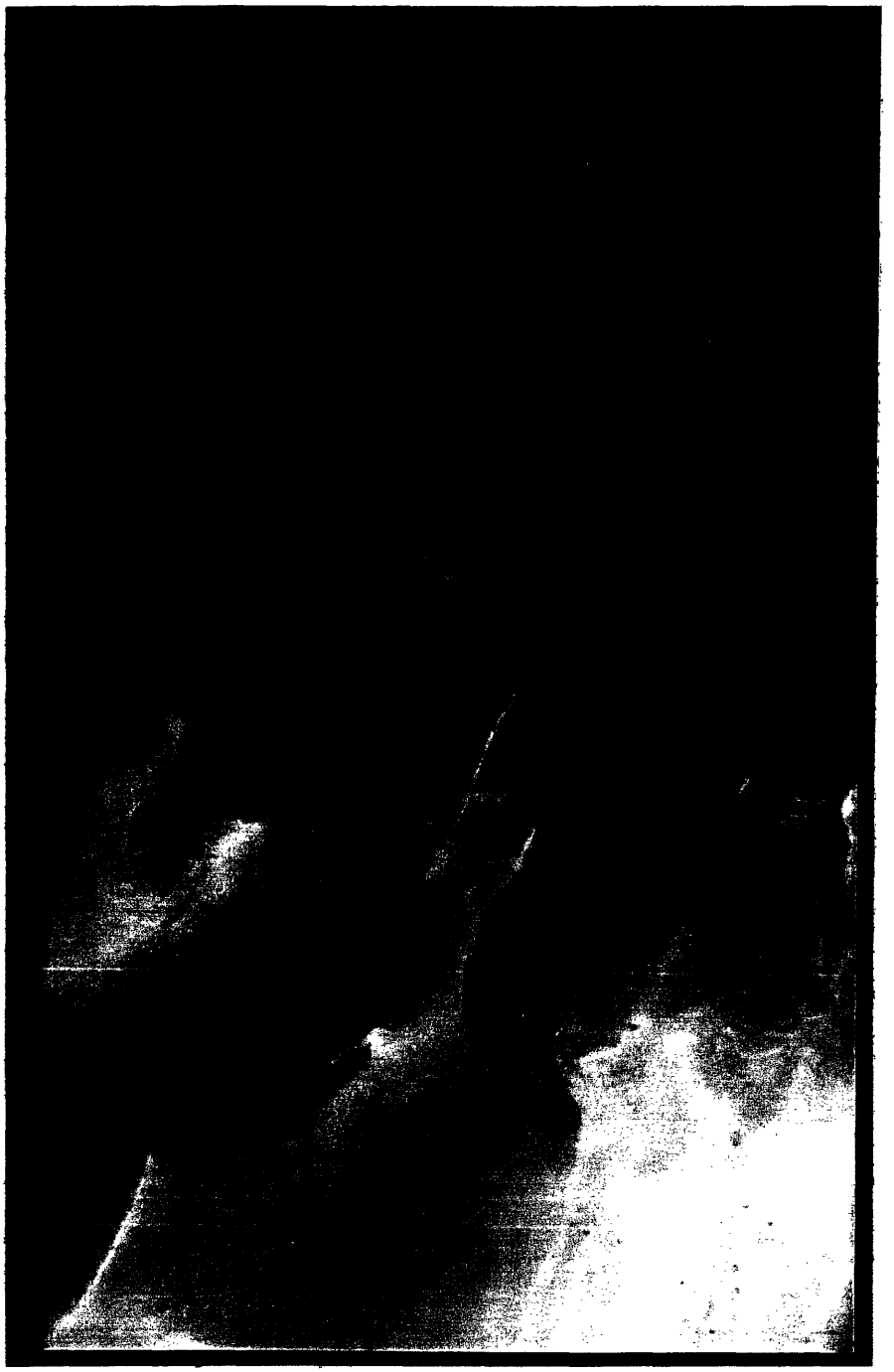

Figure 3.1c: Fluorescent photomicrograph of the trabecular bone adjacent to the smooth implant in experimental patella S2.

Figure 3.1d: Fluorescent photomicrograph of ingrown trabecular spicules surrounded by the sintered beads of experimental patella P7.

all of the void space in the porous layer was occupied by ingrown trabecular bone. Green (calcein) and yellow (oxytetracycline) bands were most apparent in the ingrown spicules and in the adjacent trabecular bone. The green label was given in the middle of the experimental period, followed by the yellow label, indicating that there was active bone formation in the porous layer several months after the surgical insertion of the implants.

The smooth and porous coated spheres induced a significant remodeling response, especially in the immediate vicinity of the implants. Photographs of the sections which were analyzed from the control and experimental patellae are shown in Figure 3.2. The stereologic analyses were performed on the experimental patellae using the array of test regions shown in Figure 3.3. This array was designed to provide data in two distinct groups at different relative locations around the implants. The "A" locations were centered a distance of 2.1 mm from the bone/implant interface, and the "B" locations were centered a distance of 6.3 mm from the bone/implant interface. Thus, the data may be examined as a function of their proximity to the implant. The analyses were also performed on the contralateral control patellae using the same array. The geometric reference point for the experimental patellae was the center of the implant. The corresponding location on each matched control patella was determined by superimposing the contact radiographs. After obtaining the images using the black and white camera and video digitizer, the images were mathematically rotated and/or inverted, as necessary, such that all images were in the same orientation as the finite element models.

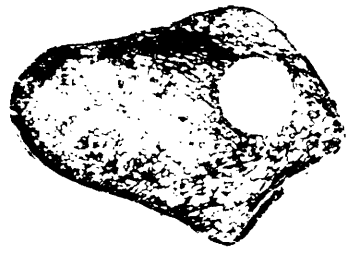

S1 Left

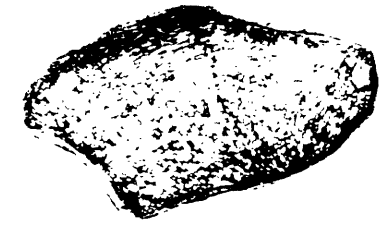

S1 Right

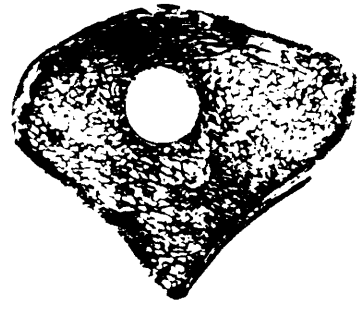

S2 Left

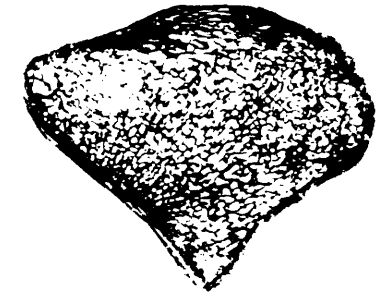

S2 Right

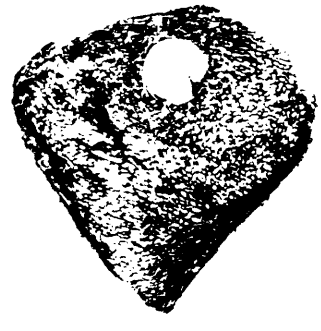

S3 Left

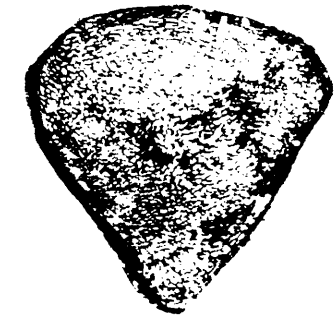

S3 Right

Figure 3.2a: Sagittal sections on which the stereologic analyses were performed for the smooth surfaced implants.

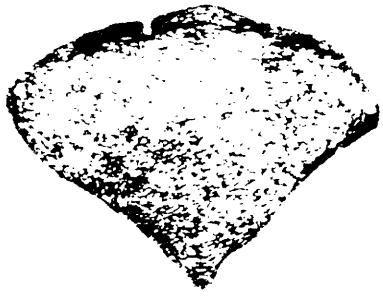

P6 Left

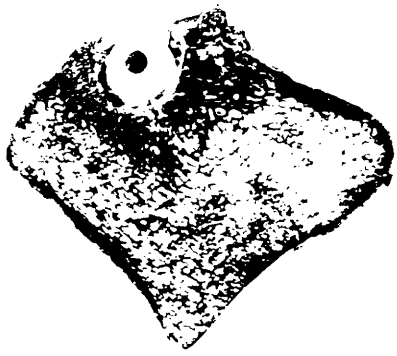

P6 Right

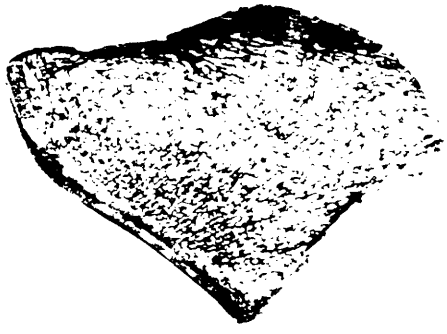

P7 Left

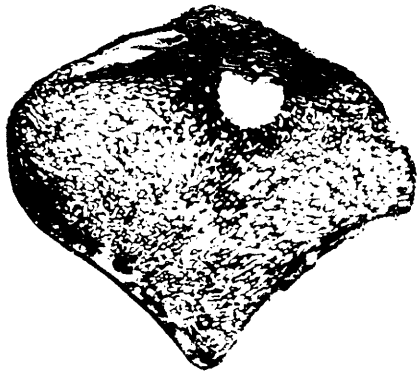

P7 Right

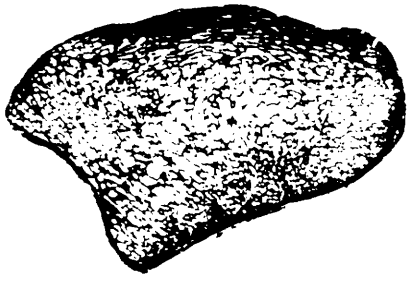

P8 Left

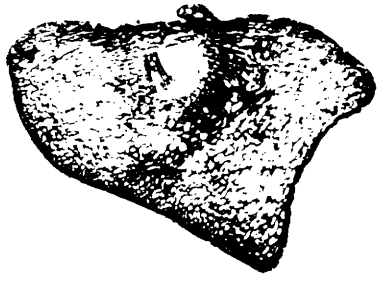

P8 Right

Figure 3.2b: Sagittal sections on which the stereologic analyses were performed for the porous coated implants.

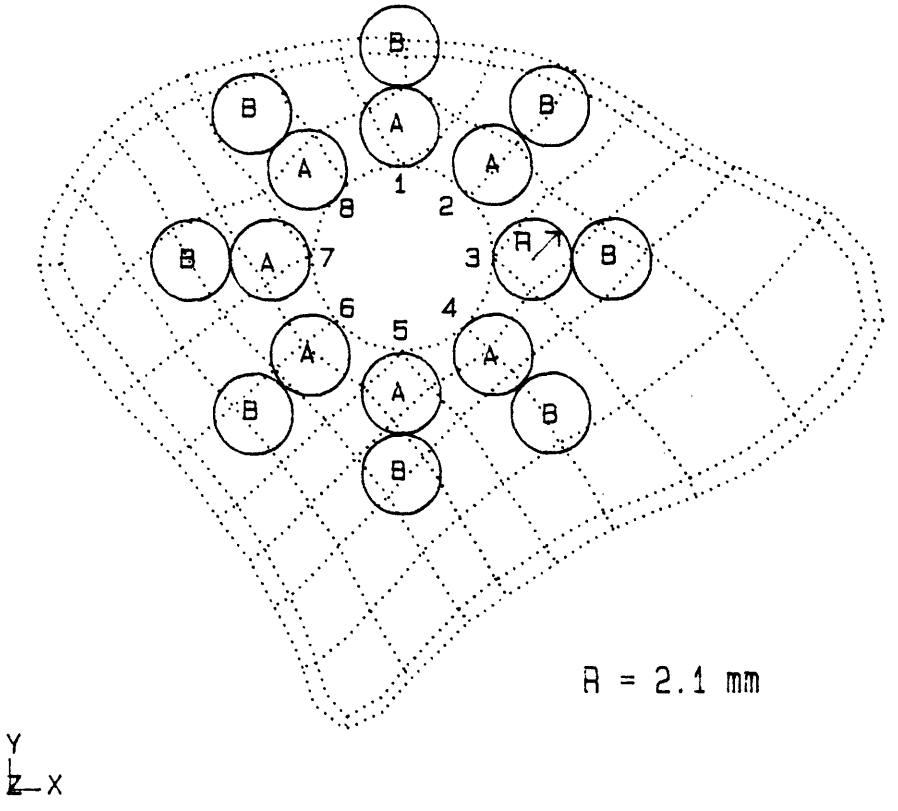

Figure 3.3: Array of image regions used for the stereologic analyses of the equine patellae.

An example of the morphologic data from specimen S3, which received a smooth surfaced implant, is shown in Figure 3.4. The region of analysis was "4A" (see Figure 3.3), and the images and results from both the control and experimental patellae are included. The resolution of the digitized images was 512 by 512 pixels with 256 grey levels. The resolution of the displayed images in these figures was much lower and the image was converted to black and white using a grey level threshold.

Some of the parameters which were measured using stereology can be estimated by visual inspection. The entire area of the control patella in Figure 3.4a appears fairly homogeneous, with a somewhat oriented architecture in the lower right portion and an isotropic architecture in the region of analysis. This observation was confirmed by the stereologic analyses. In contrast, the corresponding area (Figure 3.4b) in the experimental patella is clearly not homogeneous. There is a region of remodeled trabecular bone with an increased areal density adjacent to the implant. This finding was quite consistent for the three patellae which received the smooth surfaced implants (Figure 3.2). The extent of the intensely remodeled region visually appeared to be about 4 mm. It was this finding on which the selection of a 4.2 mm diameter for the regions of analysis was based. The most clear and convincing finding from this example, and indeed from virtually all of the areas analyzed on the experimental patellae which received smooth implants, was that there was a significant increase in bone density adjacent to the implants and little to no change beyond about 4 or 5 mm from the implants. This observation was confirmed by the results of the stereologic analyses. These data are presented below.

BETH ISRAEL HOSPITAL - IMAGE PROCESSING LABORATORY

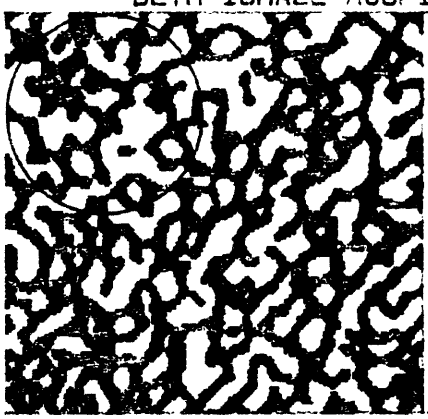

IMAGE TITLE: S4R4
COMMENT: Image 4
SUBREGION: 2
LENGTHSCALE: 57.18
GRAY THRESHOLD: 120
SOLID PHASE: BLK
TESTLINE LENGTH: 795.1
TESTLINE SPACING <PIXELS> : 1

[AREA FRACTION ANALYSIS:]
REGION AREA = 13.91
AREA FRACTION = 0.443
SOLID AREA = 6.164

[STEREOLOGY ANALYSIS:]

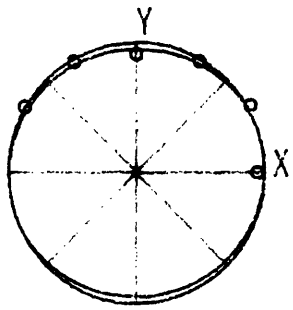

PERIMETER = 52.296
PERIM/AREA = 3.7608

ELLIPSE OF MEAN INTRCPT LENGTHS:
$A*N_1^2 + B*N_1N_2 + C*N_2^2 = MNINCPTLN^{-2}$
A = 6.935
B = -0.1787
C = 7.6768
CORRELATION COEFF = 0.444
MAX MN INTRCPT LNTH = 0.38003
ANGLE MAX ORIENTATION = 7 DEGS
MIN MN INTRCPT LNTH = 0.36067
ANGLE MIN ORIENTATION = 97 DEGS
EXTENT OF ANISOTROPY = 3.330 %

Figure 3.4a: Stereologic analysis of region "4A" from the control specimen S3.

BETH ISRAEL HOSPITAL - IMAGE PROCESSING LABORATORY

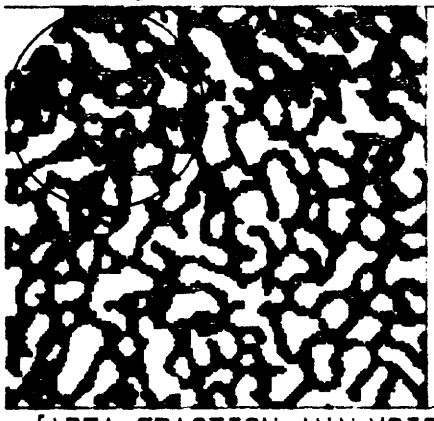

IMAGE TITLE: S4L4
COMMENT: Image 4
SUBREGION: 2
LENGTHSCALE: 57.18
GRAY THRESHOLD: 120
SOLID PHASE: BLK
TESTLINE LENGTH: 795.1
TESTLINE SPACING <PIXELS> : 1

[AREA FRACTION ANALYSIS:]
REGION AREA = 13.91

AREA FRACTION = 0.614
SOLID AREA = 8.532

[STEREOLOGY ANALYSIS:]

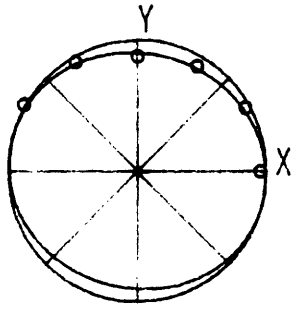

PERIMETER = 49.576
PERIM/AREA = 3.5652

ELLIPSE OF MEAN INTRCPT LENGTHS:

$A*N_1^2 + B*N_1N_2 + C*N_2^2 = MNINCPTLN^{-2}$

A = 3.111
B = 0.3601
C = 3.7458

CORRELATION COEFF = 0.815
MAX MN INTRCPT LNTH = 0.57135
ANGLE MAX ORIENTATION = -15 DEGS
MIN MN INTRCPT LNTH = 0.51344
ANGLE MIN ORIENTATION = 75 DEGS
EXTENT OF ANISOTROPY = 6.794 %

Figure 3.4b: Stereologic analysis of region "4A" from the experimental specimen S3. Note implant in upper left corner.

The trabecular bone remodeling was most intense around the porous implant in specimen P6 in which there was fibrous tissue encapsulation rather than bone ingrowth (Figure 3.2). An example of the stereologic analyses is shown in Figure 3.5. Again, images from both the control and experimental patellae are included. There was a very striking increase in bone density around the implant. As in the specimens with smooth implants, the intensely remodeled region appeared to be limited, in this case, to about 5 or 6 mm from the implant. This observation also was supported by the results of the stereologic analyses.

The other two specimens which received porous implants, but had successful bone ingrowth, appeared to have undergone the least amount of trabecular bone remodeling (Figures 3.2). Example stereologic data from specimen P7 is shown in Figure 3.6. There was a marginal increase in bone density around the implant in this specimen, suggesting moderate remodeling, as determined by the stereologic analyses. One other important observation was that the control patella from specimen P8 was generally less dense than the other five control patellae. This is discussed further below.

These observations of changes in bone density were confirmed by the stereologic measurements of bone area fraction. The means and standard deviations of the area fractions are presented in Table 3.1. The data for the "A" locations and the "B" locations were grouped separately based on the observed density changes in close proximity to the implants. The present objective was to examine the density changes as a function of the distance from the implants and as a function of the

BETH ISRAEL HOSPITAL - IMAGE PROCESSING LABORATORY

IMAGE TITLE: P66L5
COMMENT: Image 5
SUBREGION: 2
LENGTHSCALE: 57.18
GRAY THRESHOLD: 120
SOLID PHASE: BLK
TESTLINE LENGTH: 795.1
TESTLINE SPACING <PIXELS> : 1

[AREA FRACTION ANALYSIS:]
REGION AREA = 13.91

AREA FRACTION = 0.429
SOLID AREA = 5.963

[STEREOLOGY ANALYSIS:]

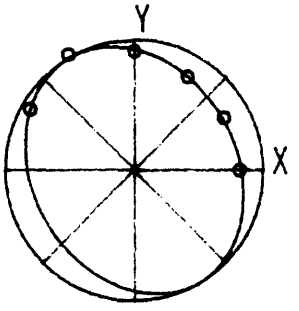

PERIMETER = 55.688
PERIM/AREA = 4.0048

ELLIPSE OF MEAN INTRCPT LENGTHS:

$A*N_1^2 + B*N_1N_2 + C*N_2^2 = MNINCPTLN^{-2}$

A = 9.909
B = 3.651
C = 7.8959

CORRELATION COEFF = 0.982
MAX MN INTRCPT LNTH = 0.38299
ANGLE MAX ORIENTATION = 121 DEGS
MIN MN INTRCPT LNTH = 0.30169
ANGLE MIN ORIENTATION = 31 DEGS
EXTENT OF ANISOTROPY = 15.069 %

Figure 3.5a: Stereologic analysis of region "5A" from the control specimen P6.

BETH ISRAEL HOSPITAL - IMAGE PROCESSING LABORATORY

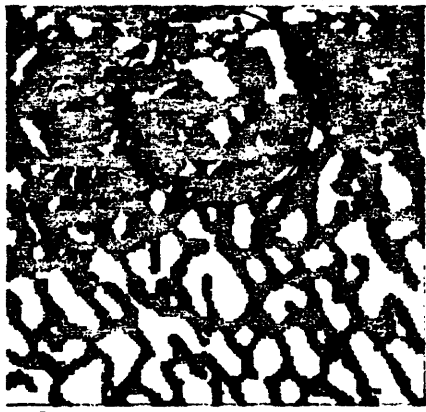

IMAGE TITLE: P66R5
COMMENT: Image 5
SUBREGION: 2
LENGTHSCALE: 57.18
GRAY THRESHOLD: 115
SOLID PHASE: BLK
TESTLINE LENGTH: 795.1
TESTLINE SPACING <PIXELS> : 1

[AREA FRACTION ANALYSIS:]
REGION AREA = 13.91

AREA FRACTION = 0.738
SOLID AREA = 10.27

[STEREOLOGY ANALYSIS:]

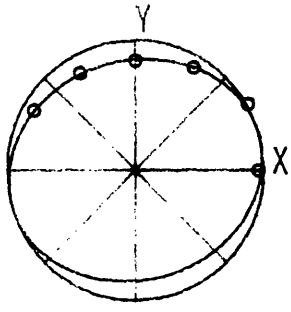

PERIMETER = 43.372
PERIM/AREA = 3.1191

ELLIPSE OF MEAN INTRCPT LENGTHS:
$A*N_1^2 + B*N_1N_2 + C*N_2^2 = MNINCPTLN^{-2}$
A = 1.552
B = -0.3173
C = 2.0770
CORRELATION COEFF = 0.969
MAX MN INTRCPT LNTH = 0.81430
ANGLE MAX ORIENTATION = 16 DEGS
MIN MN INTRCPT LNTH = 0.68660
ANGLE MIN ORIENTATION = 106 DEGS
EXTENT OF ANISOTROPY = 10.815 %

Figure 3.5b: Stereologic analysis of region "5A" from the experimental specimen P6.

BETH ISRAEL HOSPITAL - IMAGE PROCESSING LABORATORY

IMAGE TITLE: P67L5
COMMENT: Image 5
SUBREGION: 2
LENGTHSCALE: 57.18
GRAY THRESHOLD: 115
SOLID PHASE: BLK
TESTLINE LENGTH: 795.1
TESTLINE SPACING <PIXELS> : 1

[AREA FRACTION ANALYSIS:]
REGION AREA = 13.91

AREA FRACTION = 0.374
SOLID AREA = 5.205

[STEREOLOGY ANALYSIS:]

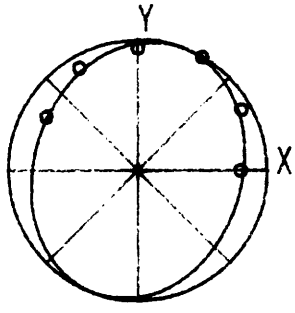

PERIMETER = 47.191
PERIM/AREA = 3.3937

ELLIPSE OF MEAN INTRCPT LENGTHS:
$A*N_1^2 + B*N_1N_2 + C*N_2^2 = MNINCPTLN^{-2}$
A = 9.848
B = -2.093
C = 6.9165
CORRELATION COEFF = 0.940
MAX MN INTRCPT LNTH = 0.38980
ANGLE MAX ORIENTATION = 72 DEGS
MIN MN INTRCPT LNTH = 0.31337
ANGLE MIN ORIENTATION = 162 DEGS
EXTENT OF ANISOTROPY = 13.803 %

Figure 3.6a: Stereologic analysis of region "5A" from the control specimen P7.

BETH ISRAEL HOSPITAL - IMAGE PROCESSING LABORATORY

IMAGE TITLE: P67R5
COMMENT: Image 5
SUBREGION: 2
LENGTHSCALE: 57.18
GRAY THRESHOLD: 115
SOLID PHASE: BLK
TESTLINE LENGTH: 795.1
TESTLINE SPACING <PIXELS> : 1

[AREA FRACTION ANALYSIS:]
REGION AREA = 13.91

AREA FRACTION = 0.402
SOLID AREA = 5.586

[STEREOLOGY ANALYSIS:]

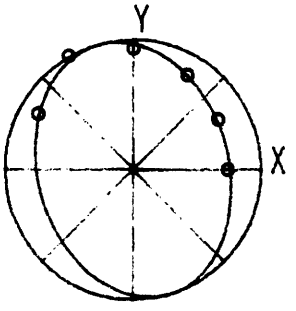

PERIMETER = 49.750
PERIM/AREA = 3.5777

ELLIPSE OF MEAN INTRCPT LENGTHS:

$A*N_1^2 + B*N_1N_2 + C*N_2^2 = MNINCPTLN^{-2}$

A = 10.11
B = 2.523
C = 6.1487

CORRELATION COEFF = 0.976
MAX MN INTRCPT LNTH = 0.41592
ANGLE MAX ORIENTATION = 106 DEGS
MIN MN INTRCPT LNTH = 0.30900
ANGLE MIN ORIENTATION = 16 DEGS
EXTENT OF ANISOTROPY = 18.683 %

Figure 3.6b: Stereologic analysis of region "5A" from the experimental specimen P7.

Table 3.1

Statistics on Bone Area Fraction Data
Equine Patella

		Control		Experimental		Difference		
Spec	Reg	Mean	SD	Mean	SD	Mean	SD	N
S1	A	0.473	0.039	0.665	0.035	0.192	0.058	3
	B	0.370	0.064	0.527	0.102	0.156	0.037	2
S2	A	0.393	0.024	0.652	0.078	0.259	0.075	7
	B	0.576	0.171	0.499	0.145	-0.077	0.052	7
S3	A	0.423	0.086	0.720	0.101	0.298	0.079	7
	B	0.500	0.086	0.539	0.125	0.039	0.053	5
P6	A	0.393	0.032	0.744	0.016	0.351	0.039	3
	B	0.533	0.180	0.596	0.186	0.063	0.047	4
P7	A	0.500	0.229	0.588	0.222	0.088	0.106	6
	B	0.476	0.230	0.494	0.178	0.017	0.091	5
P8	A	0.222	0.040	0.531	0.060	0.309	0.071	5
	B	0.235	0.061	0.366	0.050	0.131	0.027	4

different specimens. The data from the control and experimental patellae and the algebraic difference between the two for each group are included. All groups of data, with the exception of the "B" regions of specimen "S2", had, on the average, an increase in the area fraction, when comparing the experimental patella to the control patella. In all cases, the means of the changes in area fraction were greater for the "A" regions than the "B" regions, confirming the above observations of increased bone density in the vicinity of the implants. The greatest increase in area fraction occurred in the "A" regions in specimen P6.

The relatively small number of data points was due to the criterion that, for the image to be acceptable, the trabecular bone must appear homogeneous in the corresponding locations on both the control and experimental patellae. Specimen S1 had the fewest number of acceptable images due to the surgical placement of the implant (see Figure 3.2). An example of an image which was rejected due to inhomogeneity is shown in Figure 3.7.

Statistical comparisons were made to test whether the remodeling response was significant and to examine the possibility of grouping data from different specimens. These comparisons were made on the area fraction data because this was the simplest, and therefore most reliable, stereologic measurement. Also, the area fraction is directly related to the trabecular bone density, which is a critical parameter in determining the mechanical properties (see Section 1.1).

To prove that the remodeling response was significant, paired

BETH ISRAEL HOSPITAL - IMAGE PROCESSING LABORATORY

IMAGE TITLE: S1R3
COMMENT: Image 3
SUBREGION: 2
LENGTHSCALE: 57.18
GRAY THRESHOLD: 120
SOLID PHASE: BLK
TESTLINE LENGTH: 795.1
TESTLINE SPACING <PIXELS> : 1

[AREA FRACTION ANALYSIS:]
REGION AREA = 13.91

AREA FRACTION = 0.797
SOLID AREA = 11.09

[STEREOLOGY ANALYSIS:]

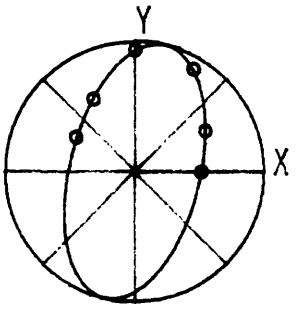

PERIMETER = 26.935
PERIM/AREA = 1.9370

ELLIPSE OF MEAN INTRCPT LENGTHS:
$A*N_1^2 + B*N_1N_2 + C*N_2^2 = MNINCPTLN^{-2}$
A = 0.9593
B =-0.3387
C = 0.29719
CORRELATION COEFF = 0.999
MAX MN INTRCPT LNTH = 1.9750
ANGLE MAX ORIENTATION = 76 DEGS
MIN MN INTRCPT LNTH = 0.99994
ANGLE MIN ORIENTATION = 166 DEGS
EXTENT OF ANISOTROPY = 40.640 %

Figure 3.7: Stereologic analysis of region "3A" from the experimental specimen S1.

comparisons were made with each pair consisting of the area fraction from a location on an experimental patellae and the area fraction from the corresponding location on the contralateral control patellae. The null hypothesis, that of an assumption of equal means, could be rejected at a significance level of 0.05 or less for all of the following groups of paired data: 1) all data from the equine patellae; 2) all "A" regions; 3) all "B" regions; 4) all data from the smooth implant specimens (S1, S2, and S3); 5) all "A" regions from S1, S2, and S3; 6) all "B" regions from S1, S2, and S3; 7) all data from the porous implant specimens (P6, P7, and P8); 8) all "A" regions from P6, P7, and P8; 9) all "B" regions from P6, P7, and P8; 10) all "A" regions from each individual specimen. The only exceptions were the "B" regions from specimens S3 and P7 when tested individually. There were significant differences in the bone area fraction, reflecting significant remodeling, in the immediate vicinity of the implants for all specimens (the "A" regions), and more distant to the implants for four of the six specimens (the "B" regions).

The next objective was to examine the validity of combining data from specimens which received similar implants. A one way analysis of variance was performed on the change in bone area fraction to test whether there was significant variation from specimen to specimen. The results of these tests were as follows: at a significance level of 0.05, 1) the null hypothesis (that of equal means) could not be rejected for the "A" regions of specimens S1, S2, and S3, or the "B" regions of specimens S1, S2, and S3; 2) the null hypothesis could not be rejected for the "B" regions of specimens P6, P7, and P8; 3) there was

sufficient evidence to reject the null hypothesis for the "A" regions of specimens P6, P7, and P8. The latter conclusion was not surprising since bone ingrowth did not occur in specimen P6 but did occur in the other two specimens. Unfortunately, there were also significant differences between the "A" regions of specimens P7 and P8 when these two were tested separately from specimen P6. This conclusion was undoubtedly due to the relatively low areal densities measured for the control patella of specimen P8. These tests provided support for combining the data from the three patellae which received the smooth implants and also demonstrated that the morphologic data from the three patellae which received the porous coated implants were inconsistent.

The changes in bone area fraction for all patellae are shown graphically in Figure 3.9. The key for the symbols in this figure is given in Figure 3.8. Points lying on the line Y = X exhibited no difference between the area fraction on the experimental side when compared to the corresponding location on the contralateral control side. Only a few points lie below this line, with the majority of points displaying an increase in density. This further emphasizes the difference between the "A" locations (filled symbols) and the "B" locations.

The principal material orientation, as determined using the method of directed secants (see Section 2.3), was also significantly different between the control and experimental patellae (Figure 3.10). The lines Y = X, indicating no change, and Y = X + 90 and Y = X - 90, indicating the possible range of data, are included for reference. While more data

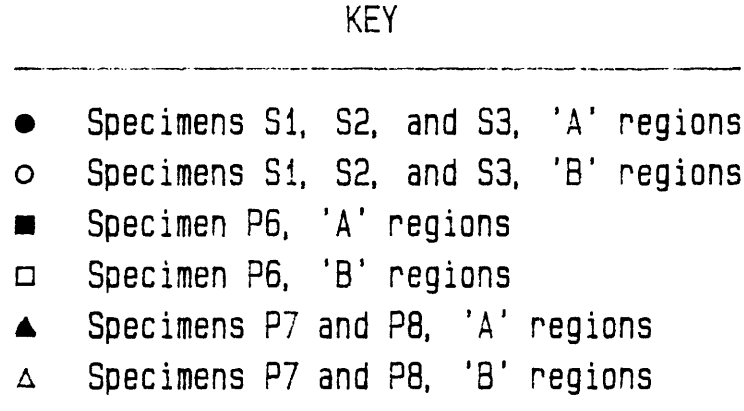

Figure 3.8: Key for all figures with corresponding symbols.

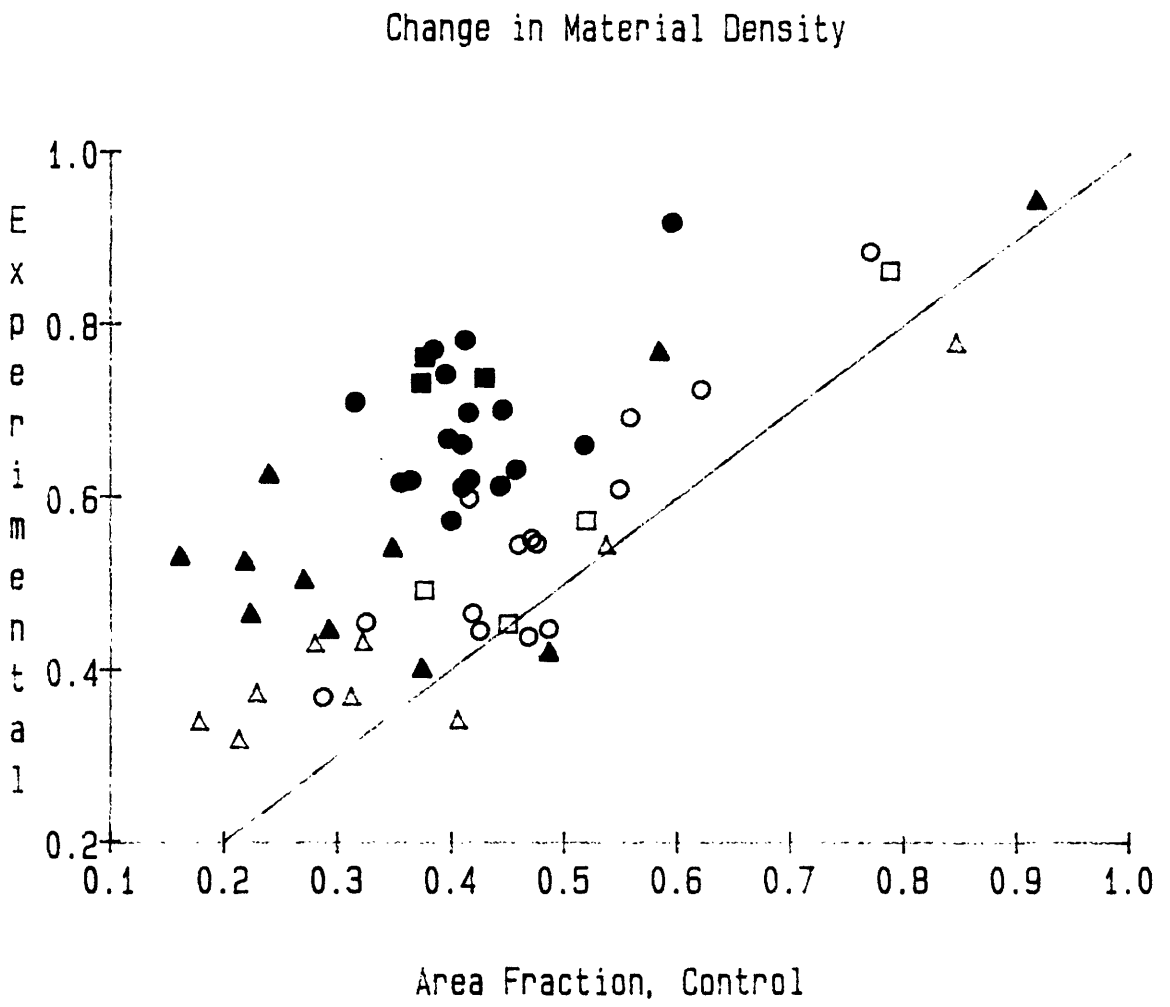

Figure 3.9: The bone area fraction in the "A" and "B" regions in the experimental patellae as a function of the bone area fraction in the corresponding regions in the control patellae. See Figure 3.8 for Key.

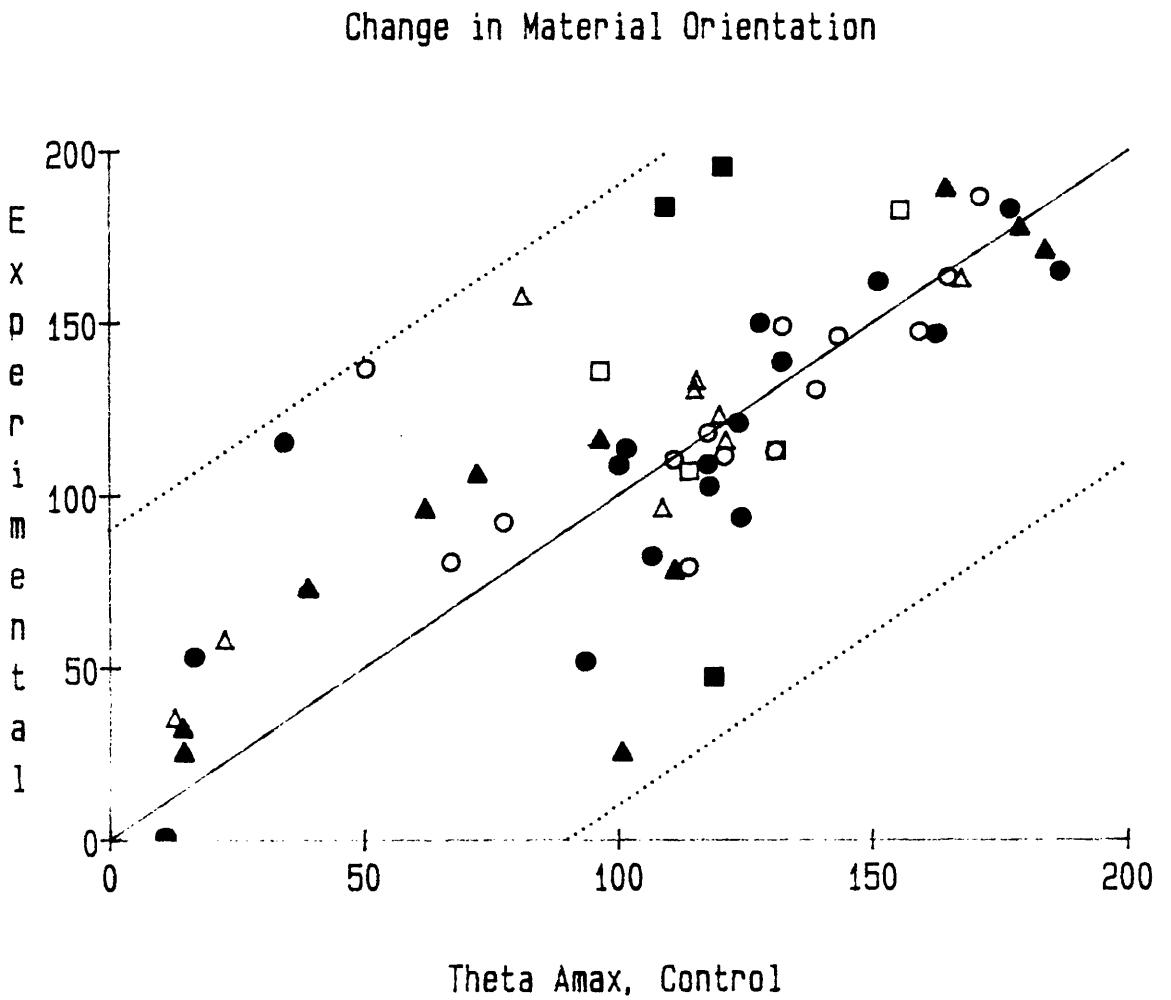

Figure 3.10: The principal material orientation in the "A" and "B" regions in the experimental patellae as a function of the principal material orientation in the control patellae. See Figure 3.8 for Key.

from the "B" locations lie near the line Y = X, large changes in the material orientation were apparent for many locations, both "A" and "B". This further demonstrates that the remodeling around the implants was significant and that the measured changes in the trabecular bone morphology were greater for regions adjacent to the implants.

The eccentricity of the anisotropy ellipse (see Equation 3.3 for definition) was different when comparing the experimental patellae to the control patellae. These data are presented graphically in Figure 3.11. While more data points from "A" locations lie below the line Y = X than above the line, indicating a change toward isotropy, the general scatter of data points does not allow conclusions to be drawn. However, it is possible that material anisotropy may be sensitive to parameters other than the implant proximity which have not yet been correlated.

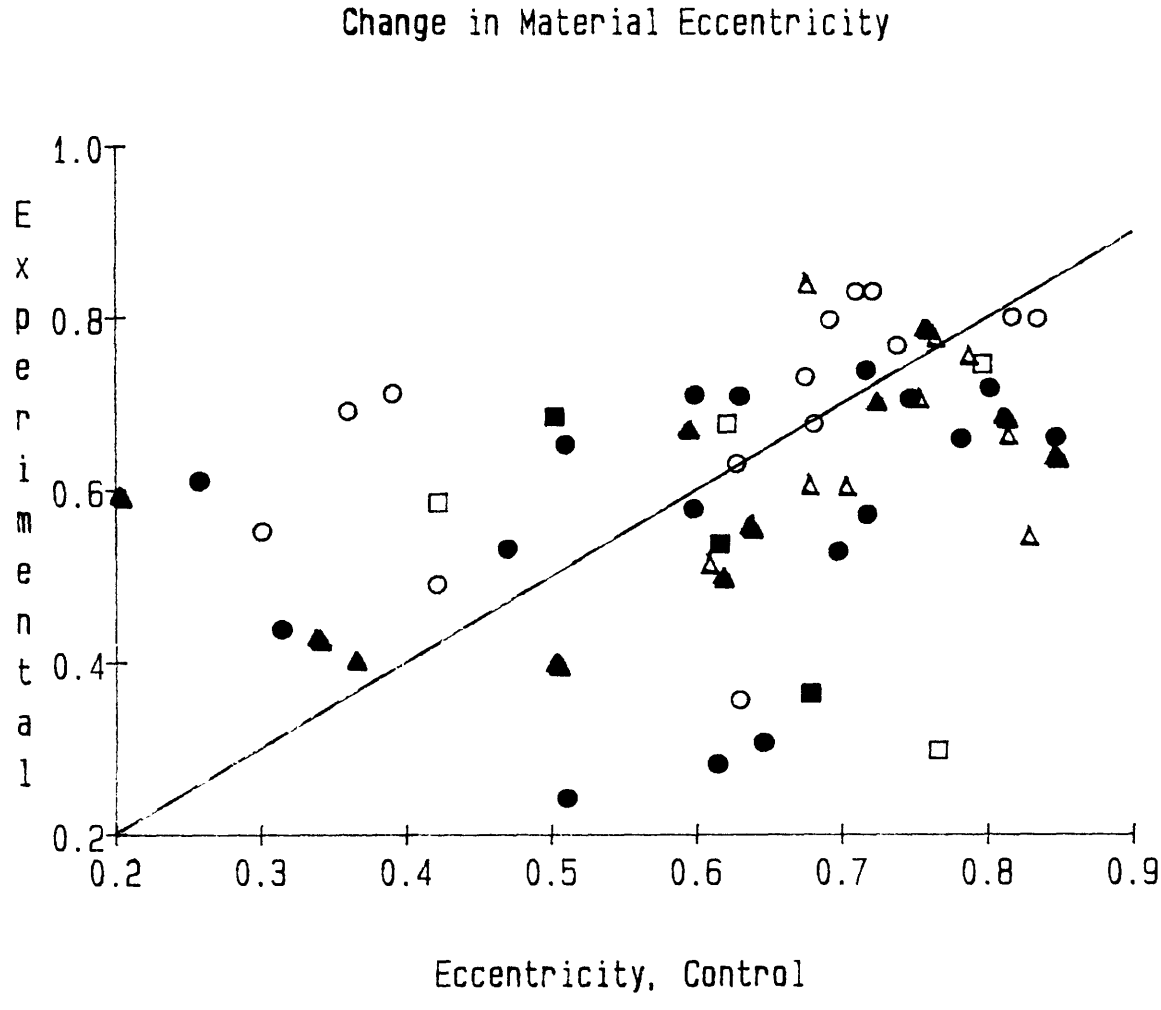

Figure 3.11: The eccentricity of the material anisotropy ellipse in the "A" and "B" regions in the experimental patellae as a function of the eccentricity of the material anisotropy ellipse in the control patellae. See Figure 3.8 for Key.

3.1.2 Ovine Calcaneus

The surgical implantation of the porous coated cobalt chromium cylinders was well tolerated. There were no complications during the 10 to 16 week post-surgical period. The five experimental and five control calcanei were embedded and sectioned as described in Section 2.3.1. Contact radiographs of mid-sagittal sections were analyzed using the automated stereologic system. The implant placement was unacceptable for one of the sixteen week specimens so it was excluded from further study.

The cobalt chromium cylinders resulted in significant changes in the trabecular bone density in the immediate vicinity of the implants. Photographic prints from the contact radiographs for specimens C1 and C4 are shown in Figure 3.12. All four experimental specimens had extensive bone ingrowth into the porous layer of sintered beads as well as new bone formation and remodeling within one or two millimeters of the implants.

The trabecular bone morphology was first analyzed to specifically examine the changes in the areal density of the trabecular bone (Figure 3.13). A fine grid was used to provide a large number of data points at various locations around the implants and at various distances from the implants. Statistical comparisons were made between the areal densities of the control specimens and the areal densities of the experimental specimens. Paired t tests were performed to establish the significance of the differences between the control and experimental sides. The data were organized in two different formats. The first format consisted of four data sets corresponding to four concentric annular regions with a 2

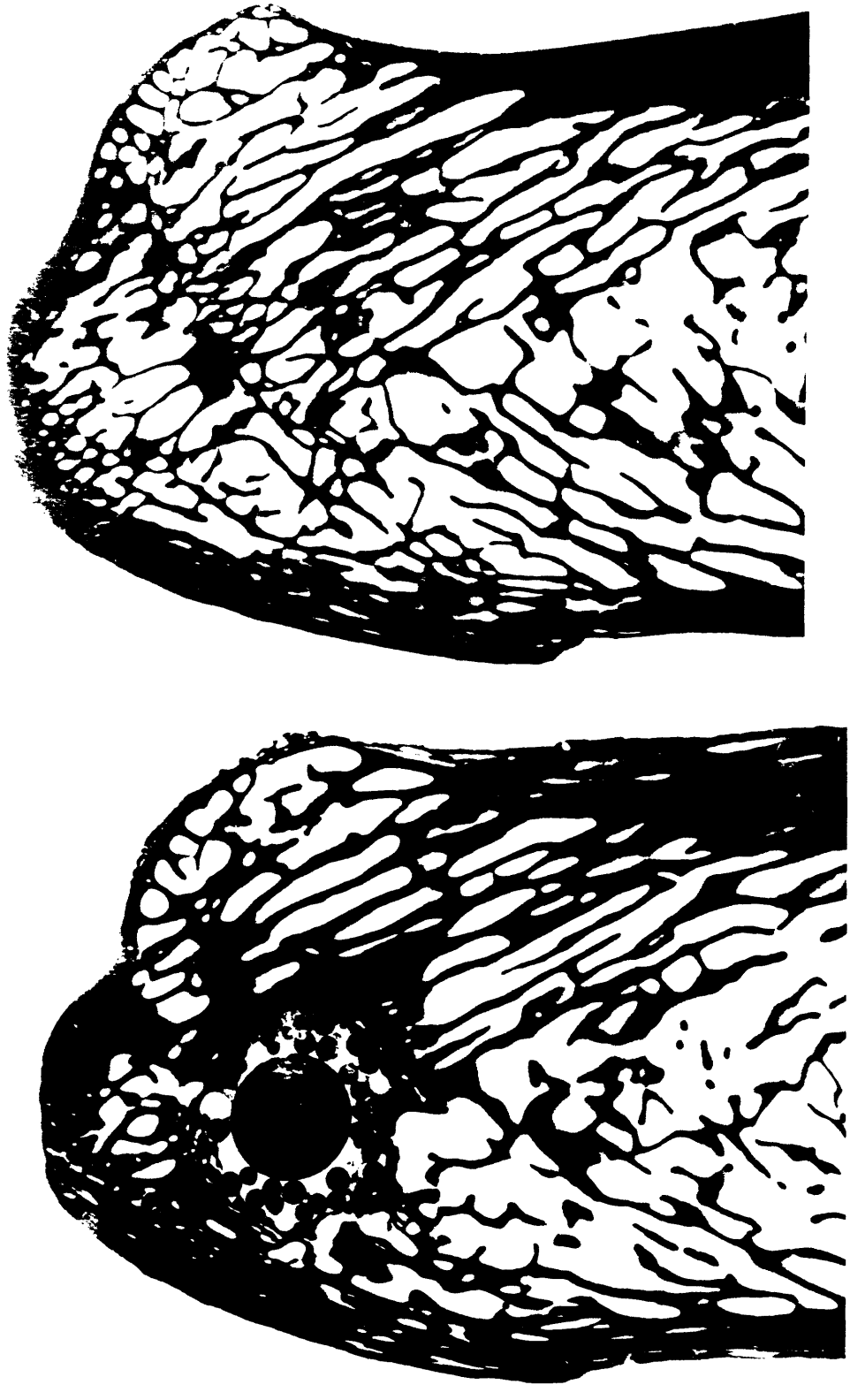

Figure 3.12a: Sagittal sections from the control (top) and experimental (bottom) ovine specimen C1.

Figure 3.12b: Sagittal sections from the control (top) and experimental (bottom) ovine specimen C4.

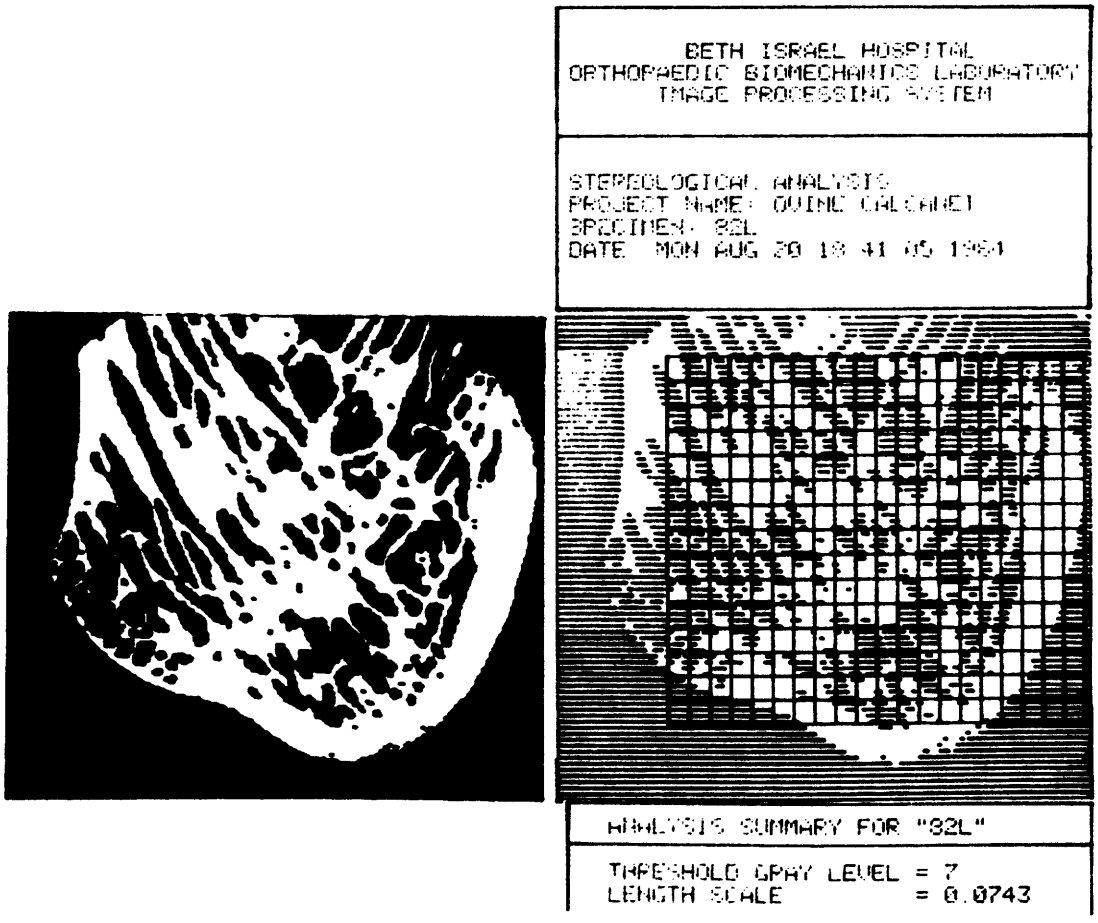

Figure 3.13a: Morphologic analysis for the determination of areal densities, control specimen C1.

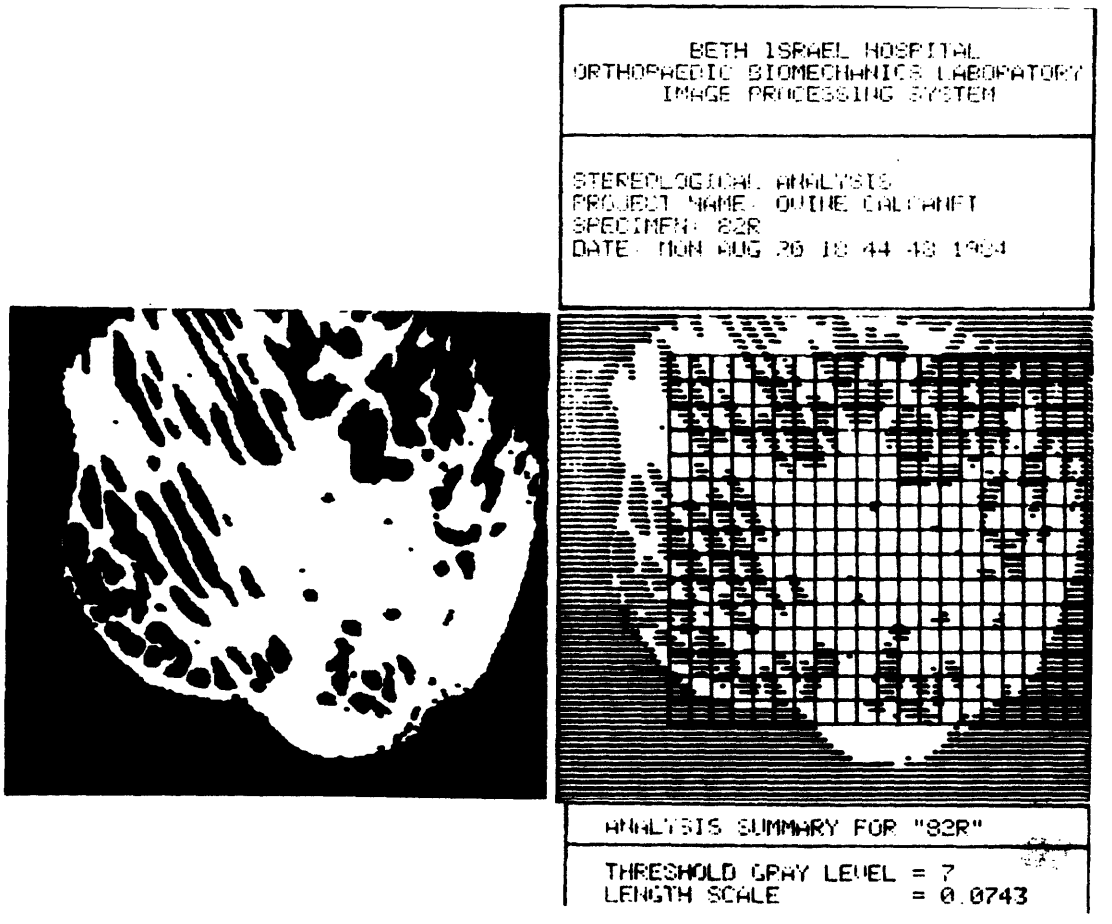

Figure 3.13b: Morphologic analysis for the determination of areal densities, experimental specimen C1.

mm radial width for each of the regions. The second format consisted of twelve data sets corresponding to twelve equal circumferentially partitioned regions around the implant. The first format was designed to test the dependence of the density changes on the radial distance from the implant. The second format was designed to test the dependence of the density changes on the relative circumferential location.

The results of these analyses for specimen C1 are summarized in Figure 3.14. All of the experimental specimens had a statistically significant increase in the trabecular bone areal density within 2 mm of the implants, but no significant changes beyond 2 mm. A majority of the circumferentially partitioned regions also displayed a significant increase in the trabecular bone density. Some regions showed no significant difference, which may be partially explained by the inclusion of data points which were distant from the implants. The only significant decrease in bone areal density occurred in the region shown in Figure 3.14 of specimen C1. In summary, the changes in trabecular bone areal density were limited to a 2 mm distance from the implants, with some variation in the density changes as a function of the circumferential location.

The stereologic analyses of the trabecular bone orientation as well as the areal density were performed on the experimental calcanei using the array of test regions shown in Figure 3.15. This array was designed to provide the maximum number of data points from the trabecular bone adjacent to the implants. The diameter of each region was 4 mm. The control specimens were similarly analyzed with care taken to properly

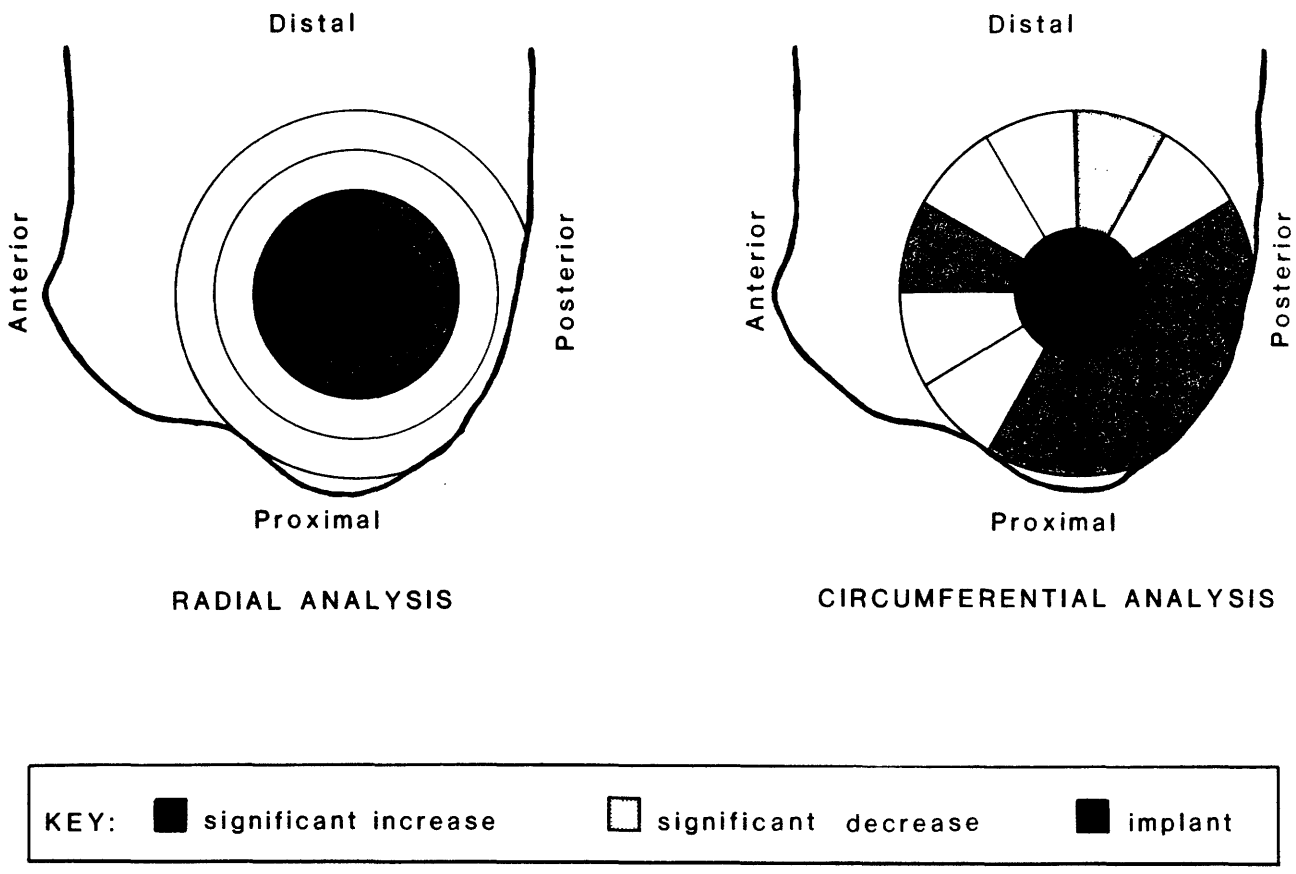

Figure 3.14: Statistical analysis of the changes in the trabecular bone areal density, ovine specimen C1.

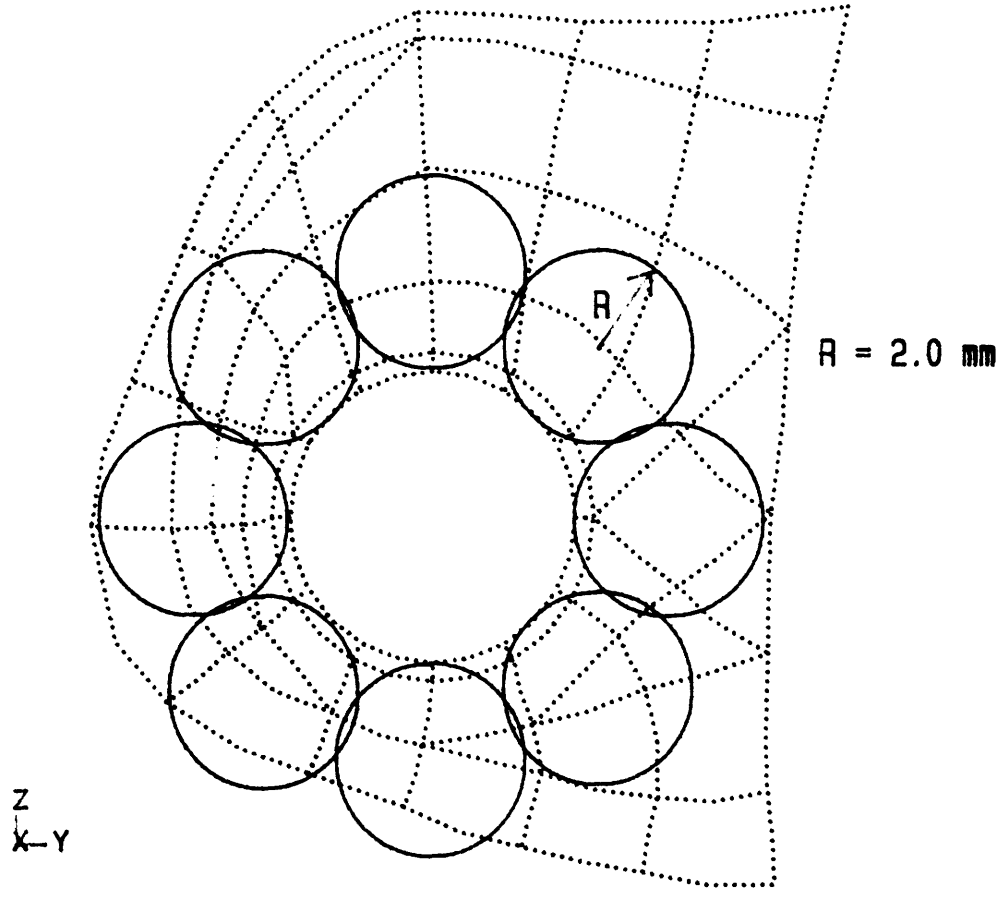

Figure 3.15: Array of image regions used for the stereologic analyses of the ovine calcanei.

orient the test arrays for paired comparisons. One representative example stereologic analysis from each specimen are shown in Figures 3.16 to 3.19. All four specimens had a higher areal density on the experimental side at this location in comparison to the control side. It is also apparent that the density changes were primarily limited to a distance of about 2 mm, which was the radius of the analyzed regions. This observation was confirmed by the above statistical analyses.

The example analyses in Figures 3.16 to 3.19 demonstrate an important point about the morphologic changes. The direction of principal trabecular orientation was virtually unchanged in this region for specimen C1. The increased bone density was reflected by an increase in the bone area fraction but the orientation of the trabeculae slightly removed from the implant was unchanged. In specimen C2 the remodeling in this region was more extensive and resulted in a large change (54 degrees) in the direction of principal material orientation. However, the significance of the direction of maximum orientation in this region must be questioned due to the disorganized appearance of the mineralized bone. Similarly, there was a large change in the principal trabecular orientation for specimen C3 due to the influence of the dense bone immediately adjacent to the implant. This region of specimen 4C was more similar to that of specimen 1C in that there was little change in the direction of maximum orientation. In summary, in some regions adjacent to the implants, there was little change in the principal trabecular orientation due to minimal remodeling of the trabeculae slightly removed from the implant. In other regions, the principal direction of orientation was greatly changed, due to the increased

BETH ISRAEL HOSPITAL - IMAGE PROCESSING LABORATORY

IMAGE TITLE: 82C
COMMENT:
SUBREGION: 3
LENGTHSCALE: 34.29
GRAY THRESHOLD: 120
SOLID PHASE: BLK
TESTLINE LENGTH: 427.6
TESTLINE SPACING <PIXELS> : 1

[AREA FRACTION ANALYSIS:]
REGION AREA = 12.47

AREA FRACTION = 0.511
SOLID AREA = 6.372

[STEREOLOGY ANALYSIS:]

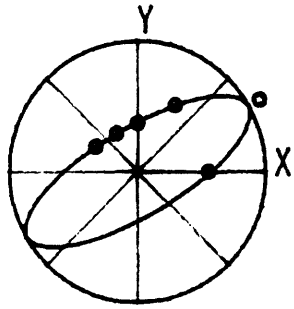

PERIMETER = 33.659
PERIM/AREA = 2.6987

ELLIPSE OF MEAN INTRCPT LENGTHS:

$A*N_1^2 + B*N_1N_2 + C*N_2^2 = MNINCPTLN^{-2}$

A = 1.900
B = -4.388
C = 4.3960

CORRELATION COEFF = 0.998
MAX MN INTRCPT LNTH = 1.2659
ANGLE MAX ORIENTATION = 30 DEGS
MIN MN INTRCPT LNTH = 0.41989
ANGLE MIN ORIENTATION = 120 DEGS
EXTENT OF ANISOTROPY = 60.260 %

Figure 3.16a: Stereologic analysis of region "2" from the control specimen C1.

BETH ISRAEL HOSPITAL - IMAGE PROCESSING LABORATORY

IMAGE TITLE: 82E
COMMENT: 82 exp, porous
SUBREGION: 3
LENGTHSCALE: 34.29
GRAY THRESHOLD: 110
SOLID PHASE: BLK
TESTLINE LENGTH: 427.6
TESTLINE SPACING <PIXELS> : 1

[AREA FRACTION ANALYSIS:]
REGION AREA = 12.47

AREA FRACTION = 0.632
SOLID AREA = 7.886

[STEREOLOGY ANALYSIS:]

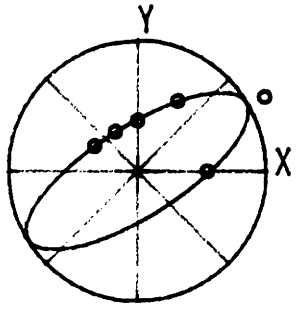

PERIMETER = 24.458
PERIM/AREA = 1.9610

ELLIPSE OF MEAN INTRCPT LENGTHS:
$A*N_1^2 + B*N_1N_2 + C*N_2^2 = MNINCPTLN^{-2}$
A = 0.7129
B = -1.541
C = 1.4548
CORRELATION COEFF = 0.997
MAX MN INTRCPT LNTH = 2.0906
ANGLE MAX ORIENTATION = 32 DEGS
MIN MN INTRCPT LNTH = 0.71816
ANGLE MIN ORIENTATION = 122 DEGS
EXTENT OF ANISOTROPY = 58.949 %

Figure 3.16b: Stereologic analysis of region "2" from the experimental specimen C1.

BETH ISRAEL HOSPITAL - IMAGE PROCESSING LABORATORY

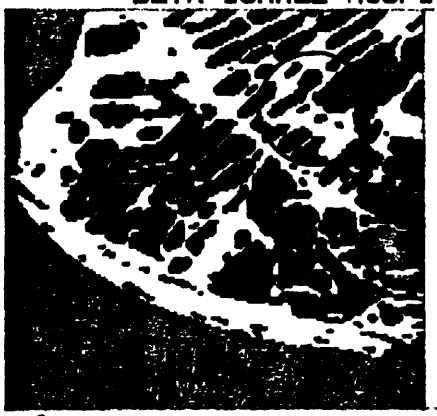

IMAGE TITLE: 429C
COMMENT: 429 control, Co Cr
SUBREGION: 3
LENGTHSCALE: 34.29
GRAY THRESHOLD: 135
SOLID PHASE: BLK
TESTLINE LENGTH: 427.6
TESTLINE SPACING <PIXELS> : 1

[AREA FRACTION ANALYSIS:]
REGION AREA = 12.47

AREA FRACTION = 0.551
SOLID AREA = 6.878

[STEREOLOGY ANALYSIS:]

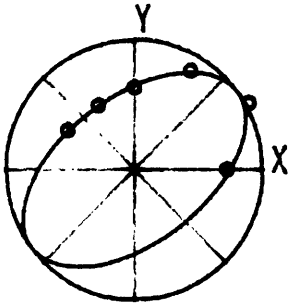

PERIMETER = 28.535
PERIM/AREA = 2.2879

ELLIPSE OF MEAN INTRCPT LENGTHS:

$A*N_1^2 + B*N_1N_2 + C*N_2^2 = MNINCPTLN^{-2}$

A = 1.544
B = -1.809
C = 2.0834

CORRELATION COEFF = 0.993
MAX MN INTRCPT LNTH = 1.0724
ANGLE MAX ORIENTATION = 37 DEGS
MIN MN INTRCPT LNTH = 0.60219
ANGLE MIN ORIENTATION = 127 DEGS
EXTENT OF ANISOTROPY = 35.098 %

Figure 3.17a: Stereologic analysis of region "2" from the control specimen C2.

BETH ISRAEL HOSPITAL - IMAGE PROCESSING LABORATORY

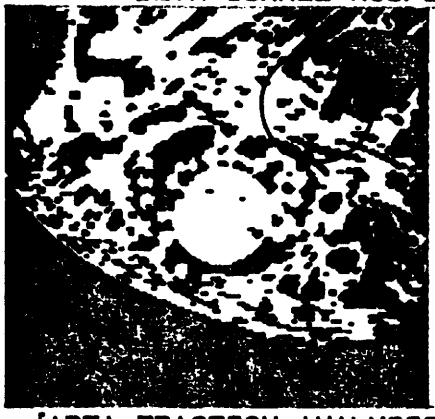

IMAGE TITLE: 429E
COMMENT: 429 exp, Co Cr
SUBREGION: 3
LENGTHSCALE: 34.29
GRAY THRESHOLD: 120
SOLID PHASE: BLK
TESTLINE LENGTH: 427.6
TESTLINE SPACING <PIXELS> : 1

[AREA FRACTION ANALYSIS:]
REGION AREA = 12.47

AREA FRACTION = 0.604
SOLID AREA = 7.529

[STEREOLOGY ANALYSIS:]

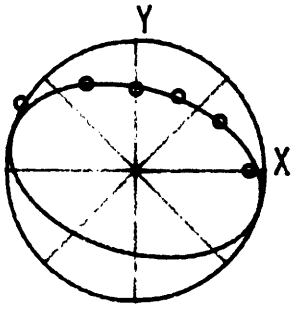

PERIMETER = 31.437
PERIM/AREA = 2.5206

ELLIPSE OF MEAN INTRCPT LENGTHS:
$A*N_1^2 + B*N_1N_2 + C*N_2^2 = MNINCPTLN^{-2}$
A = 1.161
B = 0.8544
C = 2.4652
CORRELATION COEFF = 0.976
MAX MN INTRCPT LNTH = 0.98385
ANGLE MAX ORIENTATION = -17 DEGS
MIN MN INTRCPT LNTH = 0.62105
ANGLE MIN ORIENTATION = 73 DEGS
EXTENT OF ANISOTROPY = 28.440 %

Figure 3.17b: Stereologic analysis of region "2" from the experimental specimen C2.

BETH ISRAEL HOSPITAL - IMAGE PROCESSING LABORATORY

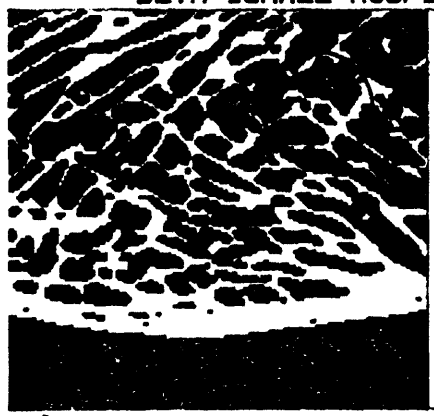

IMAGE TITLE: 191C
COMMENT: 191 control, porous
SUBREGION: 3
LENGTHSCALE: 34.29
GRAY THRESHOLD: 110
SOLID PHASE: BLK
TESTLINE LENGTH: 427.6
TESTLINE SPACING <PIXELS> : 1

[AREA FRACTION ANALYSIS:]
REGION AREA = 12.47

AREA FRACTION = 0.329
SOLID AREA = 4.098

[STEREOLOGY ANALYSIS:]

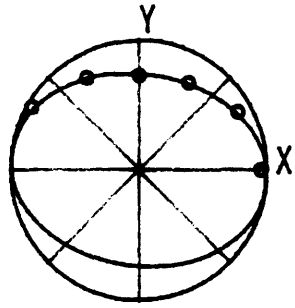

PERIMETER = 28.253
PERIM/AREA = 2.2653

ELLIPSE OF MEAN INTRCPT LENGTHS:
$A*N_1^2 + B*N_1N_2 + C*N_2^2 = MNINCPTLN^{-2}$
A = 3.493
B = 0.7526
C = 6.2461
CORRELATION COEFF = 0.982
MAX MN INTRCPT LNTH = 0.53894
ANGLE MAX ORIENTATION = -8 DEGS
MIN MN INTRCPT LNTH = 0.39852
ANGLE MIN ORIENTATION = 82 DEGS
EXTENT OF ANISOTROPY = 18.966 %

Figure 3.18a: Stereologic analysis of region "2" from the control specimen C3.

BETH ISRAEL HOSPITAL - IMAGE PROCESSING LABORATORY

IMAGE TITLE: 191E
COMMENT: 191 exp, porous
SUBREGION: 3
LENGTHSCALE: 34.29
GRAY THRESHOLD: 90
SOLID PHASE: BLK
TESTLINE LENGTH: 427.6
TESTLINE SPACING <PIXELS> : 1

[AREA FRACTION ANALYSIS:]
REGION AREA = 12.47

AREA FRACTION = 0.580
SOLID AREA = 7.234

[STEREOLOGY ANALYSIS:]

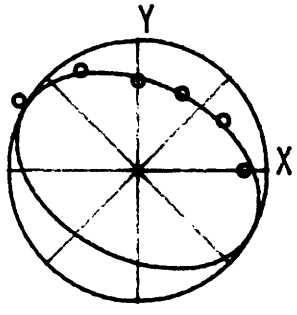

PERIMETER = 24.992
PERIM/AREA = 2.0038

ELLIPSE OF MEAN INTRCPT LENGTHS:

$A*N_1^2 + B*N_1N_2 + C*N_2^2 = MNINCPTLN^{-2}$

A = 0.9682
B = 0.7675
C = 1.5032

CORRELATION COEFF = 0.948
MAX MN INTRCPT LNTH = 1.1411
ANGLE MAX ORIENTATION = -28 DEGS
MIN MN INTRCPT LNTH = 0.76618
ANGLE MIN ORIENTATION = 62 DEGS
EXTENT OF ANISOTROPY = 24.828 %

Figure 3.18b: Stereologic analysis of region "2" from the experimental specimen C3.

BETH ISRAEL HOSPITAL - IMAGE PROCESSING LABORATORY

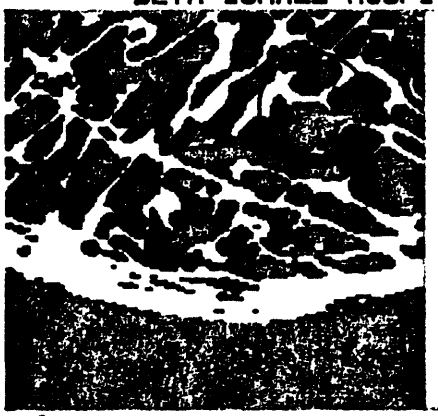

IMAGE TITLE: 4C
COMMENT: 4 control, porous Co Cr
SUBREGION: 3
LENGTHSCALE: 34.29
GRAY THRESHOLD: 130
SOLID PHASE: BLK
TESTLINE LENGTH: 427.6
TESTLINE SPACING <PIXELS> : 1

[AREA FRACTION ANALYSIS:]
REGION AREA = 12.47

AREA FRACTION = 0.257
SOLID AREA = 3.210

[STEREOLOGY ANALYSIS:]

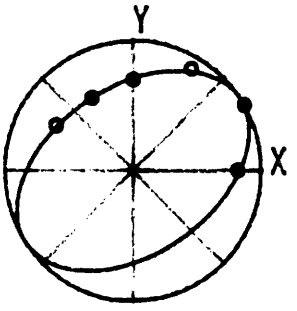

PERIMETER = 18.311
PERIM/AREA = 1.4681

ELLIPSE OF MEAN INTRCPT LENGTHS:

$A*N_1^2 + B*N_1N_2 + C*N_2^2 = MNINCPTLN^{-2}$

A = 2.827
B = -2.574
C = 3.9218

CORRELATION COEFF = 0.994
MAX MN INTRCPT LNTH = 0.71142
ANGLE MAX ORIENTATION = 33 DEGS
MIN MN INTRCPT LNTH = 0.45772
ANGLE MIN ORIENTATION = 123 DEGS
EXTENT OF ANISOTROPY = 27.314 %

Figure 3.19a: Stereologic analysis of region "2" from the control specimen C4.

BETH ISRAEL HOSPITAL - IMAGE PROCESSING LABORATORY

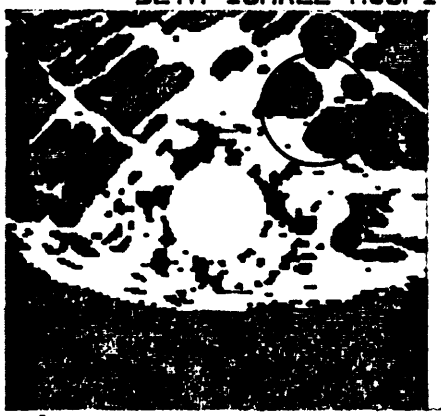

IMAGE TITLE: 4E
COMMENT: 4 exp, porous Co Cr
SUBREGION: 3
LENGTHSCALE: 34.29
GRAY THRESHOLD: 120
SOLID PHASE: BLK
TESTLINE LENGTH: 427.6
TESTLINE SPACING <PIXELS> : 1

[AREA FRACTION ANALYSIS:]
REGION AREA = 12.47

AREA FRACTION = 0.406
SOLID AREA = 5.067

[STEREOLOGY ANALYSIS:]

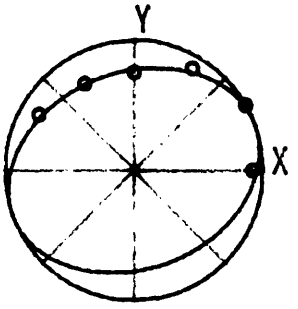

PERIMETER = 17.173
PERIM/AREA = 1.3769

ELLIPSE OF MEAN INTRCPT LENGTHS:
$A*N_1^2 + B*N_1N_2 + C*N_2^2 = MNINCPTLN^{-2}$
A = 0.9312
B = -0.4132
C = 1.4201
CORRELATION COEFF = 0.959
MAX MN INTRCPT LNTH = 1.0811
ANGLE MAX ORIENTATION = 20 DEGS
MIN MN INTRCPT LNTH = 0.81766
ANGLE MIN ORIENTATION = 110 DEGS
EXTENT OF ANISOTROPY = 17.586 %

Figure 3.19b: Stereologic analysis of region "2" from the experimental specimen C4.

trabecular bone density immediately adjacent to the implants.

The changes in trabecular bone areal density for all experimental calcanei are shown in Figure 3.20. The line Y = X was included for reference. Points above this line had a higher areal density in the experimental specimen in comparison to the areal density in the corresponding region of the paired control specimen. Twenty-one of twenty-two points lie above this line confirming that the trabecular bone density adjacent to the implants was increased regardless of the relative location around the implants.

The changes in the principal direction of trabecular orientation are shown in Figure 3.21. The lines Y = X, indicating no change, and Y = X + 90 and Y = X - 90, indicating the possible range of data, are included for reference. Approximately half of the data points lie within 10 degrees of the line Y = X indicating that there was only a small change in the direction of orientation. The remainder of the points lie outside of this range indicating that the dense bone immediately adjacent to the implants resulted in large changes in the principal direction of orientation.

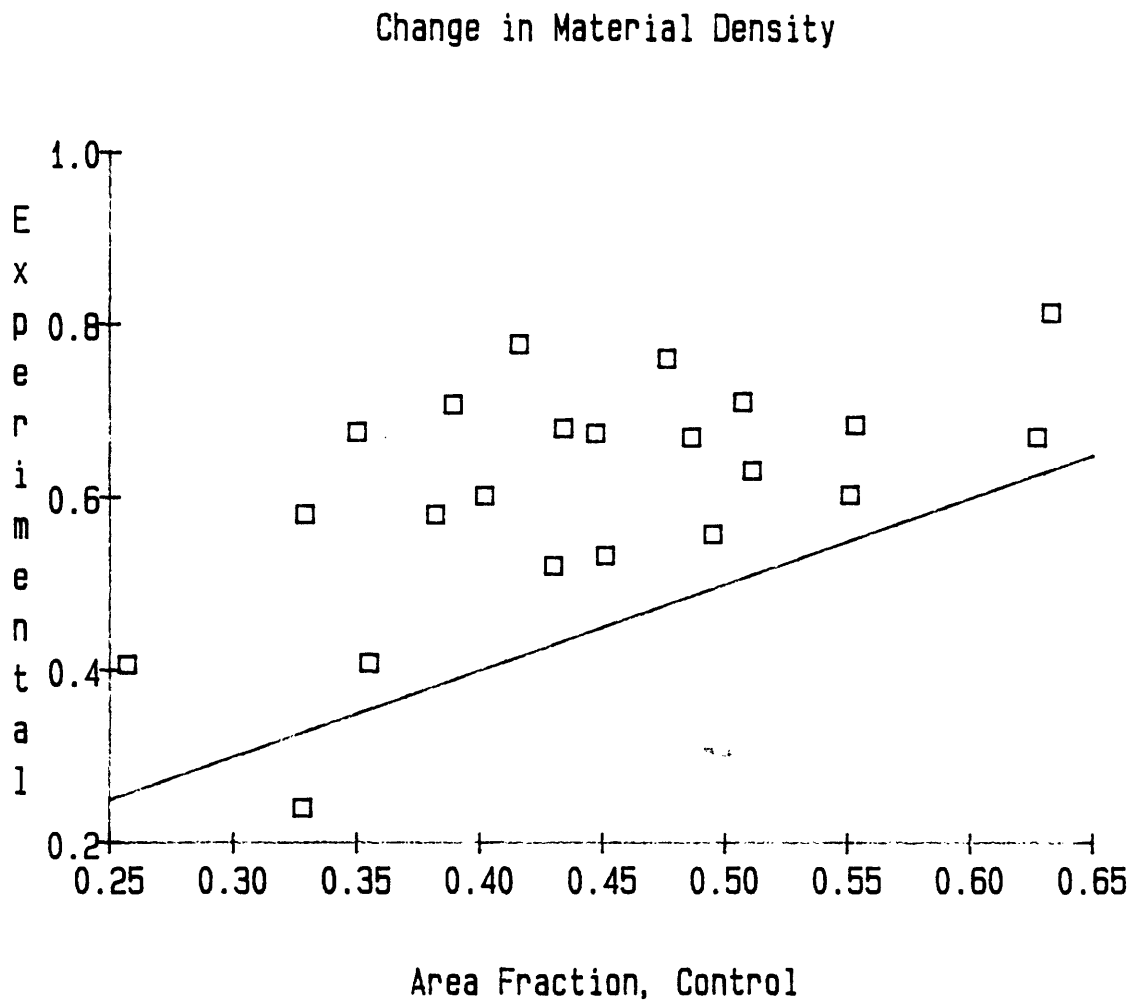

Figure 3.20: The bone area fraction in the experimental calcanei as a function of the bone area fraction in the corresponding regions in the control calcanei.

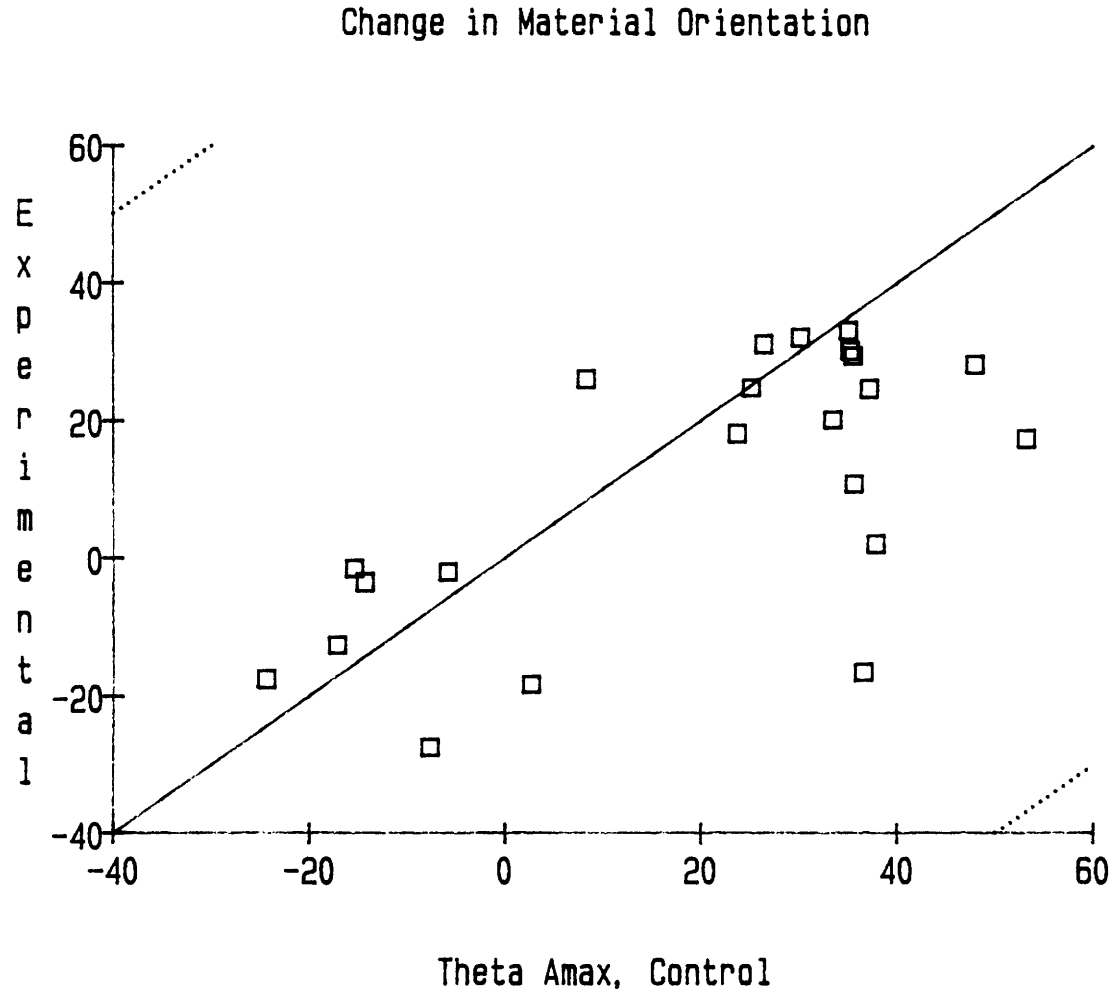

Figure 3.21: The principal material orientation in the experimental calcanei as a function of the principal material orientation in the control calcanei.

3.2 Structural Analyses

The stresses in the control and experimental specimens were predicted using finite element analysis. Two- and three-dimensional continuum models were analyzed using a displacement-based formulation. The stresses in the control specimens were characterized to provide reference for evaluation of the stresses in the experimental specimens. The stresses in the trabecular bone surrounding the implants were also compared between specimens to characterize the influence of the boundary conditions at the bone/implant interface.

3.2.1 Equine Patella

The assumed boundary conditions at the bone/implant interface were based on the histology of the experimental patellae. Nonlinear contact was assumed for the smooth surfaced implants based on the observation of a thin fibrous tissue membrane separating the implant from the trabecular bone. For two of the three patellae with porous coated implants, specimens P7 and P8, there was successful bone ingrowth into the porous coating. For these patellae, rigid mechanical coupling was assumed for the bone-implant interface. Porous coated specimen P6 displayed a thick fibrous tissue layer with the specimen incompletely surrounded by bone. For this specimen, it was assumed that the implant acted as a void, with no mechanical coupling between the implant and the adjacent trabecular bone.

The stress fields in the trabecular bone of the equine patellae were

altered by the presence of the stainless steel implants. As in the preliminary studies of the cylindrical implants in the ovine calcanei, the stresses around the implants are dependent on the assumed boundary conditions at the bone/implant interface (see Section 2.2.4). In general, tight mechanical bonding, as occurs with bone ingrowth, results in stress fields which are most similar to the normal condition of no implant. Nonlinear contact, which is expected for smooth implants or porous coated implants prior to bony ingrowth, results in greatly altered stress fields. The stress fields are also greatly altered for any implant in which the implant is mechanically uncoupled from the adjacent bone by a thick, compliant, fibrous tissue layer. While the compliance of the tissue layer formed in experimental specimen P6 was not measured, it can certainly be considered compliant when compared to the trabecular bone.

The finite element models were fully three-dimensional. However, only the stresses in the plane of interest were considered in this presentation and in the subsequent examination of the stress-morphology relationships. The plane of interest corresponded to the sagittal section through the implant centers which were analyzed using stereology. The two-dimensional stresses were obtained by simply neglecting all out-of-plane stress components. This corresponds to the projection of the three-dimensional stress ellipsoid onto the plane of interest yielding the familiar two-dimensional stress ellipse. This is a reasonable approach provided the primary and secondary principal axes of the ellipsoid approximately coincide with the plane of interest. To provide a measure of the appropriateness of the plane on which the data

were examined, the strain energy density was calculated using all of the stress and strain components and also using only the in-plane components. The average ratio of the in-plane strain energy to the total strain energy, evaluated at the locations of morphologic data for all of the specimens, was 0.80. In other words, 80 % of the strain energy was accounted for by considering only the in-plane stresses. This ratio varied from model to model, ranging from a maximum of 0.93 for the experimental model of specimen S2 to a minimum of 0.62 for the control model of specimen P8.

The stresses were displayed graphically to examine the stress fields in the control and experimental patellae (Figures 3.22 to 3.29). Vector plots were used to display the principal tensile and compressive stress components. Each vector direction corresponds to the principal stress direction and the vector length is proportional to the stress magnitude. Cross-bars on the vectors indicate compression. Contour plots were used to display the distribution of strain energy density and von Mises effective stress. Two views were used for each model, the first being a sagittal section through the center of the implant. This plane corresponded to the plane which was analyzed using the stereology system. The second view was an enlargment of the implant region and the surrounding trabecular bone on the same section.

Plots from three representative model pairs are included. The first pair of models was for specimen S2, including the control side and the experimental side with the smooth implant. The second pair was for specimen P6, again including the control side and the experimental side

with the porous coated implant which was not ingrown. The third pair was for specimen P7, again including the control side and the experimental side with the porous coated implant with demonstrated bone ingrowth.

In general, the stresses on the control patellae were similar for each of the specimens. On first examination, the stresses on the entire sagittal section for the three specimens (Figure 3.22) appears to vary greatly. However, it must be pointed out that an unavoidable aspect of the vector plotting program was that the maximum absolute principal stress vector for the elements in the plot was scaled to a specific length and the rest of the vectors were scaled relative to the maximum vector. For specimen S2, very high magnitude compressive stresses occurred in the region of patellofemoral contact (lower right region of the cortical shell in Figure 3.22a). As a consequence, the stress vectors over the remainder of the section appear to be smaller than the corresponding vectors for the other patellae. This technical problem was partially solved by using enlarged views which include smaller portions of the mesh restricted to the areas of interest. This eliminated from the plots high peak stresses which were not of interest.

The highest stresses for both the control and the experimental patellae occurred in the cortical shell, especially in the region of patellofemoral contact. The high compressive stresses in specimen S2 were the result of the implant placement coinciding with the plane of peak contact forces. In addition, the accuracy of the contact stresses was probably poor. The articular cartilage was not represented and an

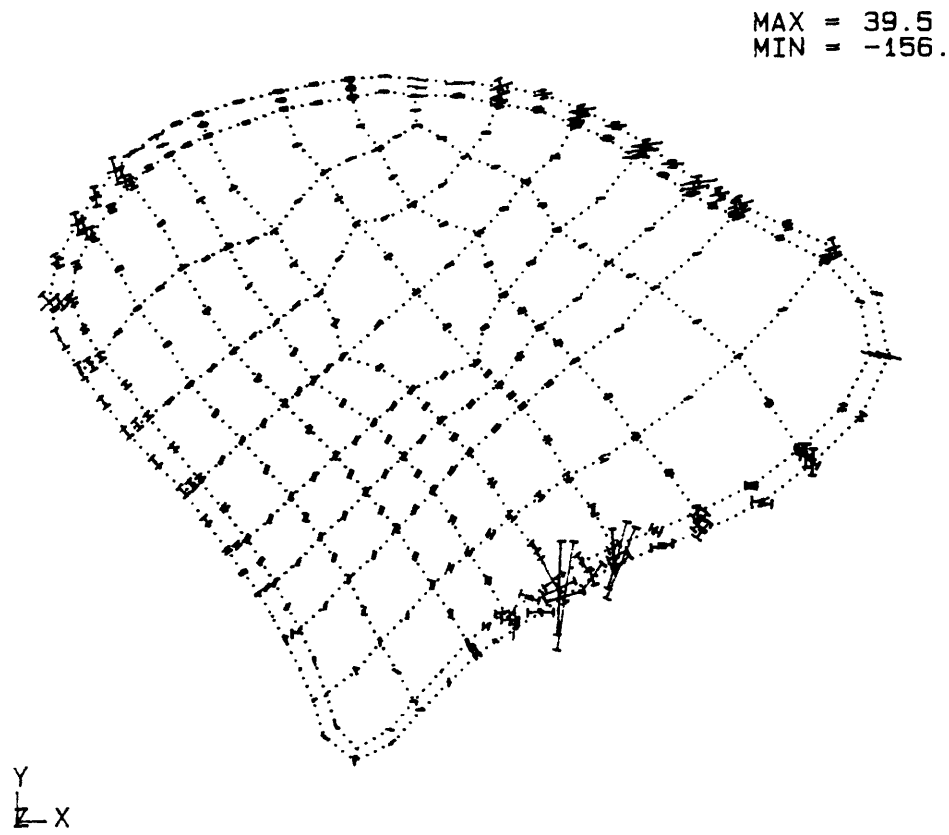

Figure 3.22a: Principal stress vectors on a sagittal section of the control specimen S2 (MPa). The positive X axis points in the distal direction and the positive Y axis points in the anterior direction. The patellofemoral contact area is in the lower right.

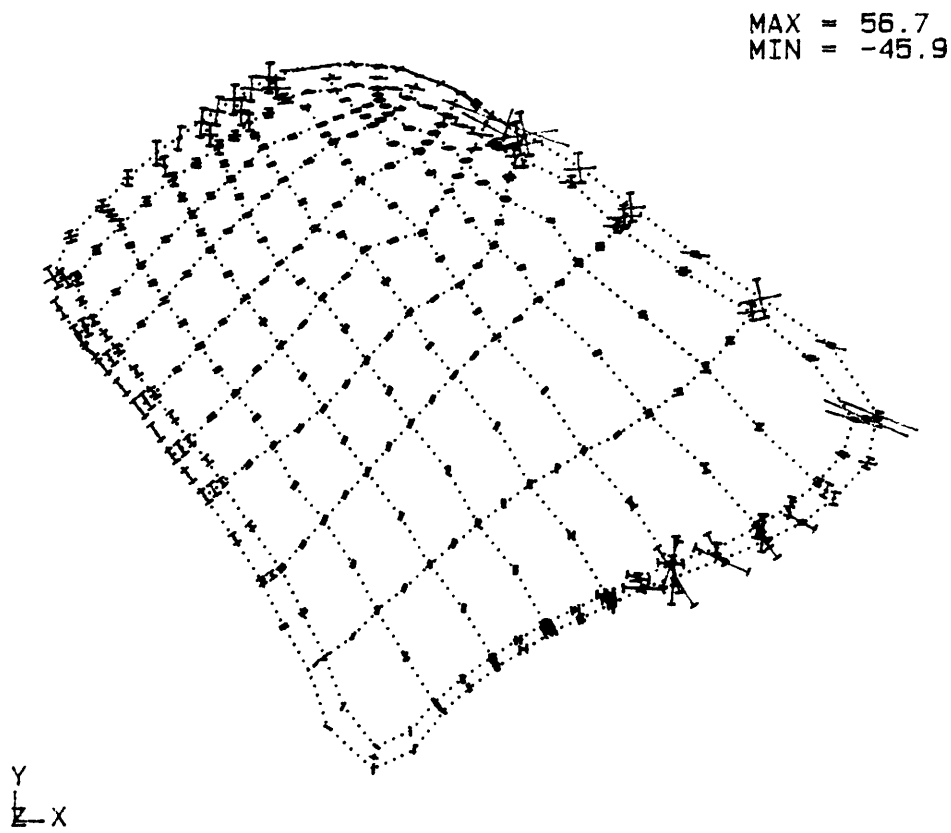

Figure 3.22b: Principal stress vectors on a sagittal section of the control specimen P6 (MPa).

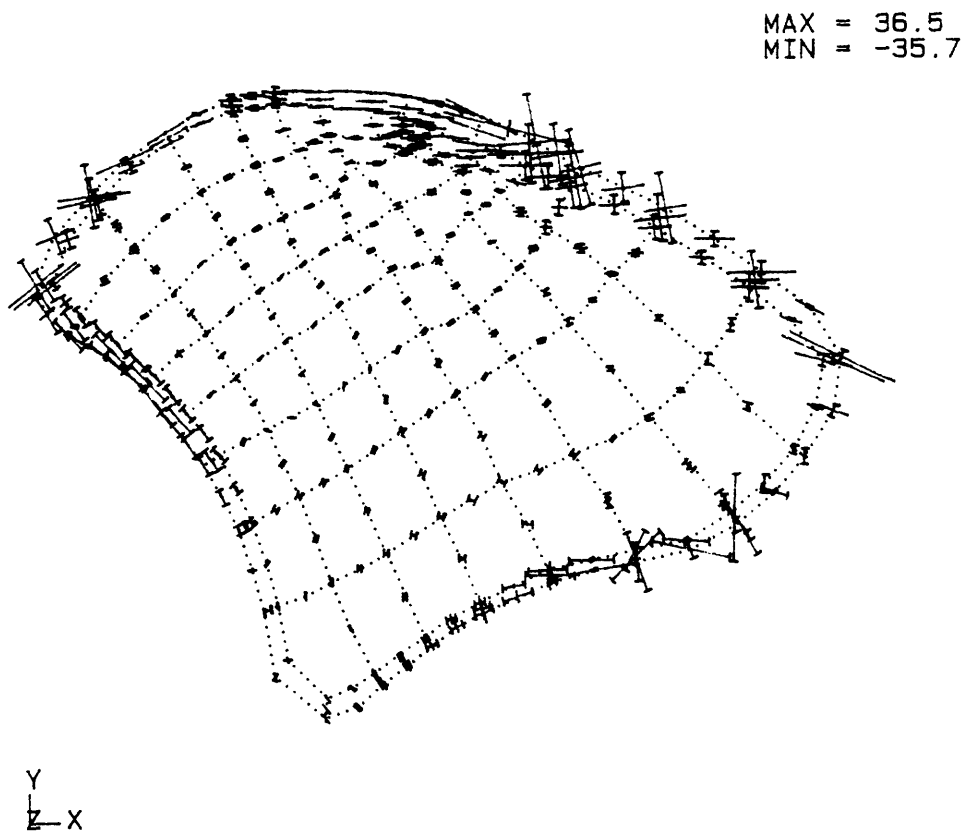

Figure 3.22c: Principal stress vectors on a sagittal section of the control specimen P7 (MPa).

accurate representation of surface contact generally requires a nonlinear formulation, such as that applied at the bone/implant interface. Also, in general, stresses adjacent to concentrated loads are not reliable. To represent a surface traction exactly it is necessary to use nodal loads which are consistent with the element interpolation functions (Bathe 1982). In the present models, consistent loads were approximated by simply distributing each load evenly over the surface nodes which corresponded to the patellofemoral contact area or the attachment area of the ligament or muscle. Each load had the proper net effect but a consequence was that the stresses in the areas of the applied loads, namely the cortical shell, were not very accurate. The stresses in the trabecular bone, away from the applied loads, were not affected by this approximation.

High tensile stresses were seen in the anterior region and at the proximal and distal poles of all the specimens. These stresses are due to the action of the quadriceps musculature, proximally, and the middle patellar ligament, distally. High shear stresses, indicated by high coincident tensile and compressive principal stresses, appear in the anterior cortical shell, especially in specimen P7 (Figure 3.22c). These shear stresses are due the component of the load which was tangential to the surface.

The principal stresses in the control patellae in the region which correspond to the implant location in the experimental patellae were consistent from specimen to specimen (Figures 3.23). There was a general flow of compression from the patellofemoral contact area to the

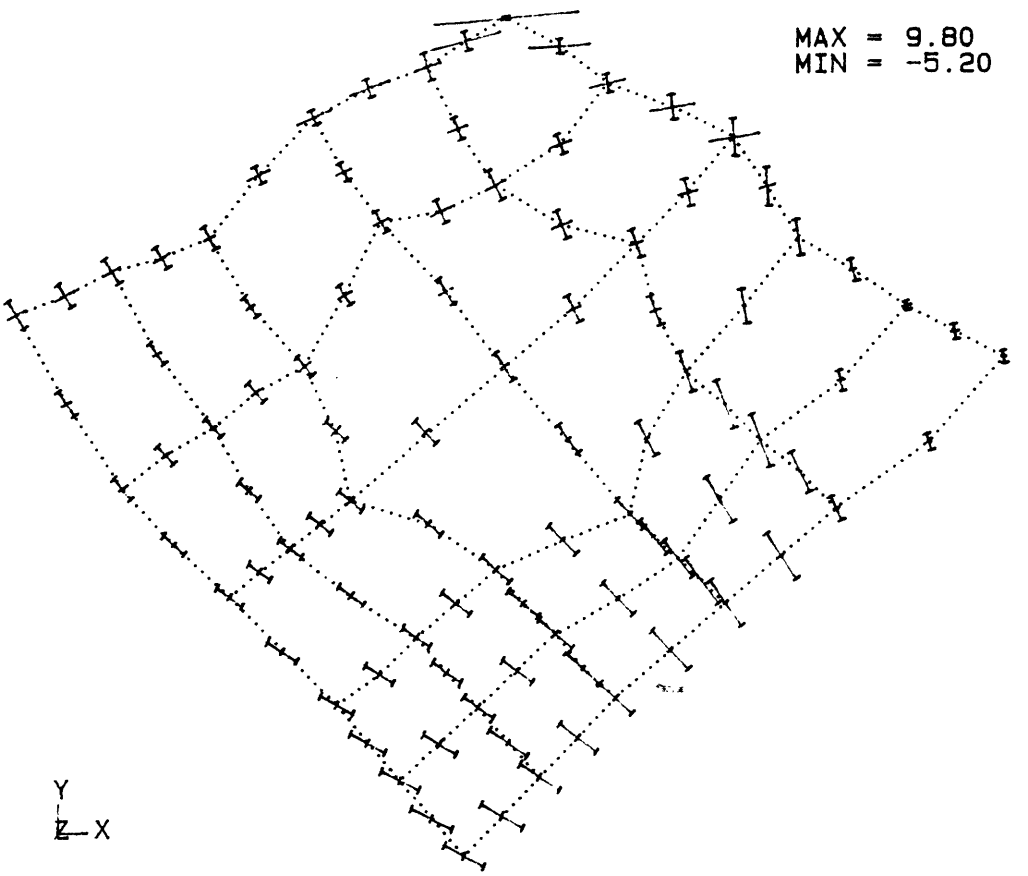

Figure 3.23a: Principal stress vectors on an enlarged view of control specimen S2 (MPa). The mesh region corresponds to the implant location in the experimental specimen.

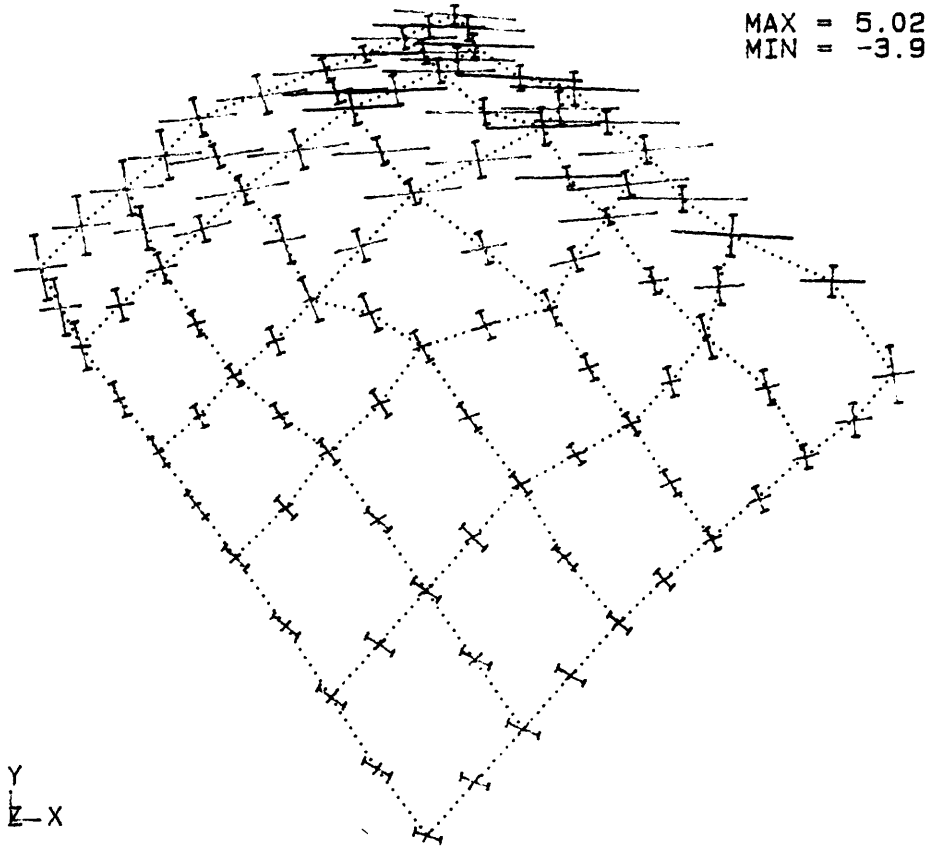

Figure 3.23b: Principal stress vectors on an enlarged view of control specimen P6 (MPa).

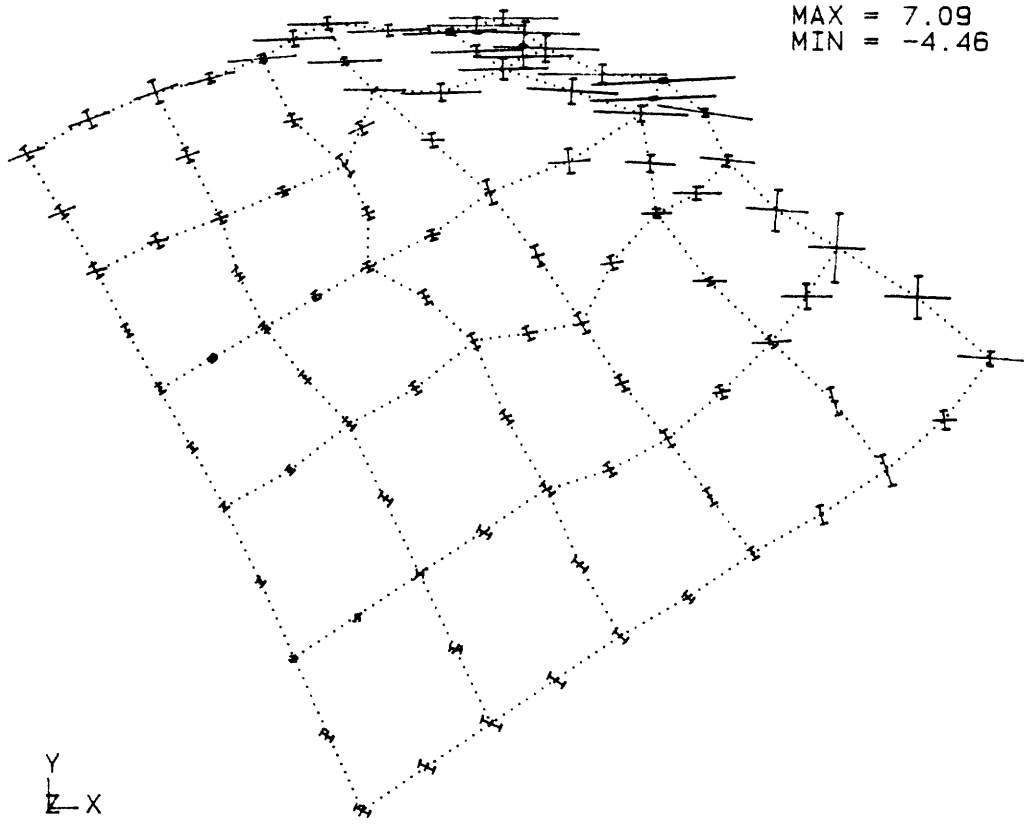

Figure 3.23c: Principal stress vectors on an enlarged view of control specimen P7 (MPa).

anterior-proximal cortical bone. The highest tensile stresses were in the anterior region in a proximal-distal orientation. These tensile stresses were less apparent for specimen S2 (Figure 3.23a) because the implant in this specimen was deeper to the anterior surface and thus the region shown is further removed from the anterior cortical shell. This combination of biaxial tension and compression results in significant shear stresses anteriorly, seen especially in specimen P7. Specimen P7 had the most anterior implant placement of the three shown.

To examine the distribution of shear stress in the control patellae, contour plots of von Mises effective stress were generated for the implant region (Figure 3.24). Von Mises effective stress was chosen because this stress parameter is often applied as a failure criterion to engineering materials. Von Mises stress reflects the shear stress because von Mises stress is linearly related to octahedral shear stress. The results were comparable for the three specimens shown. In general, there was a gradient from posterior to anterior. This gradient was least pronounced in specimen S2 again due to the more posterior placement of the implant in the experimental patella. All three specimens had a von Mises stress of about 1.5 MPa in the most posterior region shown. In the most anterior trabecular bone the predicted von Mises stress was about 3.0 MPa for specimen S2, 5.8 MPa for specimen P7, and 4.8 MPa for specimen P6. The implant was placed most anteriorly in specimen P7. This location corresponds to a point immediately anterior to the implant in the experimental patellae.

Note that the stress magnitudes are important in a relative sense

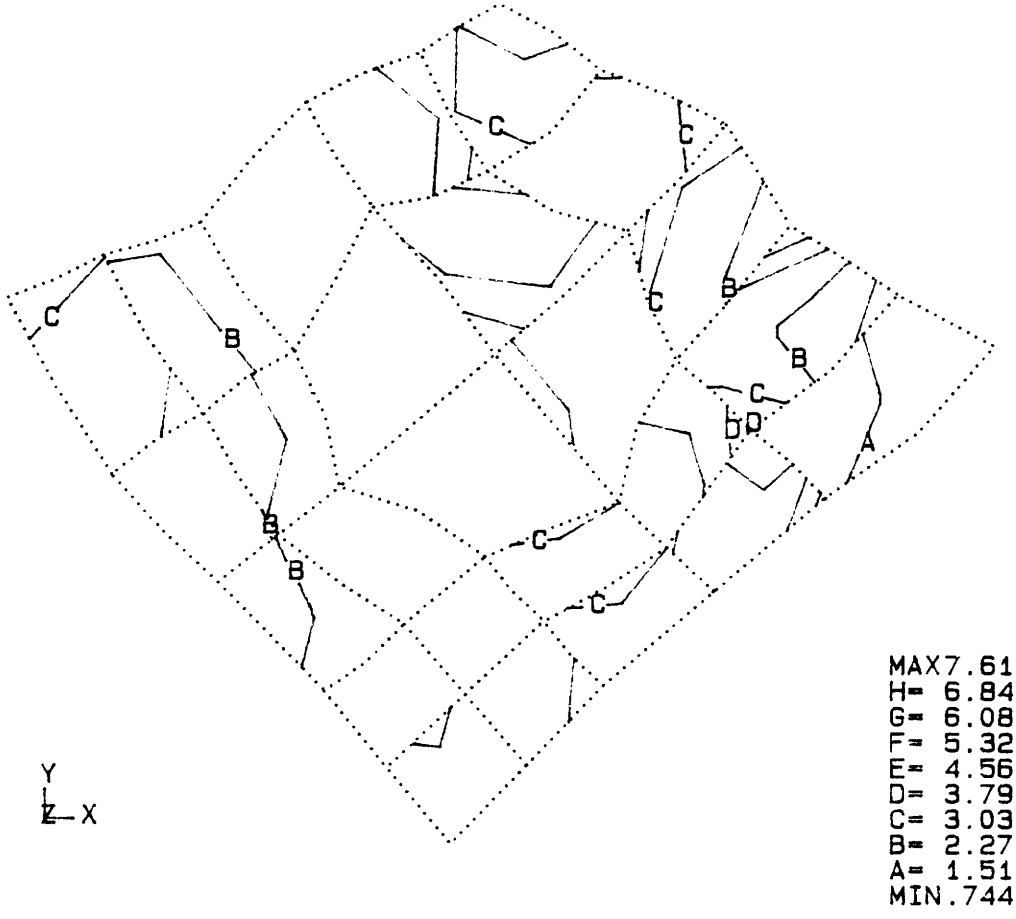

Figure 3.24a: Von Mises stress contours on an enlarged view of control specimen S2 (MPa).

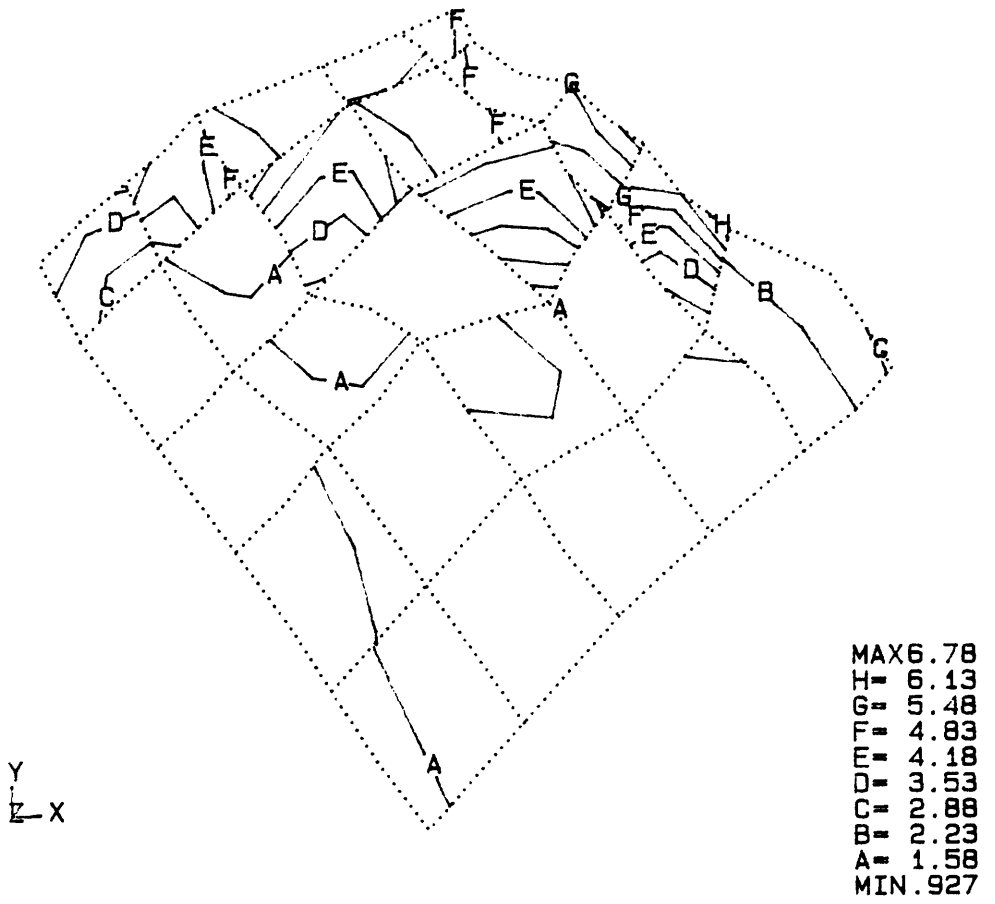

Figure 3.24b: Von Mises stress contours on an enlarged view of control specimen P6 (MPa).

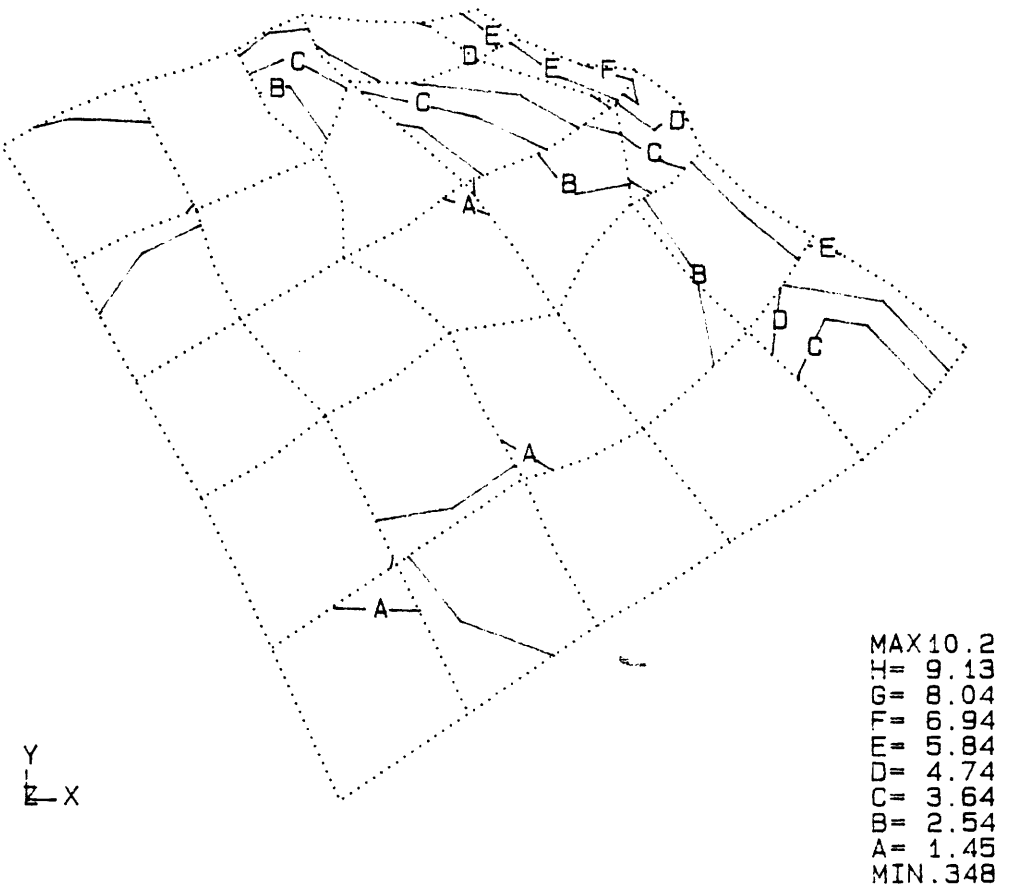

Figure 3.24c: Von Mises stress contours on an enlarged view of control specimen P7 (MPa).

only. The total load due to the quadriceps musculature on each model was set equal to 1000 N. No attempt was made to relate the applied loads to absolute in vivo loads since these data were not available. Throughout this study, the stress data were used in a relative sense; stresses were compared between specimens or between control and experimental patellae and thus the importance of absolute magnitudes must be minimized.

Contour plots of the strain energy density in the control patellae are shown in Figure 3.25. The distributions were similar to those for von Mises effective stress, with the exception that the strain energy density was more constant in the posterior region and several extreme local gradients occurred at element boundaries. This was a direct consequence of the discontinuous material property distribution. This point is examined further in Section 3.3.2.

For the most part, the stresses in the cortical shell of the experimental patellae were similar to those in the control patellae (Figures 3.26). The presence of the implants could not be expected to significantly influence the stresses in any region of the patellae more than one diameter from the implant. Stress changes in the vicinity of the implants were apparent, especially for specimens P6 and P7. Note that there was no bone covering the implant anteriorly in specimen P6, seen in Figure 3.26b.

The enlarged views of the implant region (Figure 3.27) revealed significant stress changes in the trabecular bone adjacent to the

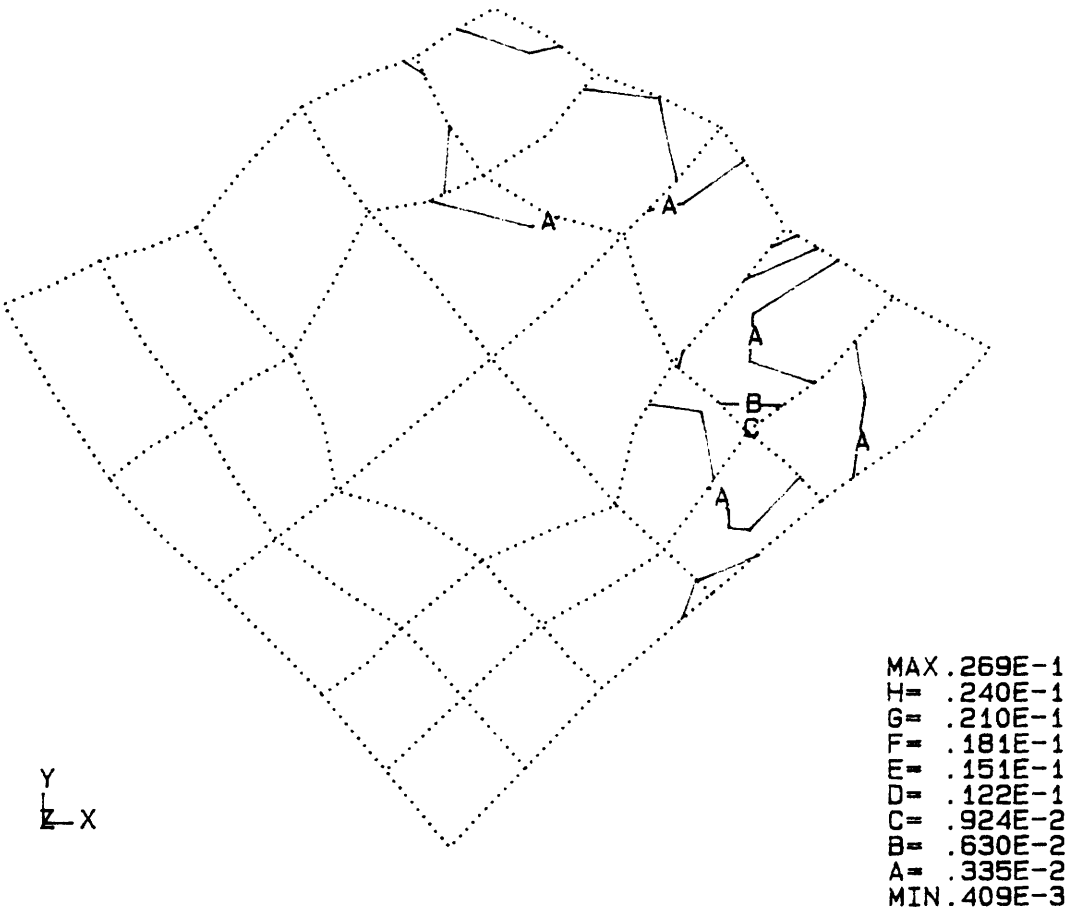

Figure 3.25a: Strain energy density contours on an enlarged view of control specimen S2 (MPa).

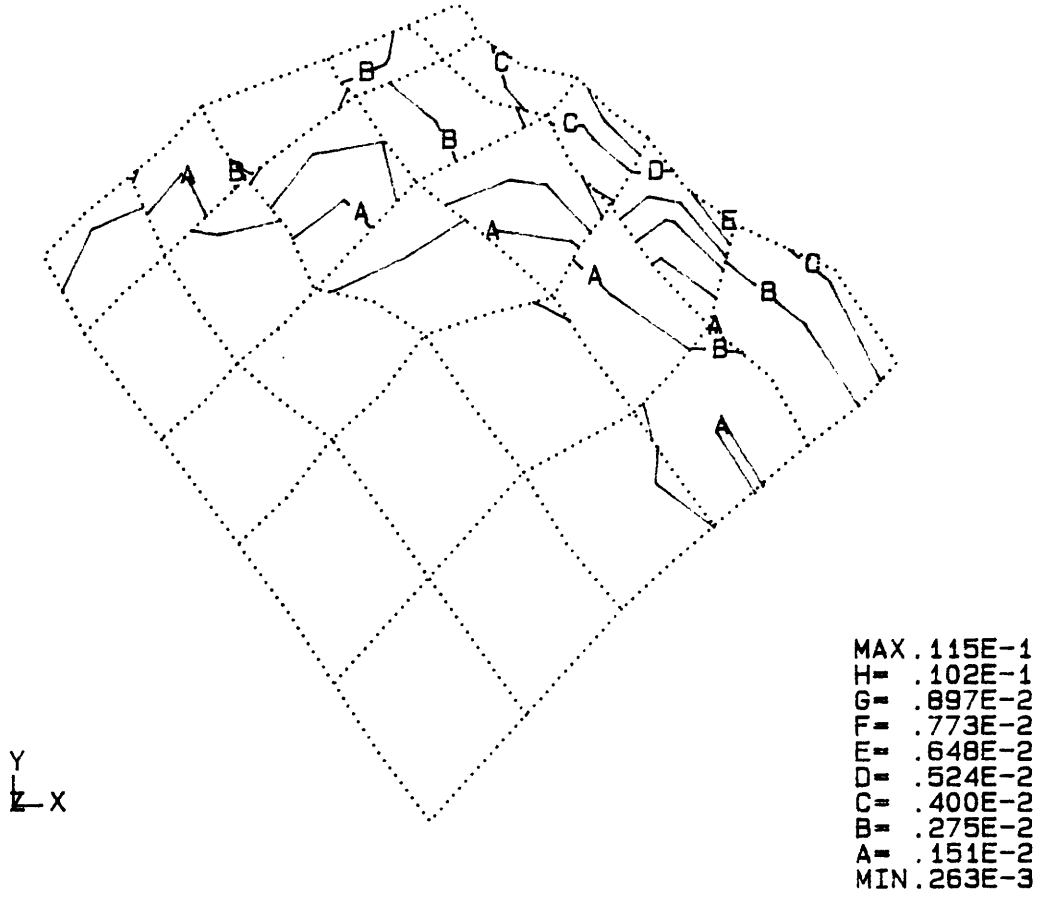

Figure 3.25b: Strain energy density contours on an enlarged view of control specimen P6 (MPa).

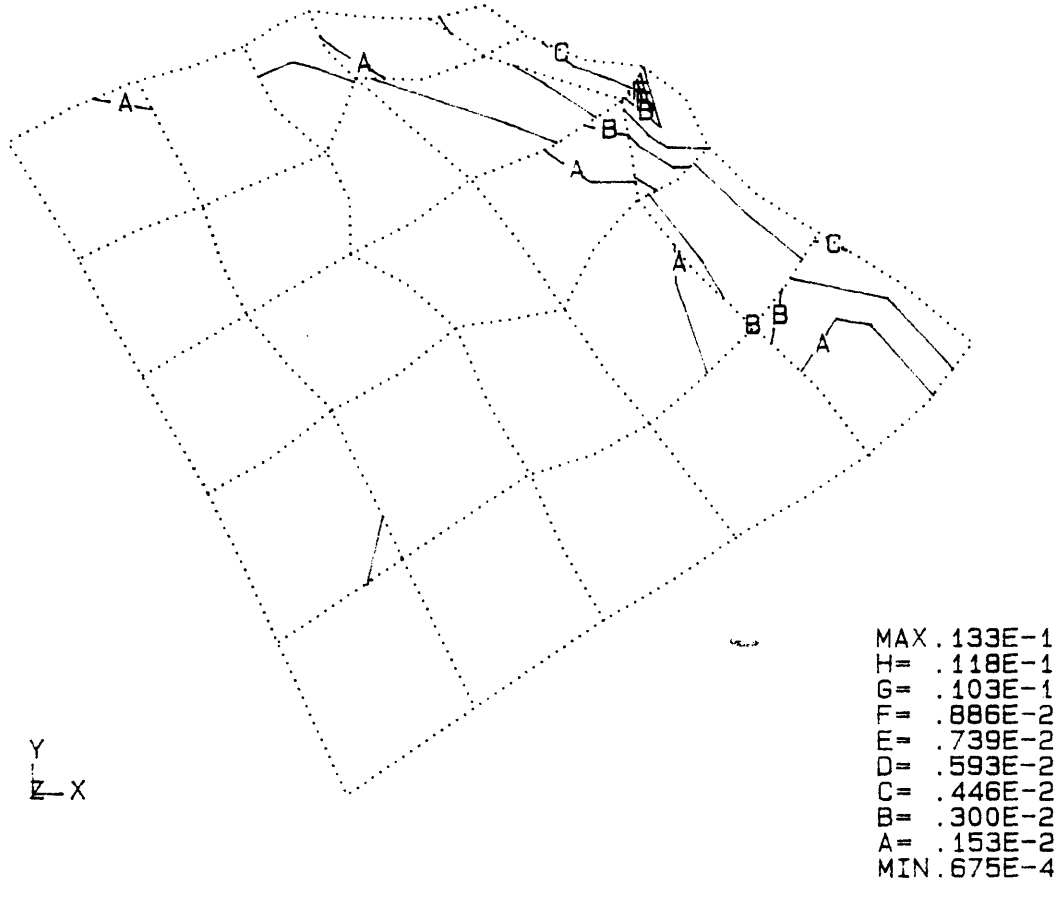

Figure 3.25c: Strain energy density contours on an enlarged view of control specimen P7 (MPa).

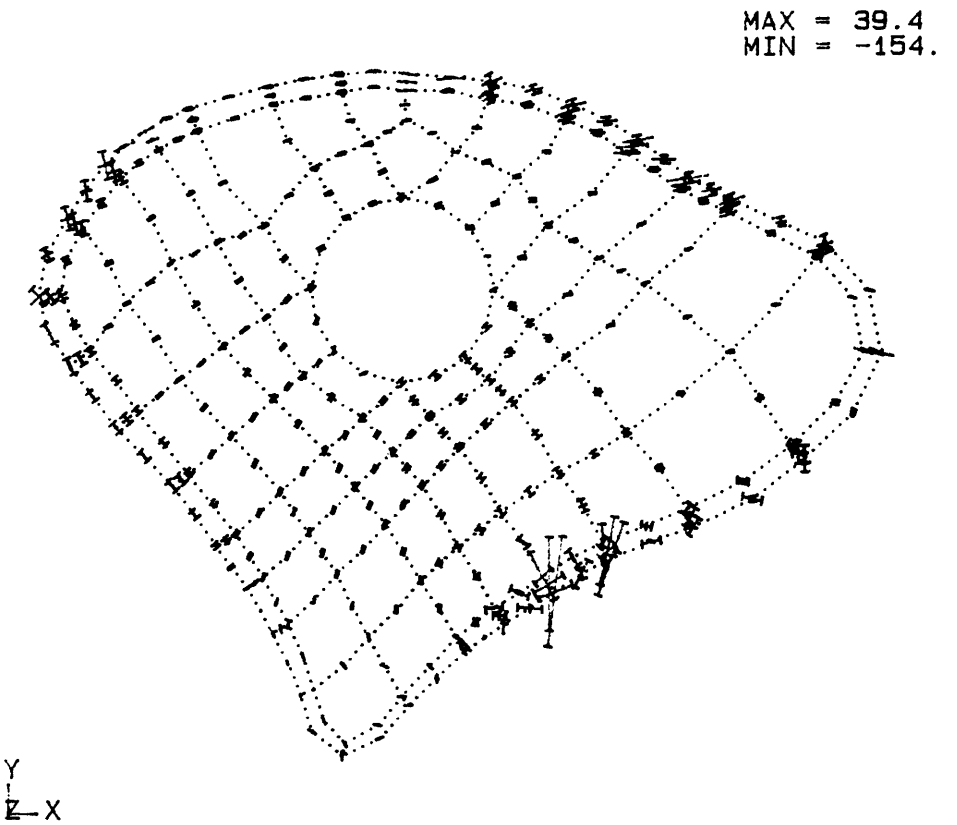

Figure 3.26a: Principal stress vectors on a sagittal section of the experimental specimen S2 (MPa).

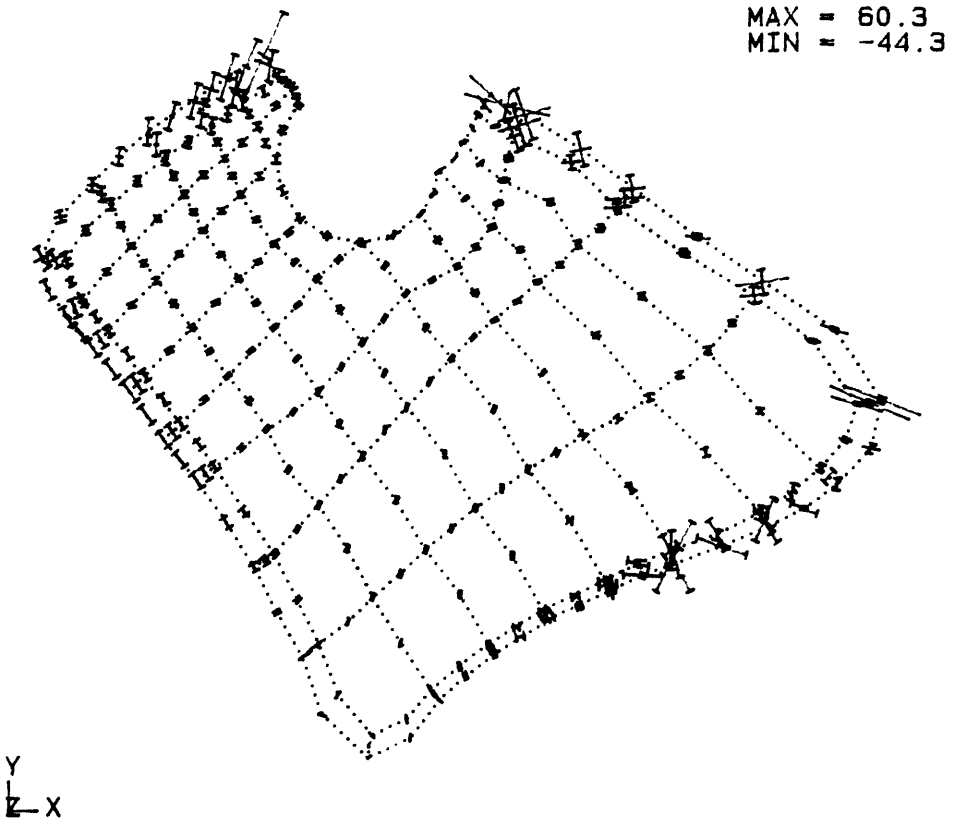

Figure 3.26b: Principal stress vectors on a sagittal section of the experimental specimen P6 (MPa).

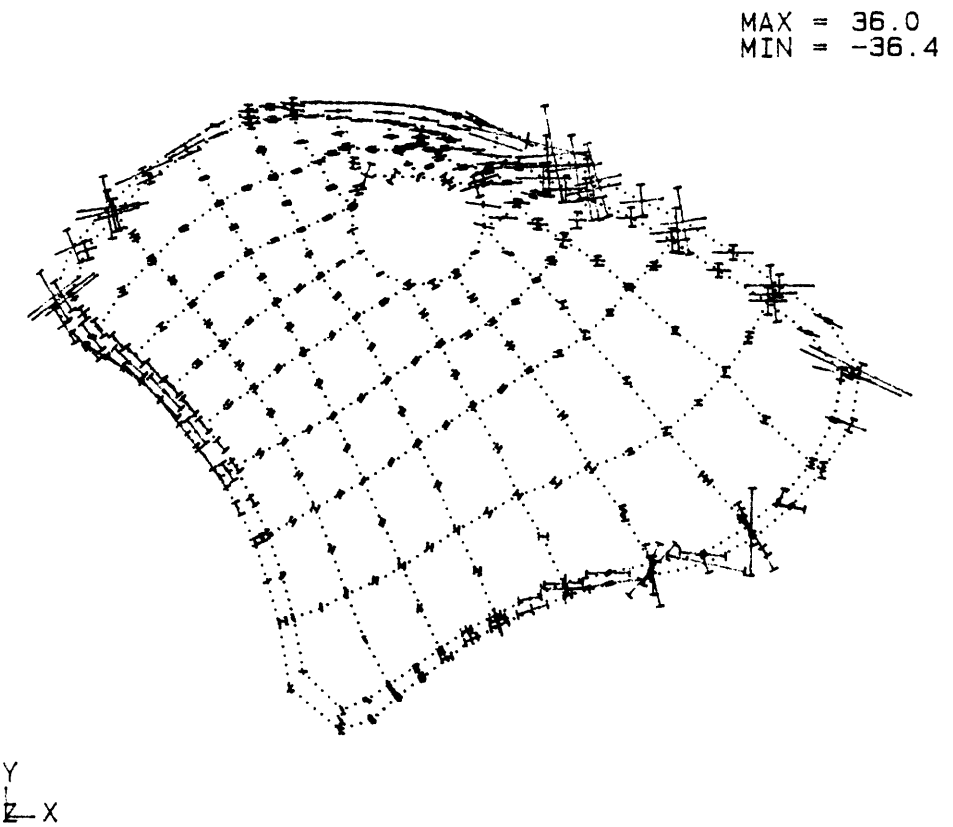

Figure 3.26c: Principal stress vectors on a sagittal section of the experimental specimen P7 (MPa).

implant for all specimens. The stresses were altered when comparing the control patellae to the experimental patellae, and the stresses in the experimental patellae varied greatly between the different specimens as a function of the assumed bone/implant boundary conditions. To examine the influence of the implants on the stress fields, the principal and effective stresses in each experimental patella were contrasted to those in the contralateral control.

The principal stresses in the trabecular bone surrounding the implant in specimen S2 (Figure 3.27a), as in the other two patellae which received smooth spherical implants, were altered in both orientation and absolute magnitude. The principal tensile stresses tended to flow around the implants, although the tensile stresses were not oriented tangential to the implant at the bone/implant interface as might be expected for nonlinear frictionless contact. With the exception of one nodal point on this section, the tensile stresses at the interface were associated with significant principal compressive stresses. The orientation of these stresses were approximately 45 degrees to the interface, indicating that the maximum shear stress orientation was approximately tangential to the implant surface. This result indicates that there were shear stresses at the bone/implant which correspond to frictional forces between the implant and the adjacent trabecular bone.

The technique used to represent the nonlinear boundary conditions, namely three mutually perpendicular nonlinear truss elements does not represent friction exactly. A specific relationship between the surface

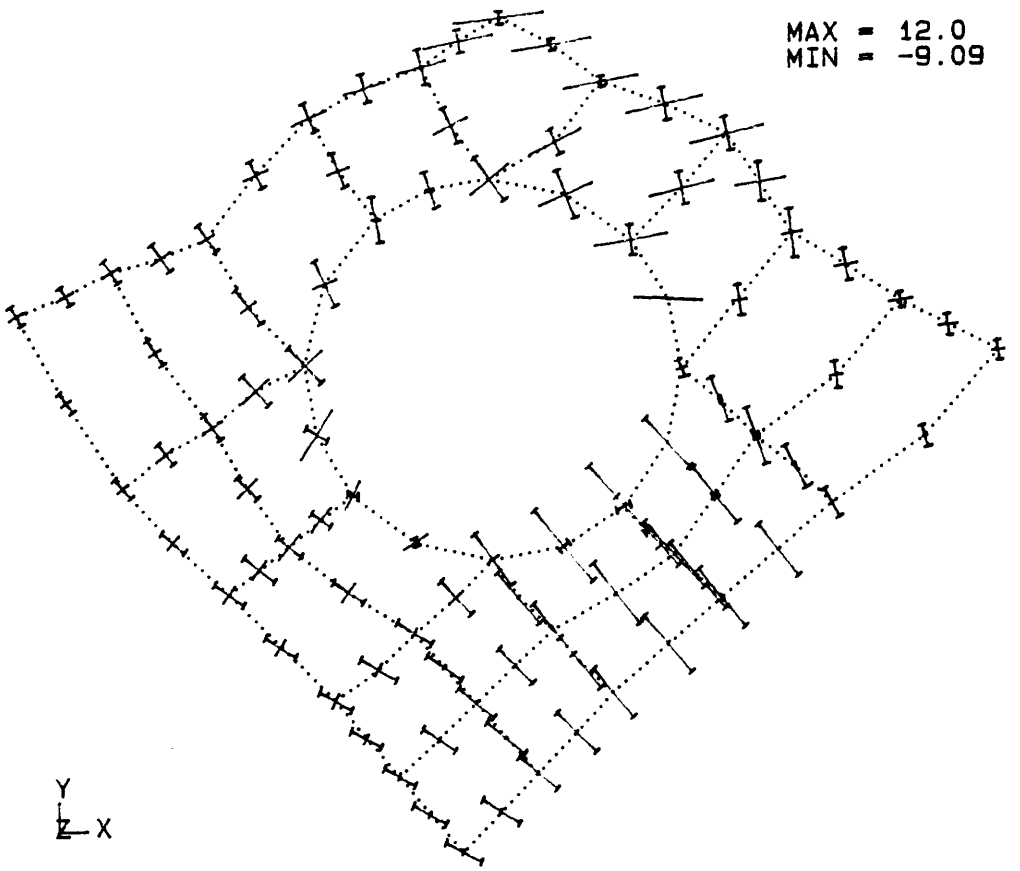

Figure 3.27a: Principal stress vectors on an enlarged view of experimental specimen S2 (MPa).

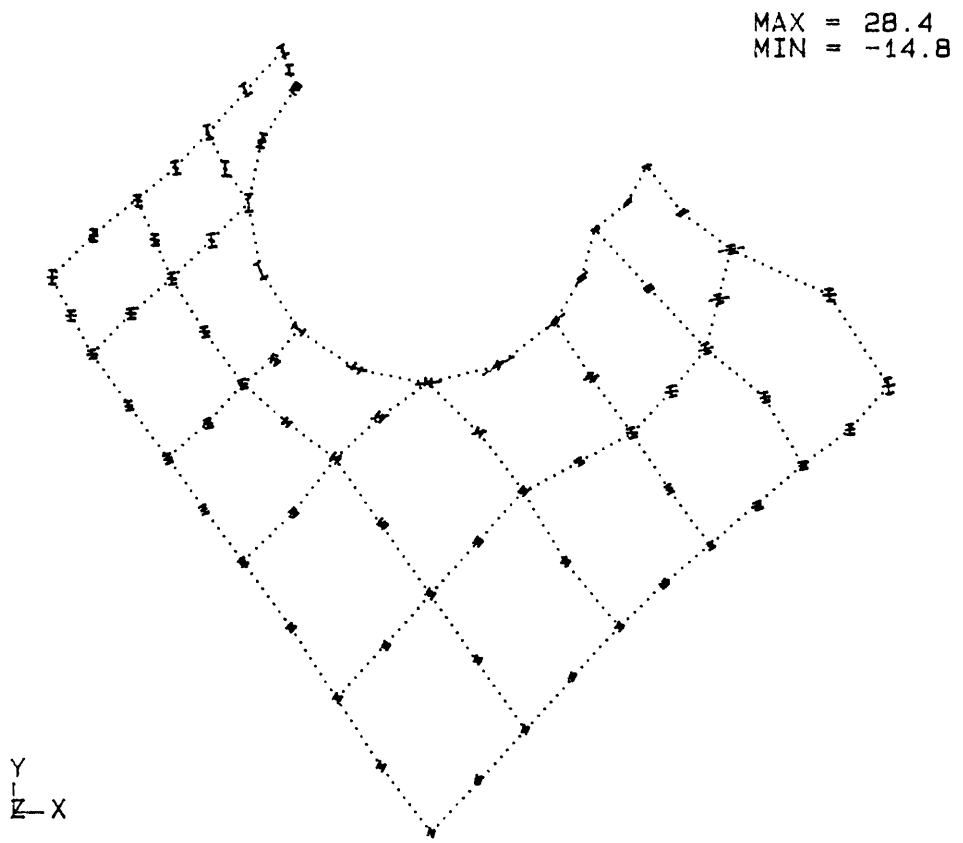

Figure 3.27b: Principal stress vectors on an enlarged view of experimental specimen P6 (MPa).

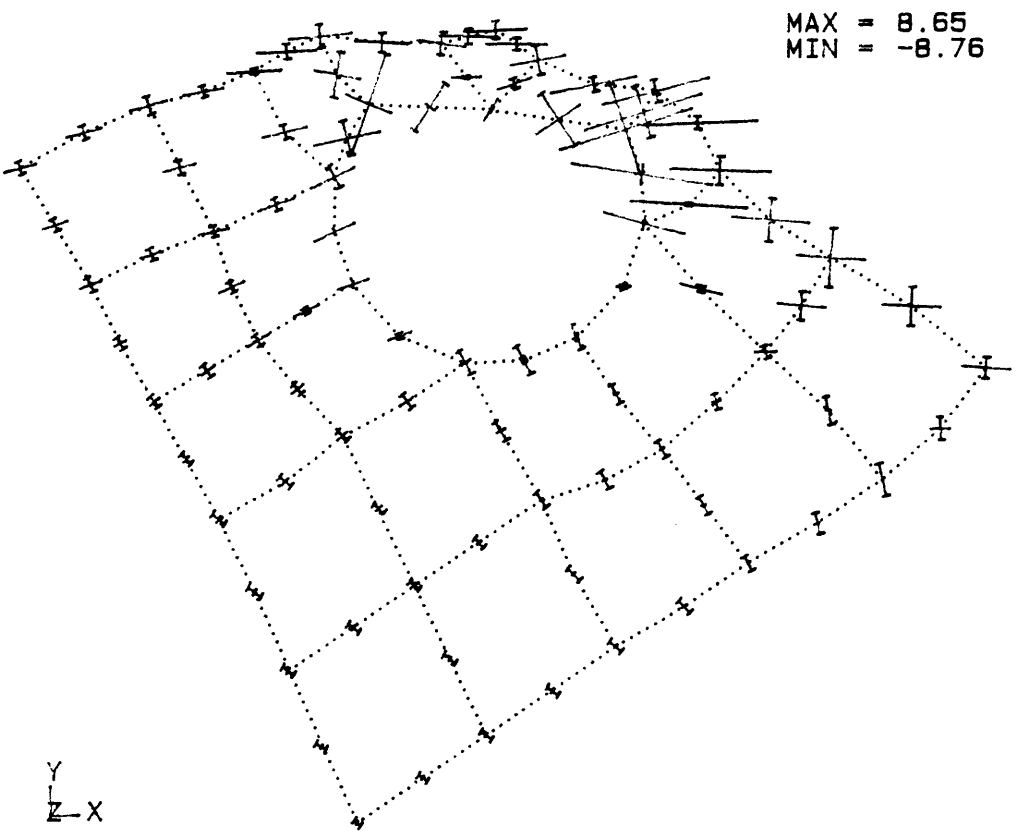

Figure 3.27c: Principal stress vectors on an enlarged view of experimental specimen P7 (MPa).

normal stress and the surface shear stress, such as Coulomb friction, was not maintained. A polished implant surface surrounded by a fibrous tissue layer probably has a very low coefficient of friction. However, the absence of surface friction at the implant would only have a local effect. The smooth implants were entirely surrounded by bone, were not loaded directly, and thus micromotion at the bone/implant interface was unlikely. There were significant shear stresses in the trabecular bone of the control patellae in areas which corresponded to the shear stresses seen in the experimental patellae. As expected, the implants had a stress concentrating effect in the implant vicinity. The error due to the presence of surface shear stresses on the stress-morphology comparisons was probably small since the stress data were taken from the centers of the circular regions which were analyzed with the stereology system. This corresponded to a distance of 2.1 mm from the bone/implant interface for the "A" regions and 6.3 mm from this interface for the "B" regions (see Figure 3.3).

The contour plot of von Mises effective stress confirms the finding of shear stress at the bone/implant interface for specimen S2 (Figure 3.28a). The peak shear stress occurred at the most anterior point of the interface. However, with the exception of that single point, the von Mises stress gradients adjacent to the implant were not excessive, suggesting that surface friction does not account for the general increase in von Mises stress seen in the surrounding trabecular bone. The plot of strain energy density is similar to the plot of von Mises stress (Figure 3.29a). The strain energy density contour plots are included here primarily for later reference (see Section 3.3.2).

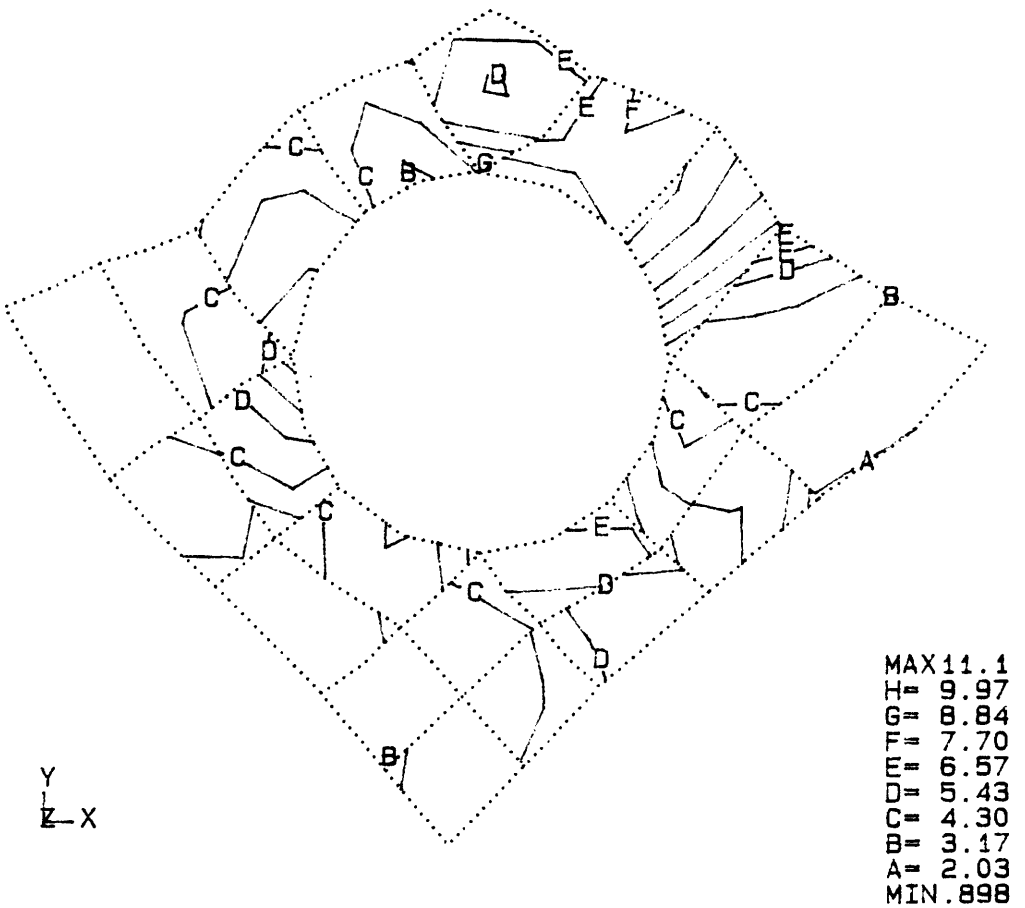

Figure 3.28a: Von Mises stress contours on an enlarged view of experimental specimen S2 (MPa).

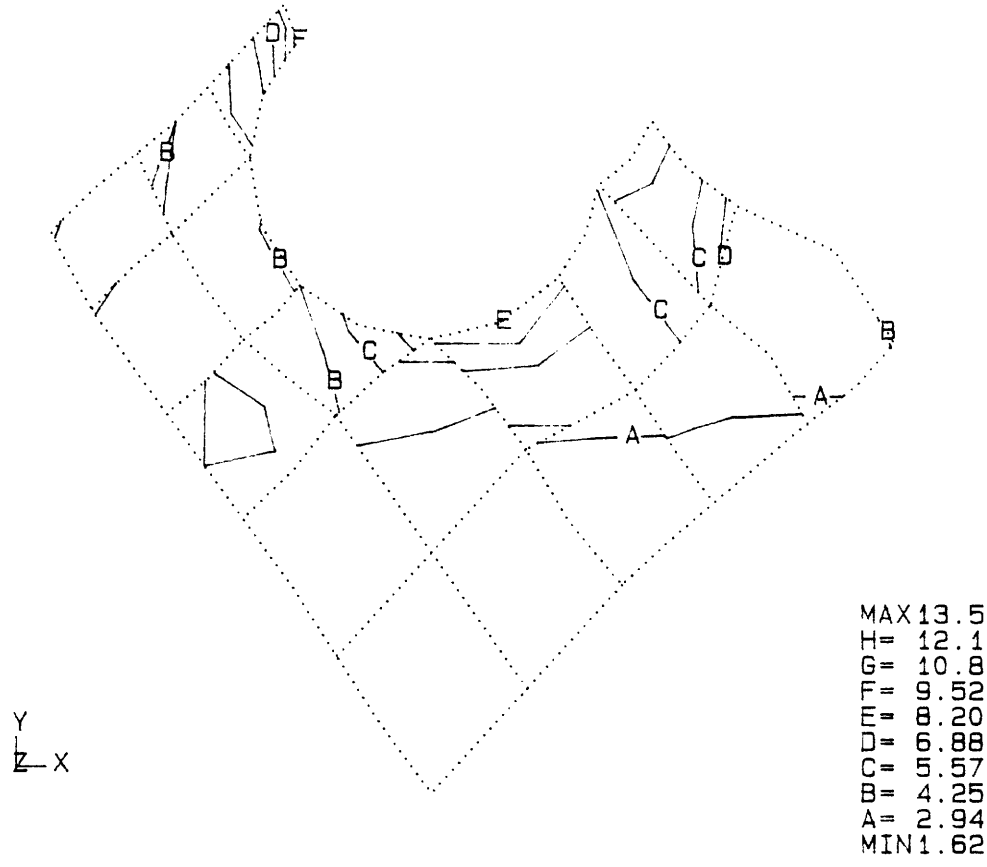

Figure 3.28b: Von Mises stress contours on an enlarged view of experimental specimen P6 (MPa).

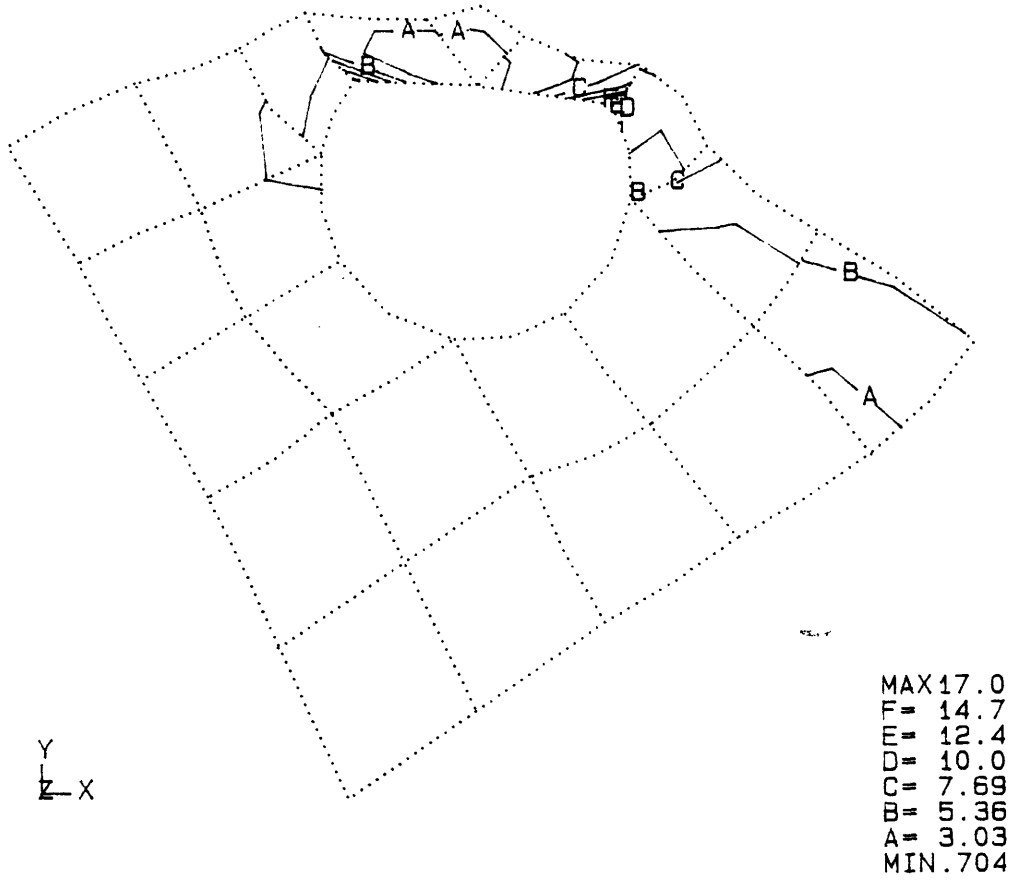

Figure 3.28c: Von Mises stress contours on an enlarged view of experimental specimen P7 (MPa).

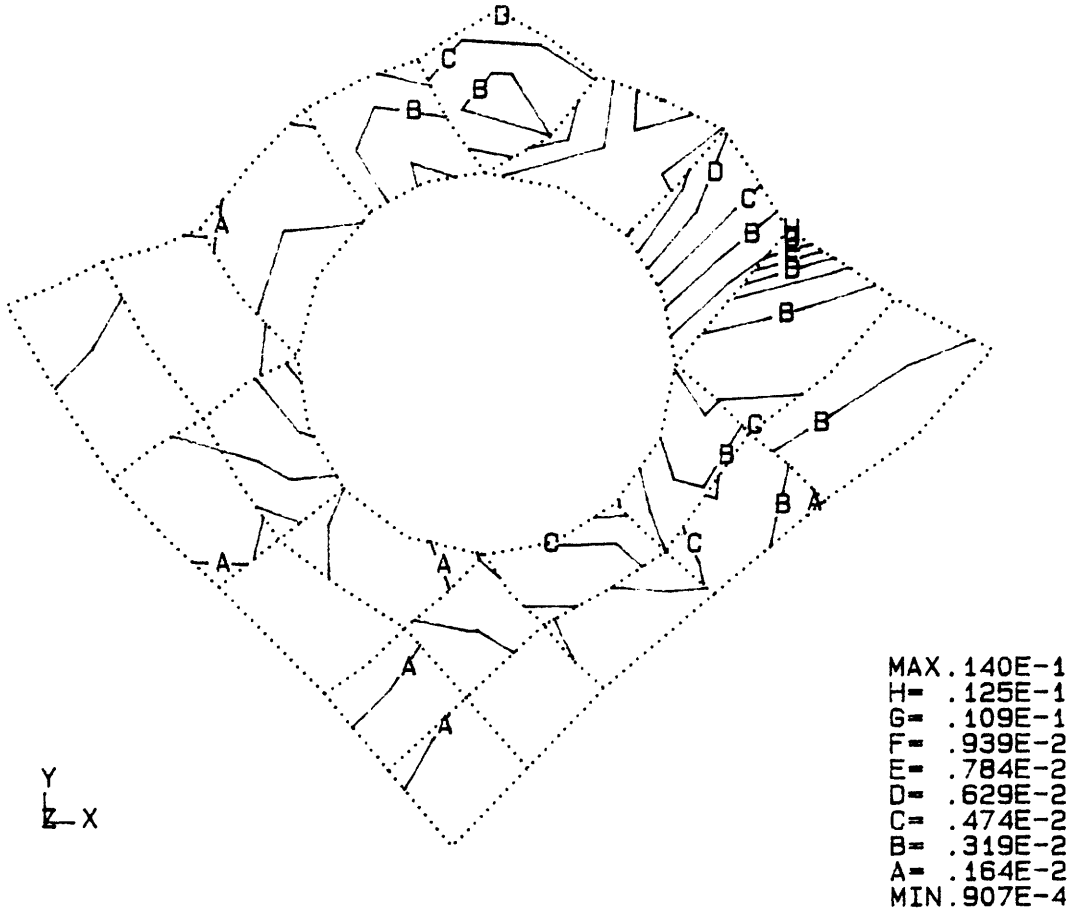

Figure 3.29a: Strain energy density contours on an enlarged view of experimental specimen S2 (MPa).

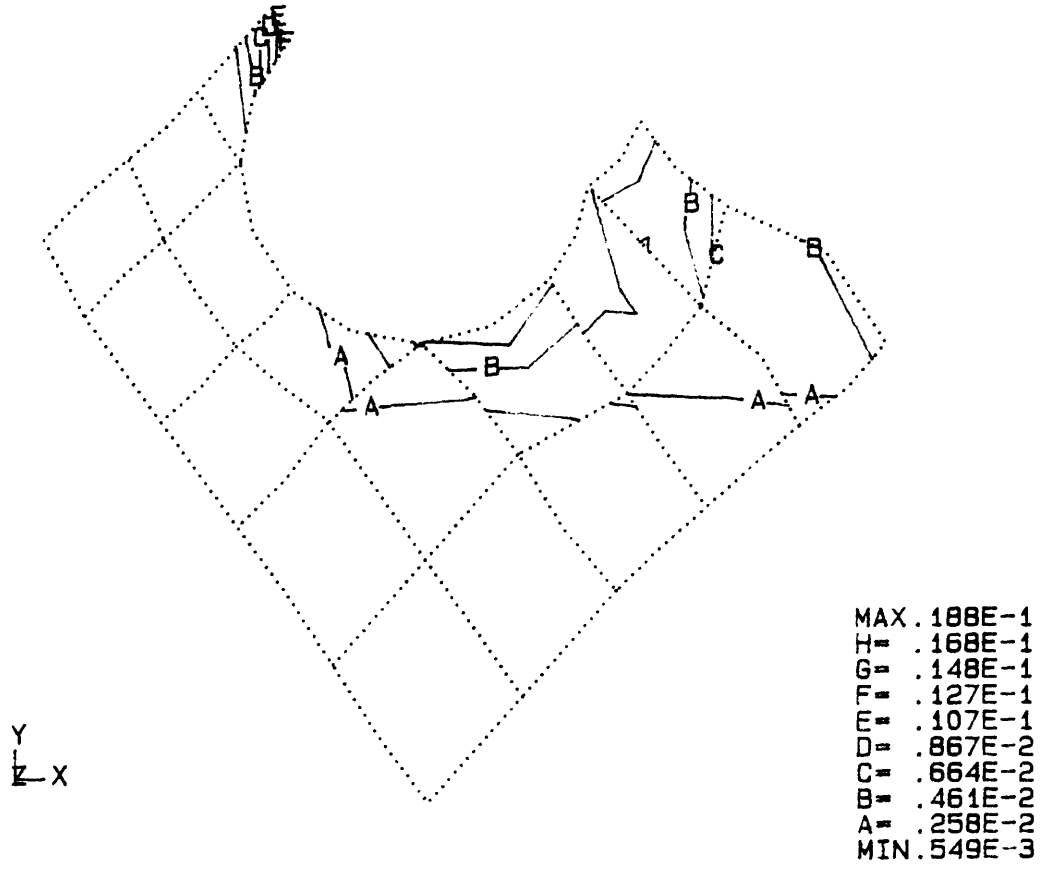

Figure 3.29b: Strain energy density contours on an enlarged view of experimental specimen P6 (MPa).

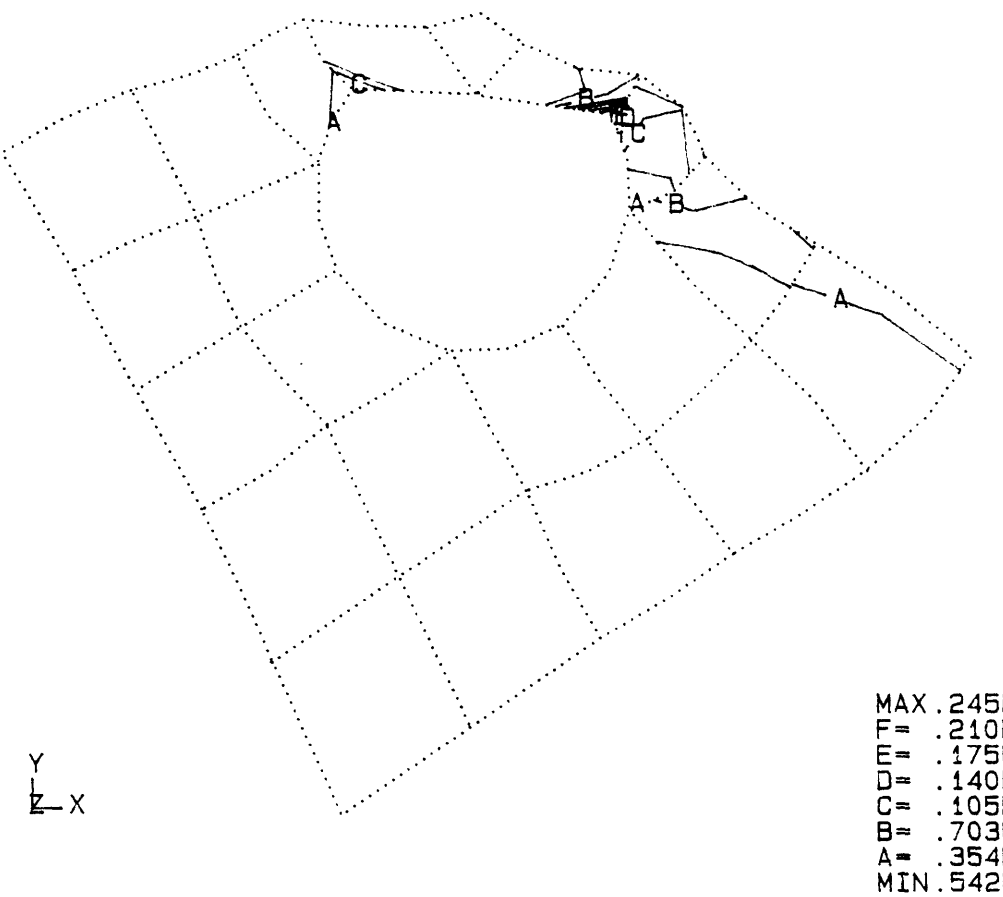

Figure 3.29c: Strain energy density contours on an enlarged view of experimental specimen P7 (MPa).

The principal stresses around the implant in specimen P6 were also significantly altered when compared to the contralateral control (Figure 3.27b). Unfortunately it is difficult to compare the vector magnitudes between Figures 3.23b and 3.27b due to the problem with vector scaling mentioned above. The peak stresses on the section of the mesh included in Figure 3.27b occurred on the opposite faces of the three-dimensional elements, parallel to those shown, at a different Z coordinate. The stresses on the sections corresponding to one element thickness in either direction from the section shown are high due to the flow of stress around the implant region in the medial and lateral directions. Recall that the implant for this specimen is represented as a void with no mechanical coupling between the trabecular bone and the implant. It can be seen in Figure 3.27b that the principal stresses around the void were directed tangential to the surface, as expected.

The stress magnitudes are more easily compared using the contour plots of von Mises effective stress and strain energy density for the control (Figures 3.24b and 3.25b) and the experimental patellae (Figures 3.28b and 3.29b). There was an increase in von Mises stress in the trabecular bone surrounding the implant. The shear stress at the bone/implant interface, indicated by the von Mises stress contours, was in the plane tangential to the plane of this interface. The shear stress could not have been oriented otherwise or principal stress vectors would be apparent which were not oriented tangential to the bone/implant interface (Figure 3.27b).

The principal stresses around the ingrown, porous coated implants

were generally less altered than those of the other specimens (Figure 3.27c). High stresses were seen at the sharp corners of the implant which were near the anterior cortical shell. Recall that the porous coated implants were not perfectly spherical due to manufacturing requirements. However, this stress concentrating effect was well localized, as demonstrated by the contour plots of von Mises stress (Figure 3.28c) and strain energy density (Figure 3.29c). With the exception of these locations, rigid mechanical coupling of the implant to the adjacent trabecular bone resulted in some stress concentrating effect, but in general, had the least impact on the stresses in the surrounding areas.

To compare the stress concentrating effect of the implants, as a function of the bone/implant boundary conditions, the von Mises stress was calculated at a particular location at the bone/implant interface. It was not possible to strictly define a stress concentration factor for these models due to the nonuniform stress fields in the control patellae. The stress at the most posterior point on the bone/implant interface was used since the stress fields at this location in the control patellae were most similar from specimen to specimen. Von Mises effective stress was used, rather than a single stress component as is usually done in defining stress concentration factors, due to the complex multiaxial nature of the stress fields in the patellae. The ratio of the von Mises stress in the experimental patella to the von Mises stress in the control patella was 2.04 for specimen S2, 4.84 for specimen P6, and 1.54 for specimen P7. For comparison, the stress concentration factor for a rigid spherical inclusion in an infinite

member under uniaxial tension, assuming perfect bonding, is (Peterson 1974):

$$K_t = \frac{\sigma_{max}}{\sigma} = \frac{2}{1+\nu} + \frac{1}{4-5\nu} \qquad (3.1)$$

For $\nu = 0.2$, $K_t = 2.0$. For a spherical void under similar conditions, the stress concentration factor is (Peterson 1974):

$$K_t = \frac{27-15\nu}{14-10\nu} \qquad (3.2)$$

Again, for $\nu = 0.2$, $K_t = 2.0$. Compared to these values, the stress ratio of 4.84 for specimen P6 appears high. This is probably due to the fact that the bone does not surround the implant (void) in this specimen (see Figure 3.26b). The stress ratios for specimens S2 and P7 compare well with that for a rigid spherical inclusion.

The changes in the stress fields described above may be further examined by plotting the stresses in the experimental patellae as a function of the stresses at the corresponding locations in the contralateral control patellae. The changes in strain energy density for all six specimens are presented in Figure 3.30. The line Y = X is included to indicate those data points for which there was no change in this quantity. The locations of the data points corresponded to the locations of the available morphologic data from the stereologic analyses. In general, the strain energy density was more greatly altered in the regions close to the implant (the "A" regions, shown with filled

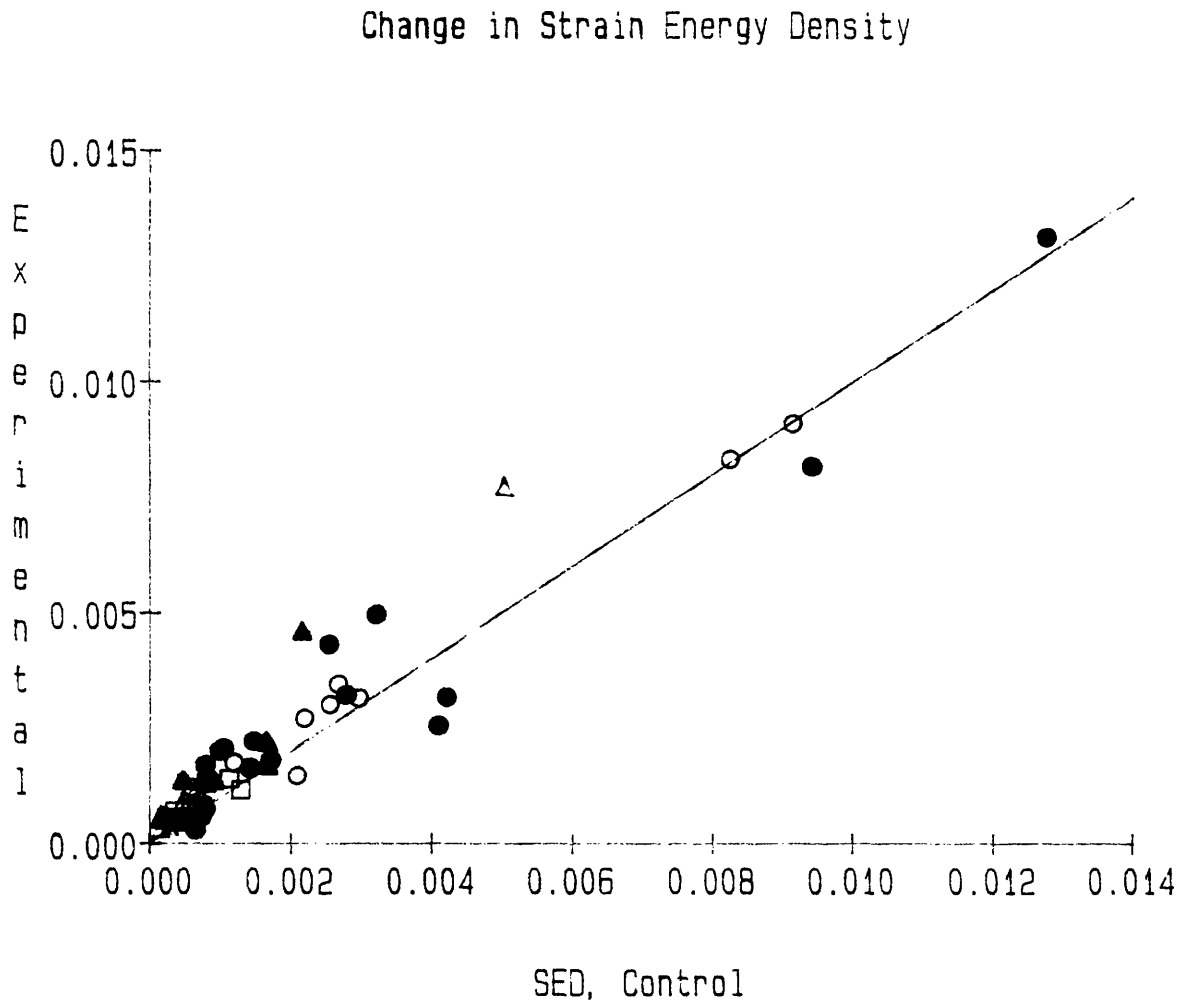

Figure 3.30: The strain energy density in the "A" and "B" regions in the experimental patellae as a function of the strain energy density in the corresponding regions in the control patellae. See Figure 3.8 for Key.

symbols). Also, more data points lie above the line than below the line, indicating higher stresses in the experimental patellae.

The means and standard deviations of the predicted strain energy density are presented in Table 3.2. A higher average strain energy density was predicted for all experimental patellae when compared to the control patellae. However, the coefficient of variation (the ratio of the standard deviation over the mean) was much greater for these data than for the bone area fraction data (see Table 3.1). This demonstrates the wide variation of stress conditions around the implants. The above contour plots of von Mises stress and strain energy density show this graphically. In contrast, the changes in bone area fraction were much more consistent, as reflected by the lower coefficients of variation. The specimen-to-specimen variation in strain energy density was also great, when comparing the three specimens with smooth implants and the two specimens with ingrown porous coated implants. This was due to the inconsistent location of the implants. As demonstrated above, the proximity of the implants to the anterior cortical shell greatly influenced the stresses surrounding the implants. Also, the number and location of usable images varied, depending on the specimen geometry and morphology. Recall that the stress data presented in Table 3.2 were taken from the locations of available morphologic data.

The changes in the principal stress orientation are presented in Figure 3.31. The angle of orientation in this graph was that of the principal stress which was maximum in absolute magnitude. The lines $Y = X + 90$ and $Y = X - 90$ are included to indicate the possible range of

Table 3.2

Statistics on Strain Energy Density
Equine Patella
[kPa]

		Control		Experimental		Difference		
Spec	Reg	Mean	SD	Mean	SD	Mean	SD	N
S1	A	0.736	0.074	0.960	0.720	0.224	0.657	3
	B	1.113	0.440	1.213	0.634	0.100	0.194	2
S2	A	2.231	1.147	2.889	1.312	0.658	0.997	7
	B	3.043	2.743	3.314	2.663	0.271	0.470	7
S3	A	4.544	4.729	4.546	4.498	0.002	1.034	7
	B	2.598	3.323	2.918	3.175	0.320	0.219	5
P6	A	0.607	0.165	0.788	0.467	0.181	0.302	3
	B	0.777	0.502	0.966	0.395	0.189	0.210	4
P7	A	0.967	0.757	1.636	1.595	0.668	0.936	6
	B	1.350	2.068	2.083	3.172	0.732	1.108	5
P8	A	0.640	0.656	0.943	0.554	0.303	0.168	5
	B	0.430	0.242	0.758	0.232	0.328	0.128	4

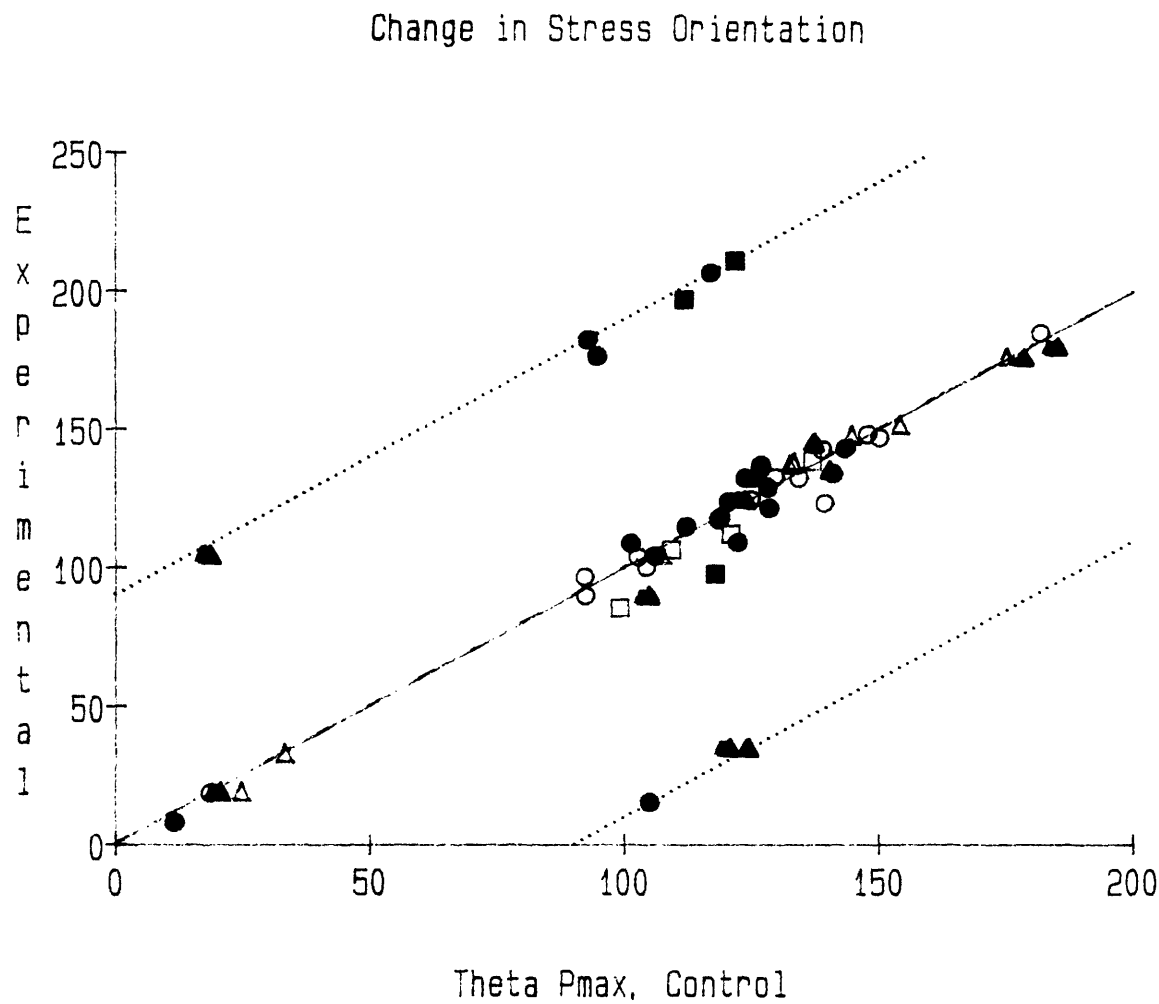

Figure 3.31: The maximum principal stress direction in the "A" and "B" regions in the experimental patellae as a function of the maximum principal stress direction in the corresponding regions in the control patellae. See Figure 3.8 for Key.

data. For points on the line Y = X there was no difference in the maximum principal stress direction between corresponding regions in the control and experimental specimens. For the nine points which lie on or near these lines, there was a reversal in the sign of the maximum principal stress. In other words, the predominant stress changed from tension to compression or from compression to tension. For eight of these nine data points, the predominant stress was compression in the control patella and tension in the experimental patella. Again, in general, the stresses in the "A" locations were affected by the implants more than the "B" locations. This demonstrates that there were significant changes in the orientation of the principal stress directions due to the presence of the implants.

The change in the eccentricity of the stress ellipse (see Equation 3.4 for definition) is presented graphically in Figure 3.32. Four distinct populations of data points are apparent. For the majority of data points, the dominant stress was compression, and thus had a negative eccentricity, for both the control and experimental patellae. For the next largest number of data points, the dominant stress was tension for both the control and experimental patellae. For eight data points, as mentioned above, the dominant stress changed from compression to tension, and for one data point the reverse occurred. There was generally less change in the eccentricity of the stress ellipse, as predicted by the finite element models, then there was for the eccentricity of the material anisotropy ellipse, as measured using stereology (see Figure 3.11). The relationship between these parameters is examined in Section 3.3. There were significant changes in the

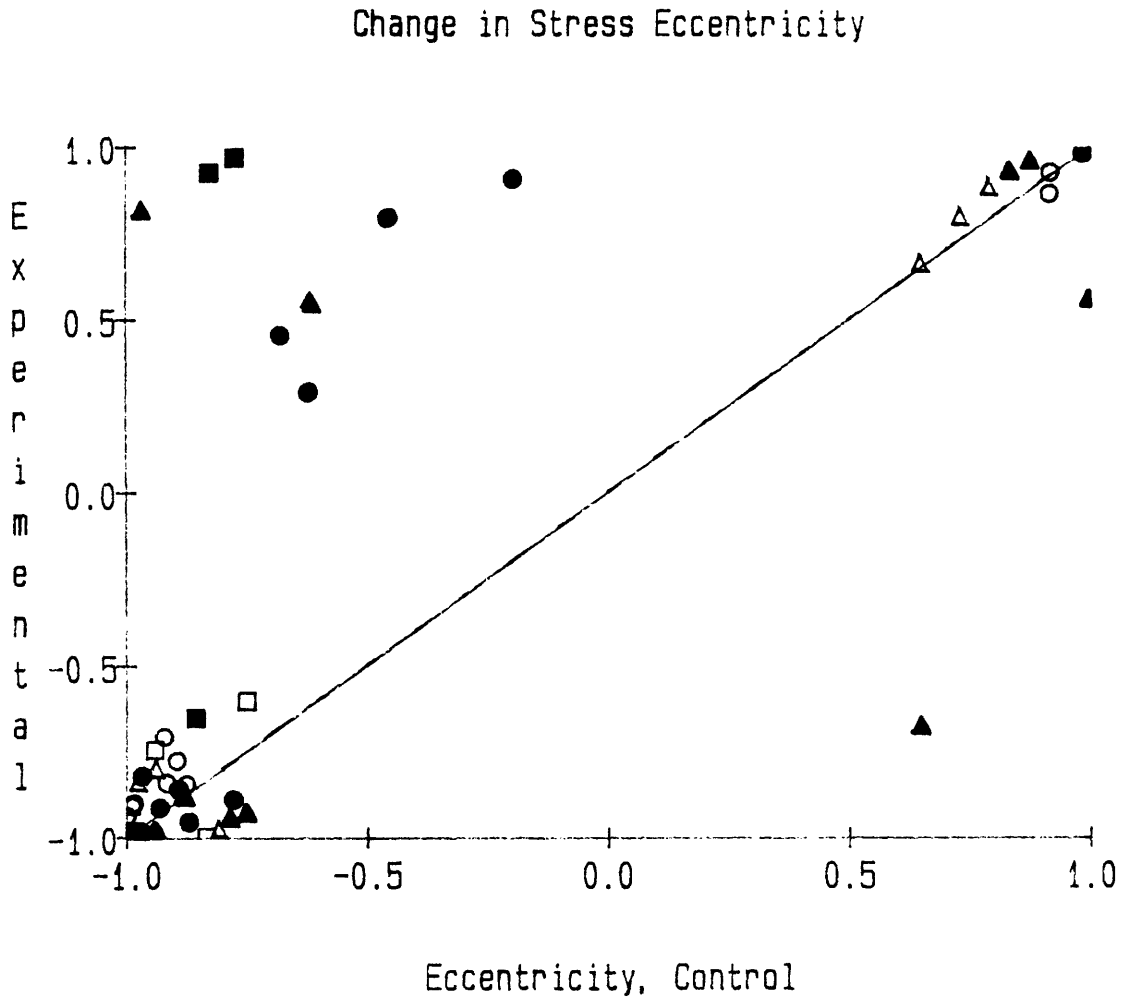

Figure 3.32: The eccentricity of the stress ellipse in the "A" and "B" regions in the experimental patellae as a function of the eccentricity of the stress ellipse in the corresponding regions in the control patellae. See Figure 3.8 for Key.

stress state, as reflected by the eccentricity of the stress ellipse, when comparing the experimental specimens to the control specimens. For nine data points, the dominant stress changed from compression to tension, or vice versa, as reflected by large changes in the stress eccentricity.

As discussed in Section 3.3, the nature of the stress state may critically influence the correlation between the predicted stresses and the measured morphology. One important parameter is the relative magnitude of the hydrostatic stress component compared to the shear stress component. To examine this parameter, the hydrostatic stress is shown as a function of the octahedral shear stress, for the control and experimental patellae, in Figure 3.33. With the exception of one data point, the ratio of hydrostatic stress to octahedral shear stress was always less than one in absolute magnitude. There were numerous data points for which this ratio was close to zero. By definition, these data points also have an eccentricity which approaches zero, as seen in Figure 3.32. This demonstrates that, according to the finite element model predictions, there were areas which approached pure shear stress but no areas of hydrostatic compression or tension.

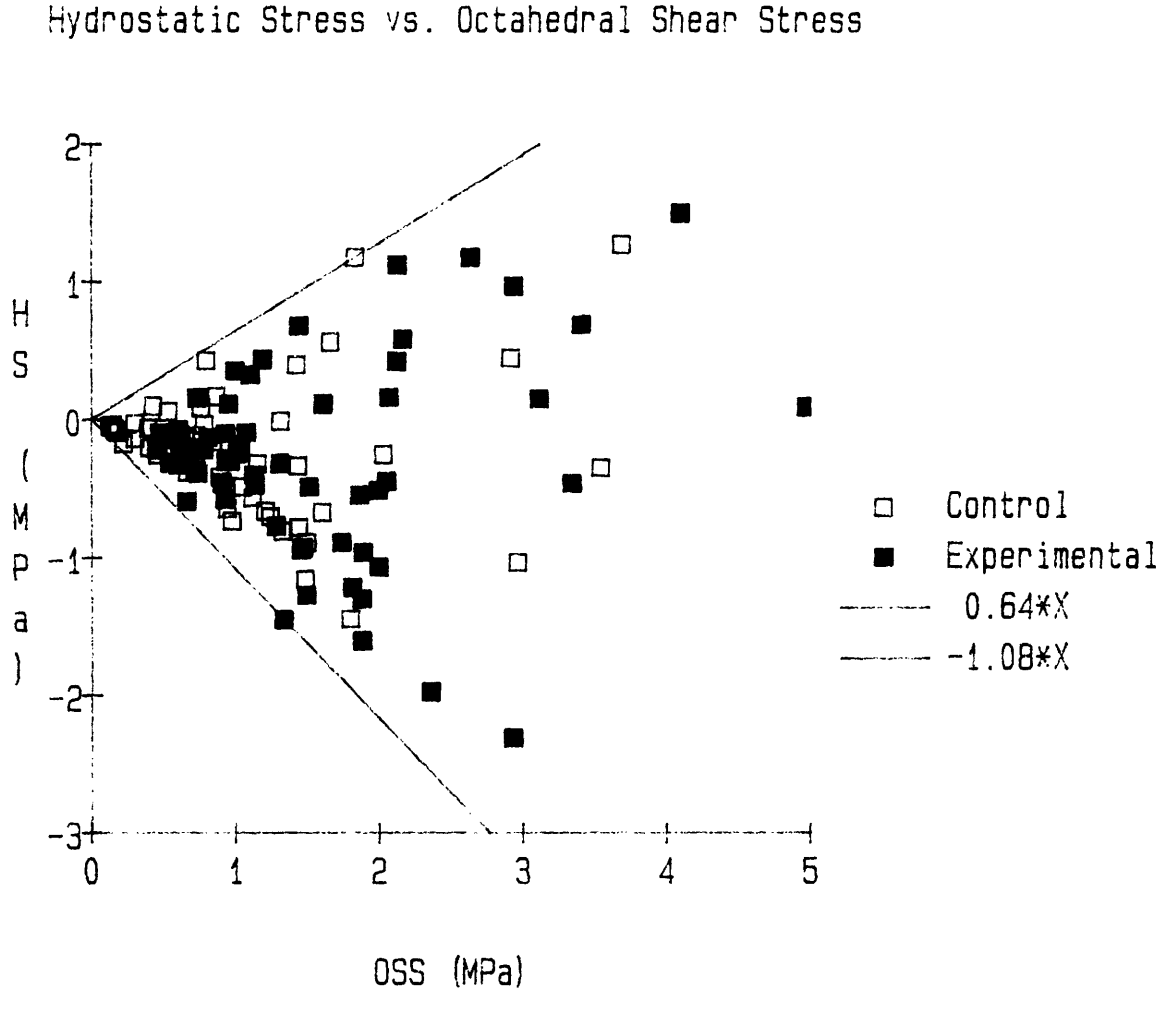

Figure 3.33: Hydrostatic stress as a function of the octahedral shear stress for all locations in the control and experimental specimens.

3.2.2 Ovine Calcaneus

The two-dimensional finite element models of the ovine calcanei were based on the morphologic data presented in Section 3.1.2. Rigid mechanical coupling was assumed between the implants and the trabecular bone due to the observed bone ingrowth into the porous coating on all of the specimens. The nonhomogeneous isotropic material properties were established based on the measured areal densities as described in Section 2.2.2.

The load due to the tendo calcaneus primarily resulted in bending deformations. The deformed mesh, as predicted for the control specimen C1, is shown in Figure 3.34. Note that the nodal points at the distal section, to which rigid truss elements were fixed, remained approximately co-linear. This confirmed that the condition of plane sections remaining plane, at this distal section, was maintained. The principal stress vectors for this specimen are shown in Figure 3.35. Most apparent were the compressive stresses in the anterior cortex and the tensile stresses in the posterior cortex corresponding to the bending deformations.

The overall deformations and stress distribution for the experimental specimens were similar to those for the control specimens. The deformed mesh for experimental specimen C1 is shown in Figure 3.36. The truss elements at the distal section were replaced by the resultant loads calculated for the control specimens. The rigid body modes were eliminated and the cobalt chromium implants were represented using truss

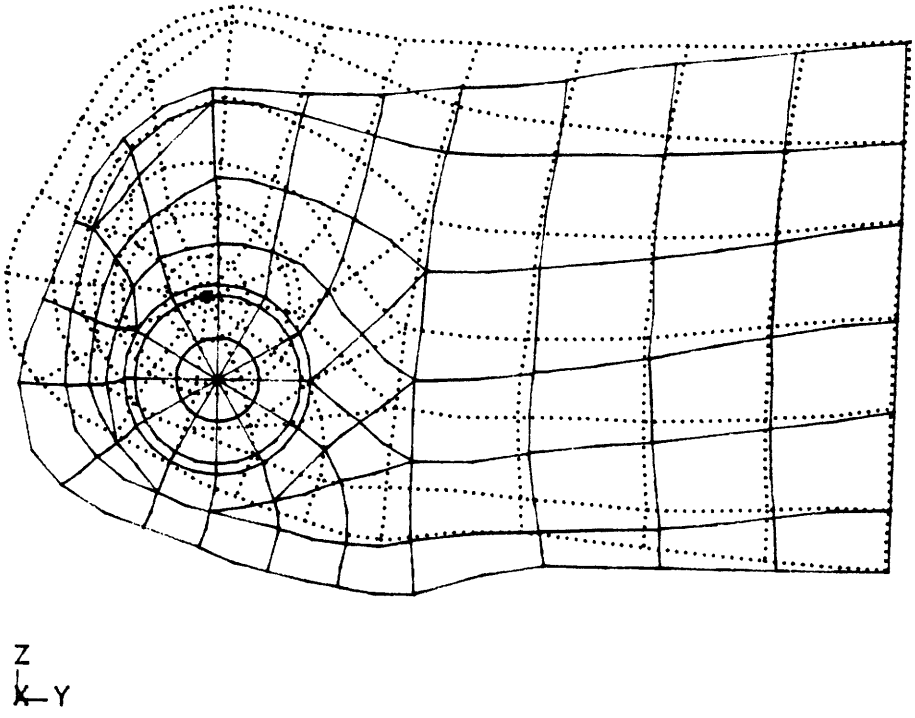

Figure 3.34: Undeformed (solid lines) and deformed (dotted lines) mesh for control specimen C1. The positive Y axis points in the distal direction and the positive Z axis points in the anterior direction.

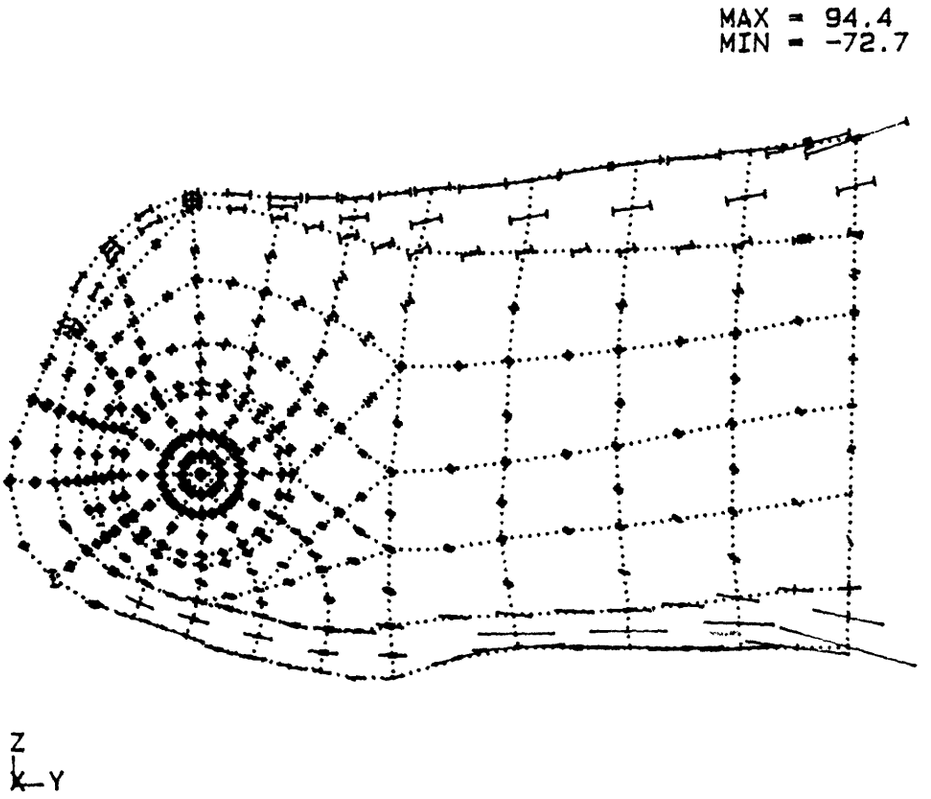

Figure 3.35: Principal stress vectors on a sagittal section of the control specimen C1 (MPa).

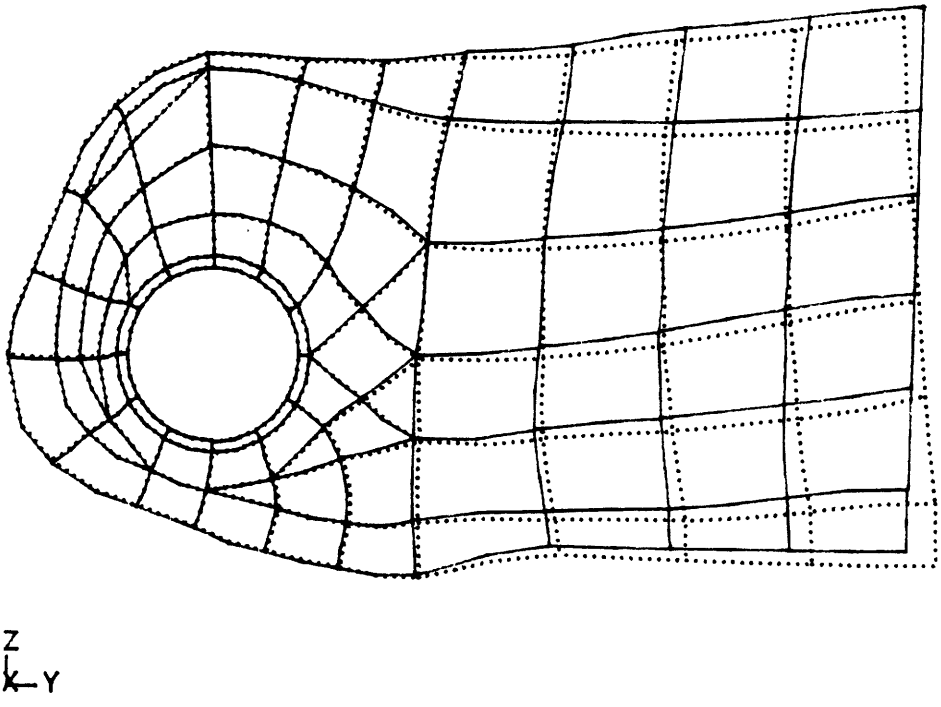

Figure 3.36: Undeformed (solid lines) and deformed (dotted lines) mesh for experimental specimen C1.

elements at the bone/implant interface (see Section 2.2.4 for further detail). The principal stress vectors, shown in Figure 3.37, confirmed that the overall mesh deformation was equivalent to that for the control specimen. The principal stresses away from the implant in the experimental specimens were essentially identical to those in the control specimens.

The stresses around the implants in the experimental specimens and in the corresponding regions in the control specimens were examined using enlarged views of that portion of the mesh. The principal stress vectors for control specimen C1 are shown in Figure 3.38a. There was a general flow of tension from the posterior-distal region, where the highest magnitude tensile stresses occurred, to the anterior-proximal region. The orthogonal compressive stresses were approximately a mirror image of the tensile stresses with the maximum stresses in the anterior-distal region. The stresses approached uniaxial tension adjacent to the posterior cortex and uniaxial compression adjacent to the anterior cortex. The tensile and compressive stress components were approximately equal in magnitude around the center of the implant indicating significant shear stress. There were no regions where the stress components were either both tensile or both compressive at the same location indicating that the hydrostatic stress component throughout the models was small.

A small distance from the implants, the orientation of the principal stresses in the experimental specimens was similar to that in the corresponding region in the control specimens. The principal stress

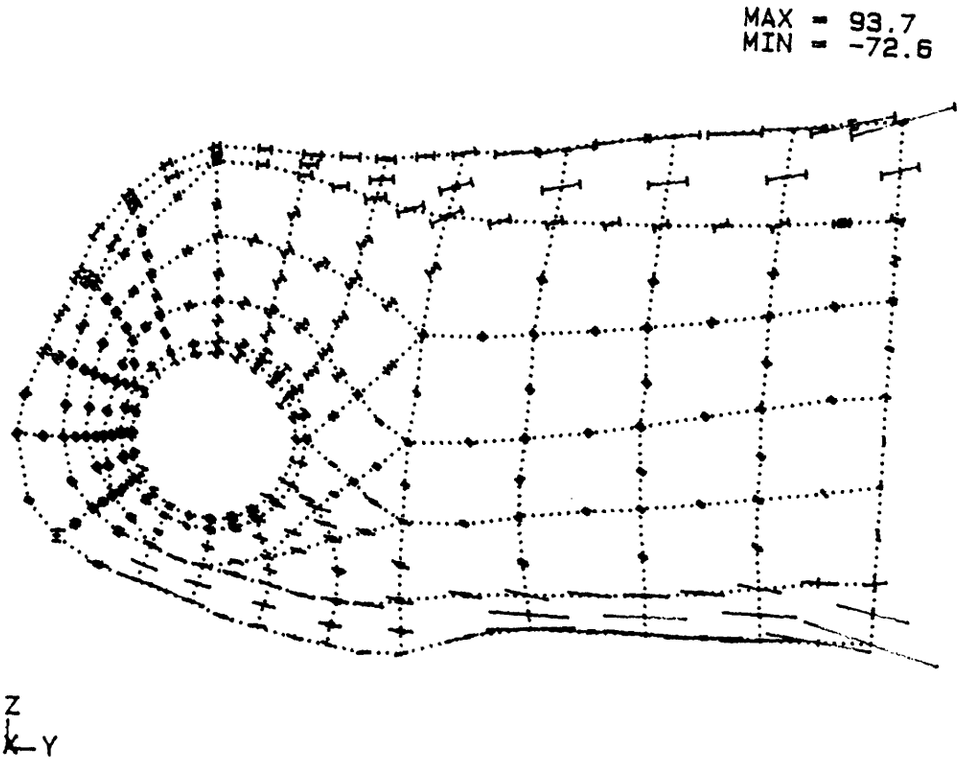

Figure 3.37: Principal stress vectors on a sagittal section of the experimental specimen C1 (MPa).

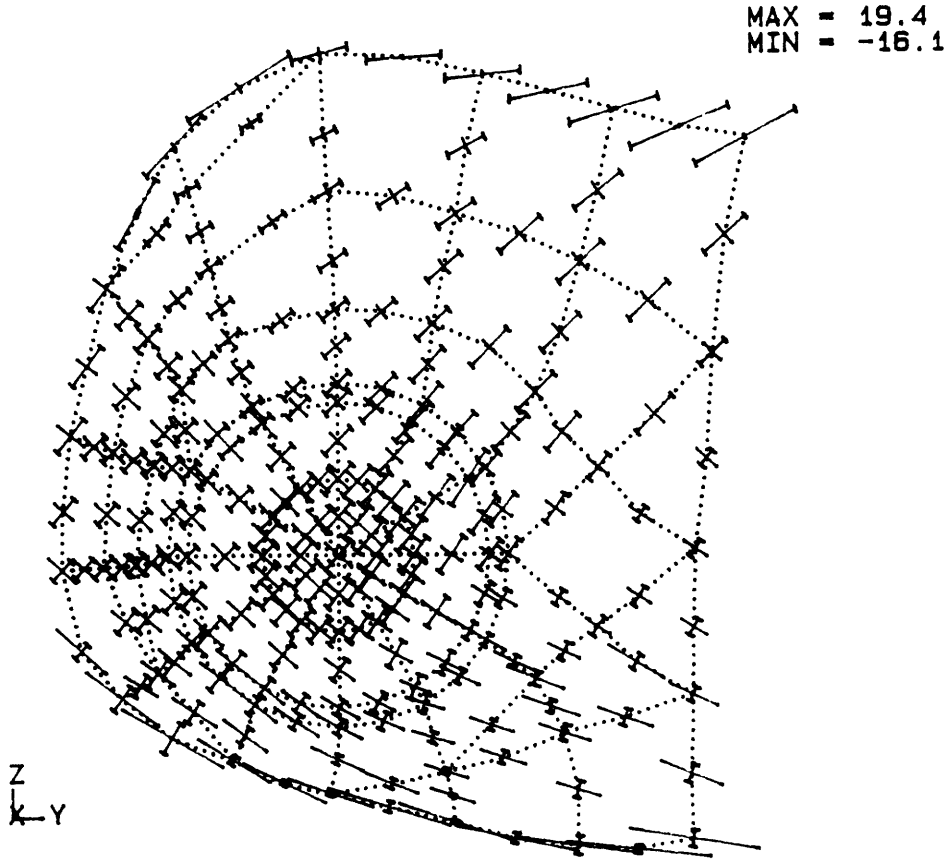

Figure 3.38a: Principal stress vectors on an enlarged view of control specimen C1 (MPa).

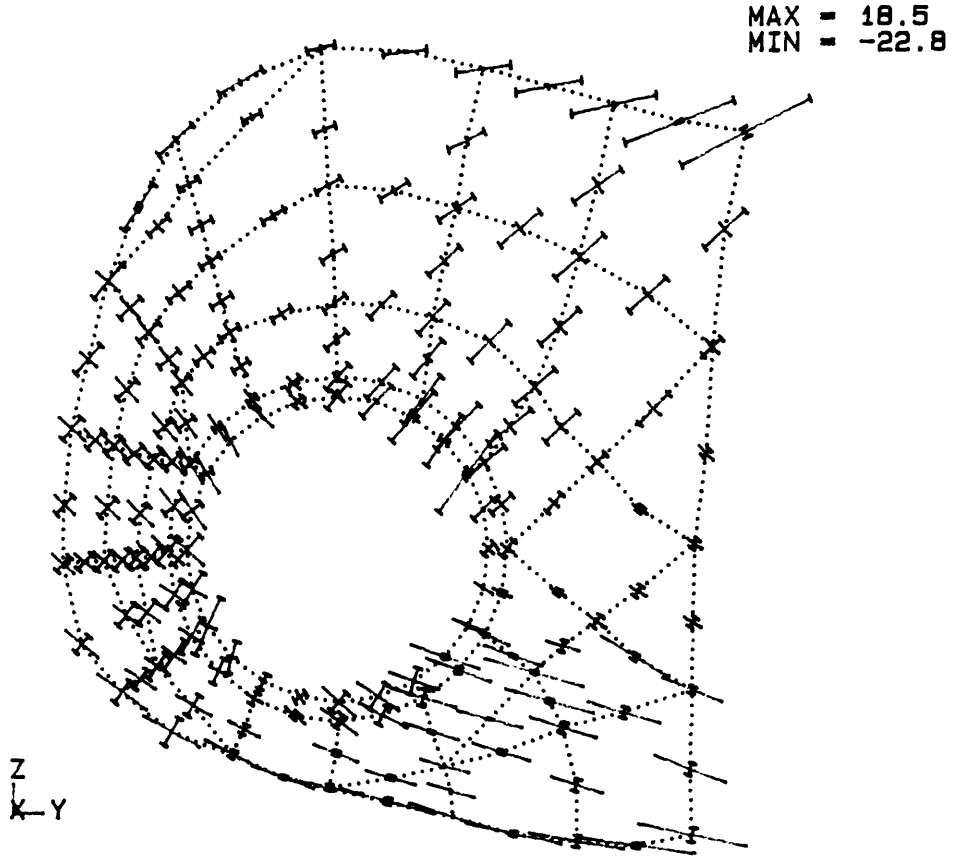

Figure 3.38b: Principal stress vectors on an enlarged view of experimental specimen C1 (MPa).

vectors around the implant in experimental specimen C1 are shown in Figure 3.38b. The stresses were significantly altered immediately adjacent to the implant, with some areas displaying higher magnitude stresses and other areas displaying lower magnitude stresses than in the corresponding areas of the control specimens. The stresses were markedly lower at around 7 o'clock, using a clock reference system for the implant, and markedly higher at around 2 o'clock. This was confirmed by comparison of the von Mises effective stress contours for the control and experimental specimens (Figure 3.39). The highest stresses adjacent to the implant occurred at about 9 and 2 o'clock and the lowest stresses occurred at about 7 and 12 o'clock. The ratio of the von Mises stress in the experimental specimen to the von Mises stress in the control specimen ranged from a high of 1.53, at 2 o'clock, to a low of 0.45, at 7 o'clock.

The highest stress gradients occurred adjacent to the cortical shell in several locations in the control specimen. The corresponding gradients were less severe in the experimental specimen due to the higher bone densities in these regions. The higher trabecular bone densities reduced the material property gradient between the cortical shell and the adjacent trabecular bone.

The principal stress vectors in the vicinity of the implant for the other three specimens are shown in Figures 3.40 to 3.42. In general, the orientation of the principal stresses was similar for all specimens. The differences between the specimens were due to the different implant locations. There was a greater extent of tensile stresses in the

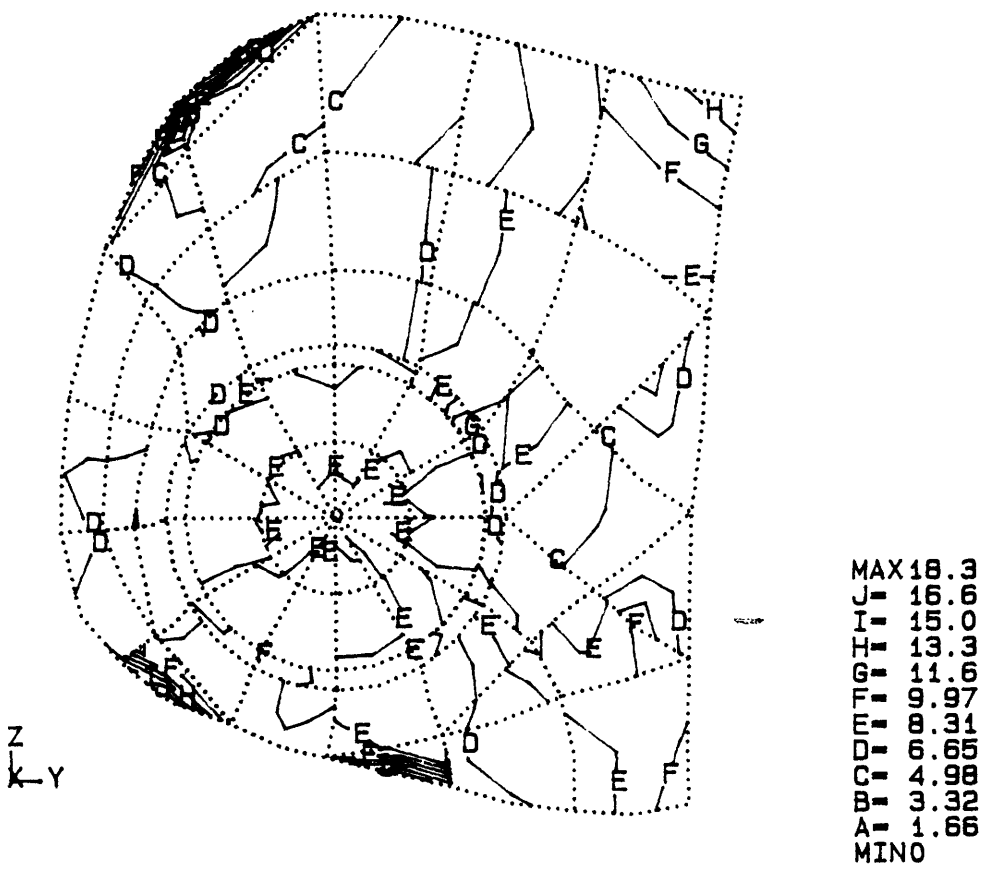

Figure 3.39a: Von Mises stress contours on an enlarged view on control specimen C1 (MPa).

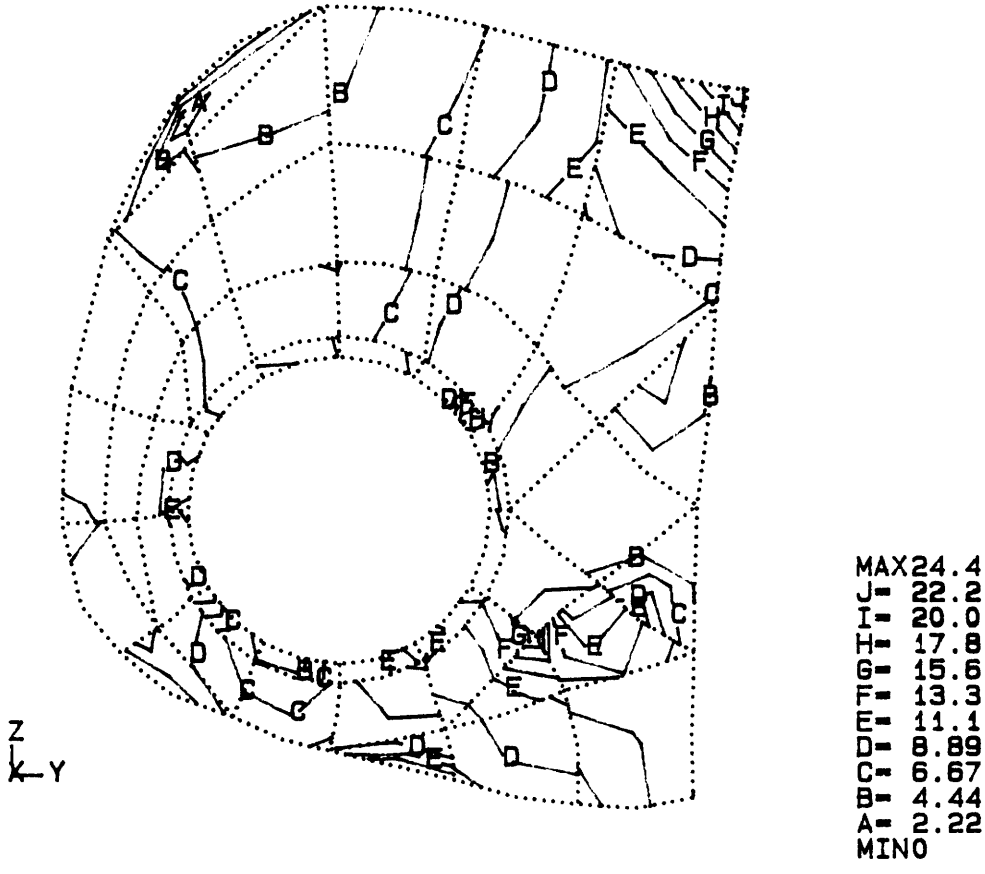

Figure 3.39b: Von Mises stress contours on an enlarged view on experimental specimen C1 (MPa).

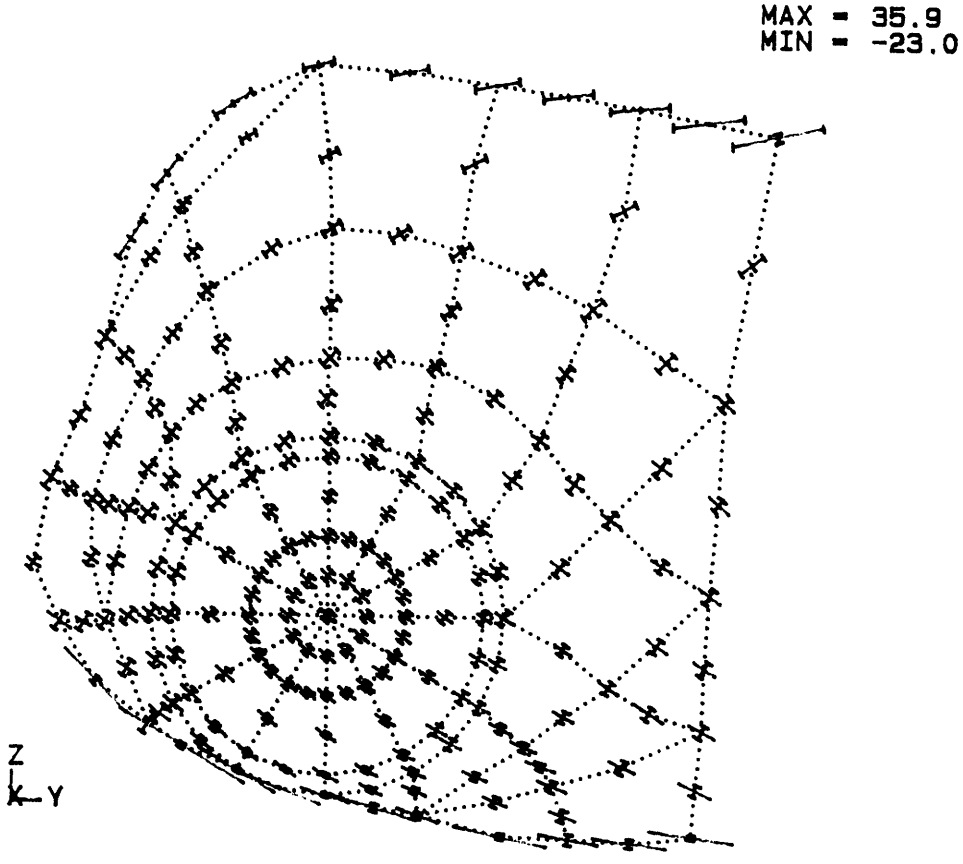

Figure 3.40a: Principal stress vectors on an enlarged view of control specimen C2 (MPa).

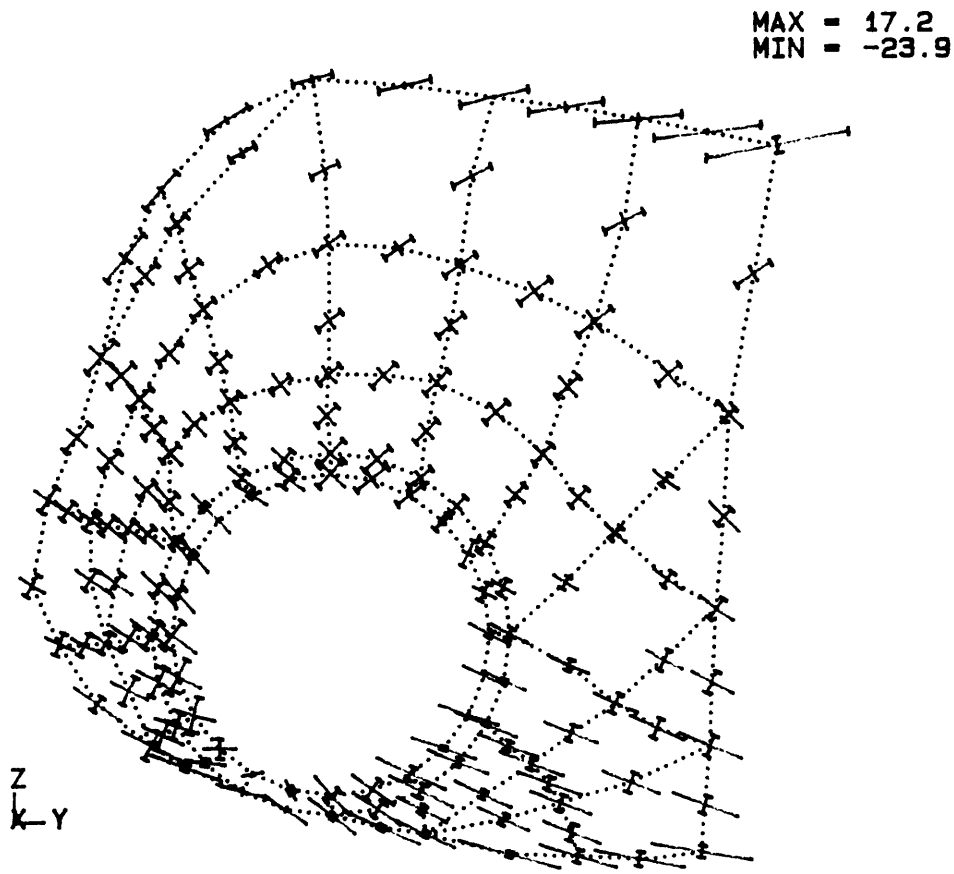

Figure 3.40b: Principal stress vectors on an enlarged view of experimental specimen C2 (MPa).

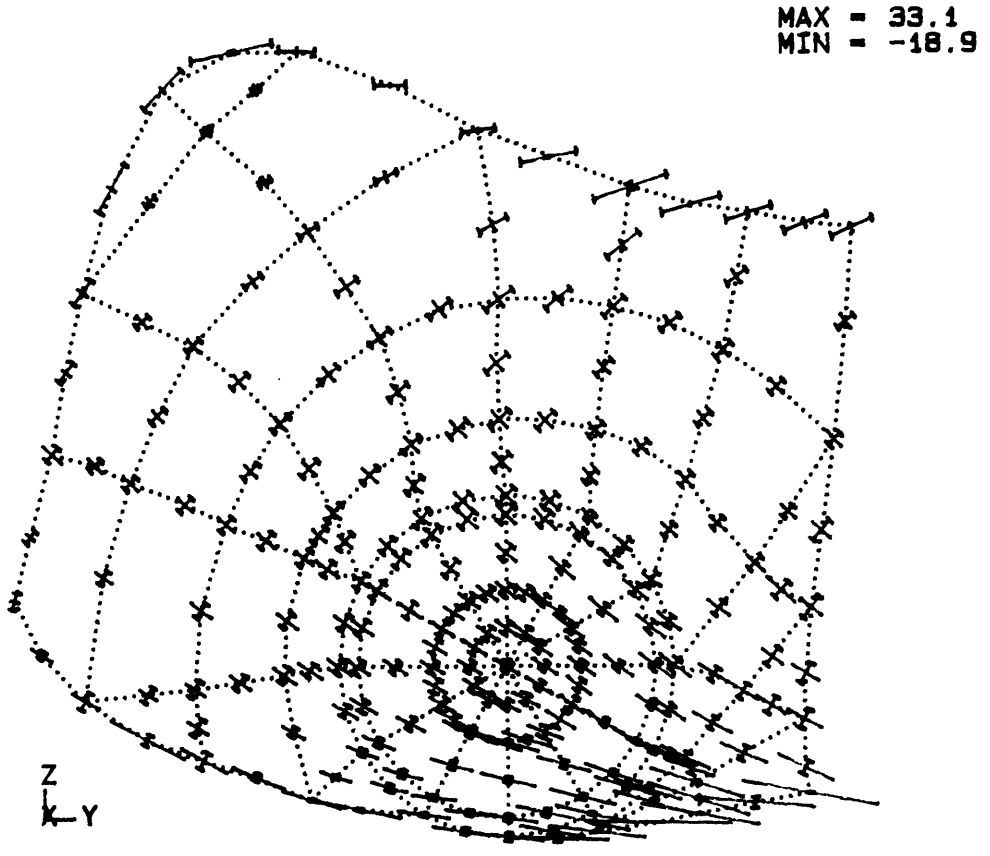

Figure 3.41a: Principal stress vectors on an enlarged view of control specimen C3 (MPa).

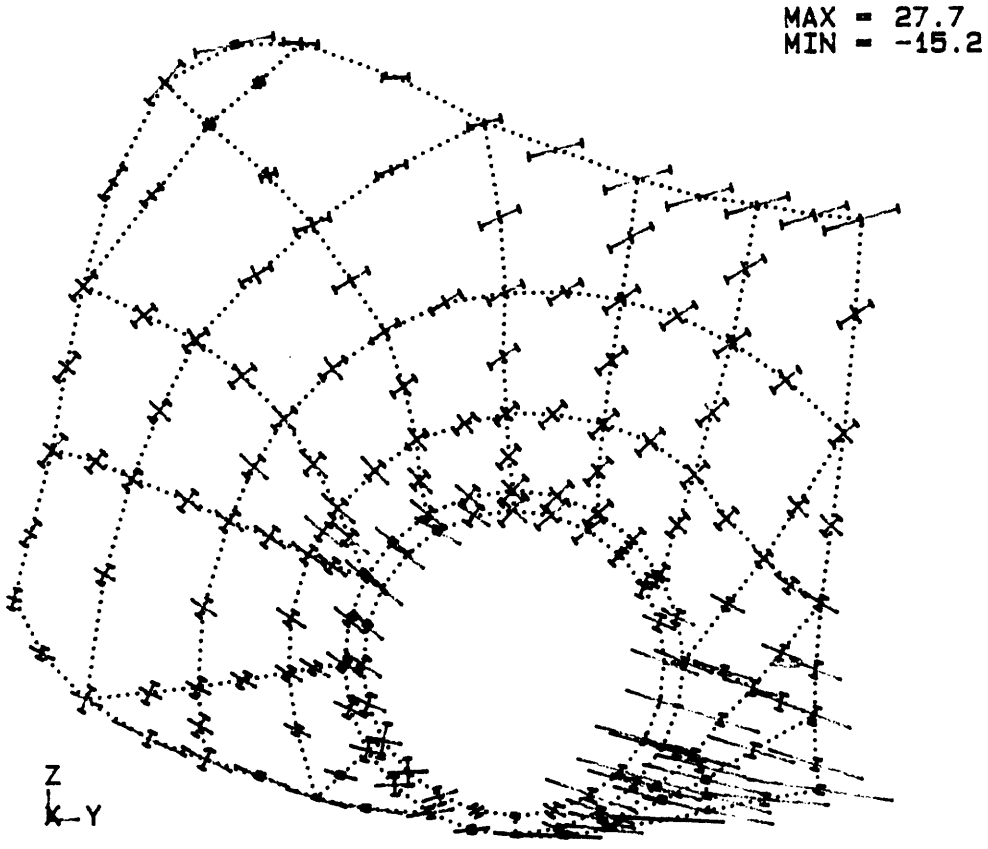

Figure 3.41b: Principal stress vectors on an enlarged view of experimental specimen C3 (MPa).

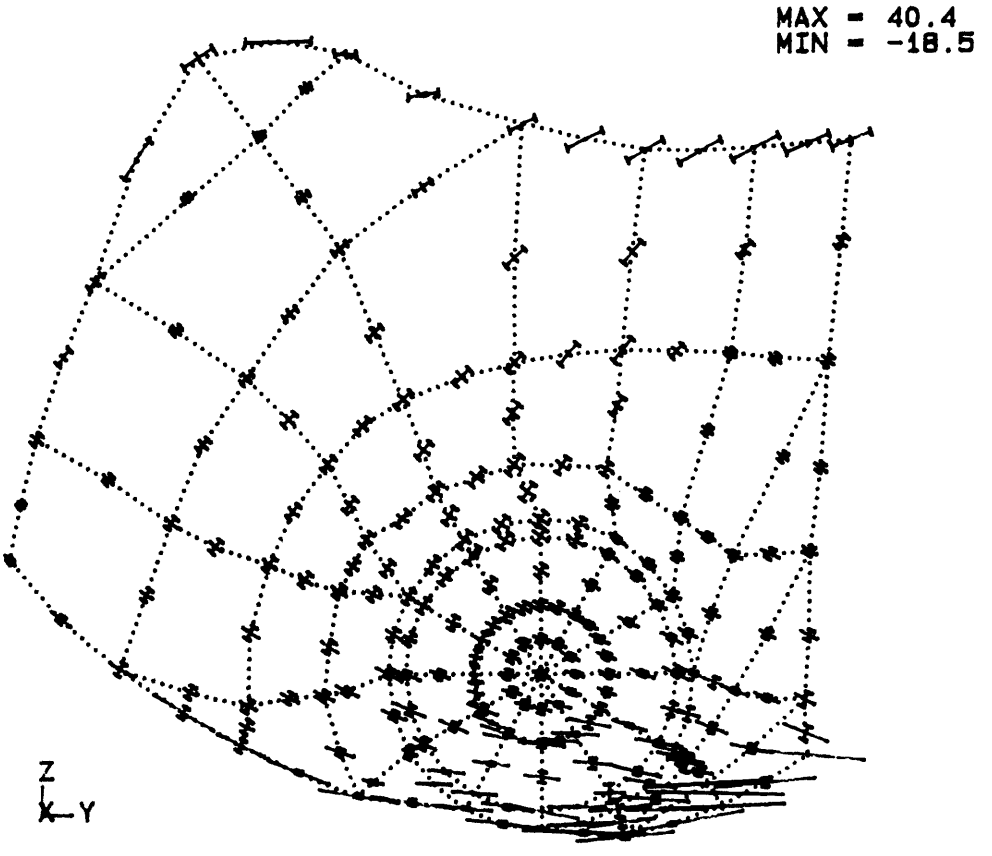

Figure 3.42a: Principal stress vectors on an enlarged view of control specimen C4 (MPa).

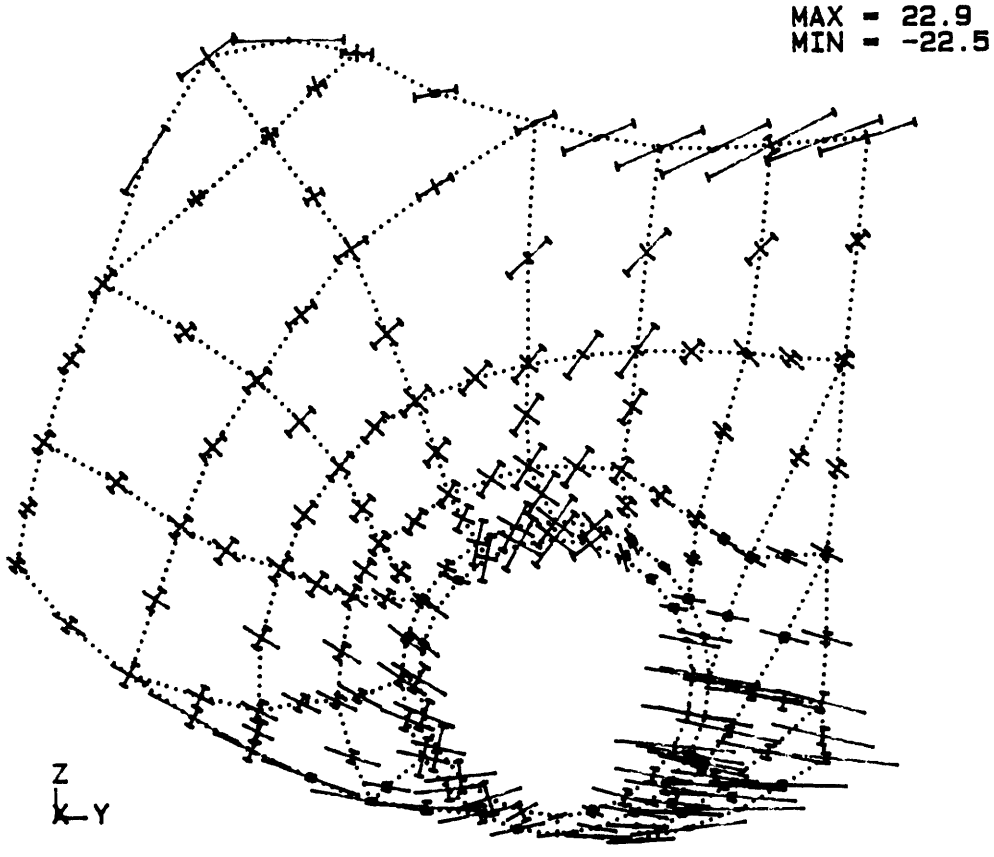

Figure 3.42b: Principal stress vectors on an enlarged view of experimental specimen C4 (MPa).

vicinity of the implants in specimens C3 and C4 due to the more posterior and distal position of the implants.

The von Mises stress contours for specimens C2, C3, and C4 are shown in Figures 3.43 to 3.45. All experimental specimens displayed both increased and decreased stresses, relative to the control specimens, at various locations around the implants. In summary, the rigid implants tightly coupled to the trabecular bone resulted in stress magnitudes ranging from approximately 50 % to 150 % of the stresses in the corresponding locations in the control specimens.

To further examine the influence of the implants on the stresses in the surrounding trabecular bone, the principal stress orientation in the experimental specimens were plotted as a function of the principal stress orientation in the control specimens (Figure 3.46). The angle of orientation in this graph was that of the principal stress which was maximum in absolute magnitude. The data points correspond to the interpolated stress values at the locations of available morphologic data. The lines $Y = X + 90$ and $Y = X - 90$ are included to indicate the possible range of data. For data points on the line $Y = X$ there was no change in the maximum principal stress orientation resulting from the implant. The changes in orientation were generally small, with most points lying within 5 to 10 degrees of the line $Y = X$. Four points lie near the lines $Y = X + 90$ and $Y = X - 90$ indicating that the maximum principal stress changed from tension to compression or vice versa. In comparison to the measured changes in the trabecular orientation (see Figure 3.21), the predicted changes in the principal stress orientation

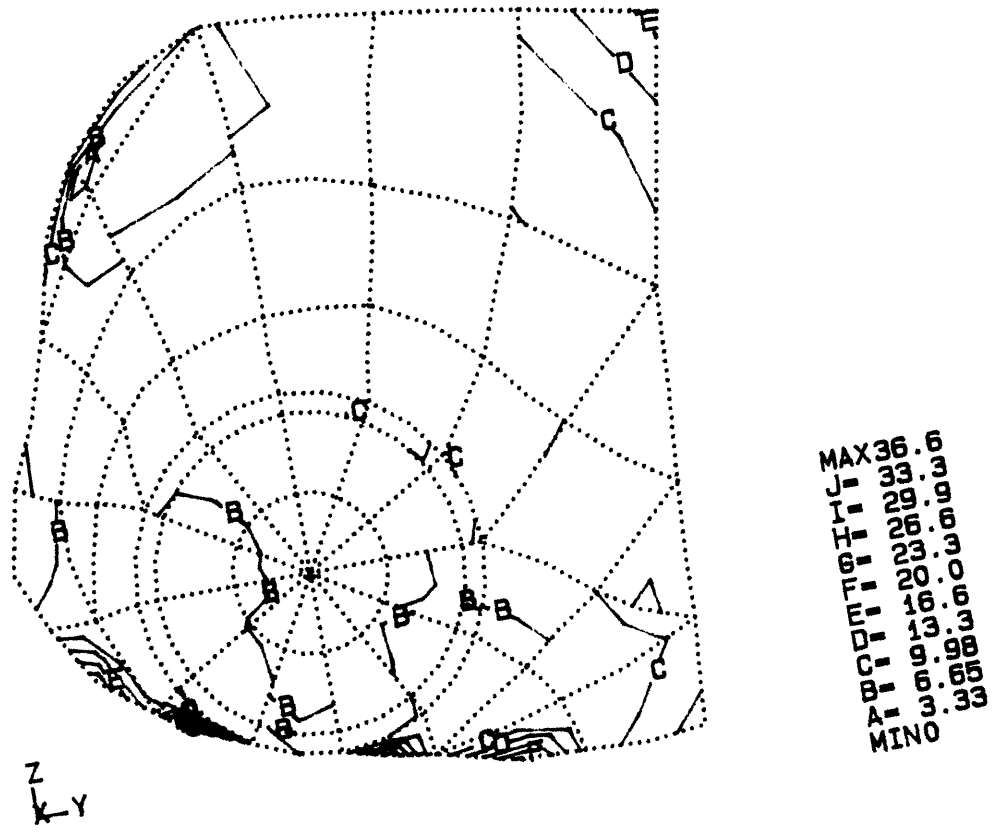

Figure 3.43a: Von Mises stress contours on an enlarged view of control specimen C2 (MPa).

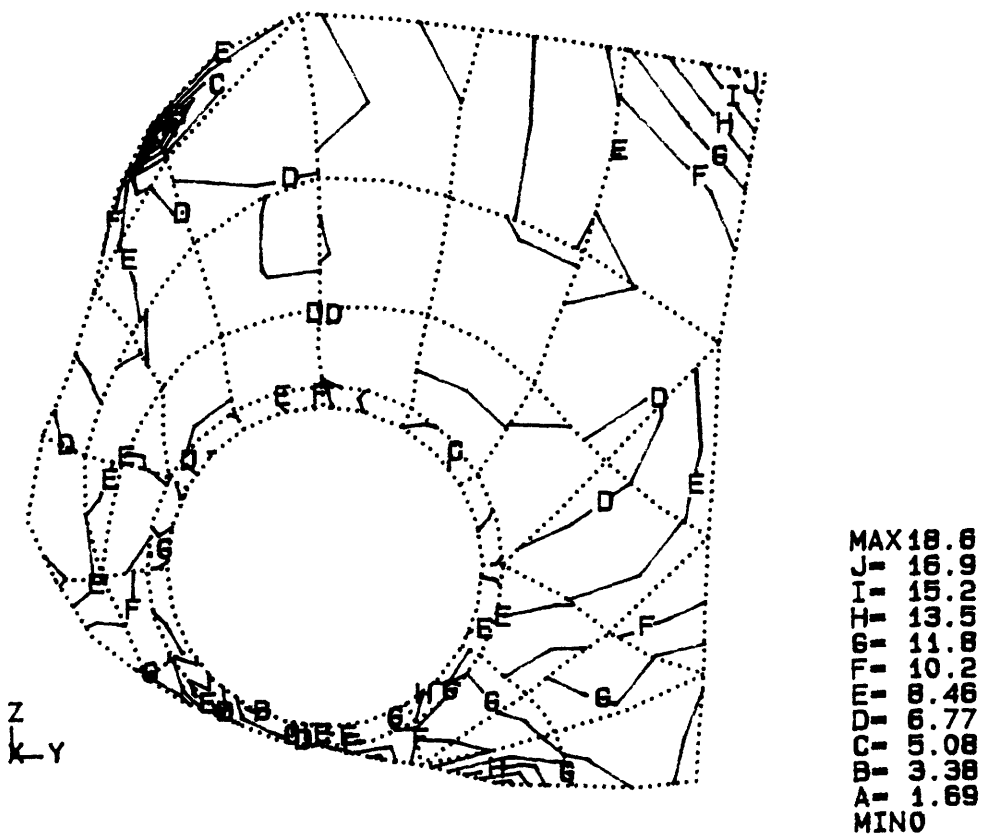

Figure 3.43b: Von Mises stress contours on an enlarged view of experimental specimen C2 (MPa).

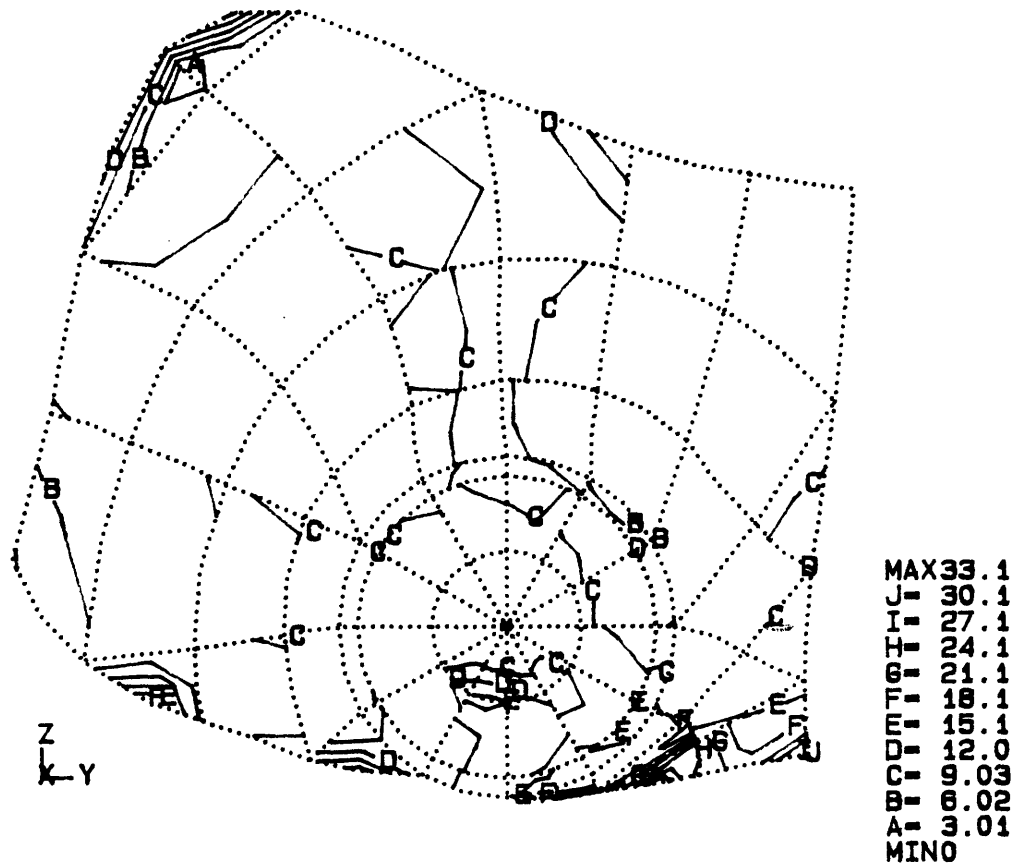

Figure 3.44a: Von Mises stress contours on an enlarged view of control specimen C3 (MPa).

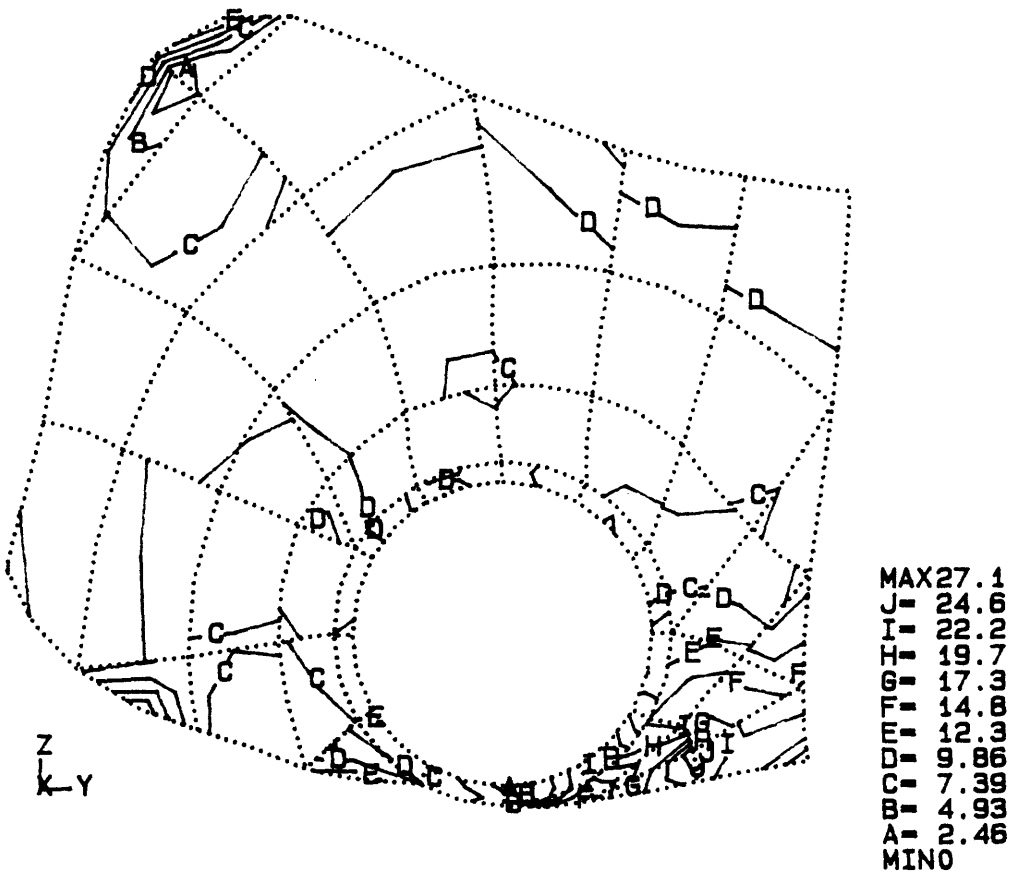

Figure 3.44b: Von Mises stress contours on an enlarged view of experimental specimen C3 (MPa).

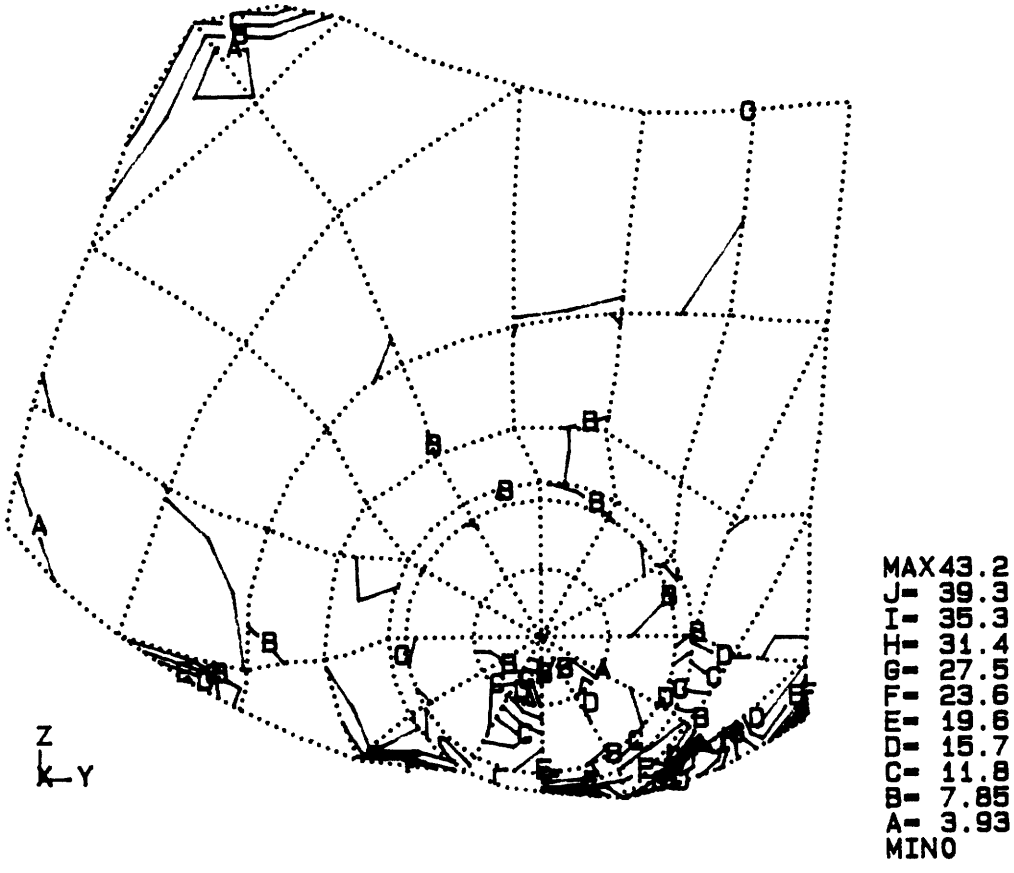

Figure 3.45a: Von Mises stress contours on an enlarged view of control specimen C4 (MPa).

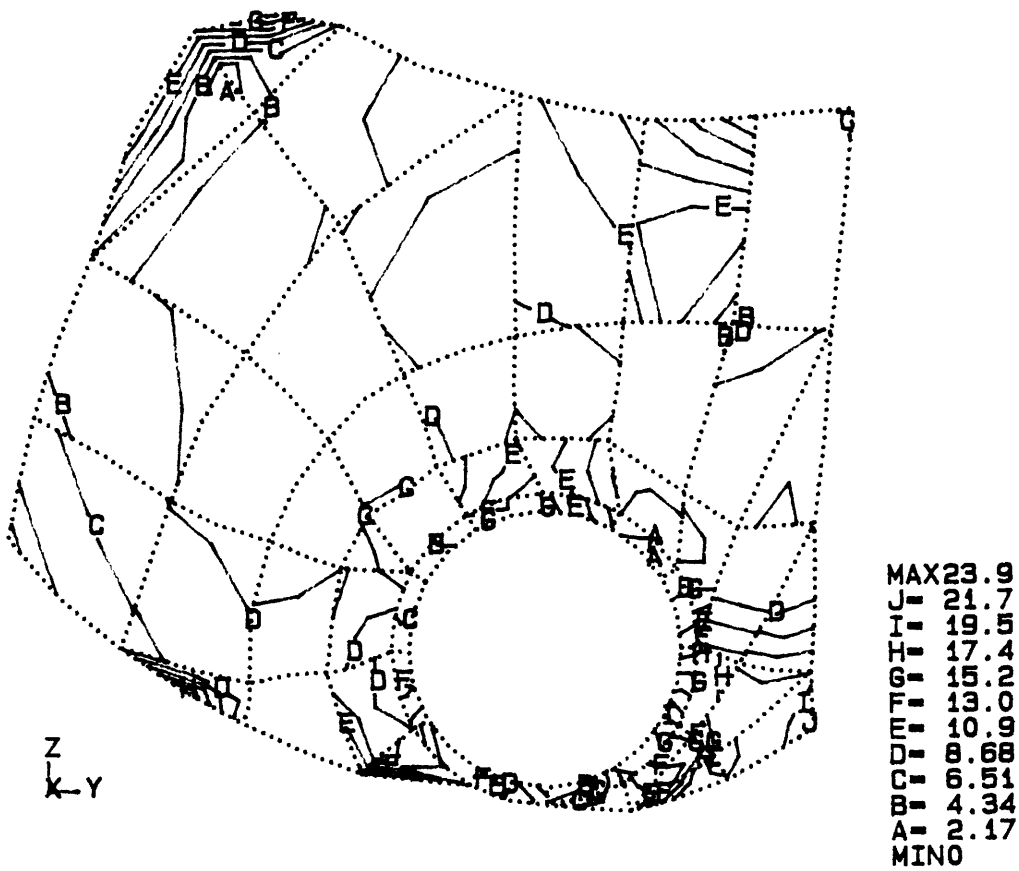

Figure 3.45b: Von Mises stress contours on an enlarged view of experimental specimen C4 (MPa).

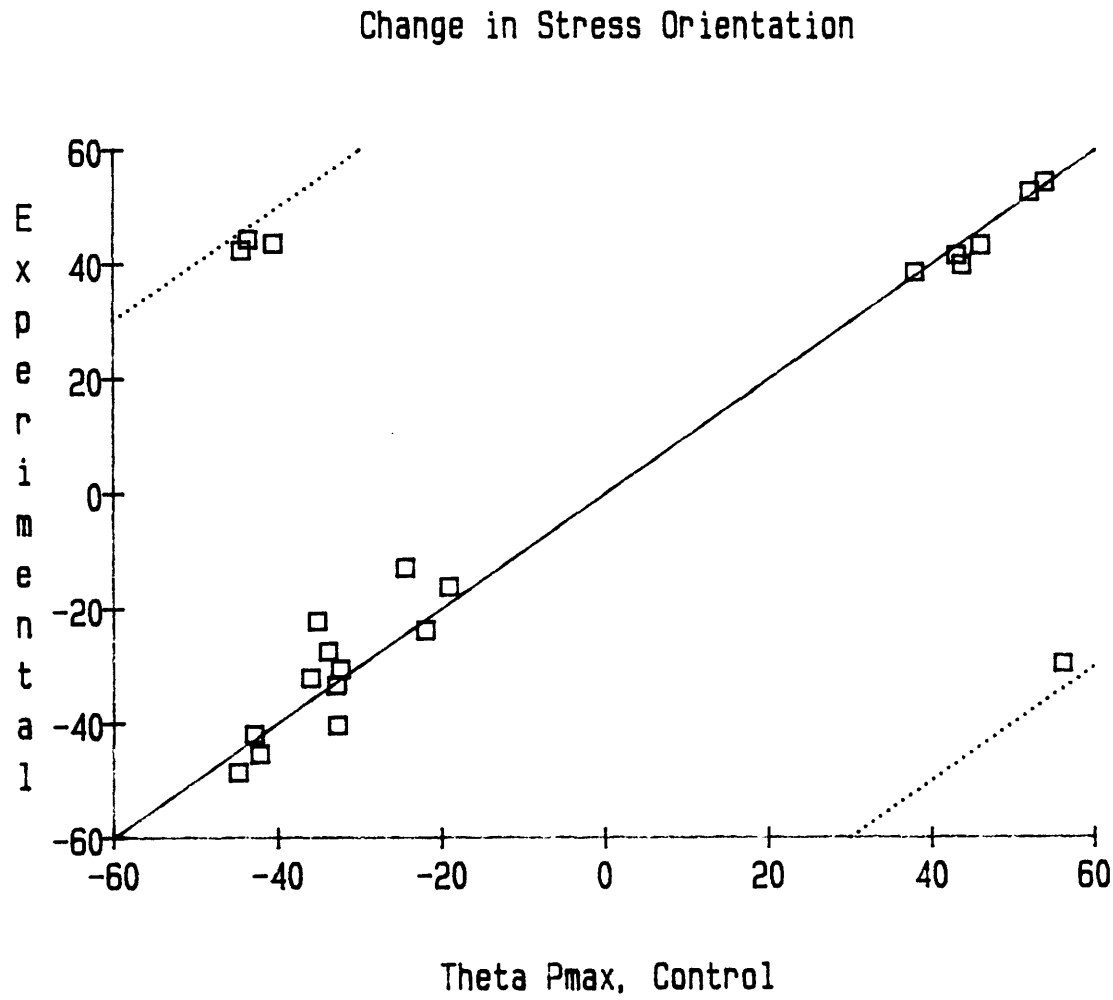

Figure 3.46: The maximum principal stress direction in the experimental calcanei as a function of the maximum principal stress direction in the corresponding regions in the control calcanei.

were small.

The von Mises stresses were similarly plotted for the experimental specimens as a function of the von Mises stresses in the control specimens (Figure 3.47). Again, the line Y = X was included to indicate those data points for which there was no difference between the experimental and control data. More points lie above this line than below, indicating that the stresses were more often increased than decreased due to the presence of the implants.

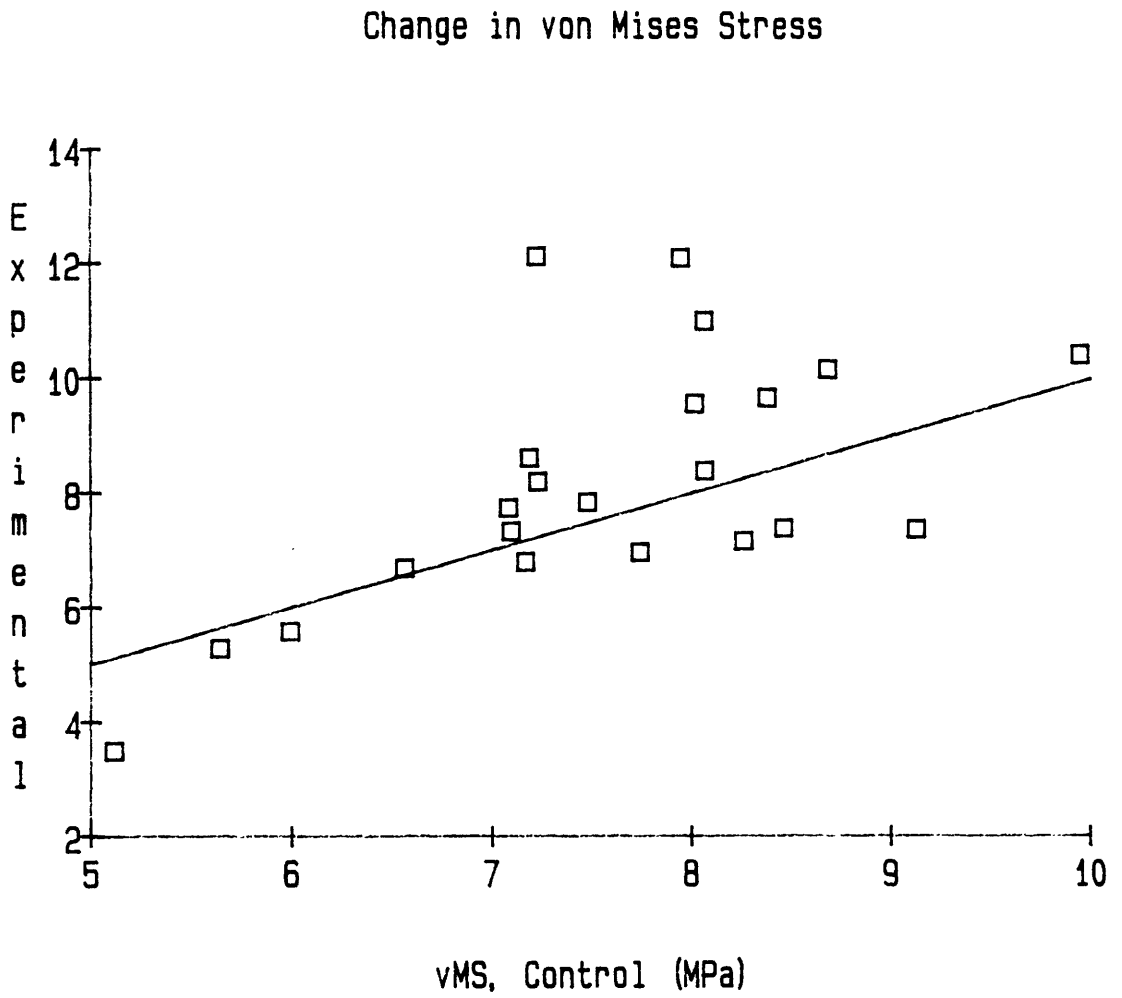

Figure 3.47: The von Mises stress in the experimental calcanei as a function of the von Mises stress in the corresponding regions in the control patellae.

3.3 Stress-Morphology Relationships

To assess the accuracy of the finite element model predictions, the orientation of the principal stresses were compared to the orientation of the material anisotropy ellipses for the control specimens. The critical assumption was that the trajectorial theory of trabecular bone architecture holds for the specimens which did not receive implants. This theory states that, under homeostatic conditions, the principal material axes of the trabecular bone are aligned with the principal stress axes.

One aspect of this theory which requires detailed examination is the dependence of the alignment on the nature of the stress state. For stress conditions approaching uniaxial tension or uniaxial compression, it is reasonable to assume that the material will align with the maximum principal stress, namely tension or compression, respectively. However, for stress conditions which approach hydrostatic tension or compression, or pure shear, the expected relationship between the material axes and the principal stress axes is less clear. For hydrostatic tension or compression, a random architecture is expected with no direction of preferred orientation. As shown in Section 3.2.1, a hydrostatic stress state did not occur in the present models, and is probably uncommon in bone under physiologic conditions. Of greater relevance is the state of pure shear which, in two-dimensions, was approached for some locations in the present models. For pure shear, an architecture with crossing trabeculae is expected, with trabecular struts oriented in both the directions of principal tensile stress and principal compressive stress

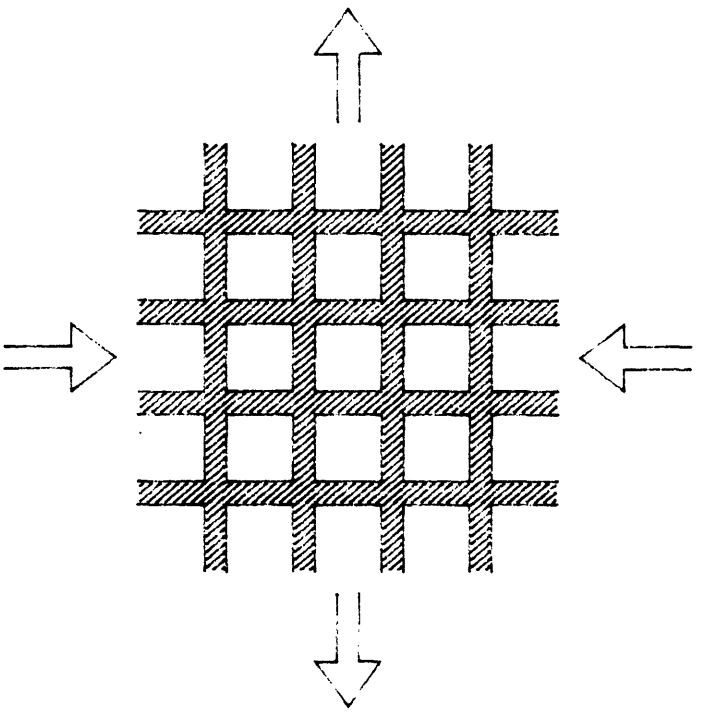

Optimal structure for pure shear has an isotropic material ellipse

Figure 3.48: The optimal structure based on a minimum weight criterion for a stress state of pure shear (see also Hayes et al. 1982).

(Figure 3.48; see also Hayes et al. 1982). However, using the present stereologic methods, this architecture appears isotropic, and cannot be distinguished from a random architecture with no direction of preferred orientation. Furthermore, the adaptive remodeling response to tension and compression may differ, resulting in a weakly oriented structure in either the direction of principal tensile stress or principal compressive stress. In the case of a weakly oriented structure, it is expected that the stereologic predictions for the direction of material orientation will be less accurate and therefore result in poorer correlations with the directions of principal stress.

A useful parameter for examining these issues is the eccentricity of the anisotropy ellipse and the eccentricity of the stress ellipse. The eccentricity of the anisotropy ellipse is defined as:

$$E_A = \frac{\sqrt{d_1^2 - d_2^2}}{d_1} \tag{3.3}$$

where d_1 is the major axis and d_2 is the minor axis. These terms come from the two-dimensional equivalent of Equation 2.68. For an isotropic material, $d_1 = d_2$, and thus $E_A = 0$. As the material approaches a perfectly oriented structure, E_A approaches 1. Similarly, the eccentricity of the stress ellipse is defined as:

$$E_S = \frac{\sqrt{P_1^2 - P_2^2}}{P_1} \qquad \text{if } |P_1| \geq |P_2| \tag{3.4}$$

$$E_S = \frac{\sqrt{P_2^2 - P_1^2}}{P_2} \qquad \text{otherwise.} \qquad (3.5)$$

where P_1 and P_2 are the principal stresses ($P_1 \geq P_2$). An important distinction between E_A and E_S is that E_A ranges from zero to one while E_S ranges from minus one (for uniaxial compression) to plus one (for uniaxial tension). E_S is equal to zero for hydrostatic tension, hydrostatic compression, or pure shear.

After validation of the models of the control specimens, the stress-morphology relations for implant-induced remodeling were studied using the models of the experimental specimens. The critical assumption was that the finite element predictions were accurate based on the validation of the models of the control specimens. The most critical examination of the stress-morphology relationships was then performed by relating the changes in the predicted stress fields to the changes in the measured morphology, as reflected by the differences between paired locations from the control and experimental specimens.

3.3.1 Model Validation

Equine Patella

The present objective was to validate the finite element predictions based on the assumption that the trajectorial theory of trabecular bone architecture holds for the control patellae. The correspondence between

the principal stress directions and the principal material directions for the control patellae is shown in Figures 3.49 and 3.50. The maximum principal stress (Θ_{PM}) is defined as the principal stress which was maximum in absolute magnitude. In Figure 3.49, the direction of the principal stress component which agreed most closely with the principal material direction (Θ_{PO}) is shown as a function of the principal material direction (Θ_{A1}). In Figure 3.50, the direction of the maximum principal stress is shown as a function of the principal material direction. For 60 out of 71 locations, the maximum principal stress was, in fact, the principal stress component which best aligned with the principal material direction. In other words, the difference between the direction of the maximum principal stress and the direction of the principal material orientation was less than or equal to 45 degrees. In equation form, when $|\Theta_{PM} - \Theta_{A1}| \leq 45_o$, $\Theta_{PO} = \Theta_{PM}$.

A linear regression was performed on Θ_{PO} as a function of Θ_{A1}. The direction of the principal material orientation was chosen as the independent variable since this was a measured parameter, whereas the directions of principal stress were predicted by the finite element models. The first assumption for this regression was that the values of the principal material orientations were fixed. In other words, the stereologic measurement of the principal material orientation was exact. This assumption can be tested through validation experiments of the stereologic system, and in fact, for the system used, such experiments have been carried out (Snyder et al. 1986). The second assumption was that, for each principal material orientation, there was a population of principal stress orientations predicted by the finite element models

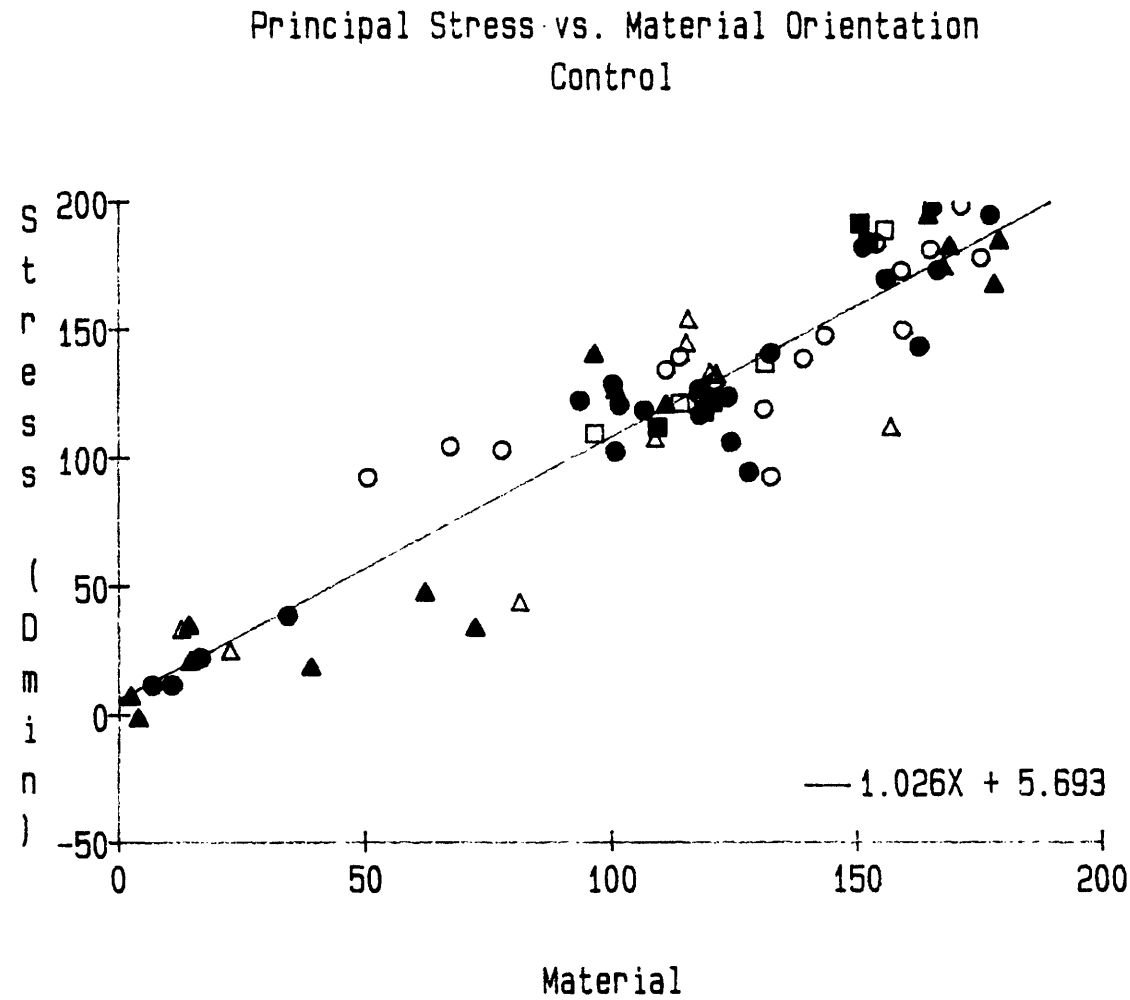

Figure 3.49: The principal stress direction which best aligned with the principal material direction (Θ_{P0}) as a function of the principal material direction (Θ_{A1}) for the control patellae. See Figure 3.8 for Key.

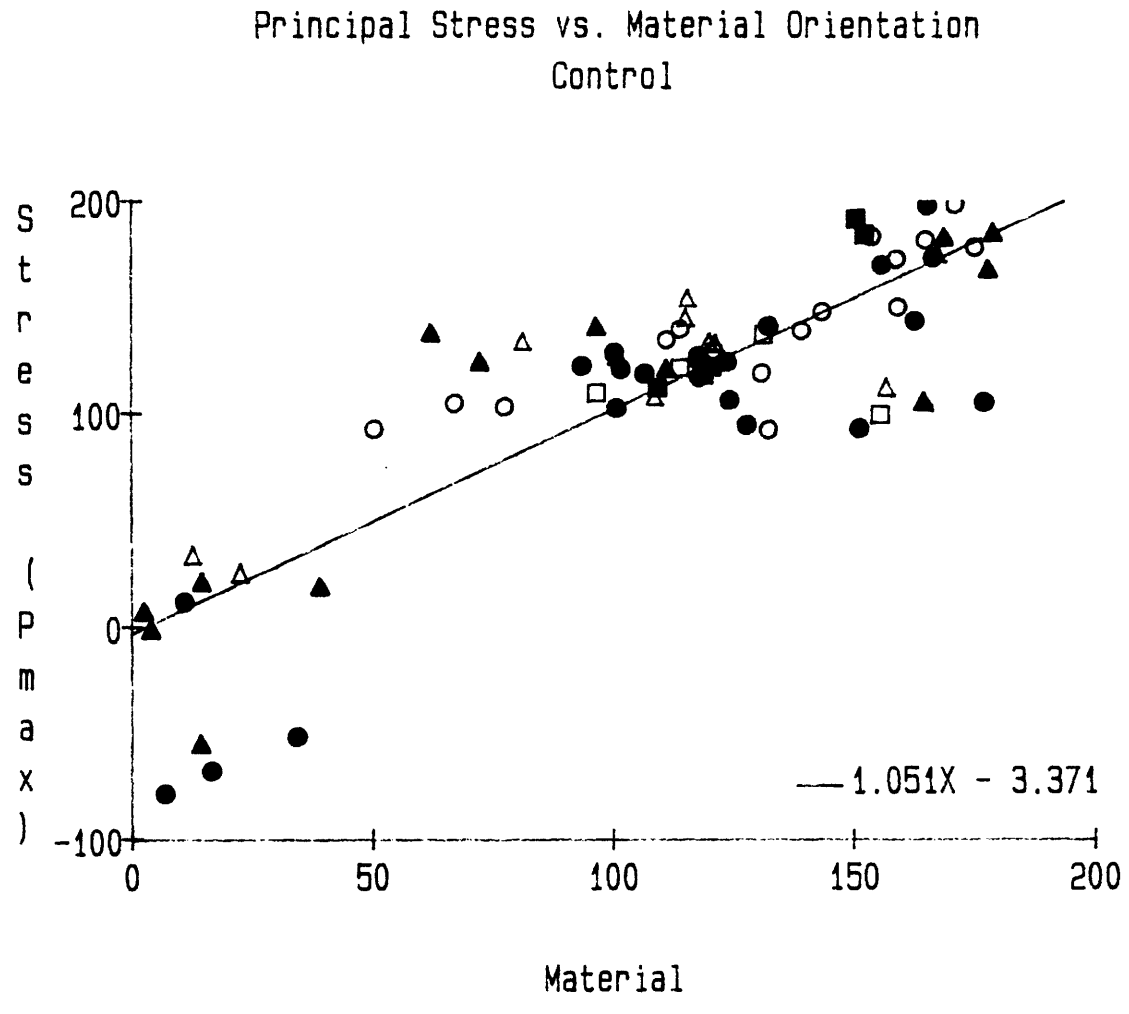

Figure 3.50: The maximum principal stress direction (Θ_{PM}) as a function of the principal material direction (Θ_{A1}) for the control patellae. See Figure 3.8 for Key.

which had a normal distribution. Furthermore, the variance of this population was the same for each principal material orientation. This assumption could not be tested using the present data due to an insufficient number of data points. However, this is not an unreasonable assumption for the predicted principal stress orientations since there is no obvious inherent reason for these orientations to err in any particular direction or by any particular amount. However, the assumption of a normal distribution cannot strictly hold because the range of data is limited to a 45 degree deviation from the line $\Theta_{PO} = \Theta_{A1}$. This point is discussed further below. The most critical assumption underlying this regression was that the trajectorial theory of trabecular bone architecture holds for the control patellae. More specifically, for a particular stress condition, known exactly, the principal material direction, measured using stereology, was invariant, and that these directions corresponded exactly. This appeared to be a reasonable assumption based from the literature on this subject (see Section 1.2.1). This assumption is discussed further in Section 4.0.

The best fit line from the linear regression on Θ_{PO} and Θ_{A1} is shown in Figure 3.49. The statistical data are summarized in Table 3.3. The intercept had a p-value of 0.32 and standard deviation of 5.79 degrees, indicating that the intercept of 5.69 degrees was not significant. The slope had a p-value of 0.0001 and a standard deviation of 0.048, indicating that the slope was not significantly different from 1.0. The regression had a p-value of 0.0001, standard deviation of 20.09 degrees, and an R^2 of 0.87. In other words, 87 % of the variation of the principal stress direction could be explained by the variation of the

Table 3.3

Linear Regression for Model Validation
Equine Patella

	Slope			Intercept			Regression		
	Value	SD	Sig	Value	SD	Sig	SD	Sig	R^2
Θ_{PO} vs Θ_{A1}	1.026	0.048	.0001	5.693	5.790	0.330	20.09	.0001	0.870
Θ_{PM} vs Θ_{A1}	1.051	0.080	.0001	-3.371	9.730	0.730	33.74	.0001	0.714

principal material direction.

While an R^2 of 0.87 is encouraging, the standard deviation of the regression must be examined critically. If the comparison were made on the direction of the maximum principal stress and the direction of the principal material orientation, then the maximum possible difference for any data pair would be 90 degrees. If this difference were greater than 90 degrees, the direction of either parameter could be changed by 180 degrees thus decreasing this difference. However, the regression was performed using the principal stress direction which corresponded more closely to the principal material direction. Therefore, the maximum possible difference for each data pair, and thus the maximum possible deviation from the line $\Theta_{PO} = \Theta_{A1}$, is 45 degrees. The standard deviation of 20.1 degrees indicates that 68 % of the data points were within 20.1 degrees of the best fit line, assuming a normal distribution about this line. If these data were random, 50 % of the data points would lie within 22.5 degrees of the line $\Theta_{PO} = \Theta_{A1}$, or 68 % within 30.6 degrees.

A stronger argument for the validity of the finite element model predictions may be made by using the maximum principal stress directions for the linear regression (Figure 3.50). As mentioned above, for 60 out of 71 data points, the principal stress direction which agreed most closely with the principal material direction was the principal stress which was maximum in absolute magnitude. The results of the linear regression between the maximum principal stress direction and the principal material direction are also given in Table 3.3. If these data

were random, 50 % of the data points would lie within 45 degrees of the line $\Theta_{PM} = \Theta_{A1}$, and 68 % of the data points would lie within 61.2 degrees. The standard deviation of the regression, equal to 33.7 degrees, is much less then 61.2 degrees, indicating that the data were not random.

As mentioned above, the degree of correspondence between the principal stress and material directions may be a function of the nature of the stress field. To examine this concept, the degree of alignment is shown graphically as a function of the eccentricity of the stress ellipse in Figure 3.51. The Y axis represents the absolute difference between the maximum principal stress direction (Θ_{PM}) and the principal material direction (Θ_{A1}). A negative eccentricity indicates that the maximum principal stress was compressive whereas a positive eccentricity indicates that the maximum principal stress was tensile. The data points for which the maximum principal stress was not the stress which best aligned with the principal material direction ($\Theta_{PM} \neq \Theta_{PO}$) are highlighted using filled circles. All eleven of these data points had a stress eccentricity of less then zero, indicating that compression was the dominant stress. It is particularly striking that, despite fewer data points, the alignment between the maximum principal stress direction and the principal material direction in regions where tension predominated was considerably better than in regions where compression predominated. Furthermore, for the eleven data points where $\Theta_{PM} \neq \Theta_{PO}$, the tensile principal stress aligned more closely to the principal material direction than the compressive principal stress. This suggests that either the trabeculae tended to align with the direction of the

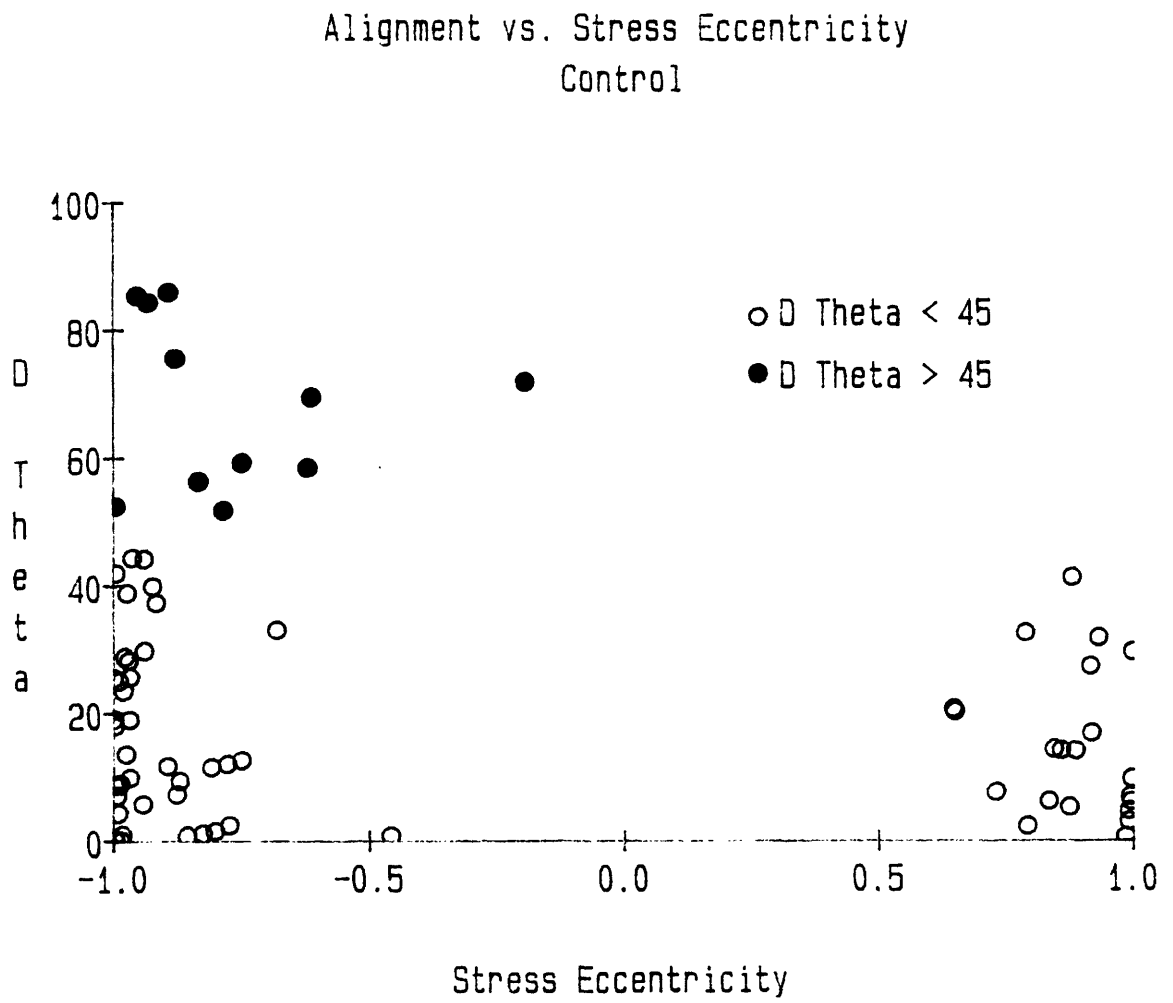

Figure 3.51: The absolute difference between the maximum principal stress direction and the principal material direction ($|\Theta_{PM} - \Theta_{A1}|$) as function of the eccentricity of the stress ellipse for the control patellae.

principal tensile stress or, alternatively, that the trabeculae tended to align at 90 degrees to the direction of the principal compressive stress. The latter hypothesis was supported by the several data points which were very close to 90 degrees and had a stress eccentricity very close to -1 (indicating that the stress state was near uniaxial compression). This point is discussed further in Section 4.0.

To further examine the relationship between the alignment of the principal stresses with the material axes, the stress eccentricity is shown as a function of the material eccentricity in Figure 3.52. Again, the 11 points for which $\Theta_{PM} \neq \Theta_{PO}$ are highlighted using filled circles. Three of these data points had a material eccentricity of less than 0.5, indicating that the material in these locations was not highly anisotropic. This point is examined further below. One of these 11 data points had a stress eccentricity of about -0.2, indicating that the stress state was approaching pure shear. In general, this graph demonstrates a poor correspondence between the measured material eccentricity and the predicted stress eccentricity.

The degree of alignment between the stress and material axes was also examined as a function of the material eccentricity (Figure 3.53). It was expected that the correlation between the principal stress axes and the principal material axes would decline as the material approaches isotropy. For the 11 data points with an angle difference of greater than 45 degrees, there was a tendency for poorer alignment (higher angle difference) for lower material eccentricities. For reference, the eccentricity of the analyzed image in Figure 3.54 was 0.51. The

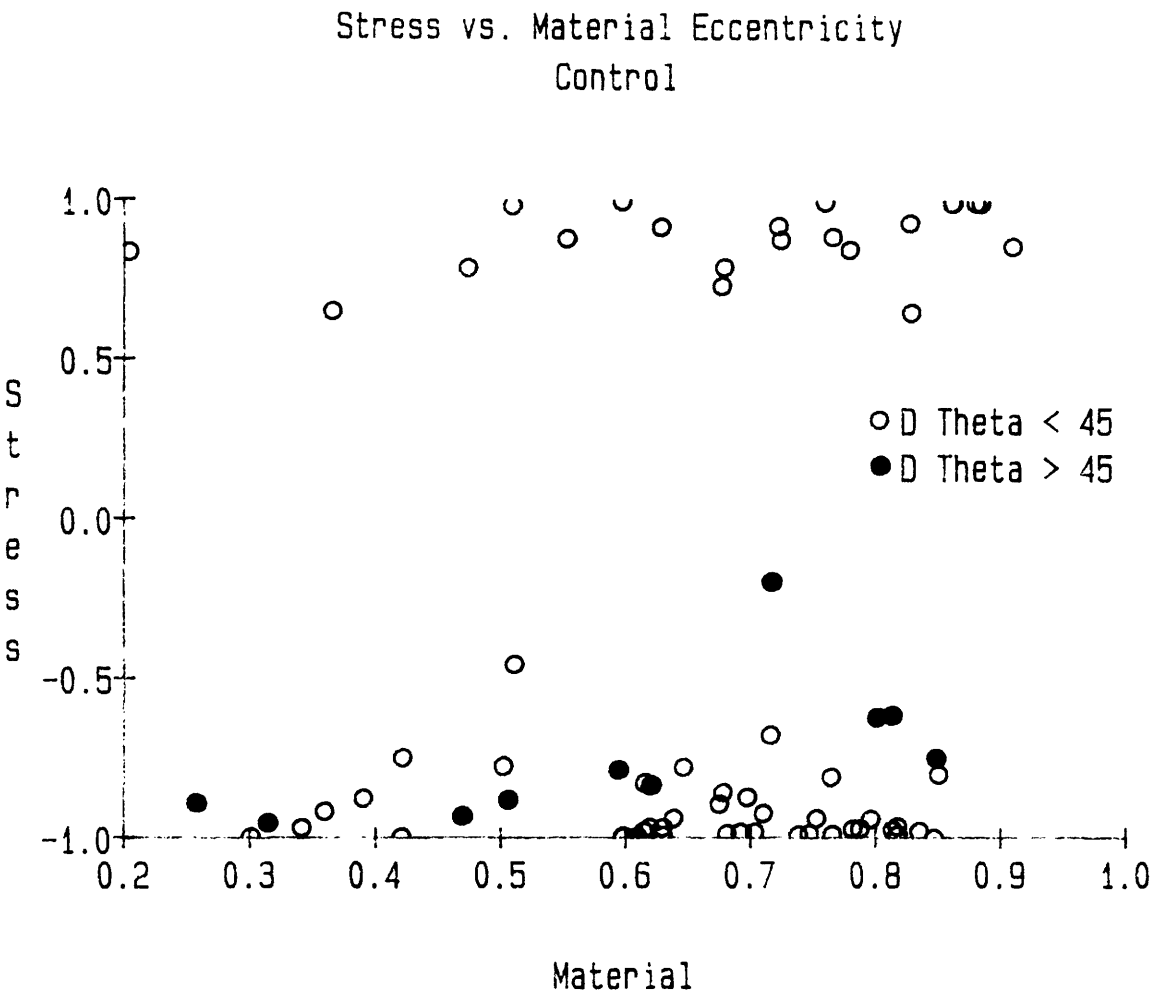

Figure 3.52: The eccentricity of the stress ellipse as a function of the eccentricity of the material ellipse for the control patellae. The points for which $|\Theta_{PM} - \Theta_{A1}| > 45$ degrees are highlighted with filled circles.

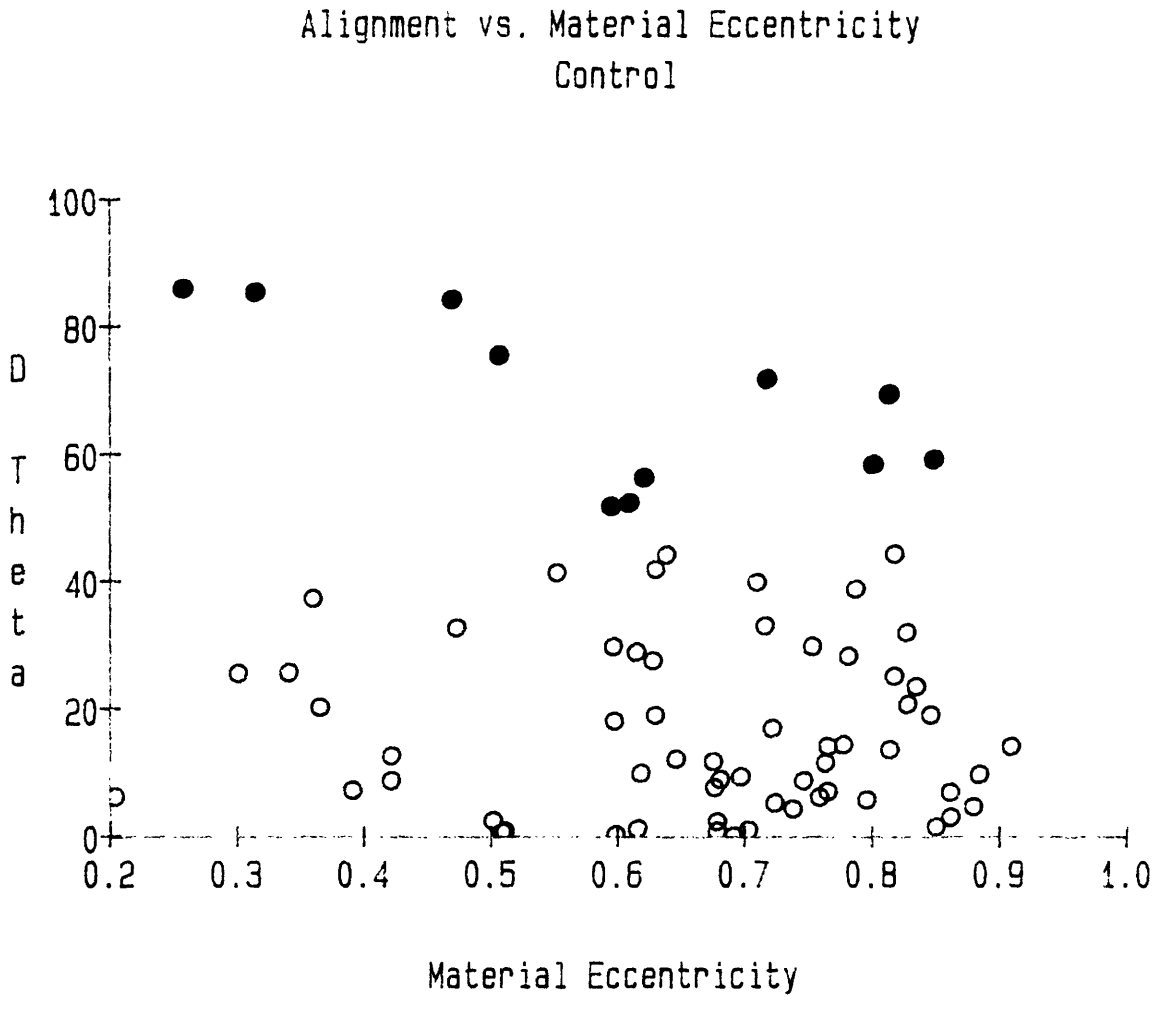

Figure 3.53: The absolute difference between the maximum principal stress direction and the principal material direction ($|\Theta_{PM} - \Theta_{A1}|$) as function of the eccentricity of the material anisotropy ellipse for the control patellae.

BETH ISRAEL HOSPITAL - IMAGE PROCESSING LABORATORY

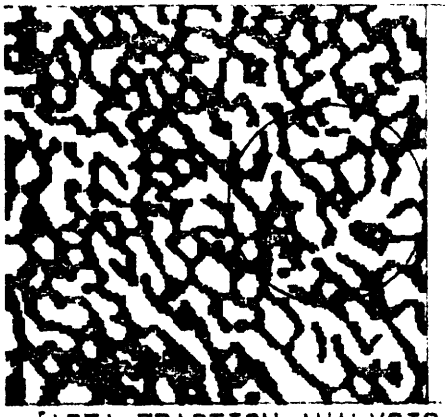

IMAGE TITLE: S4R7
COMMENT: Image 7
SUBREGION: 2
LENGTHSCALE: 57.18
GRAY THRESHOLD: 130
SOLID PHASE: BLK
TESTLINE LENGTH: 795.1
TESTLINE SPACING <PIXELS> : 1

[AREA FRACTION ANALYSIS:]
REGION AREA = 13.91

AREA FRACTION = 0.384
SOLID AREA = 5.334

[STEREOLOGY ANALYSIS:]

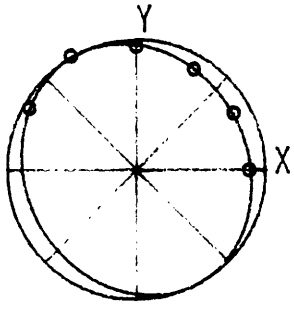

PERIMETER = 56.568
PERIM/AREA = 4.0680

ELLIPSE OF MEAN INTRCPT LENGTHS:
$A*N_1^2 + B*N_1N_2 + C*N_2^2 = MNINCPTLN^{-2}$

A = 12.39
B = 2.842
C = 10.469

CORRELATION COEFF = 0.979
MAX MN INTRCPT LNTH = 0.32084
ANGLE MAX ORIENTATION = 118 DEGS
MIN MN INTRCPT LNTH = 0.27580
ANGLE MIN ORIENTATION = 28 DEGS
EXTENT OF ANISOTROPY = 9.598 %

Figure 3.54: Stereologic analysis of region "7A" from the control specimen S3. The eccentricity of the anisotropy ellipse equals 0.51.

trabecular architecture in this example does not appear to be highly oriented. An argument could be made that there were two mutually perpendicular directions of trabecular orientation, one of which corresponds to Θ_{A1} and the second of which corresponds to Θ_{A2}, as depicted by the anisotropy ellipse. However, for trabecular bone which had a lower eccentricity than this example, and therefore approached an isotropic architecture, the significance of the directions of material orientation must be questioned. It was not surprising that the correlation between the principal stress directions and the principal material direction for less oriented trabecular bone was poor in some instances.

Finally, the degree of alignment between the stress and material axes was examined as a function of the bone area fraction (Figure 3.55). There was a weak, but not significant, tendency for better alignment with higher area fractions. This is not surprising since, as demonstrated below, the control patellae displayed a tendency for higher material eccentricities with higher area fractions (see Figure 3.66). An illustrative example from the control patella of specimen P6 is shown in Figure 3.56. The dense trabecular bone was highly oriented in a direction parallel to the cortical shell. In fact, there was no clear division between the trabecular bone and the cortical shell. The correspondence between the finite element model predictions and the measured morphology was very good in such instances. Conversely, the more isotropic trabecular bone in the control patellae tended to have lower area fractions. As a consequence, the data points with the poorest alignment tended to have lower area fractions.

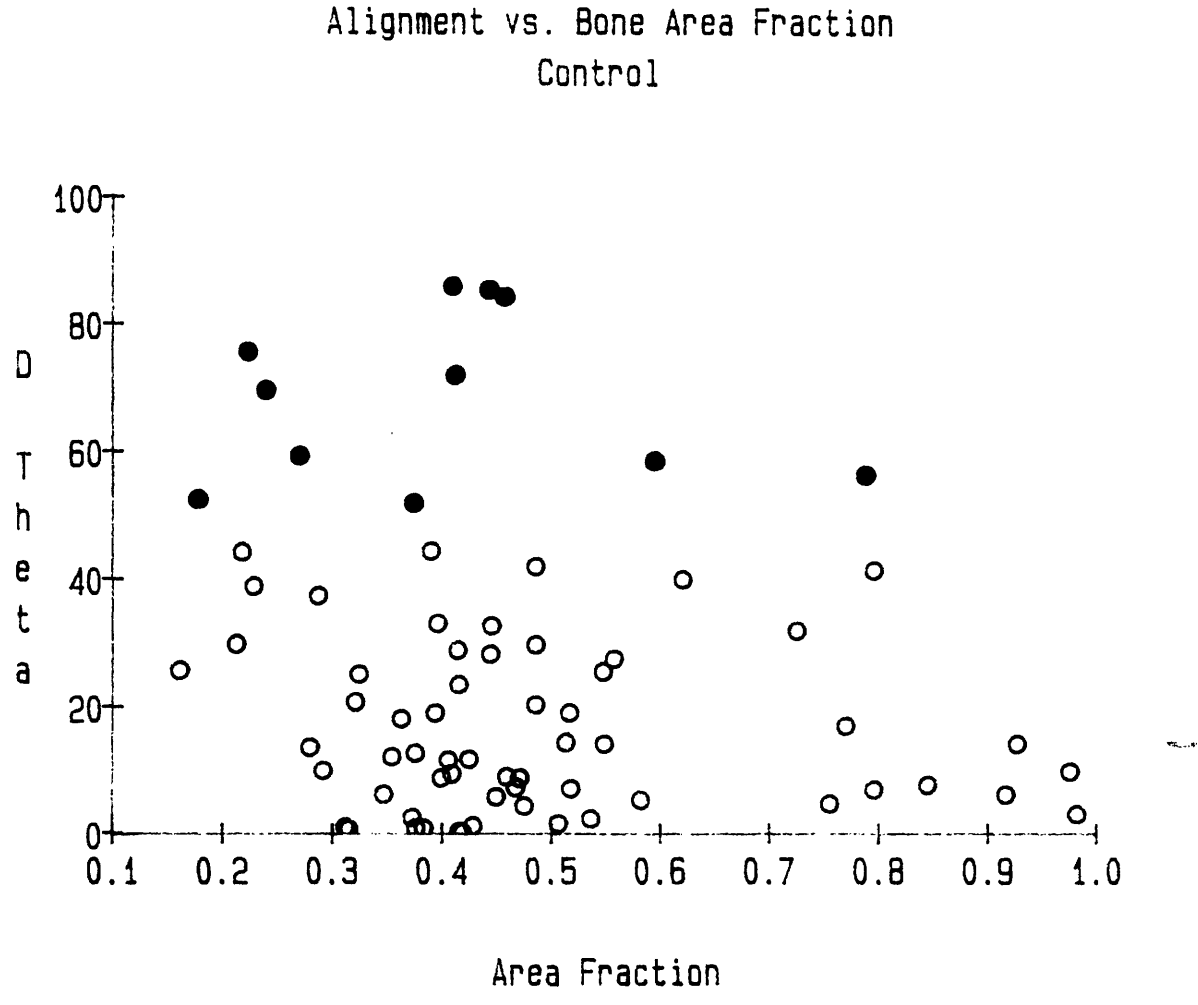

Figure 3.55: The absolute difference between the maximum principal stress direction and the principal material direction ($|\Theta_{PM} - \Theta_{A1}|$) as function of the bone area fraction for the control patellae.

BETH ISRAEL HOSPITAL - IMAGE PROCESSING LABORATORY

IMAGE TITLE: P66L3
COMMENT: Porous 66 Left Image 3
SUBREGION: 2
LENGTHSCALE: 57.18
GRAY THRESHOLD: 115
SOLID PHASE: BLK
TESTLINE LENGTH: 795.1
TESTLINE SPACING <PIXELS> : 1

[AREA FRACTION ANALYSIS:]
REGION AREA = 13.91
AREA FRACTION = 0.726
SOLID AREA = 10.09

[STEREOLOGY ANALYSIS:]

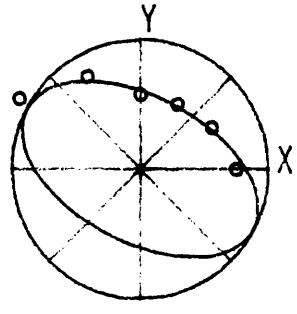

PERIMETER = 44.782
PERIM/AREA = 3.2205

ELLIPSE OF MEAN INTRCPT LENGTHS:
$A*N_1^2 + B*N_1N_2 + C*N_2^2 = MNINCPTLN^{-2}$
A = 1.467
B = 1.787
C = 2.6966
CORRELATION COEFF = 0.961
MAX MN INTRCPT LNTH = 1.0011
ANGLE MAX ORIENTATION = -28 DEGS
MIN MN INTRCPT LNTH = 0.56198
ANGLE MIN ORIENTATION = 62 DEGS
EXTENT OF ANISOTROPY = 35.174 %

Figure 3.56: Stereologic analysis of region "3A" from the control specimen P6. The eccentricity of the anisotropy ellipse equals 0.82.

Ovine Calcaneus

The validation of the finite element models of the control ovine specimens was based on the same assumptions as those for the equine patellae (see above). The critical assumption was that the trajectorial theory of trabecular architecture holds for the control calcanei. The correspondence between the principal stress directions and the principal material directions for the control calcanei is shown in Figure 3.57. The principal stress component which most closely agreed with the principal material direction (Θ_{PO}) is shown as a function of the principal material direction (Θ_{A1}). For 18 out of 26 locations, the principal stress which was maximum in absolute magnitude (Θ_{PM}) was the stress component which was best aligned with the principal material direction ($\Theta_{PM} = \Theta_{PO}$).

Included in Figure 3.57 are the best-fit line from a linear regression and the line $\Theta_{PO} = \Theta_{A1}$ for reference. The data were clearly separable into two groups, forming two clouds, and thus the linear regression was not justified. The cloud of data with positive angles of principal stress orientation corresponded to the compressive principal stress components and the other cloud of data corresponded to the tensile principal stress components. A paired t test, using Θ_{PO} and Θ_{A1}, indicated that, at a significance level of 0.05, there was no significant difference between these parameters. However, the strongest argument for the model validity can be made by visual comparison of the principal stress vectors with the trabeculae of the control calcanei (Figures 3.12 and 3.38a). The trabeculae in the anterior portion were

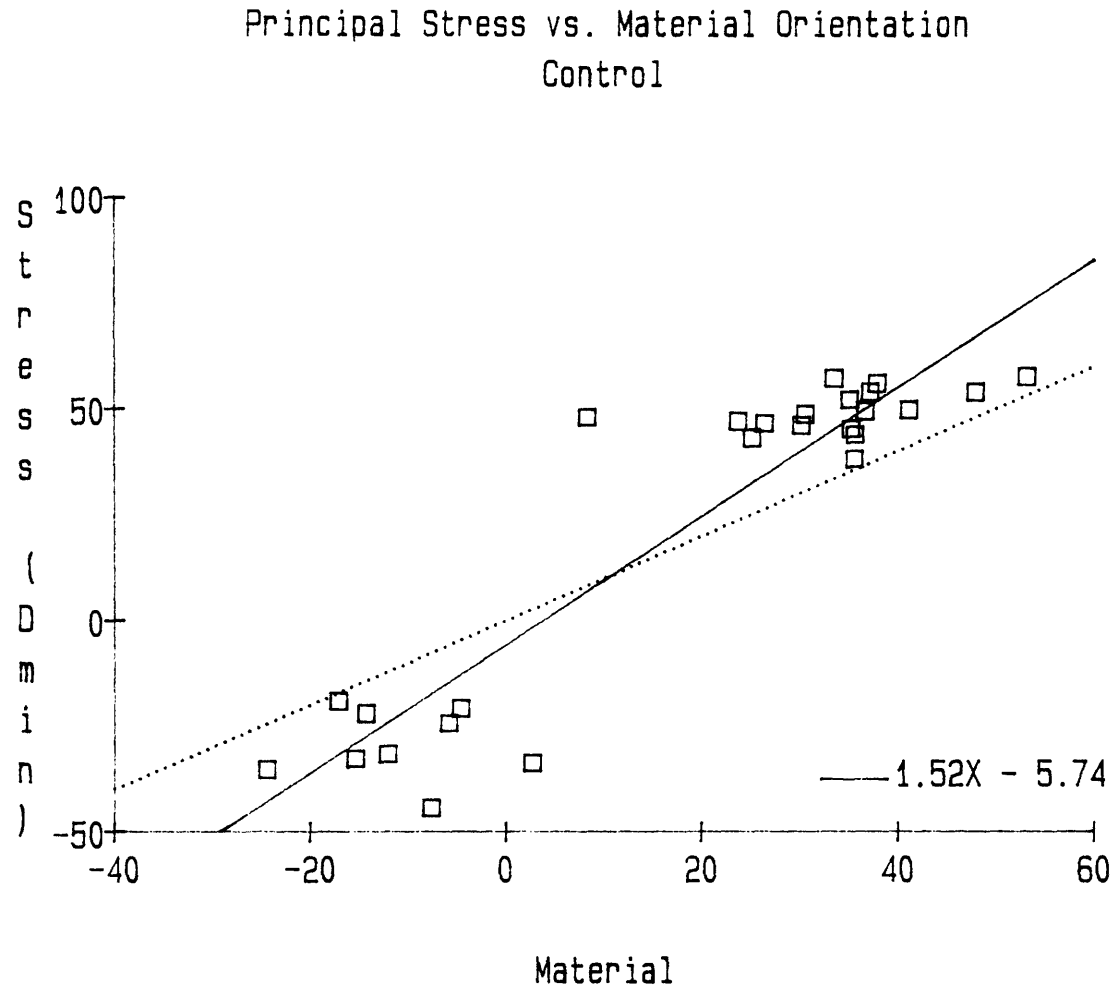

Figure 3.57: The principal stress direction which best aligned with the principal material direction (Θ_{PO}) as a function of the principal material direction (Θ_{A1}) for the control calcanei.

well aligned with the compressive stress vectors in the corresponding regions of the finite element models. The trabeculae adjacent to the posterior cortex were well aligned with the tensile stress vectors. The linear regression was inappropriate because, unlike the equine models, there was very little variation in the directions of principal stress which resulted in the two clouds of data seen in Figure 3.57.

The relationship between the degree of alignment ($|\Theta_{PM} - \Theta_{A1}|$) and the eccentricity of the stress ellipse for the control calcanei is shown in Figure 3.58. In contrast to the equine patellae, all of the points for which the maximum principal stress was not the stress which best aligned with the principal material direction ($\Theta_{PM} \neq \Theta_{PO}$) had a positive stress eccentricity, indicating that tension was the dominant stress. The alignment generally was better in regions where compression predominated. All eight of the data points where $\Theta_{PM} \neq \Theta_{PO}$ came from the proximal regions where the stress state often had a large shear component. In summary, the trabeculae were most often aligned with the direction of the maximum principal stress component. However, in some regions where tension was the dominant stress, the trabeculae were aligned with the compressive stress component, especially in regions of high shear stress.

The relationship between the degree of alignment and the material eccentricity is shown in Figure 3.59. Similar to the equine patellae, there was a tendency for worse alignment with lower material eccentricities. As expected, the alignment of the principal stress with the trabeculae in more isotropic regions was worse than the alignment in very highly oriented regions.

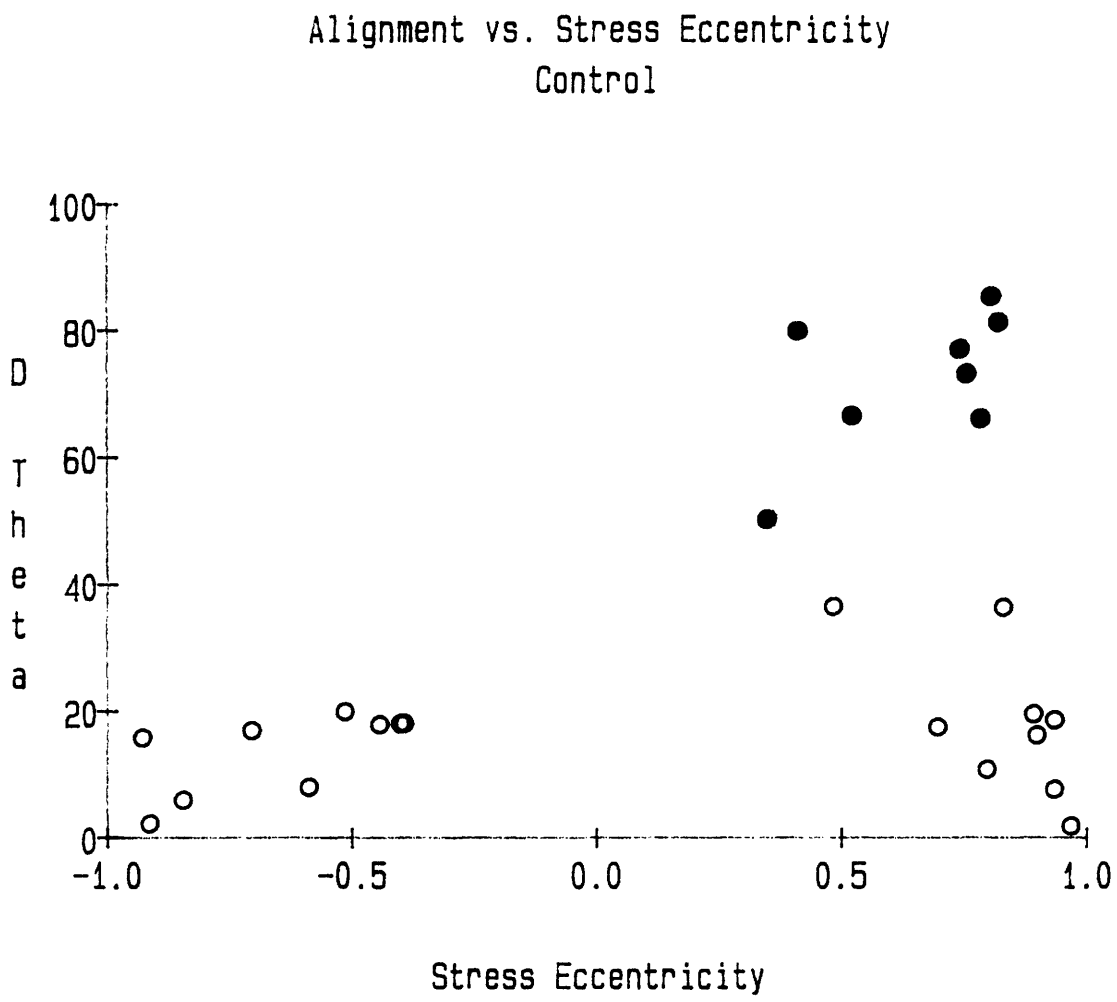

Figure 3.58: The absolute difference between the maximum principal stress direction and the principal material direction ($|\Theta_{PM} - \Theta_{A1}|$) as a function of the eccentricity of the stress ellipse for the control calcanei.

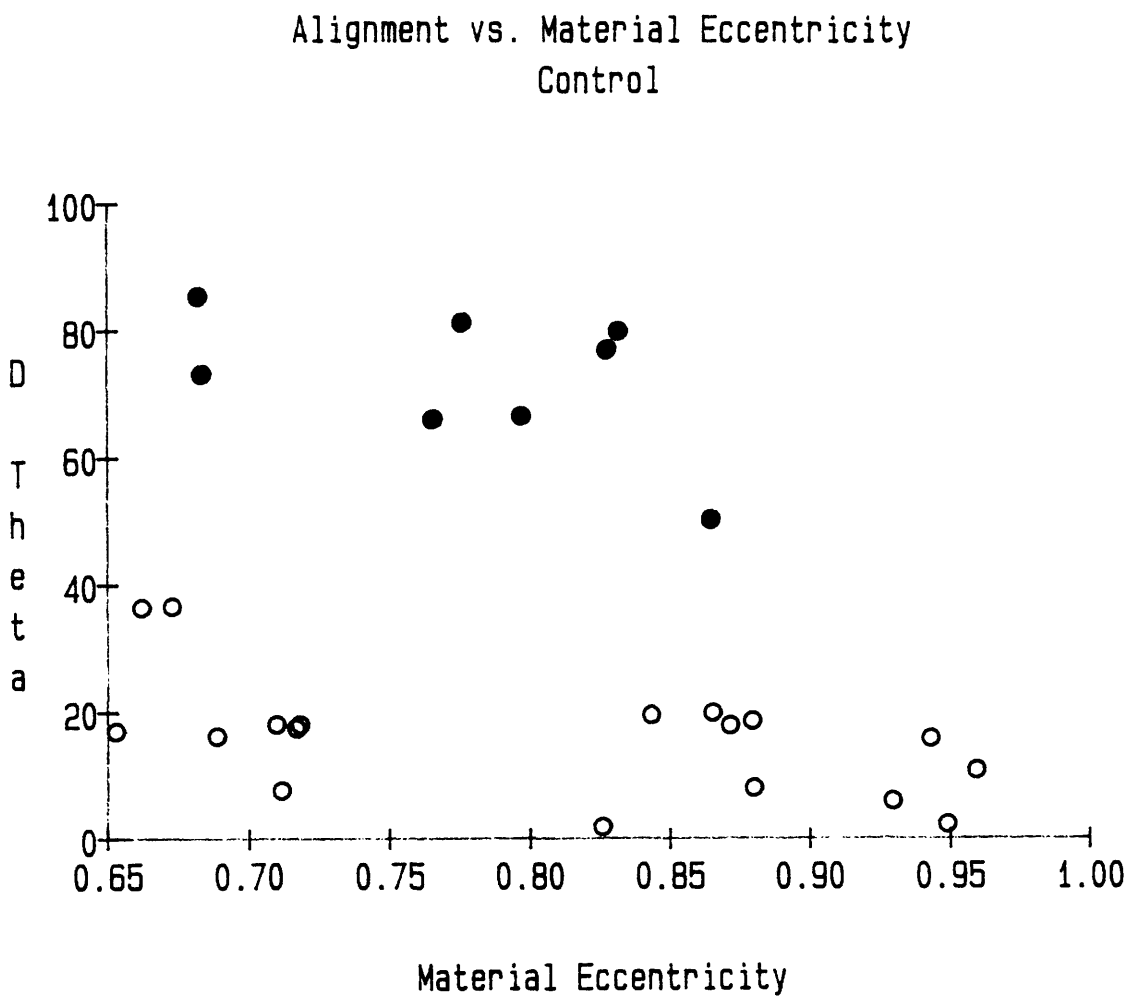

Figure 3.59: The absolute difference between the maximum principal stress direction and the principal material direction ($|\Theta_{PM} - \Theta_{A1}|$) as a function of the eccentricity of the material anisotropy ellipse for the control calcanei.

3.3.2 Relations for Equine Model

The present objective was to examine the correlation between the predicted stresses and the measured morphology in the experimental equine patellae. The correspondence between the principal stress directions and the principal material directions for the experimental patellae is shown in Figures 3.60 and 3.61. In Figure 3.60, the principal material direction (Θ_{A1}) is shown as a function of the principal stress direction which agreed most closely to the principal material direction (Θ_{PO}). In Figure 3.61, the principal material direction is shown as a function of the maximum principal stress direction (Θ_{PM}). For 60 out of 73 locations, $\Theta_{PO} = \Theta_{PM}$.

A linear regression was performed on Θ_{A1} as a function of Θ_{PO}. It is important to note that for this analysis, unlike the analysis of the control patellae, the principal stress direction was chosen as the independent variable and the principal material direction was chosen as the dependent variable. The first assumption for this regression was that the values of the principal stress orientations were fixed. In other words, the predictions of the finite element models were assumed to be exact. The measure of the goodness-of-fit for the control patellae from the previous section was 0.87. The applied loads and the finite element meshes for the models of the experimental patellae were identical to those for the control patellae with the exception of the implant region. If the assumptions of the analysis of the control patellae are accepted, then those results may be extended to make the statement that the goodness-of-fit of the predicted stress directions to

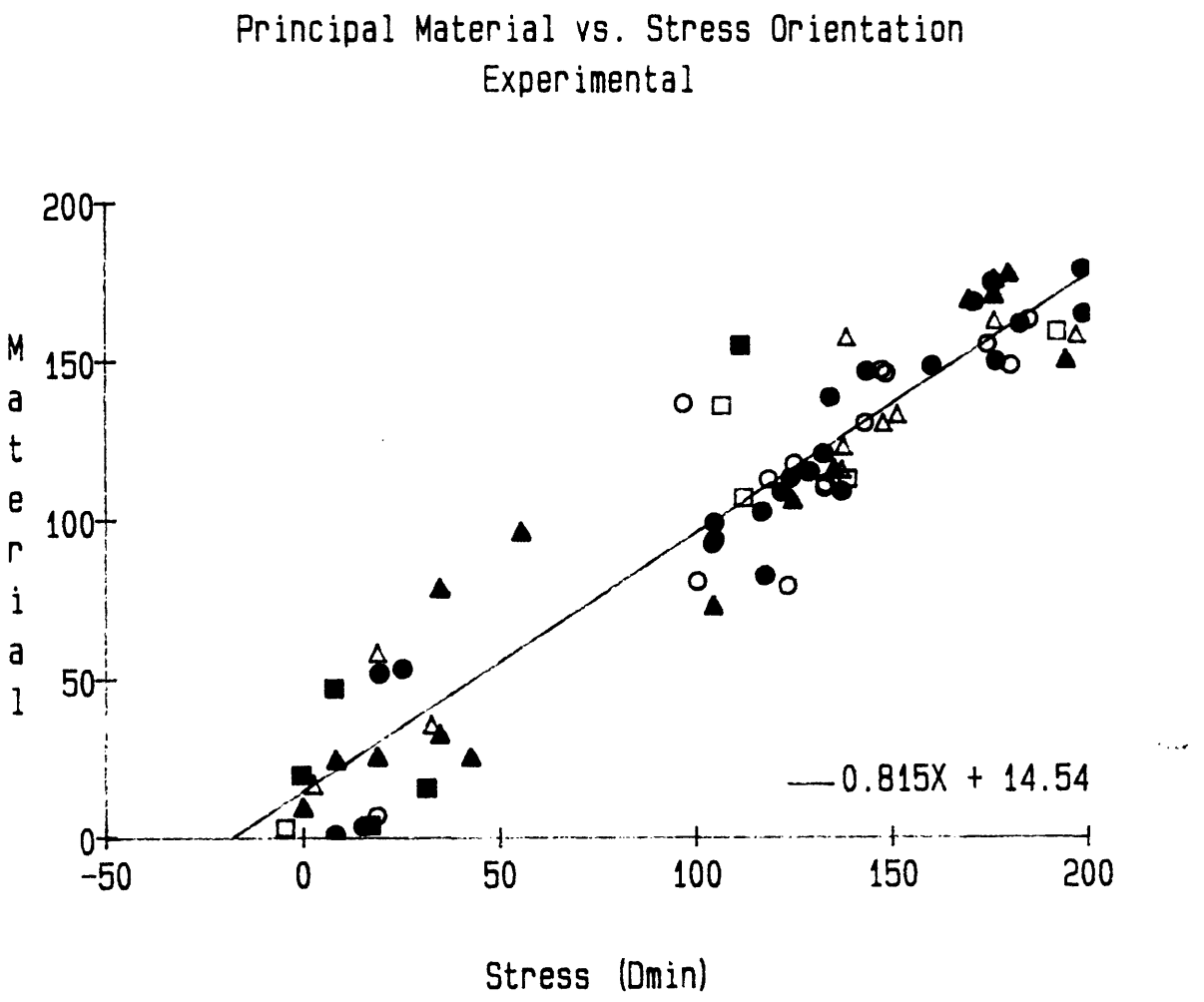

Figure 3.60: The principal stress direction which best aligned with the principal material direction (Θ_{P0}) as a function of the principal material direction (Θ_{A1}) for the experimental patellae. See Figure 3.8 for Key.

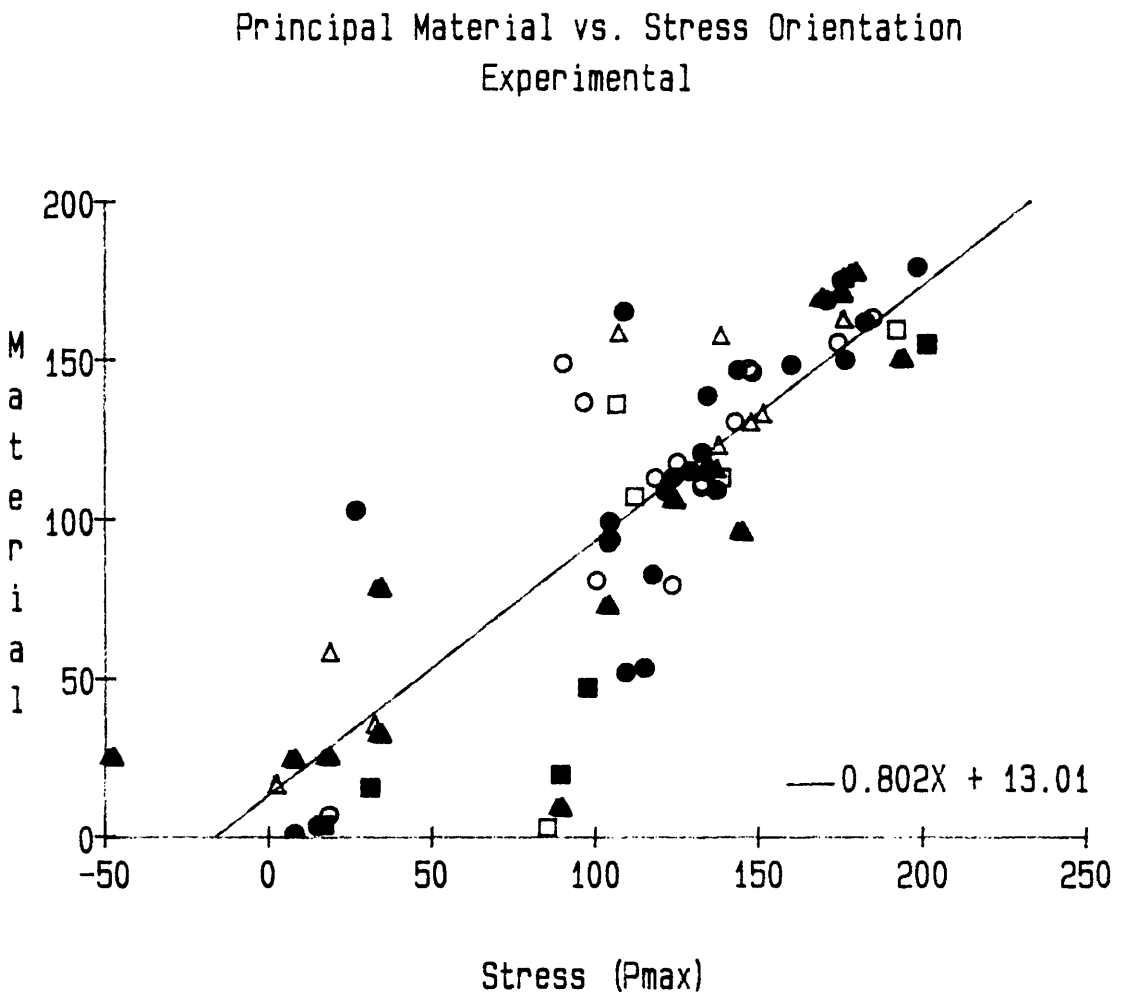

Figure 3.61: The maximum principal stress direction (Θ_{PM}) as a function of the principal material direction (Θ_{A1}) for the experimental patellae. See Figure 3.8 for Key.

the 'actual' stress directions for the control patellae was 0.87. The word actual is in quotes because the in vivo stresses vary cyclically, whereas in this investigation only a single static load case was considered. This point is discussed further in Section 4.0. It is not unreasonable to expect similar accuracy for the stress predictions for the experimental patellae. The most critical aspect of the mechanics of the experimental patellae in contrast to the control patellae was the representation of the bone/implant interface conditions. The accuracy of the boundary conditions at this interface were specifically examined in Section 3.1.1. The second assumption was that, for each predicted principal stress direction, there was a population of principal material orientations with a normal distribution and that the variance of this population was the same for each principal stress orientation. This assumption could not be tested using the present data due to an insufficient number of data points. However, this is also not an unreasonable assumption since there was no inherent reason for the principal material orientation to differ from the principal stress orientation in any particular direction or by any particular amount. However, a similar caveat must be stated in regards to a normal distribution, in that the range of data is limited to a 45 degree deviation from the line $\Theta_{A1} = \Theta_{PO}$. In summary, the objective for the control patellae was to validate the finite element predictions assuming that the trajectorial theory for trabecular architecture holds for the control patellae. The critical assumption for the analysis of the experimental patellae was that the finite element predictions were accurate. The proposed linear regression was a test of whether the trajectorial theory holds for the experimental patellae.

The best fit line from the linear regression of Θ_{A1} as a function of Θ_{PO} is shown in Figure 3.60. The statistical data are summarized in Table 3.4. The intercept had a p-value of 0.001 and a standard deviation of 4.29. The slope had a p-value of 0.0001 and a standard deviation of 0.034. The regression had a p-value of 0.0001, standard deviation of 17.98 degrees, and an R^2 of 0.89. The statistics indicated that, while the slope was different from 1.0 and the intercept was different from 0, the goodness-of-fit for the experimental data was similar to that for the control patellae.

Similar comments may be made about the standard deviation of the regression as those made for the control patellae (see Section 3.3.1). To further examine the correlation between the principal material directions and the principal stress directions, the linear regression was performed using the maximum principal stress direction (Θ_{PM}) for the independent variable rather than the direction of principal stress which agreed most closely with the principal material direction (Θ_{PO}). As mentioned above, for 60 out of 73 data points, $\Theta_{PM} = \Theta_{PO}$. The results of this linear regression are also given in Table 3.4. The standard deviation of the regression was 29.19 which is comparable to that found for the control patellae.

The degree of alignment as a function of the eccentricity of the stress ellipse for the experimental patellae is shown in Figure 3.62. The Y axis represents the absolute difference between the maximum principal stress direction and the principal material direction. Eleven of the thirteen data points for which this difference was greater than

Table 3.4

Linear Regression for Implant-Induced Remodeling
Equine Patella

	Slope			Intercept			Regression		
	Value	SD	Sig	Value	SD	Sig	SD	Sig	R^2
Θ_{A1} vs Θ_{PO}	0.815	0.034	.0001	14.54	4.290	.0012	17.98	.0001	0.890
Θ_{A1} vs Θ_{PM}	0.802	0.061	.0001	13.01	7.710	0.096	29.19	.0001	0.710

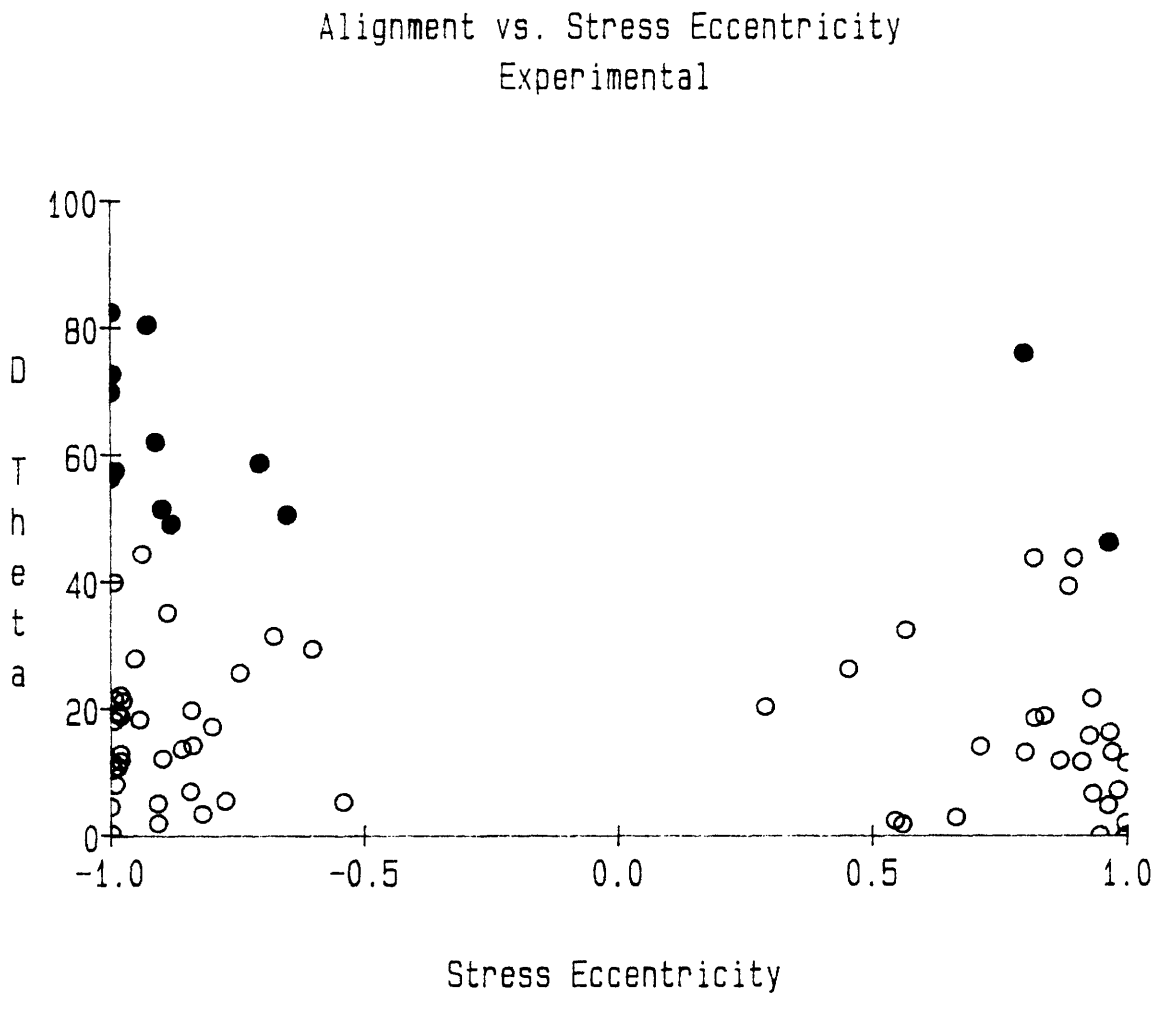

Figure 3.62: The absolute difference between the maximum principal stress direction and the principal material direction ($|\Theta_{PM} - \Theta_{A1}|$) as function of the eccentricity of the stress ellipse for the experimental patellae.

45 degrees had a stress eccentricity of less than zero, indicating that compression was the dominant stress. For the control patellae, eleven out of eleven data points for the same condition had a stress eccentricity of less than zero. Also similar to the control patellae, the alignment in regions where tension predominated was better than in regions where compression predominated.

The relationship between the eccentricity of the stress ellipse and the eccentricity of the material anisotropy ellipse for the experimental patellae is shown in Figure 3.63. Six of the thirteen data points where $\Theta_{PM} \neq \Theta_{PO}$ had a material eccentricity of less than 0.5, indicating that the material in these locations was not highly anisotropic. One of the two data points for which the stress eccentricity was greater than zero with a poor alignment had a very low material eccentricity (less than 0.25). In general, similar to the data for the control patellae, this graph demonstrates a poor correspondence between the eccentricity of the material anisotropy ellipse and the eccentricity of the stress ellipse. The degree of alignment between the stress and material axes was examined as a function of the material eccentricity (Figure 3.64). Again, as for the control patellae, there was a general tendency for poorer alignment (higher angle difference) for lower material eccentricities.

The degree of alignment for the experimental patellae as a function of the bone area fraction is shown in Figure 3.65. In contrast to the results for the control patellae, there was no clear trend for better alignment for higher area fractions. Recall that the reason for good

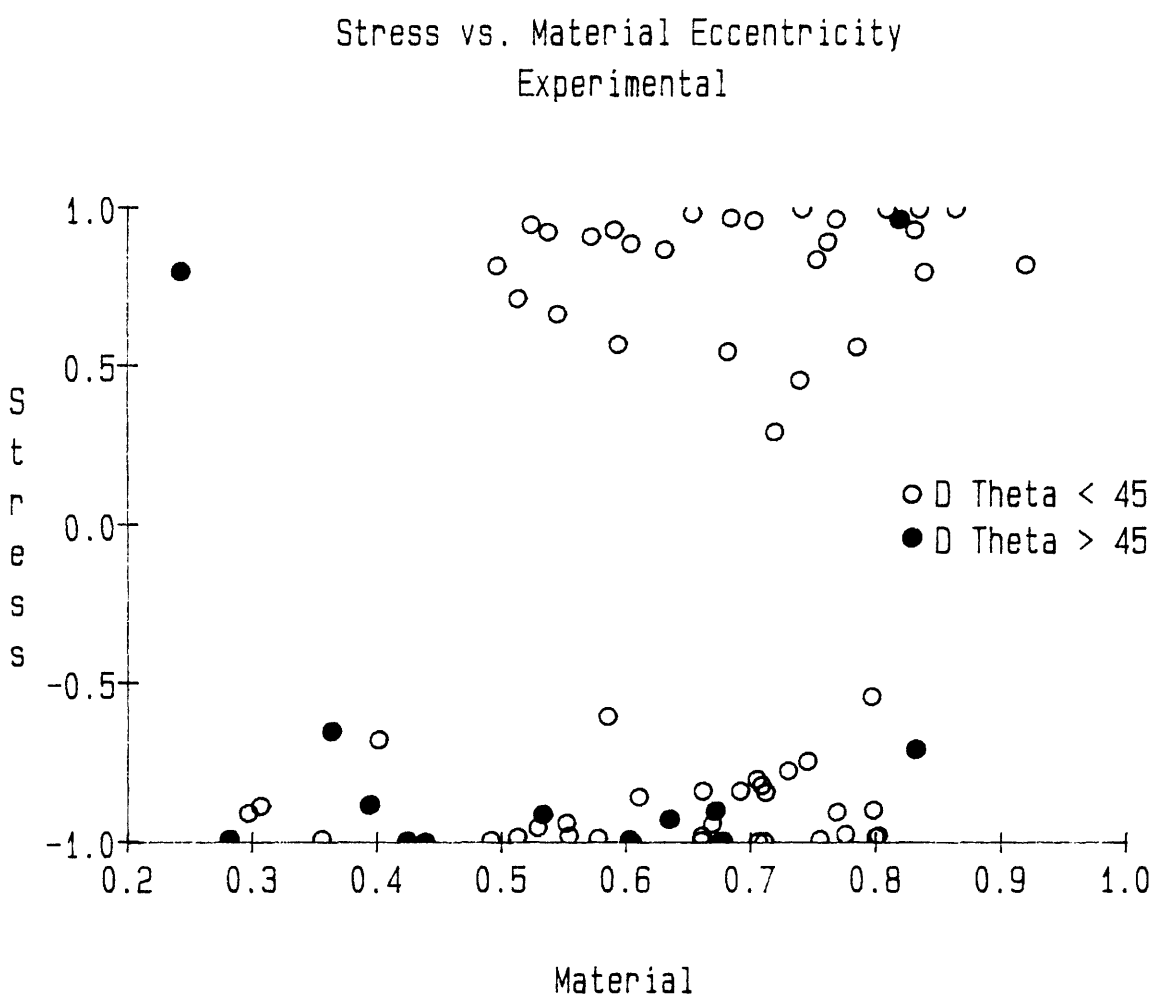

Figure 3.63: The eccentricity of the stress ellipse as a function of the eccentricity of the material ellipse for the experimental patellae. The points for which $|\Theta_{PM} - \Theta_{A1}| > 45$ degrees are highlighted with filled circles.

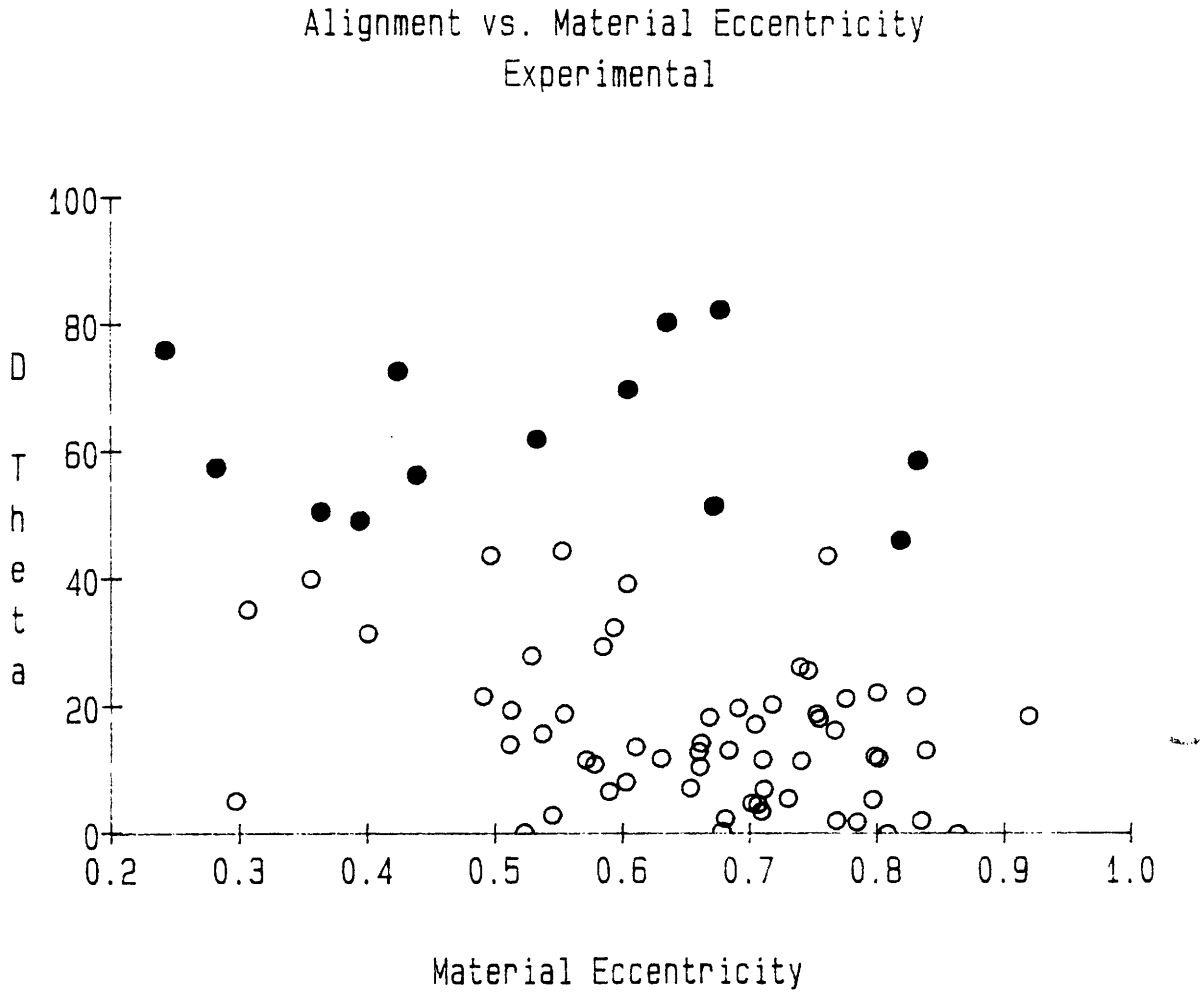

Figure 3.64: The absolute difference between the maximum principal stress direction and the principal material direction ($|\Theta_{PM} - \Theta_{A1}|$) as function of the eccentricity of the material anisotropy ellipse for the experimental patellae.

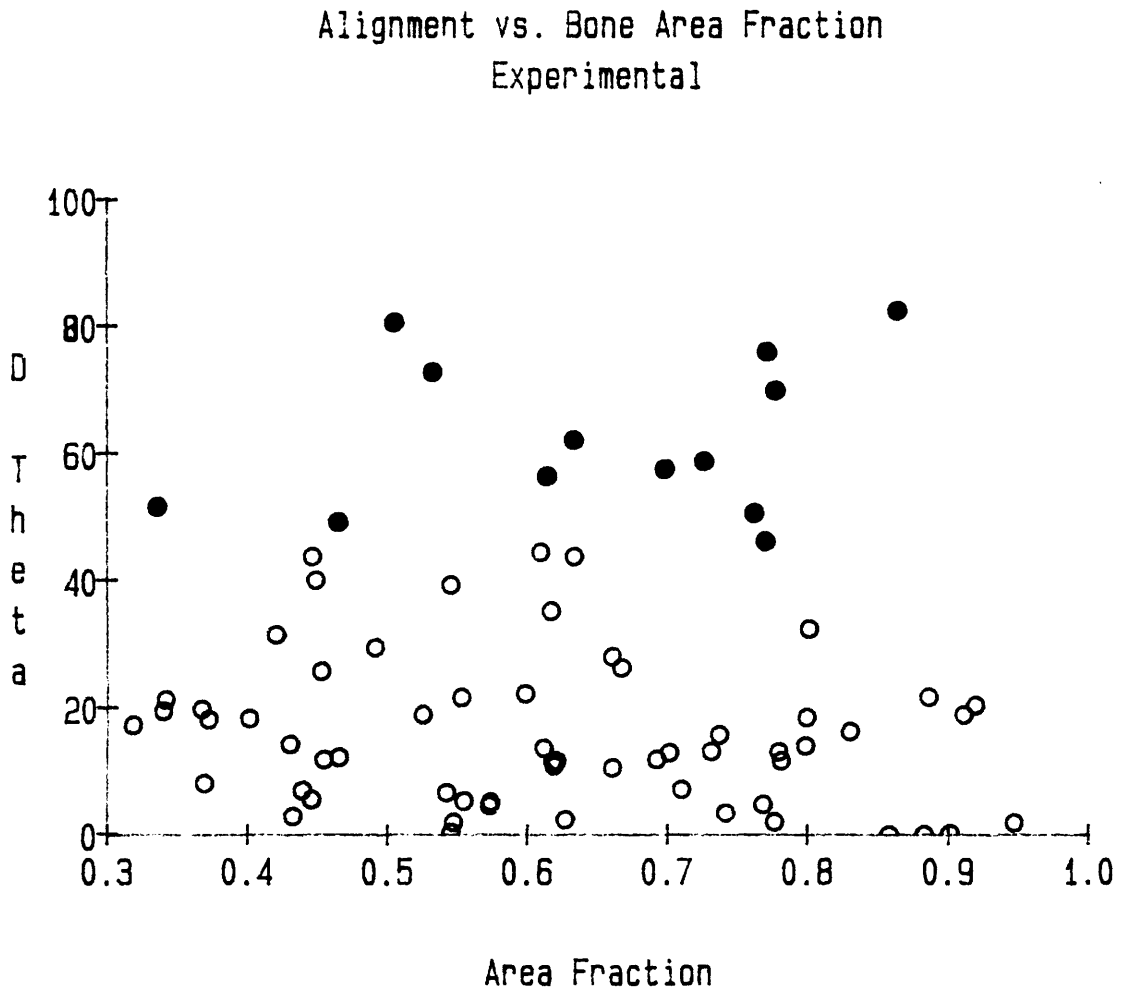

Figure 3.65: The absolute difference between the maximum principal stress direction and the principal material direction ($|\Theta_{PM} - \Theta_{A1}|$) as function of the bone area fraction for the experimental patellae.

alignment in the control patellae at high area fractions was that the dense bone areas were adjacent to and continuous with the anterior cortical shell. In these regions the trabeculae were highly oriented, resulting in good correspondence with the finite element predictions. However, for the experimental patellae, many of the data points with high area fractions were remodeled areas adjacent to the implants. It can be seen in Figure 3.66 that the experimental patellae tended to have more data points with high area fractions and low material eccentricities. An extreme example is shown in Figure 3.67. This image corresponds to image "7A" from specimen S3. The bone density was very high but virtually isotropic. Also recall that there was a tendency for the material eccentricity to decrease for the "A" locations (see Figure 3.3). However, this tendency was not pronounced or statistically significant. This is because the material eccentricity was deceptively high in some instances. An example can be seen in Figure 3.6b. This very dense bone adjacent to the implant in specimen P6 had an eccentricity of 0.53. However, it is difficult to attach meaning to the measured orientation in this region based on visual inspection of the image.

The measured area fraction is a critical parameter in determining the structural properties of the trabecular bone. As presented in Section 1.2.1, Fyhrie and Carter (1986) developed a mathematical formulation for the orientation and density of trabecular bone for a given stress state based on structural optimization. The authors demonstrated that the trajectorial theory is consistent with structural optimization. They also pointed out that if the formulation is based on

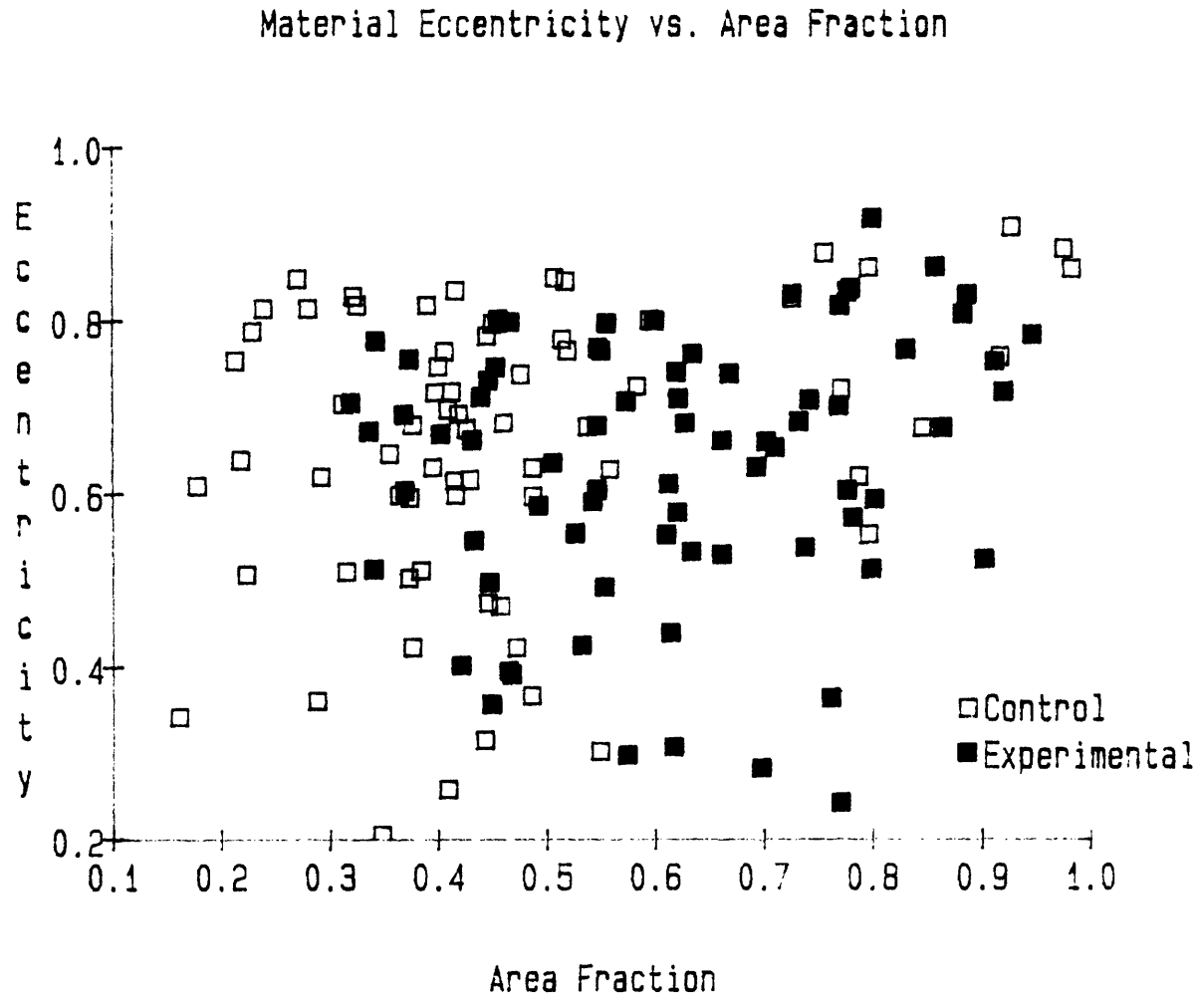

Figure 3.66: The eccentricity of the material anisotropy ellipse as a function of the trabecular bone areal density for both the control and the experimental patellae.

BETH ISRAEL HOSPITAL - IMAGE PROCESSING LABORATORY

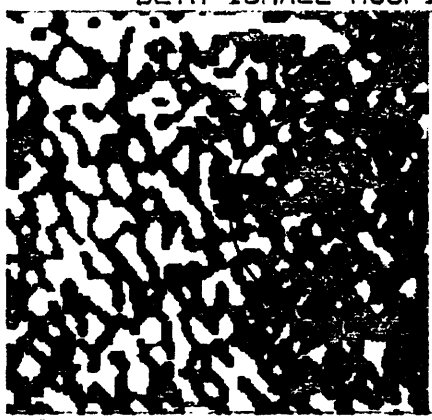

IMAGE TITLE: S4L7
COMMENT: Image 7
SUBREGION: 2
LENGTHSCALE: 57.18
GRAY THRESHOLD: 130
SOLID PHASE: BLK
TESTLINE LENGTH: 795.1
TESTLINE SPACING <PIXELS> : 1

[AREA FRACTION ANALYSIS:]
REGION AREA = 13.91

AREA FRACTION = 0.771
SOLID AREA = 10.72

[STEREOLOGY ANALYSIS:]

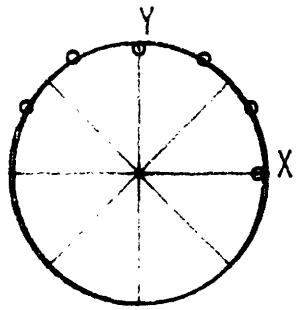

PERIMETER = 45.799
PERIM/AREA = 3.2936

ELLIPSE OF MEAN INTRCPT LENGTHS:

$A*N_1^2 + B*N_1N_2 + C*N_2^2 = MNINCPTLN^{-2}$

A = 1.902
B = 0.4855E-01
C = 1.8003

CORRELATION COEFF = 0.279
MAX MN INTRCPT LNTH = 0.74643
ANGLE MAX ORIENTATION = 103 DEGS
MIN MN INTRCPT LNTH = 0.72406
ANGLE MIN ORIENTATION = 13 DEGS
EXTENT OF ANISOTROPY = 1.939 %

Figure 3.67: Stereologic analysis of region "7A" from the experimental specimen S3.

an effective stress measure the material is optimized for strength, whereas if the formulation is based on strain energy the material is optimized for stiffness. Both formulations predict that the minimum apparent density, for an optimum structure, is proportional to a power function of an effective stress measure. The above linear regression between Θ_{A1} and Θ_{P1} was a test of the trajectorial theory as applied to the patellae with implant-induced remodeling. The next objective of the present study was to test the relationship between the predicted stress and the bone density as reflected by the measured bone area fraction.

Two effective stress measures were examined in the present investigation, von Mises effective stress and strain energy density. Both measures are commonly applied to engineering materials as failure criteria. One limitation of the von Mises failure criterion is that, in three-dimensions, the failure surface is not closed. More specifically, this criterion allows for infinite strength in hydrostatic compression and hydrostatic tension. However, this limitation is not relevant in the present studies since the data were limited to two-dimensions. Furthermore, a two-dimensional hydrostatic stress state did not occur (see Figure 3.33) and a three-dimensional hydrostatic stress state is unlikely under physiologic conditions.

The relationship between von Mises effective stress and bone area fraction for both the control and the experimental patellae is shown in Figure 3.68. Similarly, the relationship between strain energy density and bone area fraction is shown in Figure 3.69. There was roughly a linear relationship between von Mises stress and bone area fraction but

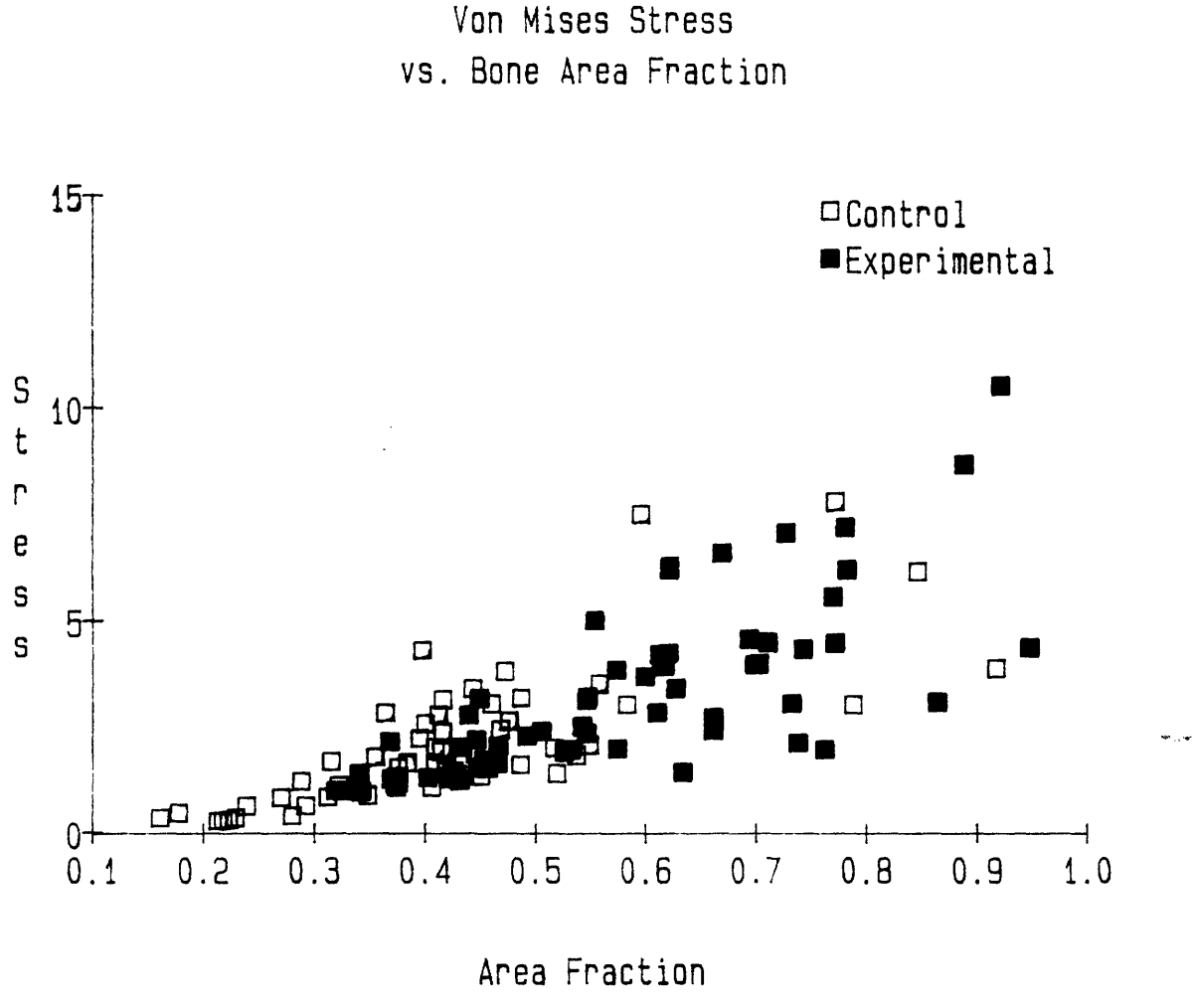

Figure 3.68: Von Mises effective stress (MPa) as a function of the trabecular bone areal density for both the control and the experimental patellae.

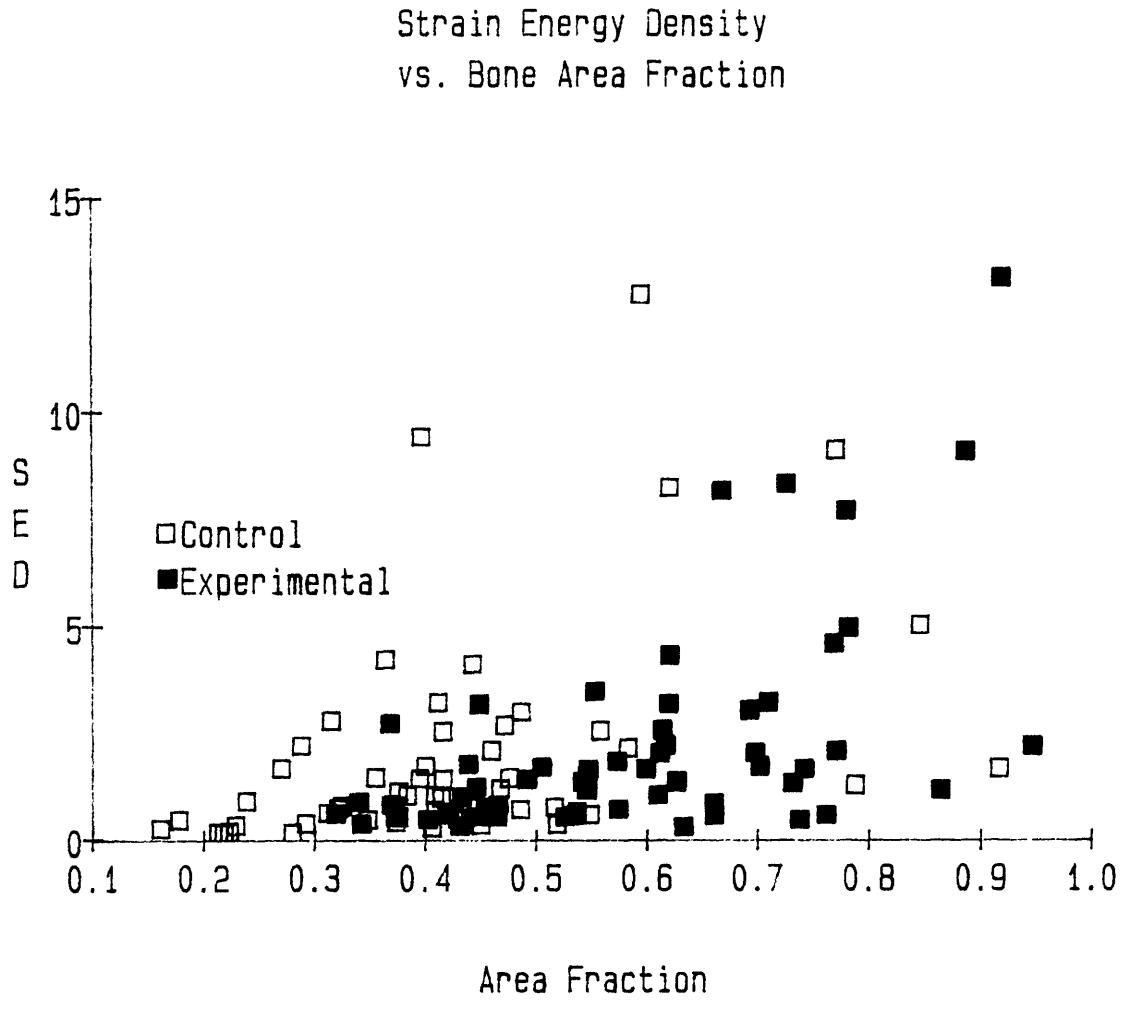

Figure 3.69: Strain energy density (MPa) as a function of the trabecular bone areal density for both the control and the experimental patellae.

a linear regression would be inappropriate because the variance of the data was not constant for different area fractions. The variance at low area fractions was much less than the variance at high area fractions. Even if a linear relationship was appropriate, this would not be a conclusive demonstration that the trabecular bone remodeling was such that this linear relationship was maintained. Recall that the isotropic elastic modulus of the control and experimental patellae was based on a linear function of the measured bone area fraction (see Section 2.2.2). It should not be surprising that a linear relationship would result between an effective stress measure and the bone area fraction. While higher modulus bone will not necessarily have higher stresses, the circular nature of this relationship is inescapable.

The scatter of data seen in the strain energy density is due to the discontinuity of the elastic modulus in the finite element models. Rather than a continuous distribution of material properties, there were abrupt changes in the elastic modulus from element to element. The resulting extreme local gradients in strain energy density were apparent in the contour plots presented in Section 3.2.1. This was an unfortunate problem inherent in the finite element method as applied in these studies. This problem may be solved by increasing the mesh density, but the present models represented a practical upper limit in complexity for the available facilities.

The most critical test of whether the trabecular bone remodeling was an adaptive response to the imposed stresses is to compare the changes in the material anisotropy ellipse to the changes in the stress ellipse.

This assumes that the finite element model predictions were accurate for both the control and the experimental patellae. While an attempt was made to validate the models of the control patellae in Section 3.3.1, no similar validation was possible for the models of the experimental patellae. It must be assumed that, if the models of the control patellae provided accurate predictions, then the models of the experimental patellae also provided accurate predictions. This is the same assumption that was made for the linear regression relating Θ_{A1} to Θ_{PO}.

The change in bone area fraction as a function of the change in von Mises effective stress is shown in Figure 3.70. The best fit line from a linear regression is included in the graph. The assumptions of this regression were the same as those for the previous linear regression. The regression had a significance level of 0.0001 and an R^2 of 0.57. An argument can be made based on this graph that the data from the "A" and "B" locations come from two distinct populations. With the exception of a single data point, the data from the "B" locations had less variance from a linear relationship. This linear regression provides a critical test of the hypothesis of Fyrie and Carter (1986) since these data are an additional step removed from the input material property data. The stress changes were the result of both the changes in the material properties and the changes in the stress fields due to the presence of the implants. A similar plot of the change in bone area fraction as a function of the change in strain energy density is shown in Figure 3.71. The scatter of data is inconclusive in light of the error resulting from the discontinuity of material properties in the finite element models.

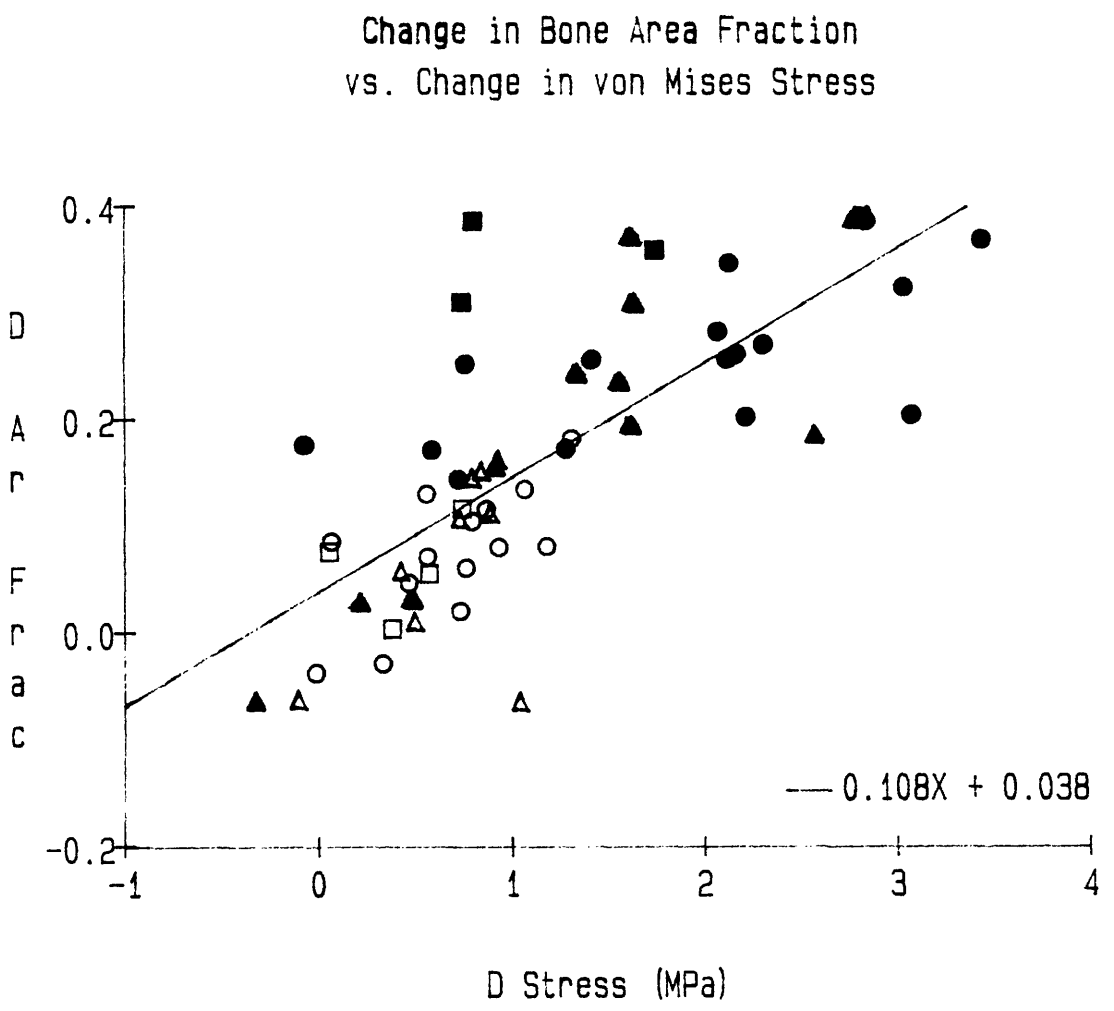

Figure 3.70: The difference in trabecular bone areal density between the experimental and control patellae as a function of the difference in von Mises stress between the experimental and control patellae. See Figure 3.8 for Key.

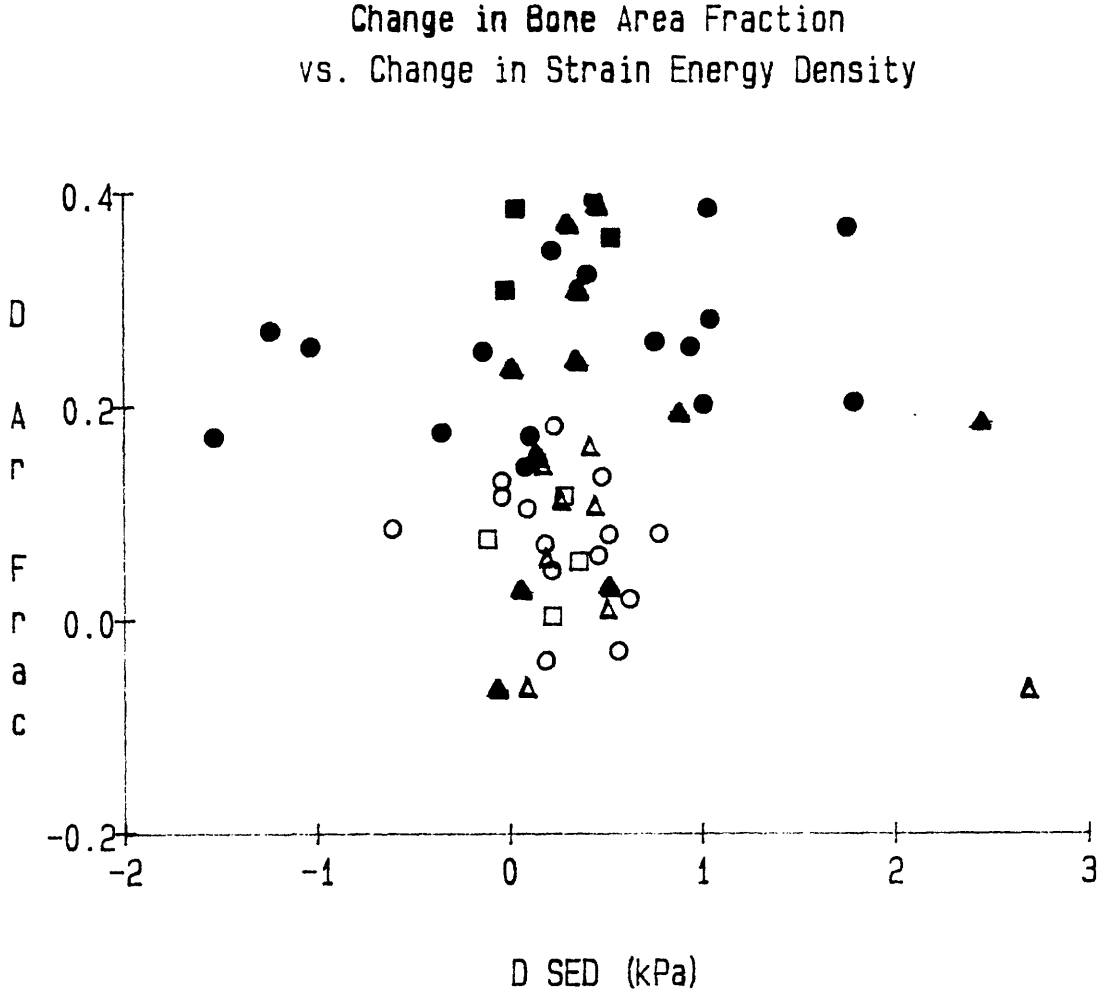

Figure 3.71: The difference in trabecular bone areal density between the experimental and control patellae as a function of the difference in strain energy density between the experimental and control patellae. See Figure 3.8 for Key.

The final comparison was made between the change in principal material orientation to the change in principal stress orientation. The relationship between the change in orientation of the maximum principal stress ($\Delta\Theta_{PM}$) and the change in the principal material axis ($\Delta\Theta_{A1}$) is shown in Figure 3.72. There are clearly two distinct populations for $\Delta\Theta_{PM}$. As mentioned above, there were nine data points in which the maximum principal stress changed from compression to tension or vice versa. This problem was eliminated by examining the relationship between the change in orientation of the principal tensile stress ($\Delta\Theta_{P1}$) and $\Delta\Theta_{A1}$, shown in Figure 3.73. This figure includes the line $\Delta\Theta_{P1} = \Delta\Theta_{A1}$ for reference. As demonstrated above, the change in principal material directions tended to be greater than the changes in principal stress directions (see Figures 3.10 and 3.31). It is clear from these figures that no definitive statement may be made from the present data about the correspondence between the changes in trabecular bone orientation and the changes in principal stress orientation.

One very important aspect of the poor correspondence demonstrated in Figure 3.73 was that the change in the orientation of the material anisotropy ellipse generally was greater than the corresponding change in the orientation of the stress ellipse. One possible explanation is that, under the right circumstances, a small change in the stress state can result in a large change in the material orientation. One carefully selected example is shown in Figure 3.74. As measured using stereology, the direction of principal material orientation was rotated 86 degrees when the experimental patella was compared to the control patella. However, by visual inspection, the trabecular architecture was not

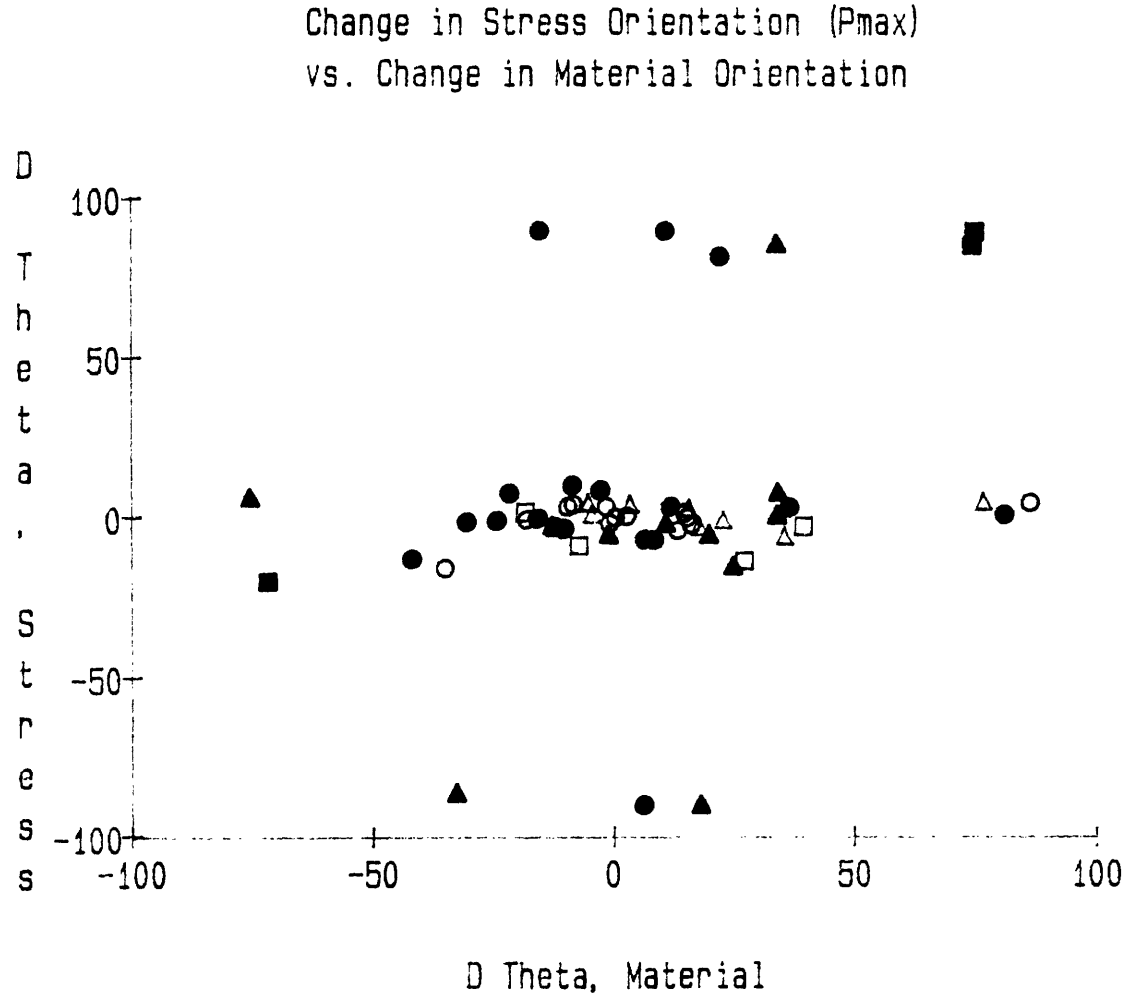

Figure 3.72: The difference in the direction of maximum principal stress between the experimental and the control patellae as a function of the difference in the direction of principal material orientation between the experimental and the control patellae. See Figure 3.8 for Key.

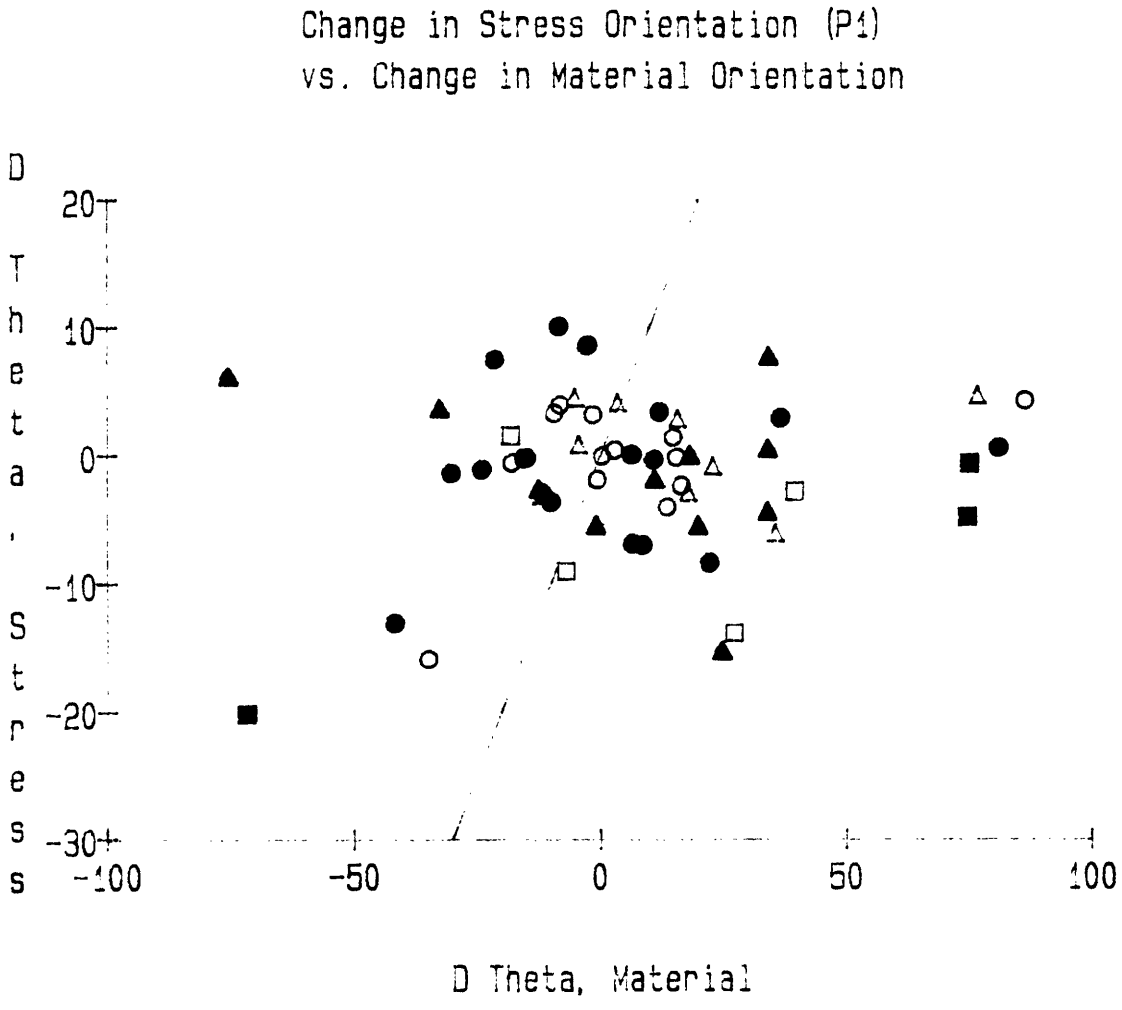

Figure 3.73: The difference in the direction of principal stress P_1 between the experimental and the control patellae as a function of the difference in the direction of principal material orientation between the experimental and the control patellae. See Figure 3.8 for Key.

BETH ISRAEL HOSPITAL - IMAGE PROCESSING LABORATORY

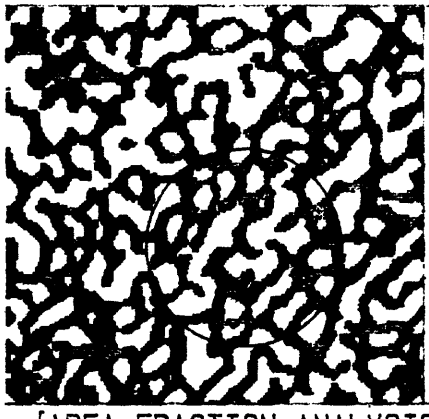

IMAGE TITLE: S4R4
COMMENT: Image 4
SUBREGION: 3
LENGTHSCALE: 57.18
GRAY THRESHOLD: 120
SOLID PHASE: BLK
TESTLINE LENGTH: 795.1
TESTLINE SPACING <PIXELS> : 1

[AREA FRACTION ANALYSIS:]
REGION AREA = 13.91

AREA FRACTION = 0.487
SOLID AREA = 6.767

[STEREOLOGY ANALYSIS:]

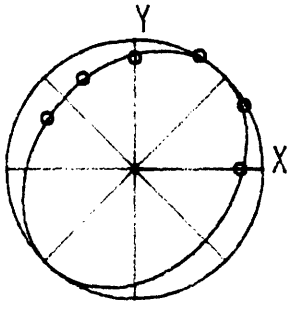

PERIMETER = 55.881
PERIM/AREA = 4.0186

ELLIPSE OF MEAN INTRCPT LENGTHS:

$A*N_1^2 + B*N_1N_2 + C*N_2^2 = MNINCPTLN^{-2}$

A = 7.292
B = -3.391
C = 6.6462

CORRELATION COEFF = 0.969
MAX MN INTRCPT LNTH = 0.43672
ANGLE MAX ORIENTATION = 50 DEGS
MIN MN INTRCPT LNTH = 0.33912
ANGLE MIN ORIENTATION = 140 DEGS
EXTENT OF ANISOTROPY = 15.961 %

Figure 3.74a: Stereologic analysis of region "4B" from the control specimen S3.

BETH ISRAEL HOSPITAL - IMAGE PROCESSING LABORATORY

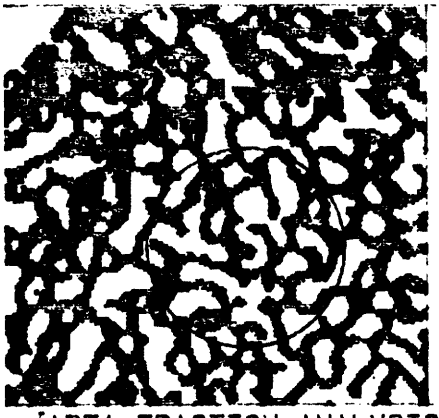

IMAGE TITLE: S4L4
COMMENT: Image 4
SUBREGION: 3
LENGTHSCALE: 57.18
GRAY THRESHOLD: 120
SOLID PHASE: BLK
TESTLINE LENGTH: 795.1
TESTLINE SPACING <PIXELS> : 1

[AREA FRACTION ANALYSIS:]
REGION AREA = 13.91

AREA FRACTION = 0.449
SOLID AREA = 6.246

[STEREOLOGY ANALYSIS:]

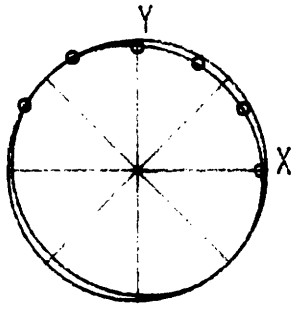

PERIMETER = 54.109
PERIM/AREA = 3.8912

ELLIPSE OF MEAN INTRCPT LENGTHS:
$A*N_1^2 + B*N_1N_2 + C*N_2^2 = MNINCPTLN^{-2}$
A = 7.580
B = 1.025
C = 7.6414
CORRELATION COEFF = 0.891
MAX MN INTRCPT LNTH = 0.37537
ANGLE MAX ORIENTATION = -43 DEGS
MIN MN INTRCPT LNTH = 0.35084
ANGLE MIN ORIENTATION = 47 DEGS
EXTENT OF ANISOTROPY = 4.300 %

Figure 3.74b: Stereologic analysis of region "4B" from the experimental specimen S3.

tremendously different between the two images. In both cases, there appeared to be two distinct directions of oriented trabeculae. In the experimental patella, the maximum direction of orientation coincided with the radial direction of the implant, whereas in the control patella the radial direction corresponded to the secondary direction of orientation. The predicted changes in stress at this location were small since this was a "B" location. The finite element models predicted essentially uniaxial compression in both cases, with about a 12 % increase in the magnitude of principal stress P_2 in the experimental patella, from -3.0 to -3.4 MPa. The orientation of this stress vector changed by only a 4 degree rotation toward the radial direction of the implant. The principal stress component P_1 changed from 0.3 to -0.5 MPa. It could be argued that, in the control patella, the principal material direction aligned with the tensile stress component, whereas in the experimental patella, the increase in compression resulted in the material alignment changing to the direction of the compressive stress component. However, these stress changes were relatively small, and it is questionable as to whether any meaning can be attached to the secondary principal stress component.

A second example of a large change in the material orientation is shown in Figure 3.75. This example was from a region adjacent to the smooth implant in specimen S2, and thus the changes in stress were more significant. In the control patella, the trabecular bone at this location was nearly isotropic, whereas in the experimental patella the trabeculae were clearly oriented in a direction running from the implant to the anterior cortical shell. The finite element models predicted an

BETH ISRAEL HOSPITAL - IMAGE PROCESSING LABORATORY

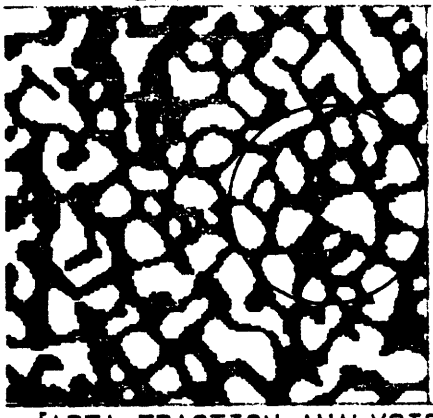

IMAGE TITLE: S2R7
COMMENT: Image 7
SUBREGION: 2
LENGTHSCALE: 57.18
GRAY THRESHOLD: 120
SOLID PHASE: BLK
TESTLINE LENGTH: 795.1
TESTLINE SPACING <PIXELS> : 1

[AREA FRACTION ANALYSIS:]
REGION AREA = 13.91

AREA FRACTION = 0.409
SOLID AREA = 5.682

[STEREOLOGY ANALYSIS:]

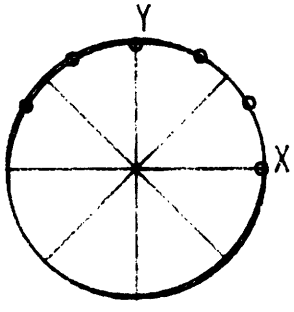

PERIMETER = 44.860
PERIM/AREA = 3.2261

ELLIPSE OF MEAN INTRCPT LENGTHS:
$A*N_1^2 + B*N_1N_2 + C*N_2^2 = MNINCPTLN^{-2}$
A = 6.238
B = -0.4023
C = 6.3959
CORRELATION COEFF = 0.670
MAX MN INTRCPT LNTH = 0.40487
ANGLE MAX ORIENTATION = 34 DEGS
MIN MN INTRCPT LNTH = 0.39124
ANGLE MIN ORIENTATION = 124 DEGS
EXTENT OF ANISOTROPY = 2.179 %

Figure 3.75a: Stereologic analysis of region "7A" from the control specimen S2.

BETH ISRAEL HOSPITAL - IMAGE PROCESSING LABORATORY

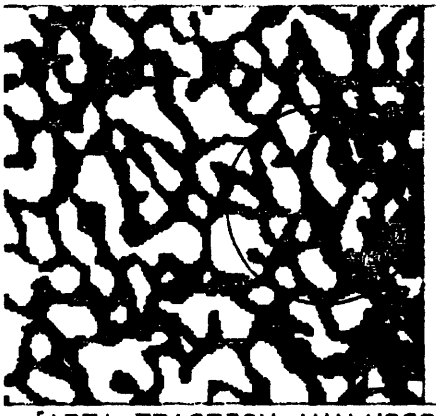

IMAGE TITLE: S2L7
COMMENT: Image 7
SUBREGION: 2
LENGTHSCALE: 57.18
GRAY THRESHOLD: 110
SOLID PHASE: BLK
TESTLINE LENGTH: 795.1
TESTLINE SPACING <PIXELS> : 1

[AREA FRACTION ANALYSIS:]
REGION AREA = 13.91

AREA FRACTION = 0.612
SOLID AREA = 8.511

[STEREOLOGY ANALYSIS:]

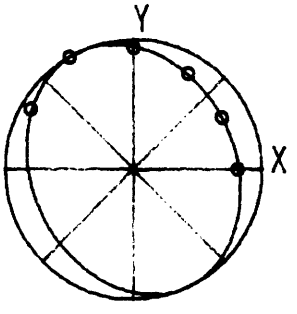

PERIMETER = 40.653
PERIM/AREA = 2.9235

ELLIPSE OF MEAN INTRCPT LENGTHS:
$A*N_1^2 + B*N_1N_2 + C*N_2^2 = MNINCPTLN^{-2}$
A = 2.667
B = 0.8254
C = 1.9879
CORRELATION COEFF = 0.995
MAX MN INTRCPT LNTH = 0.74680
ANGLE MAX ORIENTATION = 115 DEGS
MIN MN INTRCPT LNTH = 0.59112
ANGLE MIN ORIENTATION = 25 DEGS
EXTENT OF ANISOTROPY = 14.766 %

Figure 3.75b: Stereologic analysis of region "7B" from the experimental specimen S2.

approximate doubling of the stress magnitude with essentially no change in orientation. The stress predictions were, for the control patella, P_1 = 0.7 MPa and P_2 = -1.6 MPa, and for the experimental patella, P_1 = 1.6 and P_2 = -3.2. For the control patella, the principal tensile stress was well aligned with the principal material direction. However, this must be considered coincidental, considering the isotropic nature of the trabeculae. In the experimental patella, the principal compressive stress was well aligned with the principal material direction. It could be argued that the change in trabecular orientation was an adaptive response to the increase in the compressive stress component.

In summary, it did not appear that the trajectorial theory, in its simplest form, was applicable to the remodeling induced by the implants in the equine patellae. A linear regression between the principal material orientation and the principal stress orientation provided encouraging results. The alignment appeared better in areas where tension predominated, similar to the control patellae. Also similar to the control patellae, the degree of alignment was dependent on the eccentricity of the material ellipse. In contrast to the control patellae, the alignment was not necessarily better in regions with a high areal density. This was due to the presence of dense regions around the implants which were not highly oriented. A linear relationship was proposed between the change in areal density and the change in von Mises stress. This relationship provides support for the hypothesis of Fyrie and Carter (1986), that trabecular architecture corresponds to an optimum structure. Finally, the change in material

alignment appeared unrelated to the predicted change in stress alignment. Through two illustrative examples, it was suggested that, under the right conditions, small changes in the stress state can result in large changes in the measured morphologic parameters.

3.3.3 Relations for Ovine Model

The relationships between the predicted stresses and the measured morphologic parameters were examined for the experimental calcanei. The orientation of the principal material axis (Θ_{A1}) as a function of the principal stress direction which agreed most closely to the principal material direction (Θ_{PO}) is shown in Figure 3.76. For 13 out of 21 locations, Θ_{PO} corresponded to the principal stress which was maximum in absolute magnitude ($\Theta_{PO} = \Theta_{PM}$). Included in Figure 3.76 are the best fit line from a linear regression and the line $\Theta_{A1} = \Theta_{PO}$ for reference.

As in the validation of the control models (see Section 3.3.1), a linear regression between Θ_{A1} and Θ_{PO} was inappropriate. The data fell into two separate groups forming two clouds. Again, the positive angles of principal stress orientation corresponded to the compressive stress components and the negative angles corresponded to the tensile stress components. A paired t test, using Θ_{A1} and Θ_{PO}, indicated that, at a significance level of 0.05, there was no significant difference between these parameters. However, the most informative way to examine these data was the visually compare the predicted principal stress directions (Figure 3.38b) to the trabeculae in the experimental specimens (Figure 3.12b). In the anterior regions slightly removed from the implants

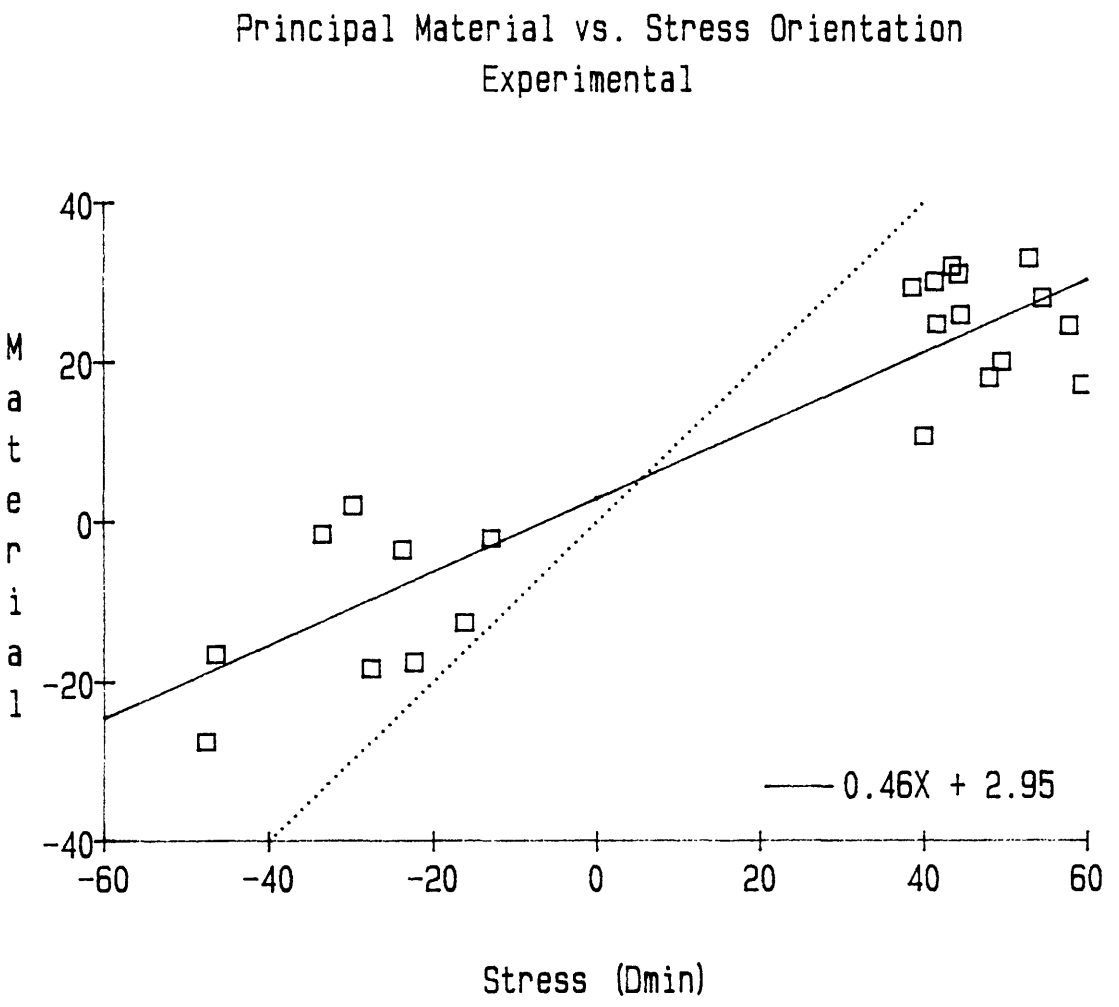

Figure 3.76: The principal stress direction which best aligned with the principal material direction (Θ_{PO}) as a function of the principal material direction (Θ_{A1}) for the experimental calcanei.

(towards the top of the figures), the orientation of the trabeculae was similar to that in the control specimens. These trabeculae were well aligned with the compressive stress components. The most important observation from the morphology of the experimental specimens was that the dense bone around the implants was not highly organized. The example stereologic analyses in Section 3.1.2 demonstrated that in some instances this dense bone resulted in a large change in the principal material orientation whereas in other instances the unaffected trabeculae resulted in little change in the principal material orientation. In summary, there was a separation of data into two groups corresponding to the regions of compressive stress and the regions of tensile stress, similar to the control specimens. However, the dense bone immediately adjacent to the implants did not appear to correspond to the principal stress vectors predicted for the experimental specimens.

The relationship between the degree of alignment ($|\Theta_{PM} - \Theta_{A1}|$) and the eccentricity of the stress ellipse for the experimental calcanei is shown in Figure 3.77. Similar to the control calcanei, the majority of points where the alignment was worse than 45 degrees had a positive stress eccentricity. Again, this was in contrast to the equine patellae. For both the control and experimental calcanei, the trabeculae were more often aligned with the compressive stress component. This is discussed further in Section 4.0.

The relationship between the degree of alignment and the material eccentricity is shown in Figure 3.78. Again, there was a tendency for

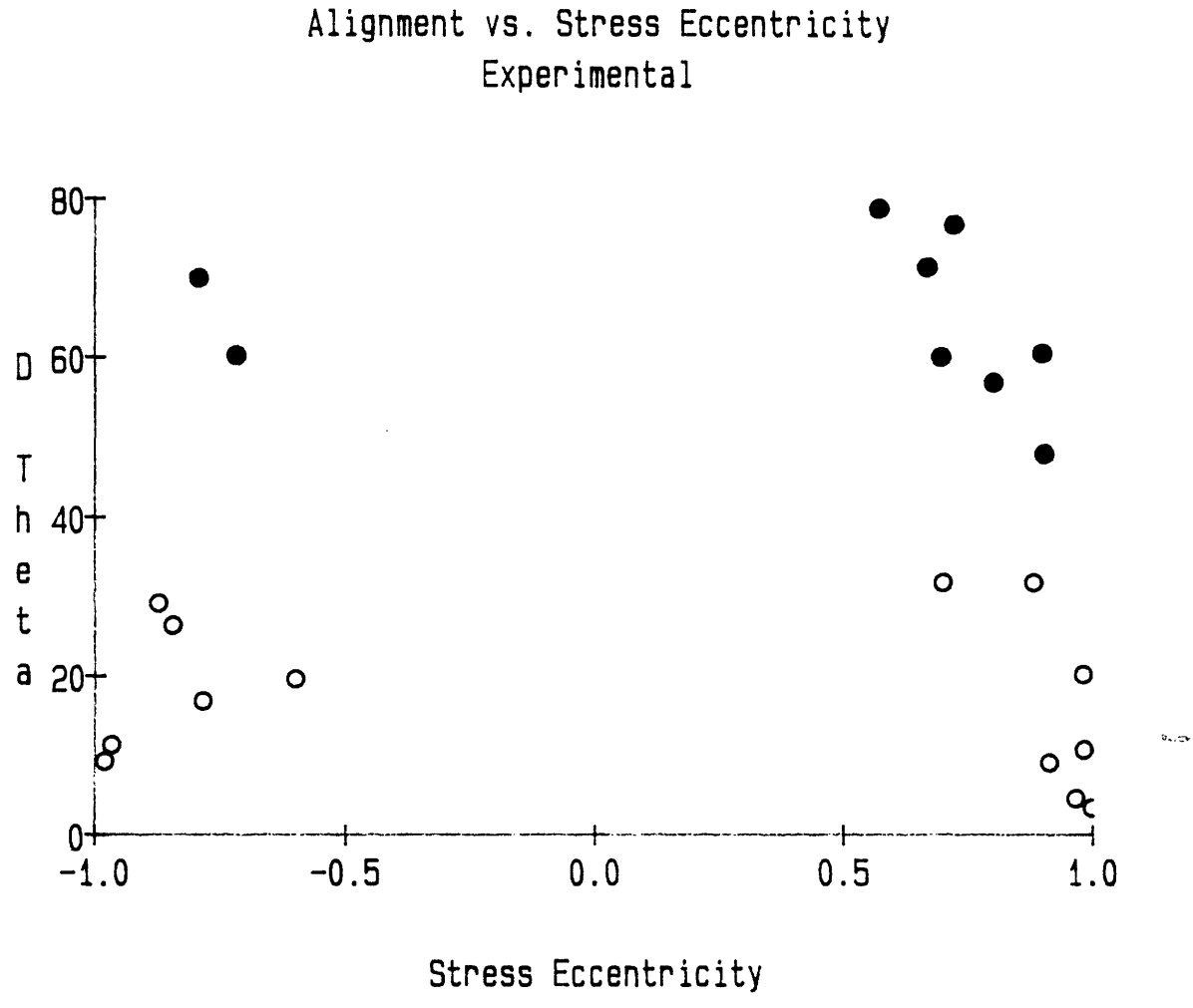

Figure 3.77: The absolute difference between the maximum principal stress direction and the principal material direction ($|\Theta_{PM} - \Theta_{A1}|$) as a function of the eccentricity of the stress ellipse for the experimental calcanei.

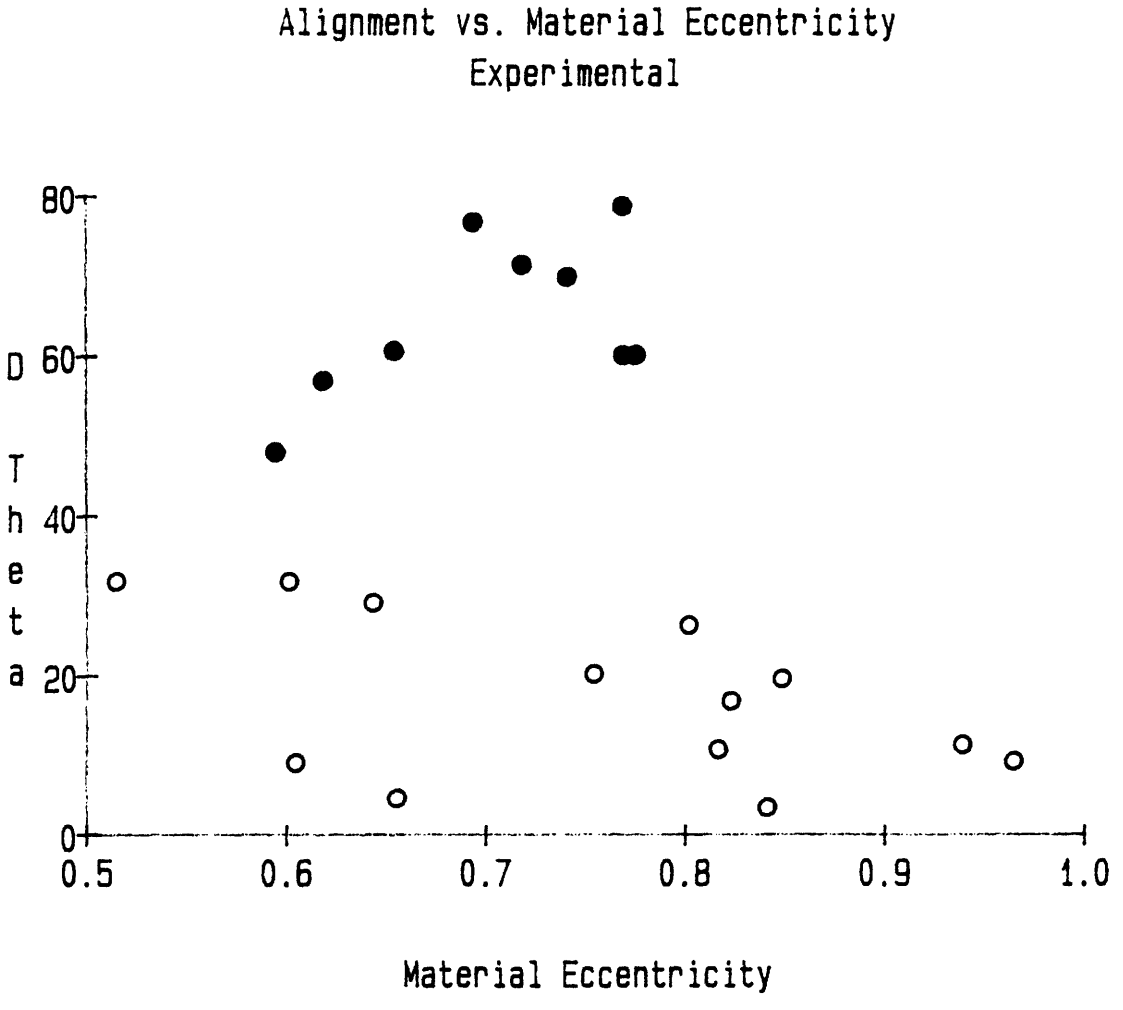

Figure 3.78: The absolute difference between the maximum principal stress direction and the principal material direction ($|\Theta_{PM} - \Theta_{A1}|$) as a function of the eccentricity of the material anisotropy ellipse for the experimental calcanei.

worse alignment with lower material eccentricities. Both the control and experimental models of the equine patellae and the ovine calcanei demonstrated that the alignment of the principal stresses with the trabeculae in more isotropic regions tended to be worse than the alignment in very highly oriented regions.

To examine the relationship between an effective stress measure and the trabecular bone density, the von Mises stress was plotted as a function of the areal density for both the control and experimental calcanei (Figure 3.79). There was more scatter in the experimental data, but it still appeared that a single linear relationship was applicable. The linear regression, included in the figure, had a significance of 0.001, standard deviation of 1.50, and R^2 of 0.234.

To further examine the predictive value of the von Mises effective stress, the change in the trabecular bone areal density was examined as a function of the change in the von Mises stress (Figure 3.80). The linear regression, included in the figure, had a significance of 0.001, standard deviation of 0.10, and R^2 of 0.18. The slope for the ovine calcanei was equal to 0.027 $(MPa)^{-1}$ in comparison to 0.108 $(MPa)^{-1}$ for the equine patellae. However, these cannot be directly compared because the slope is dependent on the load magnitude. As the load magnitude is increased, the slope is decreased. In summary, there was a weak linear relationship between the change in trabecular bone areal density and the change in von Mises effective stress.

Finally, the comparison was made between the changes in the

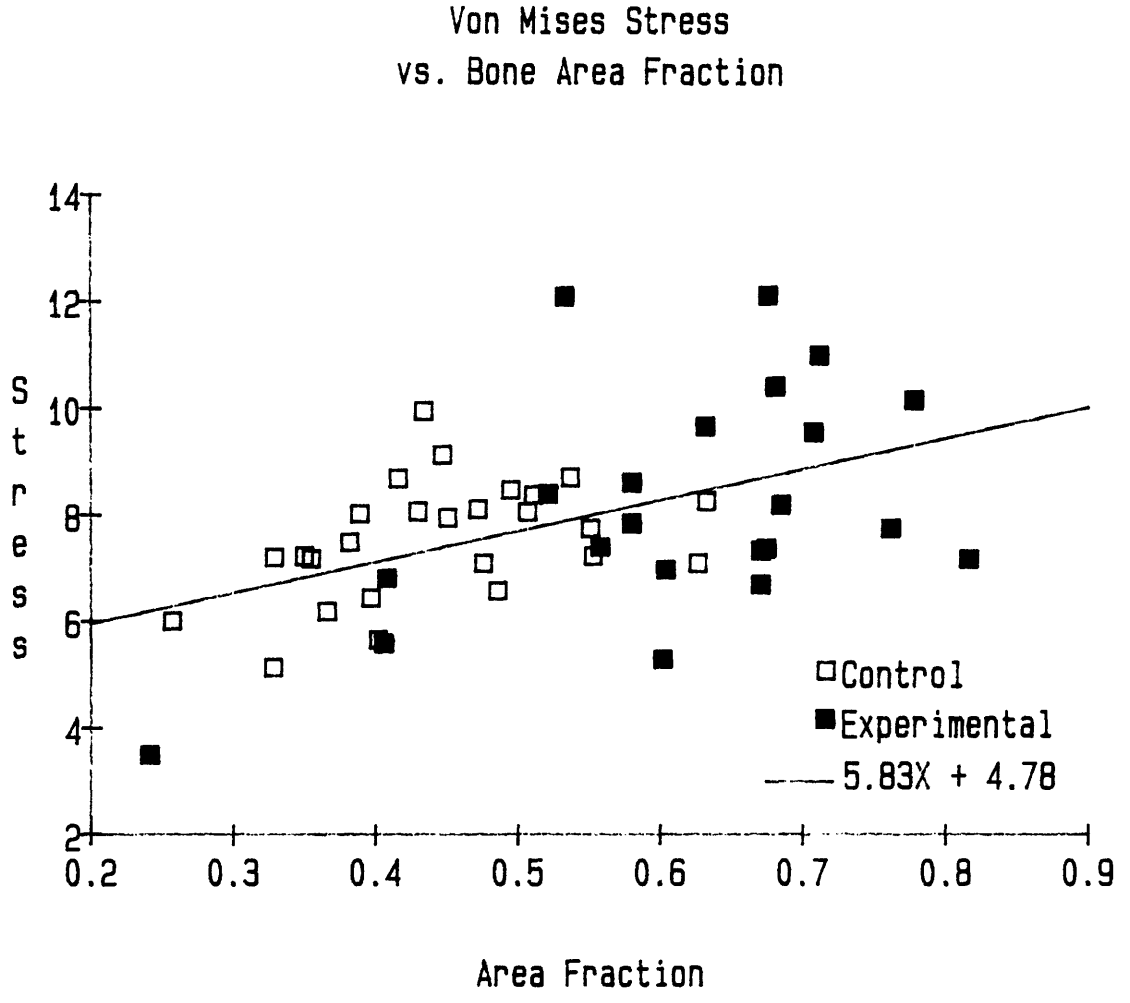

Figure 3.79: Von Mises effective stress (MPa) as a function of the trabecular bone areal density for both the control and the experimental calcanei.

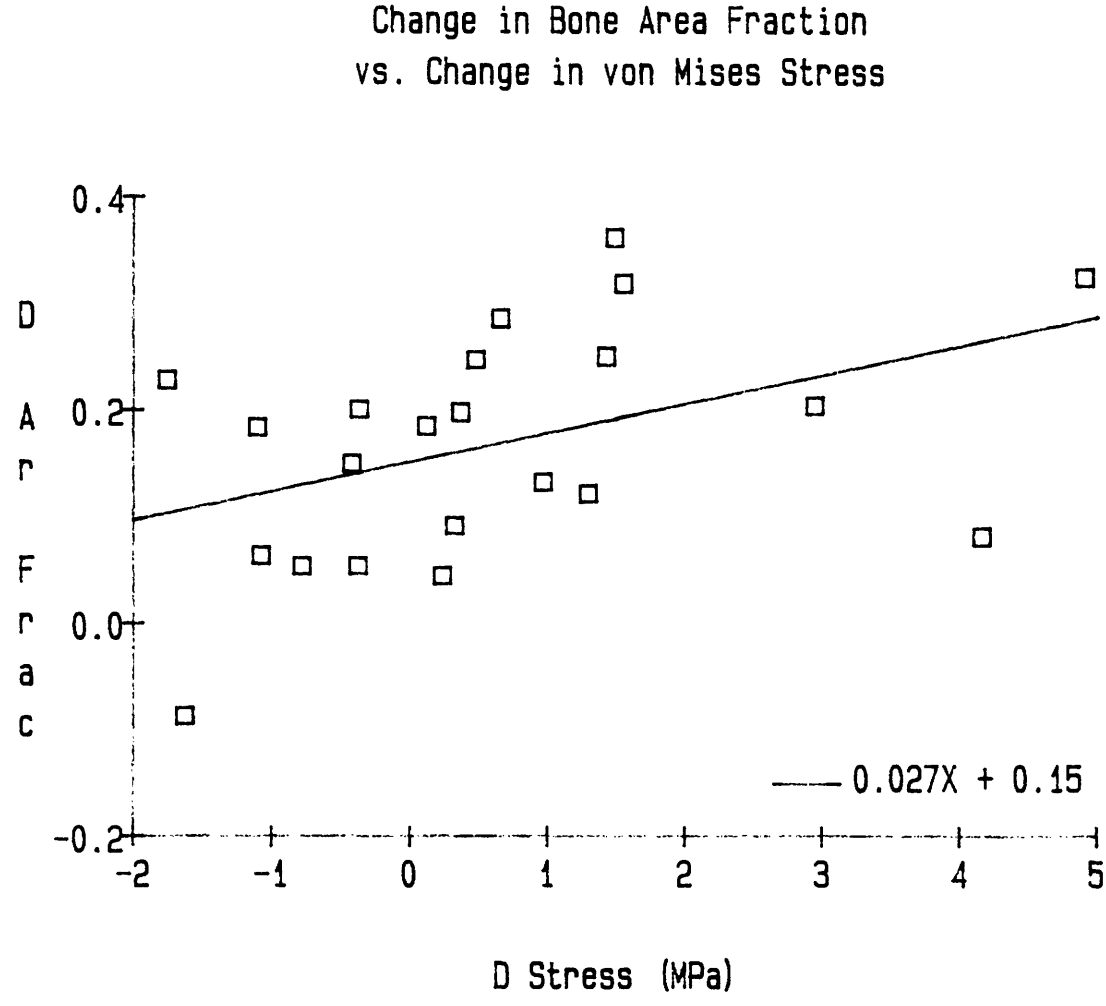

Figure 3.80: The difference in trabecular bone areal density between the experimental and control calcanei as a function of the difference in von Mises stress between the experimental and control calcanei.

orientation of the principal stresses and the changes in the orientation of the trabeculae (Figure 3.81). The line Y = X was included for reference. As in the equine models, there was no correlation between these parameters. The changes in the trabecular orientation tended to be greater than the changes in the principal stress orientation. This was due to the influence of the very dense bone immediately adjacent to the implants as discussed above.

In summary, the remodeling response immediately adjacent to the implants did not correspond to the predictions of the trajectorial theory of trabecular architecture. This very dense remodeled bone was not highly organized and the influence on the principal material directions was unpredictable. However, in agreement with the equine patellae, there was a weak linear relationship between the change in areal density and the change in von Mises stress.

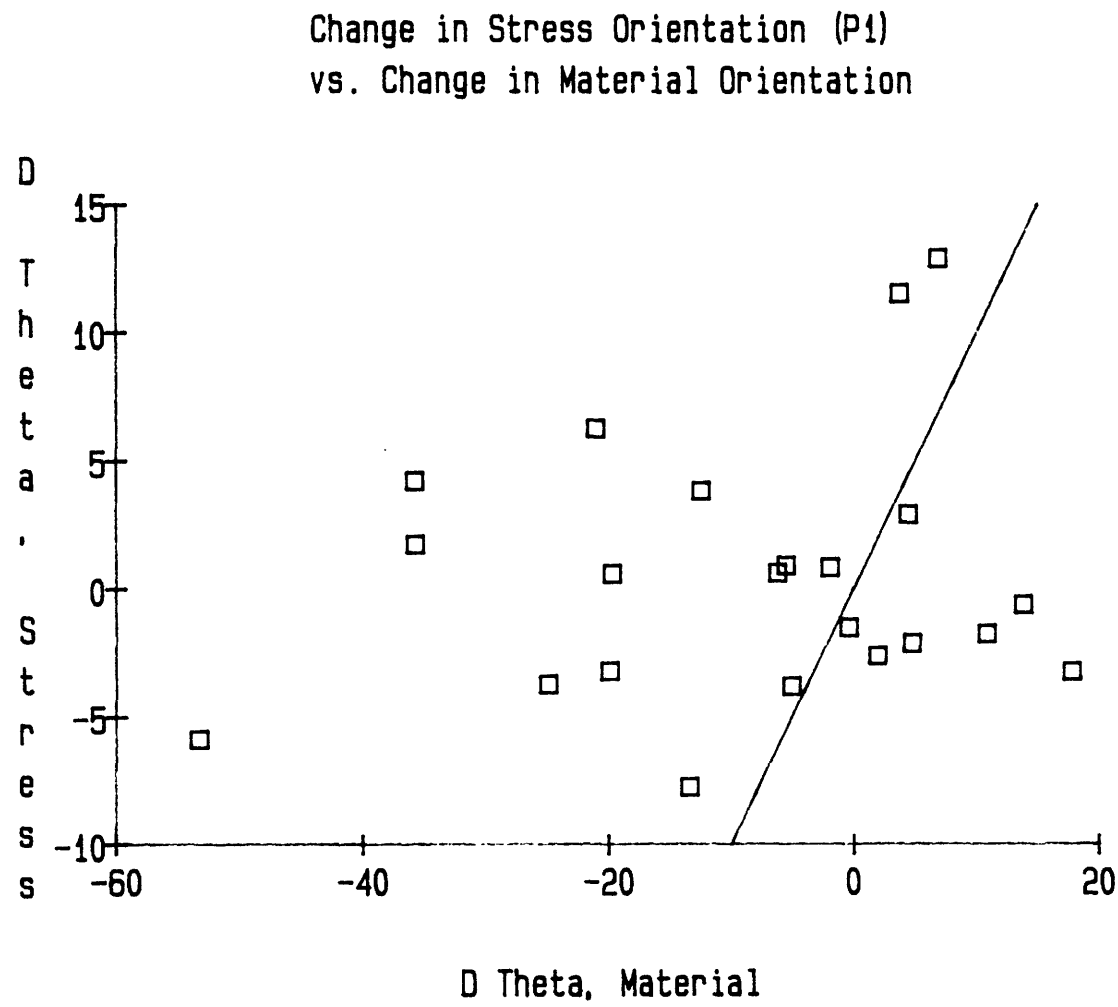

Figure 3.81: The difference in the direction of principal stress P_1 between the experimental and the control calcanei as a function of the difference in the direction of principal material orientation between the experimental and the control calcanei.

4.0 Discussion

The objective of this investigation was to examine the stress-morphology relationships around implants of various material and surface properties. To address this objective, two experimental models were developed, one using cylindrical implants in ovine calcanei and the other using spherical implants in equine patellae. For each model, the first objective was to validate the stress predictions of the control specimens based on the assumption that the directions of principal stress were aligned with the directions of principal material anisotropy. The second objective was to examine the stress-morphology relationships in the experimental specimens based on the assumption that the stress predictions were accurate.

One of the equine patellae had an infection which was at least partially resolved with antibiotics. This implant was surrounded by a thick fibrous tissue layer with no bone ingrowth. This specimen was included in the present study based on the assumption that the infection was effectively isolated from the bone tissue. It was also assumed that the fibrous tissue effectively removed the implant mechanically and thus was similar to a void. It is not known whether the infection had any other direct effect on the remodeling of the trabecular bone. However, infections are relatively common in clinical orthopaedics, and it is important to have data on the remodeling response in the presence of an infection.

The assumption that the trajectorial theory of trabecular bone

architecture holds for the control specimens can be challenged by considering that the applied external loads, and therefore the internal stresses, on the ovine calcaneus and equine patella are time varying. This is particularly true for any bone which participates in gait. While parametric load studies would provide a more complete representation, the justification for examination of a single loading condition is that, through proper selection, the cyclic loads during gait may be represented by a single "effective" load case. It is the selection of this applied load which is probably the weakest link in the analyses of the equine patellae. As discussed in Section 2.2.1, the loads on the equine patella are particularly complex. While further study of these loads might strengthen the present analyses, the demonstrated correspondence between the principal material and stress directions supports the validity of the applied loads and the finite element predictions on the whole.

The present investigation could be strengthened by the inclusion of more rigorous controls. One appropriate control experiment would be to drill the bone in preparation for an implant but close the wound without inserting an implant. Alternatively, a low modulus biologically inert material could be implanted. However, an adaptive remodeling response would be expected due to the effect of a void on the stresses. A better control experiment would be to implant a porous material which has the same modulus as the trabecular bone. This would minimize the changes in the trabecular bone stresses due to the implant. The observed remodeling would be primarily due to the biologic effects of the surgical procedure.

The ovine calcaneus proved to be a less than satisfactory model for the investigation of stress-morphology relationships. This was primarily due to the coarse trabecular architecture in the calcaneus. The selection of the regions for stereologic analysis required that the trabecular bone be homogeneous and that there be a significant number of trabeculae in each region. The coarse architecture made this especially difficult in the calcaneus.

Another problem with the ovine model may have been that the remodeling period was too short. The remodeling was apparently limited to a 2 mm distance from the implants. In general, the trabecular architecture around implants can be expected to correlate more closely with the stress state as the remodeling period is extended. Future experiments for the investigation of the long term response to implants should employ remodeling periods which are longer than those in the present study.

One likely criticism of the present investigation is that the stress-morphology comparisons were limited to two dimensions. However, the planes which were examined were the most important planes in terms of the three-dimensional stresses. It was clear that the sagittal plane was the critical plane for the ovine calcaneus since the load from the tendo calcaneus was in this plane. The maximum loads applied to the equine patellae also were approximately in the sagittal plane. As reported in Section 3.1.2, on the average, 80 % of the strain energy was accounted for by considering only the sagittal plane. It can be argued that by examining only the most critical planes, the likelihood of

obtaining valid and convincing stress-morphology correlations was increased.

The mathematical similarities between the Lame' stress ellipse and the material anisotropy ellipse suggest that further comparisons, besides the orientation of the principal axes, may be appropriate. One such comparison is to relate the eccentricity of the stress ellipse to the eccentricity of the anisotropy ellipse. However, in general, this comparison demonstrated no correspondence between these parameters for the present data. A positive correlation between these parameters would imply that the trabecular bone in areas of uniaxial stress would be highly oriented. This was true for some locations near the anterior cortical shell of the equine patellae. It would also imply that the trabecular bone in areas of pure shear stress would be nearly isotropic. The present models are inconclusive on this point due to insufficient data in which the stress state approached pure shear. The primary reason that there was no correspondence between the eccentricity of the stress and material ellipses was that there were many instances in which the stress state was highly eccentric but the material was not. One explanation is the previously discussed limitation of the examination of a single load case. The in vivo stresses may be highly oriented but also may significantly vary in direction during the gait cycle. The morphologic response to such conditions may, very logically, result in an isotropic architecture.

The examination of material eccentricity did demonstrate one important relationship. The models of the control specimens clearly

demonstrated that the degree of alignment between the stress and material directions is dependent on the degree of material eccentricity. For trabecular bone which is nearly isotropic, the alignment tends to be worse, since the morphologic data is subject to greater error. This also points to a weakness inherent in the stereology methods applied in this study. The anisotropy ellipse is a circle both for regions with randomly oriented trabeculae and for regions with two equal and orthogonal directions of oriented trabeculae. Fortunately, in regions of trabecular bone with two orthogonal directions of oriented trabeculae, one of these directions will generally dominate. This was demonstrated using an example from the equine patellae in Section 3.3.2. As the contribution from each of the two directions becomes more equal, and the material appears more isotropic, the meaning of the predicted direction of material orientation is diminished.

A very important finding from the models of the equine patellae was that the alignment between the maximum principal stress and the principal material axis was better in regions where tension was the predominant stress. There were also a number of instances where the material was aligned with the tensile stress component in regions where compression was the predominant stress. Stone et al. (1984) similarly found better alignment of the principal material direction with the tensile stress component for a three-dimensional model of the human patella. One possible explanation is the fact that bone tissue is weaker in tension than in compression, and thus, to compensate, more trabecular struts are formed in the direction of tension. A second explanation is that cross struts are formed to resist buckling of the

trabeculae which are in compression. Pugh et al. (1973a) demonstrated the importance of bending and suggested that cross struts were an effective stiffening mechanism. This mechanism was supported by the data points from the control patellae in which the stress state was near uniaxial compression yet the material was oriented in the orthogonal direction. The present data are insufficient to draw a conclusion but both mechanisms probably have a role in determining the trabecular architecture.

The most striking finding from the morphology of the experimental specimens were the increased trabecular areal densities adjacent to the implants. The least dramatic increase in areal density occurred around the implants with successful porous ingrowth. This supports the premise that the remodeling changes were critically influenced by the stresses at the bone/implant interface. In the equine patellae, the surface area of the porous coated implants was much greater than that of the smooth implants. If the density changes were a result of a foreign body response, rather than stress adaptation, the changes around the porous implants would have been much greater. However, the correlation between the stress changes and the morphologic changes adjacent to the implants were not conclusive. This may be due to limitations of the applied techniques. The stereologic method requires that the analyses be performed on circular regions of homogeneous architecture. The circular geometry results in only a small fraction of the trabeculae immediately adjacent to the implants included in the regions of analysis. As a result, the morphologic data from the bone/implant interface is essentially lost. Furthermore, the finite element predictions at this

interface are inadequate. The continuum assumption is no longer valid due to the inhomogeneity of the trabecular architecture. Examination of trabecular remodeling within several trabecular widths of the implants requires the use of microstructural models. One possibility is the application of structural optimization to these trabeculae. Snyder et al. (1983) reported results from a model of the human patella. Their study, however, was limited to the representation of pin-jointed truss elements, which are clearly inadequate for the modeling of individual trabeculae. More complex microstructural models of trabecular bone have been developed (see Section 1.1.3), but these models did not apply structural optimization techniques to predict changes in trabecular density and orientation. The development of microstructural models of stress adaptive trabeculae is a promising area for future research.

Most of the experimental specimens exhibited a region of very dense trabecular bone immediately adjacent to the implants. The only exceptions were the two porous coated spheres with bone ingrowth in the equine patellae. This dense region was poorly defined and discontinuous around the porous cylinders in the ovine calcanei. However, there was a well defined layer of compact bone around the smooth spheres in the equine patellae. This finding was similar to the corticalization of the trabecular bone around smooth implants described in the literature (Brown et al. 1984; Medige et al. 1982). Hedley et al. (1982) reported that there was a plate of dense trabecular bone adjacent to ingrown porous femoral surface components in canines. This region is critically important for the stabilization of prosthetic components and thus the mechanical parameters which govern the formation and maintenance of this

dense layer of bone should be delineated. The present investigation did not specifically address this region due to limitations of both the finite element models and the stereologic analyses. This dense layer was about 1 mm thick around the smooth implants whereas the finite elements were typically several mm in each dimension. The continuum assumption implicit to the finite element models is invalid at the microstructural level. Furthermore the circular regions for the stereologic analyses had a diameter of 4.2 mm. As a consequence, this dense layer occupied a very small portion of the images adjacent to the implants. Analysis of this dense layer requires the application of microstructural modeling techniques. However, it is apparent from the literature that the most critical parameter controlling the morphologic response at the bone/implant interface is the presence and magnitude of relative motion between the implant and the adjacent trabecular bone (see Section 1.2.2). No relative motion should have occurred in the present specimens since the implants were surrounded by trabecular bone. This accounts for the minimal thickness of this layer around the smooth implants and the total lack of a compact layer around the ingrown porous implants.

It should be re-emphasized that the present investigation was designed to study the structural aspects of the remodeling of trabecular bone around implants. The objective of this investigation was not to prove or disprove Wolff's Law. While the results do indicate that the stresses have a critical role in determining the remodeling response around implants, the degree to which stress did not correlate with the remodeling response should be interpreted as either a reflection of the

model inaccuracies or an indication that stress may not be the only important parameter. Unfortunately, the previously discussed limitations of the present investigation do not allow for a conclusive statement as to the exact relationship between the stresses and the trabecular architecture. If the objective of an investigation is to study Wolff's Law, then the experimental design should be such that the induced remodeling is not due to the presence of foreign materials, to avoid possible influences outside the realm of stress-adaptive remodeling.

The results of this investigation should provide encouragement for the further development of prostheses which do not rely on acrylic bone cement for fixation. The morphologic response of the trabecular bone to the implants was generally a positive one in terms of maintenance of viable bone at the implant boundary. The only exception was due to an infection in one of the equine patellae. For all specimens, both porous and smooth, there was no evidence of net bone resorption around the implants. The results indicate that reasonable changes from the physiologic stress conditions at an implant boundary are acceptable. Admittedly, the stress conditions at the bone/implant interface in the present models were not extreme, since the implants were not directly loaded. The experimental design did not allow for the examination of stress protection or excessive stress concentration. This study does, however, provide the basis for future studies of remodeling around implants which have extremes in stress conditions such as may be expected for total joint replacements.

This investigation provides the framework for future investigations of stress-morphology relationships in implant-induced remodeling. The design of the next experiment should employ implants with more severe stress conditions at the bone/implant interface and surrounding trabecular bone. One possible design would be to detach a tendon, insert a rectangular or cylindrical implant into a metaphyseal region, and reattach the tendon to the implant. The greater trochanter and hip abductors may be a practical site. However, the normal trabecular architecture as well as the normal geometry and loading conditions should be carefully considered prior to experimentation.

5.0 Conclusion

The objective of this investigation was to examine the stress-morphology relationships for trabecular bone around implants for which there was a controlled and predictable alteration in the stress fields. For this purpose two different experimental models were developed using geometrically simplified implants of various materials and surface conditions. Cobalt chromium cylinders with a sintered-bead porous coating were implanted unilaterally into ovine calcanei and stainless steel spheres with either a polished surface or a sintered-bead porous coating were implanted unilaterally into equine patellae. The animals were maintained for periods of 10 to 24 weeks. Stereologic methods were then used to quantify the morphology of the trabecular bone in the experimental specimens and the untreated contralateral controls. Structural analyses were performed using the displacement-based finite element method to predict the stresses surrounding the implants.

There was a significant remodeling response around the implants in all of the experimental specimens. The ovine calcanei had a significant increase in the bone areal density within 2 mm of the ingrown porous implants but no significant changes in areal density beyond 2 mm. The observed remodeling in the equine patellae was a function of the implant surface conditions. The most extensive remodeling occurred adjacent to a porous coated implant which was encapsulated by a thick fibrous tissue layer. This implant had a partially treated infection which may have influenced the remodeling response. In general, the remodeling response around the smooth implants was greater than that around those porous

implants which exhibited bone ingrowth. In accordance with these differences, the finite element models predicted greater changes in the stresses adjacent to the smooth implants due to the nonlinear boundary conditions.

The finite element models were validated by comparing the principal stress directions with the material orientation in the control specimens. The critical assumption was that the trajectorial theory of trabecular architecture holds for the control specimens. A linear regression between the principal stress orientation and the principal material orientation was not possible for the ovine specimens due to a poor distribution of data. A paired t test between the principal stress orientation and the principal material orientation indicated that there was no significant difference between these parameters. Furthermore, the model predictions appeared reasonable based on visual comparison of the principal stress vectors to the trabeculae in the control specimens. The models of the control equine patellae were validated with an R^2 = 0.87. In both models, the trabeculae were most often aligned with the stress component of the greatest magnitude. However, in the equine models, the alignment was better in regions where tension predominated. This provides support for the hypothesis that cross struts are formed to resist buckling of the trabeculae which are under compression.

The alignment of the principal stresses with the principal trabecular directions in the experimental ovine calcanei could not be evaluated satisfactorily. The trabeculae beyond 2 mm from the implants appeared to be relatively unaffected by the presence of the implants.

The stereologic analyses adjacent to the implants gave unreliable results due to the disorganized dense bone which was formed within 2 mm of the implants. Overall, the ovine calcaneus proved to be a unsatisfactory model for the investigation of stress-morphology relationships due to the coarse trabecular architecture.

To evaluate the stress-morphology relationships in the experimental patellae, the orientation of the trabeculae were compared with the orientation of the principal stresses. The critical assumption for this comparison was that the predictions of the finite element models of the experimental specimens were accurate. A linear regression between the principal stress and material orientations resulted in an $R^2 = 0.89$. However, there was no correlation between the changes in direction of principal stress and the changes in the direction of trabecular orientation. Through two examples, it was demonstrated that, under certain circumstances, small changes in the stress state may result in large changes in the principal trabecular orientation. Both models demonstrated a linear relationship between the change in bone areal density and the change in von Mises effective stress. This relationship provides support for the hypothesis that the architecture of trabecular bone corresponds to an optimal structure.

6.0 Bibliography

Albright, J., R. Martin, and R. Flohr (1978) Automatic image analysis of the bone biopsy: variations in rib architecture. Microscope **26**:15-34.

Almby, B., and T. Hierton (1982) Total hip replacement: A ten year follow up of an early series. Acta Orthop Scand **53**:397.

Amstutz, H.C., S.M. Ma, R.H. Jinnah, and L. Mai (1982) Revision of aseptic loose total hip arthroplasties. Clin Orthop Rel Res **170**:21-33.

Andersson, G.B.J., M.A.R. Freeman, and S.A.V. Swanson (1972) Loosening of the cemented acetabular cup in total hip replacement. J Bone Joint Surg **54B**:590-599.

Bathe, K-J. (1982) Finite Element Procedures in Engineering Analysis. Englewood Cliffs, Prentice-Hall, Inc.

Bathe, K-J., and A. Chaudhary (1985) A solution method for planar and axisymmetric contact problems. Int J Num Met Eng **21**:65-88.

Beaupre, G.S., and W.C. Hayes (1985) Finite element analysis of a three-dimensional open-celled model for trabecular bone. J Biomech Eng **107**:249-256.

Beckenbaugh, R.D., and D.M. Ilstrup (1978) Total hip arthoplasty: A review of 333 cases with long follow up. J Bone Joint Surg **60A**:306-313.

Beddoe, A.H. (1978) A quantitative study of the structure of trabecular bone in man, rhesus monkey, beagle and miniature pig. Calcif Tiss Res **25**:273-281.

Behrens, J.C., P.S. Walker, and H. Shoji (1974) Variations in strength and structure of cancellous bone at the knee. J Biomech 7:201-207.

Bobyn, J.D., R.M. Pilliar, H.U. Cameron, and G.C. Weatherly (1980) The

optimum pore size for the fixation of porous-surfaced metal implants by the ingrowth of bone. Clin Orthop Rel Res **150**:263-270.

Bocco, F., P. Langan, and J. Charnley (1977) Changes in the calcar femoris in relation to cement technology in total hip replacement. Clin Orthop Rel Res **128**:287-295.

Brown, T.D., E.L. Radin, R.B. Martin, and D.B. Burr (1984) Finite element studies of some juxtarticular stress changes due to localized subchondral stiffening. J Biomech **17**:11-24.

Cameron, H.U., R.M. Pilliar, B.T. Yoneda, and I. Macnab (1973) The effect of movement on the bonding of porous metal to bone. J Biomed Mat Res **7**:301.

Carlsson, A.S., and C.F. Gentz (1980) Mechanical loosening of the femoral head prosthesis in the Charnley total hip arthroplasty. Clin Orthop Rel Res **147**:262.

Carter, D.R., and W.C. Hayes (1977) The compressive behavior of bone as a two-phase porous structure. J Bone Joint Surg **59A**:954-962.

Carter, D.R., G.H. Schwab, and D.M. Spengler (1979) The effect of apparent density on the tensile and compressive properties of cancellous bone. 25th Annual ORS **4**:87.

Chandler, H.P., F.T. Reineck, R.L. Wixson, and F.C. McCarthy (1981) Total hip replacement in patients younger than thirty. J Bone Joint Surg **63A**:1426.

Charnley, J., and Z. Cupic (1973) The nine and ten year results of the low-friction arthroplasty of the hip. Clin Orthop Rel Res **95**:9-25.

Cook, S.D., R.C. Anderson, H.B. Skinner, and A.M. Weinstein (1983) An evaluation of direct skeletal attachment mechanisms for hip prostheses. Trans 29th ORS **8**:158.

Cook, S.D., J.J. Klawitter, and A.M. Weinstein (1982) A model for the implant-bone interface characteristics of porous dental implants. J Dent Res **61**:1006-1009.

Cooley, J.W., and J.W. Tukey (1965) An algorith for the machine calculation of complex Fourier series. Math of Comput **19**:297-301.

Cotterill, P., G.A. Hunter, and M. Tile (1982) A radiographic analysis of 166 Charnley-Muller total hip arthroplasties. Clin Orthop Rel Res **163**:120.

Cowin, S.C., R.T. Hart, D.H. Kohn, J.B. Meade, N.G. Sepulveda, and W. C.V.a.n. Buskirk (1984) Surface remodeling in long bone: a comparison of model predictions with animal experiments. 30th Annual ORS **9**:200.

Cowin, S.C., and D.H. Hegedus (1976) Bone remodeling I: theory of adaptive elasticity. J Elast **6**:313-326.

Crowninshield, R.D., R.A. Brand, R.C. Johnston, and J.C. Milroy (1980) An analysis of femoral component stem design in total hip arthroplasty. J Bone Joint Surg **62**A:68-78.

Cuthill, E., and J. McKee (1969) Reducing the bandwidth of sparse symmetric matrices. Proc ACM Nat Conf, San Fran, 157-172.

Dehoff, R.T., and F.N. Rhines (1968) Quantitative Microscopy. New York, McGraw-Hill, Inc.

Doty, S.B. (1981) Morphological evidence of gap junctions between bone cells. Calcif Tiss Int **33**:509-512.

Ducheyne, P., E. Aernoudt, P.D. Meester, M. Martens, J.C. Mulier, and D.V. Leeuwen (1978) Factors governing the mechanical behavior of the implant-porous coating-trabecular bone interface. J Biomech **11**:297-307.

Dunn, A.W. (1982) Total hip arthroplasty: Review of long-term results in

185 cases. South Med J 75:937.

Eftekhar, N.S. (1983) Total knee arthroplasty. Results with the intramedullary adjustable total prosthesis. J Bone Joint Surg 65A:293-309.

Engh, C.A. (1983) Hip arthroplasty with a Moore prosthesis with porous coating - A five year study. Clin Orthop Rel Res 176:52-66.

Feith, R. (1975) Side-effects of acrylic cement implanted into bone. A histological, (micro)angiographic, fluorescence-microscopic, and autoradiographic study in the rabbit femur. Acta Orthop Scand (Suppl) 161.

Ferry, J.D. (1970) Viscoelastic Properties of Polymers. New York, John Wiley and Sons, Inc.

Freeman, M.A.R., S.A.V. Swanson, B. Vernon-Roberts, and B. Weightman (1977) The Scientific Basis of Joint Replacement. New York, John Wiley and Sons Inc.

Frost, H.M. (1969) Tetracycline-based histological analysis of bone remodeling. Calcif Tiss Res 3:211-237.

Fukada, E., and I. Yasuda (1957) On the piezoelectric effect in bone. J Phys Soc Japan 12:1158.

Fyhrie, D.P., and D.R. Carter (1986) A unifying principle relating stress to trabecular bone morphology. J Orthop Res (accepted for publication).

Galante, J. (1971) Total hip replacement. Orthop Clin North Am 2:139-155.

Galante, J., W. Rostoker, and R.D. Ray (1970) Physical properties of trabecular bone. Calcif Tissue Res 5:236-246.

Getty, R. (1975) Sisson and Grossman's The Anatomy of the Domestic Animals. Philadelphia, W. B. Saunders Co.

Gibbs, N.E., W.G. Poole, and P.K. Stockmeyer (1976) An algorithm for reducing the bandwidth and profile of a sparse matrix. Siam J Numer Anal **13**:236-250.

Gibson, L.J. (1985) The mechanical behaviour of cancellous bone. J Biomech **18**:317-328.

Goldring, S.R., A.L. Schiller, M. Roelke, C.M. Rourke, D.A. O'Neil, and W.H. Harris (1983) The synovial-like membrane at the bone- cement interface in loose total hip replacements and its proposed role in bone lysis. J Bone Joint Surg **65**A:575-584.

Green, T.A., G.M. McNeice, and H.C. Amstutz (1979) 'Modes of failure' of cemented stem-type femoral components. A radiographic analysis of loosening. Clin Orthop Rel Res **141**:17-27.

Gross, D., and W.S. Williams (1982) Streaming potential and the electromechanical response of physiologically-moist bone. J Biomech **15**: 277-295.

Gunst, M.A. (1980) Interference with bone blood supply through plating of intact bone. In H.K. Uhthoff (ed): Current Concepts of Internal Fixation of Fractures. New York, Springer-Verlag.

Hahn, H., and W. Palich (1970) Preliminary evaluation of porous metal surfaced titanium for orthopedic implants. J Biomed Mat Res **4**:571-577.

Hamilton, L.R. (1982) UCI total knee replacement. A follow-up study. J Bone Joint Surg **64**A:740-744.

Hampton, S.J., and T.P. Andriacchi (1980) An analytical representation of the non-linear interface condition in a bone- cement-prosthesis system. Int Conf on Finite Elements in Biomech **1**:193-206.

Harrigan, T.P. (1985) Bone Compliance and Its Effects in Human Hip Joint Lubrication. Cambridge, M.I.T. Ph.D. Thesis.

Harrigan, T.P., D.R. Carter, R.W. Mann, and W.H. Harris (1981) The influence of apparent density and trabecular orientation on the elastic medulus of cancellous bone. 27th ORS **6**:277.

Harrigan, T.P., and R.W. Mann (1984) Characterization of microstructural anisotropy in orthotropic materials using a second rank tensor. J Mater Science **19**:761-767.

Harris, W.H., F.C. McCarthy, and D.A. ONeill (1982) Femoral component loosening using contemporary techniques of femoral cement fixation. J Bone Joint Surg **64**:1063-1067.

Harris, W.H., R.E. White, J.C. McCarthy, P.S. Walker, and E.H. Weinberg (1983) Bony ingrowth fixation of the acetabular component in canine hip joint arthroplasty. Clin Orthop Rel Res **176**:7-11.

Hart, R.T., D.T. Davy, and K.G. Heiple (1984) A computational method of stress analysis of adaptive elastic materials with a view toward applications in strain-induced remodeling. J Biomech Eng **106**:342-350.

Hayes, W.C., and D.R. Carter (1976) Postyield behaviour of subchondral trabecular bone. J Biomed Mat Res Symp **7**:537-544.

Hayes, W.C., B. Snyder, B.M. Levine, and S. Ramaswamy (1982) Stress-morphology relationships in trabecular bone of the patella. In R. H. Gallagher, B.R. Simon, P.C. Johnson, and J.F. Gross (eds): Finite Elements in Biomechanics. New York, John Wiley & Sons, Inc., pp. 223-268.

Hearmon, R.F.S. (1961) An Introduction to Applied Anisotropic Elasticity. London, Oxford University Press.

Hedley, A.K., I.C. Clarke, S.C. Kozinn, I. Coster, T. Gruen, and H.C.

Amstutz (1982) Porous ingrowth fixation of the femoral component in a canine surface replacement of the hip. Clin Orthop Rel Res **163**:300-311.

Heimke, G., D. Stock, W. Seiwert, M. Busing, and J. Gottstein (1985) Load pattern controlled osseo integration of Al203 ceramic hip sockets and stepped stems of a vanadium-free titanium alloy. In S. M. Perren and E. Schneider (eds): Biomechanics: Current Interdisciplinary Research. Dordrecht, Martinus Nijhoff Publishers, pp. 141-146.

Hilliard, J.E. (1962) Specification and measurement of microstructural anisotropy. Trans Metall Soc AIME **224**:1201-1211.

Hipp, J.A., J.B. Brunski, M.S. Shephard, and G.V.B. Cochran (1985) Finite element models of implants in bone: interfacial assumptions. In S.M. Perren and E. Schneider (eds): Biomechanics: Current Interdisciplinary Research. Dordrecht, Martinus Nijhoff Publishers, pp. 447-452.

Hirschhorn, J.S., and J.T. Reynolds (1969) Powder metallurgy fabrication of cobalt alloy surgical implant materials. In E. Korostoff (ed): Research in Dental and Medical Materials. New York: Plenum Press, p. 137.

Homsy, C.A., T.E. Cain, F.B. Kessler, M.S. Anderson, and J.W. King (1972) Porous implant systems for prosthesis stabilization. Clin Orthop Rel Res **89**:220-235.

Huberti, H.H., and W.C. Hayes (1984) Patellofemoral contact pressures: The influence of Q-angle and tendofemoral contact. J Bone Joint Surg **66A**:715-724.

Huiskes, R. (1980) Some fundamental aspects of human joint replacement. Acta Orthop Scand (Suppl).

Insall, J.N., R.W. Hood, L.B. Flawn, and D.J. Sullivan (1983) The total condylar knee prosthesis in gonarthrosis. A 5-9 year follow- up of the

first 100 consecutive replacements. J Bone Joint Surg 65A:619-628.

Insall, J.N., P.F. Lachiewicz, and A.H. Burstein (1982) The posterior stabilized condylar prosthesis: A modification of the total condylar design. J Bone Joint Surg 64A:1317-1323.

Insall, J.N., C.S. Ranawat, P. Aglietti, and J. Shine (1976) A comparison of four models of total knee replacement prosthesis. J Bone Joint Surg 58A:754-765.

Insall, J.N., N.W. Scott, and C.S. Ranawat (1979) A total condylar knee prosthesis. A report of two hundred and twenty cases. J Bone Joint Surg 61A:173-180.

Itami, Y., N. Akamatsu, Y. Tomita, and M. Nagai (1982) The direct fixation system of total hip prosthesis. Arch Orthop Traumat Surg 100:11-17.

Jones, H.H., J.D. Priest, W.C. Hayes, C.C. Tichenor, and D.A. Nagel (1977) Humeral hypertrophy in response to exercise. J Bone Joint Surg 59A:204-208.

Justus, R., and J. Luft (1970) A mechanochemical hypothesis for bone remodeling induced by mechanical stress. Calcif Tiss Res 5:222-235.

Kaufer, H., and L.S. Matthews (1981) Spherocentric arthroplasty of the knee. Clinical experience with an average four year follow-up. J Bone Joint Surg 63A:545-559.

Kester, M.A., S.D. Cook, H.G. French, J. Harris, R.J. Haddad, and R. Yapp (1984) An evaluation of partially porous coated titanium hips. Trans 30th ORS 9:346.

Klever, F.J., R. Klumpert, J. Horenberg, H.J. Grootenboer, D.H.V. Campen, and T. Pauly (1985) Global mechanical properties of trabecular bone: experimental determination and prediction from a structural model.

In S.M. Perren and E. Schneider (eds): Biomechanics: Current Interdisciplinary Research. Dordrecht, Martinus Nijhoff Publishers, pp. 167-172.

Lanyon, L.E. (1974) Experimental support for the trajectorial theory of bone structure. J Bone Joint Surg **56B**:160-166.

Lanyon, L.E., W.G.J. Hampson, A.E. Goodship, and J.S. Shah (1975) Bone deformation recorded in vivo from strain gages attached to the human tibial shaft. Acta Orthop Scand **46**:256-268.

Lanyon, L.E., I.L. Paul, C.T. Rubin, E.L. Thrasher, R. DeLaura, R.M. Rose, and E.L. Radin (1981) In vivo strain measurements from bone and prosthesis following total hip replacement. J Bone Joint Surg **63A**:989-1001.

Lewallen, D.G., R.S. Bryan, and L.F.A. Peterson (1984) Polycentric total knee arthroplasty: A ten year follow-up study. J Bone Joint Surg **66A**:1211-1218.

Lindahl, O., and A.G.H. Lindgren (1967) Cortical bone in man. I. Variation in the amount and density with age and sex. II. Variation in tensile strength with age and sex. Acta Orthop Scand **38**:133-147.

Linder, L., L. Lindberg, and A. Carlsson (1983) Aseptic loosening of hip prostheses: A histologic and enzyme histochemical study. Clin Orthop Rel Res **175**:93.

Lindwer, J., and A.V.D. Hooff (1975) The influence of acrylic cement on the femur of the dog. A histological study. Acta Orthop Scand **46**:657-671.

Marmor, L. (1976) Femoral loosening in total hip replacement. Clin Orthop Rel Res **121**:116-119.

McCarthy, T.C., and M.K. Wells (1977) Mechanical properties of the bone-

prosthesis interface: A study of total hip joint prostheses stabilized with methylmethacrylate and porous ceramic. Biomed Sci Instrum **13**:41-46.

McElhaney, J.H., J.L. Fogle, J.W. Melvin, R.R. Haynes, V.L. Roberts, and N.M. Alem (1970) Mechanical properties of cranial bone. J Biomech 3:495-511.

Medige, J., E.R. Mindell, and T. Doolittle (1982) Remodeling of large, persistent bone defects. Clin Orthop Rel Res **169**:275-290.

Merz, W.A. (1967) Die streckenmessung an gerichteten strukturen im mikroskop und ihre anwendung zur bestimmung von oberflachen- volumen-relationen im knochengewebe. Mikroskopie 22:132-142.

Merz, W.A., and R.K. Schenk (1970a) Quantitative structural analysis of human cancellous bone. Acta Anat **75**:54-66.

Merz, W.A., and R.K. Schenk (1970b) A quantitative histological study on bone formation in human cancellous bone. Acta Anat **76**:1-15.

Meyer, H. (1867) Die architektur der spongiosa. Arch Anat Phys **47**:615-628.

Muellar, K.H., A. Trias, and R.D. Ray (1966) Bone density and composition. Age-related and pathological changes in water and mineral content. J Bone Joint Surg **48A**:140-148.

Murray, R.P., W.C. Hayes, W.T. Edwards, and J.D. Harry (1984) Mechanical properties of the subchondral plate and the metaphyseal shell. Trans 30th ORS **9**:197.

Oh, I., and W.H. Harris (1978) Proximal strain distribution in the loaded femur. An in vitro comparison of the distributions in the intact femur and after insertion of different hip-replacement femoral components. J Bone Joint Surg **60A**:75-85.

Park, J.B. (1979) Biomaterials. New York, Plenum Press.

Park, J.B., W. Barb, G.H. Kenner, and A.F.v.o.n. Recum (1982) Intramedullary fixation of artificial hip joints with bone cement-precoated implants. J Biomed Mat Res **16**:459-469.

Pellicci, P.M., E.A. Salvati, and H.J. Robinson (1979) Mechanical failures in total hip replacement requiring reoperation. J Bone Joint Surg **61**A:28-36.

Peterson, R.E. (1974) Stress Concentration Factors. : John Wiley & Sons, Inc.. Pilliar, R.M. (1983) Powder metal-made orthopedic implants with porous surface for fixation by tissue ingrowth. Clin Orthop Rel Res **176**:42-51.

Pilliar, R.M., H.U. Cameron, R.P. Welsh, and A.G. Binnington (1981) Radiographic and morphologic studies of load-bearing porous- surfaced structured implants. Clin Orthop Rel Res **156**:249.

Pugh, J.W., E.L. Radin, and R.M. Rose (1974) Quantitative studies of human subchondral cancellous bone. J Bone Joint Surg **56**A:313-321.

Pugh, J.W., R.M. Rose, and E.L. Radin (1973a) Elastic and viscoelastic properties of trabecular bone: Dependence on structure. J Biomech **6**:475-485.

Pugh, J.W., R.M. Rose, and E.L. Radin (1973b) A structural model for the mechanical behavior of trabecular bone. J Biomech **6**:657-670.

Radin, E.L., R.B. Orr, J.L. Kelman, I.L. Paul, and R.M. Rose (1982) Effect of prolonged walking on concrete on the knees of sheep. J Biomech **7**:487-492.

Radin, E.L., H.G. Parker, J.W. Pugh, R.S. Steinberg, I.L. Paul, and R. M. Rose (1973) Response of joints to impact loading-III. J Biomech **6**:51-57.

Rahn, B.A. (1980) Polychrome fluorescence labeling of bone formation. Instrumental aspects and experimental use. In: Zeiss Manual on Fluorescence Microscopy, pp. 36-39.

Raux, P., P.R. Townsend, R. Miegel, R.M. Rose, and E.L. Radin (1975) Trabecular architecture of the human patella. J Biomech **8**:1-7.

Reckling, F.W., M.A. Asher, and W.L. Dillon (1977) A longitudinal study of the radiolucent line at the bone-cement interface following total joint-replacement procedures. J Bone Joint Surg **59A**:355-358.

Rodan, G.A., L.A. Bourret, A. Harvey, and T. Mensi (1975) Cyclic AMP and cyclic GMP: mediators of the mechanical effects on bone remodeling. Science **189**:467-469.

Rose, R.M., R.B. Martin, R.B. Orr, and E.L. Radin (1984) Architectural changes in the proximal femur following prosthetic insertion: Preliminary observations of an animal model. J Biomech **17**:241-249.

Saltykov, S.A. (1958) Sterometric Metallography, 2nd Edition. Moskow, Metallurgizdat.

Salvati, E.A., P.D. Wilson, M.N. Jolley, F. Vakili, P. Aglietti, and G.C. Brown (1981) A ten-year follow-up study on our first one hundred consecutive Charnley total hip replacements. J Bone Joint Surg **63A**:753-767.

Schoenfeld, C.M., and G.J. Conard (1979) Monomer release from methacrylate bone cements during simulated in vivo polymerization. J Biomed Mat Res **13**:135-147.

Shoji, H., S. Karube, R.D. Dambrosia, E.J. Dabezies, and D.R. Miller (1983) Biomechanical features of pseudomembrane at the bone-cement interface of loosened total hip prostheses. J Biomed Mat Res **17**:669.

Sih, G.C., and P. Matic (1981) Failure prediction of the total hip

prosthesis system. J Biomech **14**:833-841.

Singh, I. (1978) The architecture of cancellous bone. J Anat **127**:305-310.

Snyder, B., G. Strang, W.C. Hayes, and G. Norris (1983) Application of structural geometry optimization techniques in the microstructural remodeling of trabecular bone. ASME Advances in Bioengineering, 137-138.

Snyder, B.D. (1987) Anisotropic Structure-Property Relations for Trabecular Bone. Philadelphia, U Penn PhD Thesis.

Snyder, B.D., W.C. Hayes, and W.M. Saltzman (1986) A general purpose, automated system for the quantitative description of anisotropic structures. Euro Soc of Biomech (Submitted).

Spector, M., R.J. Davis, E.M. Lunceford, and S.L. Harmon (1983) Porous polysulfone coatings for fixation of femoral stems by bony ingrowth. Clin Orthop Rel Res **176**:34-41.

Stauffer, R.N. (1982) Ten year follow-up study of total hip replacement with particular reference to roentgenographic loosening of the components. J Bone Joint Surg **64A**:983-990.

Steinemann, S.G. (1985) Bone remodeling - what are the parameters?. In S.M. Perren and E. Schneider (eds): Biomechanics: Current Interdisciplinary Research. Dordrecht, Martinus Nijhoff Publishers, pp. 215-220.

Stone, J.L., B.D. Snyder, W.C. Hayes, and G.L. Strang (1984) Three-dimensional stress-morphology analysis of trabecular bone. Trans 30th ORS **9**:199.

Strang, G. (1976) Linear Algebra and Its Applications. New York, Academic Press, Inc.

Sutherland, C.J., S.H. Wilde, L.S. Borden, and K.E. Marks (1982) A ten year follow up of 100 consecutive Muller curved-stem total hip arthroplasties. J Bone Joint Surg **64**A:970.

Svensson, N.L., S. Valliappan, and R.D. Wood (1977) Stress analysis of human femur with implanted Charnley prosthesis. J Biomech **10**:581-588.

Tarr, R.R., J.L. Lewis, D. Jaycox, A. Sarmiento, J. Schmidt, and L.L. Latta (1979) Effect of materials, stem geometry and collar-calcar contact on stress distribution in the proximal femur with total hip. Trans 25th ORS **4**:34.

Tew, M., and W. Waugh (1982) Estimating the survival time of knee replacements. J Bone Joint Surg **64**B:579-582.

Thompson, S.D. (1917) On Growth and Form. Cambridge, University Press.

Townsend, P.R., P. Raux, R.M. Rose, R.E. Miegel, and E.L. Radin (1975) The distribution and anisotropy of the stiffness of cancellous bone in the human patella. J Biomech **8**:363-367.

Townsend, P.R., R.M. Rose, and E.L. Radin (1975) Buckling studies of single human trabeculae. J Biomech **8**:199-201.

Uhthoff, H.K., and F.L. Dubuc (1971) Bone structure changes in the dog under rigid internal fixation. Clin Orthop Rel Res **81**:165-170.

Underwood, E.E. (1970) Quantitative Stereology. Reading, Addison-Wesley.

Wakamatsu, E., and H.A. Sissons (1969) The cancellous bone of the iliac crest. Calc Tiss Res **4**:147-161.

Weaver, J.K., and J. Chalmers (1966) Cancellous bone: its strength and changes with aging and an evaluation of some methods for measuring mineral content. J Bone Joint Surg **48**A:289-298.

Weibel, E.R., and H. Elias (1967) Quantitative Methods in Morphology. New York, Springer Verlag.

Welsh, R.P., R.M. Pilliar, and I. Macnab (1971) Surbical implants-the role of surface porosity in fixation to bone and acrylic. J Bone Joint Surg **53A**:963.

Whitehouse, W.J. (1974) The quantitative morphology of anisotropic trabecular bone. J Microscopy **101**:153-168.

Whitehouse, W.J. (1975) Scanning electron micrographs of cancellous bone from the human sternum. J Path **116**:213-223.

Whitehouse, W.J. (1977) Cancellous bone in the anterior part of the iliac crest. Calc Tiss Res **23**:67-76.

Whitehouse, W.J., and E.D. Dyson (1974) Scanning electron microscope studies of trabecular bone in the proximal end of the human femur. J Anat **118**:417-444.

Whitehouse, W.J., E.D. Dyson, and C.K. Jackson (1971) The scanning electron microscope in studies of trabecular bone from a human vertebral body. J Anat **108**:481-496.

Willert, H.-.G., J. Ludwig, and M. Semlitsch (1974) Reaction of bone to methacrylate after hip arthroplasty. A long-term gross, light microscopic, and scanning electron microscopic study. J Bone Joint Surg **56A**:1368-1382.

Williams, J.L., and J.L. Lewis (1982) Properties and an anisotropic model of cancellous bone from the proximal tibial epiphysis. J Biomech Eng **104**:50-56.

Wolff, J. (1892) Das Gesetz der Transformation der Knochen. Berlin, Hirschwald.

Wright, T., P.W. Hughes, P.A. Torzilli, and P.D. Wilson (1979) A method for the postmortem evaluation of an in situ total hip replacement. J Bone Joint Surg **61**A:661.